New tools for understanding cancer evolution and drug resistance

Julia Linnea Kallberg

Université Paris Cité

Ecole doctorale MTCI 563, Médicament, Toxicologie, Chimie, Imageries
Centre de Recherche des Cordeliers, Laboratoire équipe MEPPOT

New tools for understanding cancer evolution and drug resistance

Par Julia Källberg

Thèse de doctorat d'interface chimie-biologie

Dirigée par Valérie Taly

Présentée et soutenue publiquement le 07/12/2022

Devant un jury composé de :

M. Pierre Martineau – Directeur de Recherche - Université de Montpellier - Rapporteur
Mme. Charlotte Proudhon – Chargée de Recherche - Institut Curie -Rapporteur
Mme. Valérie Taly - Directeur de Recherche- Université Paris Cité - Directeur de thèse
M. Jean-Christophe Baret – Professeure - Université de Bordeaux - Examinateur
M. Xavier Coumoul – Professeure - Université Paris cité - Examinateur

Université Paris Cité

New tools for understanding cancer evolution and drug resistance

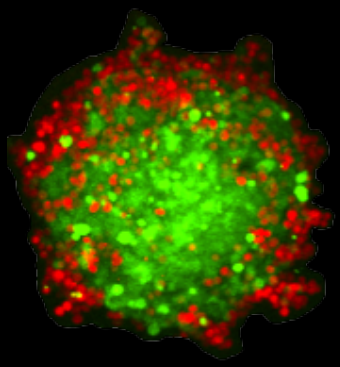

Julia Källberg

Acknowledgements

I would mainly like to give thanks to Valérie Taly and Wenjin Xiao for without whom this thesis would not have been possible. Thank you to Valerie Taly for being an excellent advisor in conducting research and career development. Her knowledge and research experience have encouraged me throughout this project. And to Wenjin Xiao for her assistance at every stage of this project, especially for all the help in planning and performing experiments. I am grateful to all of those with whom I have had the pleasure to work with during this time, mainly the all the people in the MEPPOT team whom I have learned a lot from. I would also like to thank all the members of the EVOdrops consortium for all the nice workshops. A special thanks to the Bordeaux team Jean-Christophe Baret, David van Assche, and Alejandra Gadea for a great secondment at their lab. I would like to thank the people at the Centre d'Histologie, d'Imagerie et de Cytométrie for all their assistance. Especially to Helene Fohrer and Christophe Klein for their expertise in the platforms. I would also like to thank all the team members at the company Okumera, which we had a nice collaboration with at the final stages of this thesis project Especially thanks to Layla Fuoco, Raphaël Tomasi and Sandra Jernström. Lastly, I would like to thank my family for their help and support.

Abstract

New tools for understanding cancer evolution and drug resistance

Colorectal cancer (CRC) is one of the most common cancers and one of the leading causes of cancer related deaths worldwide. CRC is a heterogeneous disease where there can be differences found between multiple tumors in the body referred to as inter-tumor heterogeneity, or there can be genetic differences found within one tumor are referred to as intra-tumor heterogeneity. Moreover, one of the largest issues in treatment of CRC is the development of drug resistant cells caused by therapeutic pressure. The underlying cause of the tumor drug resistance is largely due to the intra-tumor heterogeneity of CRC. It is therefore of great importance to increase our knowledge of the underlying resistance mechanisms as well as the impact of intra-tumor heterogeneity on these processes. After a presentation of CRC, the current manuscript describes new tools that can be used for understanding intra-tumor heterogeneity and underlying mechanisms that are responsible for drug resistance. Using Multi-Cellular Tumor Spheroids (MCTSs) as tumor models, which mimics the *in vivo* architecture of tumors, we explored the impact of inter-tumor heterogeneity on chemotherapeutic treatment (5-FU) and start to characterize resistance mechanisms. Using different tumor models we observed cell-to-cell crosstalk during chemotherapeutic treatment where sub population of cells with certain characteristics had an increased drug tolerance. To get a deeper understanding of the cause of increased drug resistance and continue our investigation of drug resistance mechanisms we have studied potential key mediators involved. These observed results suggest that intra-tumor heterogeneity have huge impact in the overall tumor development and progression.

Key words:

Colorectal Cancer (CRC), Consensus Molecular Subtype (CMS), Intra-tumor heterogeneity, Drug resistance, 5-FU, Cell crosstalk, Cell secretome, Spheroids, Microfluidics

Résumé

Nouveaux outils pour comprendre l'évolution du cancer et la résistance aux médicaments

Le cancer colorectal (CCR) est l'un des cancers les plus fréquent et la principale cause de décès due au cancer dans le monde. Le CRC est une maladie hétérogène, où il peut y trouver des différences multiples au sein de chaque tumeur s'étant propagée dans le corps, que l'on surnomme hétérogénéité inter-tumeur. De plus, l'une des problématiques les plus communes à la médication du CCR est la résistance des cellules au traitement de chimiothérapie causé par la pression thérapeutique. La causalité sous-jacente à la résistance aux traitements thérapeutique est largement dû à l'hétérogénéité intra-tumeur du CCR. Ce qui est par conséquent une opportunité inéluctable de pouvoir améliorer nos connaissances des mécanismes sous-jacents de résistance, aussi bien que notre compréhension de l'impact de l'hétérogénéité intra-tumeur sur ces processus de résistance. Après une présentation du CRC, le présent manuscrit introduit les outils pouvant être utilisés pour comprendre l'hétérogénéité intra-tumorale et les mécanismes de résistance aux traitements médicales. En utilisant des sphéroïdes multicellulaires (MCTSs) comme modèles tumoraux, permettant de mimer l'architecture des tumeurs *in vivo*, nous avons exploré l'impact de l'hétérogénéité tumorale sur la réponse à un traitement chimio-thérapeutique (5-FU) et caractérisé les mécanismes de résistance. Par conséquence, en utilisant différents modèles de cellule nous avons observé une communication transcellulaire durant un traitement thérapeutique ou une sous population cellulaire avec certaines caractéristiques ont développé une résistance au traitement. Ainsi nous avons continué nos investigations au travers des mécanismes de résistance. Enfin, nous avons étudié les médiateurs impliqués dans ces processus, afin d'avoir une meilleure compréhension des causes d'augmentation de cette résistance. Ces résultats suggèrent que l'hétérogénéité tumorale a un impact significatif sur le développement et la progression tumorale.

Mots-clés:

Cancer colorectal (CCR), Consensus Molecular Subtype (CMS), Hétérogénéité intratumorale, Résistance thérapeutique, 5-FU, Sécrétome des cellules, Sphéroïdes, Microfluidiques

Outline

Chapter 1 introduces the background behind this work, it presents cancer, specifically CRC, as a global health concern. Various factors affecting disease progression and resistance development are discussed. Different biomarkers that can be used in cancer prognosis and treatment are also introduced. Lastly, different tumor models are introduced, including *in vivo* models and *in vitro* models. A larger focus is placed on *in vitro* models as they are used throughout this thesis.

Chapter 2 begins by introducing a classification system for CRC, known as the Consensus Molecular Subtype (CMS) system. This classification system has been developed from whole tumor transcriptomic analysis where, based on gene expression patterns, CRC was divided into four subgroups (CMS1 to CMS4). Furthermore, it is well established that CRC is a heterogeneous disease, and this heterogeneity has a large impact on resistance mechanisms. Therefor we present a study where we use the CMS classification system to mimic the heterogeneity of CRC. Here we co-culture CMS cell lines as Multi-Cellular Tumor Spheroid models (MCTS). During drug treatment an increased cell survival was observed in CMS4 cells when cultivated with CMS1 cells as compared to monocellular cultures. This was investigated further by treating cells with Conditioned Media (CM) and culturing cells in transwells, whereby similar effects were observed where CMS1 cells stimulated the outgrowth and migration of CMS4 cells. We thus investigated if this crosstalk between the cells could be due to cell secreted molecules. Potential key mediators in the cell secretome were analyzed to get insights in the key components and potential pathways involved in these processes.

Chapter 3 explore further development of drug resistance in CRC. Here we studied the impact of the presence of both Drug Sensitive Cancer Cells (DSCC) and Drug Resistant Cancer Cell (DRCC) on drug efficacy using a tumor model. In this aim, DRCCs were developed from the original HCT116 CRC cell line, and co-cultured with DSCCs of the same genetic background, using MCTSs. Cell-to-cell crosstalk was observed between

the DSCCs and DRCCs where the DRCCs stimulated the outgrowth of the DSCCs. Similar effects were observed when treating the DRCCs with Conditioned Medium (CM) from the DSCCs. As cell crosstalk was also observed in this context, further investigation was done on the cell secretome to identifying the key molecular components and deeper analysis was performed to understanding how these compounds influence tumor growth.

Chapter 4 presents novel approaches for culturing cells as 3D spheroids using microfluidic platforms. Spheroids were cultured using microfluidics in form of an automated platform where homogeneous spheroids were produced at high throughput. This work, done in collaboration with the company Okumera, shows co-culture of DSCCs and DRCCs using microfluidic platforms. Here we show that spheroids can be automatically generated at a high throughput and the cells maintain a high cell viability over time.

Long résumé

Le cancer colorectal (CCR) est l'un des cancers les plus courants et l'une des principales causes de décès liés au cancer dans le monde. Le CCR est une maladie hétérogène où il peut y avoir des différences trouvées entre les tumeurs multiples dans le corps appelé hétérogénéité inter-tumeur, ou il peut y avoir des différences génétiques trouvées dans une tumeur sont appelées hétérogénéité intratumorale. De plus, le développement de cellules pharmacorésistantes causées par la pression thérapeutique est l'un des principaux problèmes de traitement du CCR. La thèse commence par présenter le contexte derrière ce travail. Le chapitre 1 traite du cancer, plus précisément du cancer de la CCR, en tant que problème de santé mondial et de divers facteurs qui influent sur la progression de la maladie et le développement de la résistance. Différents biomarqueurs qui peuvent être utilisés dans le pronostic du cancer et le traitement sont également introduits. Enfin, différents modèles de tumeurs sont introduits, y compris des modèles in vivo et in vitro. Nous nous sommes plus appuyés sur les modèles in vitro car ils sont utilisés tout au long de cette thèse.

Le but de cette thèse était d'étudier les mécanismes clés qui influencent le développement et la progression de la tumeur du CCR en utilisant de nouveaux outils et méthodes. Un accent particulier a été mis sur l'hétérogénéité intratumorale, où son impact sur la progression tumorale et la résistance aux médicaments a été étudié. Le premier objectif était alors d'étudier l'impact de l'hétérogénéité intratumorale sur le CCR en se concentrant sur la classification SMC (Sous-type Moléculaire Consensuel). Dans cette première partie de recherche, décrite au chapitre 2, nous avons cherché à imiter l'hétérogénéité tumorale du CCR en co-cultivant différentes lignées cellulaires SMC. On a signalé que les tumeurs du CCR comprennent quatre sous-types moléculaires (SMC) de consensus qui ont été identifiés à partir de profils de transcription tumorale entiers. Le système s'est avéré utile pour comprendre la biologie des tumeurs du CCR et permet de prédire le pronostic. La classification SMC sert de cadre pour mieux comprendre l'hétérogénéité intratumorale du CCR. Pour développer davantage cela,

les tumeurs CCR ont été classées en sous-types moléculaires basées sur l'analyse transcriptomique de plus de 4000 échantillons CCR. D'après le modèle d'expression génétique, quatre sous-groupes moléculaires consensuels distincts (SMC1 à SMC4) présentent des signatures biologiques différentes.

Dans la plupart des cancers, y compris dans le CCR, il a été démontré que l'hétérogénéité intratumorale favorise la résistance aux médicaments et la progression. En outre, notre groupe de recherche a déjà montré que plus de 55% des tumeurs sont composées de SMC mixte qui a été associée à des résultats tumoraux plus mauvais. Ces résultats soulèvent la question de savoir si la communication intratumorale entre les sous-types de SMC contribue à la progression tumorale et à la résistance thérapeutique dans le CCR. Ainsi, dans le chapitre 2, pour imiter l'hétérogénéité intratumorale de CCR en co-culture des cellules de différents SMC. Nous avons cherché à créer de nouvelles méthodes pour étudier la progression des tumeurs et les mécanismes de résistance en générant des STMC (Sphéroïdes Tumoraux Multi-Cellulaires) composés de SMC multiples. Ce modèle peut à l'avenir servir de système utile pour étudier les interactions cellule à cellule et l'effet de ces interactions sur la résistance aux médicaments.

Il a été observé que les systèmes de co-culture SMC avaient une tolérance accrue aux médicaments par rapport aux cellules cultivées comme témoins de monoculture. Cela a démontré que l'interaction entre le SMC1 et le SMC4 a un impact important sur la résistance aux médicaments des cellules. Pour approfondir l'étude de ces mécanismes, le CM des cellules SMC1 a été appliqué au SMC4, ce qui a montré que le sécrétome cellulaire des cellules SMC1 augmentait la tolérance du SMC4 à la chimiothérapie 5-FU. D'autres expériences ont démontré que le sécrétome SMC1 augmentait la tendance migratoire des cellules SMC4 pendant le traitement chimiothérapeutique. Cela a mené à l'étude du sécrétome cellulaire SMC1 où les métabolites clés ont été analysés pour détecter des voies spécifiques qui étaient impliquées dans ces mécanismes. Dans cette étude, nous montrons que le sécrétome cellulaire a un impact sur la prolifération cellulaire et la progression sphéroïde.

Comme évoqué précédemment, le développement de la résistance aux médicaments est l'un des principaux problèmes du CCR. Par conséquent, le deuxième objectif était d'étudier les facteurs clés qui influent sur la façon dont les cellules développent la résistance en analysant les mécanismes et les voies clés qui sont au cœur du développement de la résistance. À partir de là, nous nous sommes concentrés sur l'effet de l'hétérogénéité intratumorale sur la résistance et la progression des tumeurs, en étudiant l'effet de la co-culture des cellules cancéreuses sensibles aux médicaments (CCSM) et des cellules cancéreuses résistantes aux médicaments (CCRM). Plus précisément, nous avons décidé de privilégier l'étude des effets de la co-culture des CCSM et des CCRM et de leurs interactions sous chimiothérapie. Par conséquent, comprendre la base moléculaire de la chimiorésistance aidera à identifier de nouvelles cibles thérapeutiques qui mèneront finalement à un traitement amélioré pour les patients. Au chapitre 3, nous explorerons le développement de la résistance aux médicaments traitant le CCR. La mise au point de cellules pharmacorésistantes provoquée par la pression thérapeutique est l'un des plus grands problèmes dans le traitement du CCR. Après une exposition à long terme, la plupart des plans de traitement entraîneront une résistance aux médicaments. Il a été suggéré que la cause de cette résistance est à la fois intrinsèque et extrinsèque. Certains des facteurs biologiques comprennent l'évolution clonale des tumeurs, le développement des CSC (Cellules Souches Cancéreuses), l'expression altérée des pompes à efflux médicamenteuses, la modulation des canaux ioniques ou le métabolisme altéré des médicaments. Au cours des dernières décennies, plusieurs mécanismes de résistance moléculaire ont été démêlés, mais il y a encore de nombreuses questions qui sont inconnues concernant les mécanismes de résistance et les changements potentiels qui entraînent des cellules pharmacorésistantes sont sous-explorées. Dans nos observations précédentes, nous avons imité l'hétérogénéité intratumorale du CCR en cultivant conjointement différentes cellules du SMC sous forme de STMC. Nous avons observé que les systèmes de co-culture affectaient la progression de la tumeur via les molécules sécrétées par les cellules. On sait que les tumeurs sont souvent composées de cellules résistantes aux médicaments et de cellules sensibles. De plus, il a déjà été

démontré que les cellules cancéreuses résistantes aux médicaments (CCRM) peuvent modifier le comportement des cellules cancéreuses sensibles aux médicaments (CCSM) grâce à des molécules sécrétées par les cellules, ce qui entraîne une résistance accrue aux médicaments. Une voie de résistance médicamenteuse moins étudiée implique que les CCSM modifient le comportement des CCRM menant à la progression tumorale, observée dans le mélanome. Ces résultats soulèvent maintenant la question de savoir si des effets similaires pourraient être détectés dans d'autres cancers. Nous nous penchons ici sur les mécanismes de résistance, nous présentons notre étude de la diaphonie CCSM-CCRM dans le CCR et de ses mécanismes sous-jacents de résistance à la chimiothérapie. En cultivant conjointement les CCSM et les CCRM en tant que STMC (sphéroïdes tumoraux multi-cellulaires), nous pourrions observer une augmentation de la survie cellulaire des CCRM sous traitement médicamenteux. Pour étudier plus en détail ces mécanismes et déterminer s'ils sont dus à des molécules sécrétées par des cellules, on a appliqué le milieu conditionné (MC) des cellules souches cancéreuses du CCR. Dans le cadre du traitement médicamenteux 5-FU, une survie cellulaire accrue a été observée lorsque les CRDC ont été traités en MC à partir de CCSM. Ces résultats observés suggèrent que les CSC (cellules souches cancéreuses) peuvent avoir un impact important sur le développement et la progression globale de la tumeur. Les stratégies élaborées pourraient constituer des outils novateurs et pertinents qui pourraient nous aider à comprendre comment les cellules développent une résistance aux médicaments anticancéreux. En développant de nouvelles stratégies pour les co-cultures de cellules SMC (sous-type moléculaire consensuel), nous avons identifié des mécanismes potentiels impliqués dans la diaphonie entre ces cellules. Nous avons commencé par étudier les interactions potentielles entre diverses molécules trouvées dans le sécrétome cellulaire de HCT116 CM_5-FU et CM_DMSO en analysant les métabolites cellulaires (détails dans le chapitre 2). Par la suite, nous avons poursuivi notre enquête sur le milieu conditionné HCT116 en détectant et caractérisant leurs vésicules extracellulaires (VE). Dans de futures études, nous espérons en apprendre davantage sur ces mécanismes et leur effet sur la progression de la tumeur afin de mieux comprendre comment se développe la pharmacorésistance. Par conséquent, nous souhaitons séparer les métabolites solubles des VE pour étudier la contribution des

différents composants dans le sécrétome cellulaire. Une fois que cela a été déterminé, le séquençage de nouvelle génération (SNG) peut être effectué sur les substrats et des voies potentiellement spécifiques peuvent être démêlées.

Nous avons commencé par une étude de validation de principe dans le cadre pour laquelle les CCSM et les CCRM étaient des co-cultures en tant que STMC utilisant des plaques en "U" non adhérentes. Dans les systèmes de co-culture, la discussion croisée était observée entre les cellules lors d'un traitement médicamenteux 5-FU. Nous avons découvert que le sécrétome des cellules souches cancéreuses augmentait la prolifération du CCR. Pour consolider le travail, nous avons visé à utiliser les plateformes microfluidiques pour créer des centaines de sphéroïdes uniformes dans un délai relativement court. Le chapitre 4 présente de nouvelles approches pour la culture des cellules sous forme de sphéroïdes 3D utilisant des plateformes microfluidiques. Les sphéroïdes ont été cultivés en utilisant la microfluidique sous forme d'une plateforme automatisée où des sphéroïdes homogènes ont été produits à haut débit. Dans le groupe de *Charles Baroud, Sart et al*. ont décrit une approche microfluidique pour la culture sphéroïde sur puce. Cette méthode est basée sur la microfluidique des gouttelettes où les cellules sont encapsulées dans des gouttelettes qui peuvent être piégées sur la puce dans des pièges à gouttelettes fixés. En utilisant cette méthode, des centaines de sphéroïdes pourraient être produits dans un délai relativement court. La méthode a utilisé des pièges qui ont permis aux sphéroïdes d'être confinés sur la micropuce, par conséquent, des images précises pourraient être effectuées en temps réel. Cela a permis de surveiller la distribution cellulaire dans les sphéroïdes au fil du temps. Afin de prolonger ces travaux, Tomasi *et al* a modifié certaines des caractéristiques de conception de la puce qui a permis d'emprisonner facilement des gouttelettes secondaires. Les gouttelettes secondaires peuvent être utilisées pour ajouter de nouveaux milieux de culture cellulaire aux sphéroïdes, ce qui permet une culture cellulaire plus longue sur la puce. Il est également utile pour le dépistage des drogues, car les drogues mélangées avec du colorant fluorescent peuvent être ajoutées aux gouttelettes, permettant ainsi d'analyser différentes drogues et

concentrations de drogues sur la même puce. À l'aide de cette méthode, *Tomasi et al*. pourraient effectuer un dépistage de médicaments à haut débit où les sphéroïdes individuels pourraient être surveillés en temps réel. Ces résultats combinés ont conduit à la création d'une entreprise appelée *Okumera* qui se spécialise dans la création de plateformes microfluidiques pour la culture des sphéroïdes. Dans cette étude, nous visons à utiliser leur plateforme pour la co-culture des cellules HCT116 et HCT116-R en tant que STMC. Nous montrons donc que les sphéroïdes peuvent être générés automatiquement à un débit élevé et les cellules maintiennent une viabilité cellulaire élevée au fil du temps. En conclusion, la Microfluidique offre de nombreux avantages pour la culture sphéroïde. Elle permet la génération de sphéroïdes homogènes de manière automatique, le contrôle précis des liquides réduisant ainsi le volume de l'échantillon, la visualisation en temps réel à l'aide de la microscopie et ressemble étroitement au tumeur micro-environnementale. Tous ces facteurs combinés rendent les systèmes de microfluidiques attrayants dans les deux cas à des fins de recherche ainsi que dans des contextes cliniques. À l'avenir, ces plates-formes pourraient être mises en œuvre dans les essais de médicaments en tant que méthodes plus fiables par rapport aux systèmes 2D normalisés. En outre, l'utilisation de cette plateforme de dépistage des drogues peut être effectuée de manière rapide et automatique. Par conséquent, nous prévoyons d'effectuer d'autres tests de dépistage de drogues sur les sphéroïdes tumoraux multi-cellulaires sur puce afin de déterminer si nous pouvons observer la diaphonie cellulaire comme nous l'avons déjà observé dans les puits. À l'avenir, la plate-forme pourrait être intégrée avec d'autres puces microfluidiques pour la dissociation sphéroïde et finalement des analyses de cellules à un seul niveau cellulaire. Il serait également possible de collecter le milieu cellulaire et d'analyser son contenu sur des plates-formes microfluidiques ou non-microfluidiques séparées. Ces types de plates-formes peuvent servir d'outil utile pour analyser la progression tumorale et les interactions cellule à cellule en temps réel.

To my friends and family,

Publications

Julia Källberg, Alexandra Harrison, Santa Berzina, Valerie March, Ivan Nemazanyy, Oliver Kepp, Guido Kroemer, Sophie Mouillet-Richard, Pierre Laurent-Puig, Valérie Taly and Wenjin Xiao. ***Intra-tumor heterogeneity and secretome-induced cell communication promote colorectal cancer evolution and chemotherapy resistance.*** *Cell Death and Disease.* Submitted 2022.

Julia Källberg, Wenjin Xiao, David Van Assche, Jean-Christophe Baret and Valerie Taly. ***Frontiers in single cell analysis: multimodal technologies and their clinical perspectives***. *Lab on a Chip.* 2022. 22 pp. 2403-2422.

Thomas Bruneau, Maxime Wack, Geoffroy Poulet, Nicolas Robillard, Aurélien Philippe, Pierre Laurent-Puig, Laurent Bélec, Jérôme Hadjadj, Wenjin Xiao, **Julia Källberg,** Solen Kernéis, Jean-Luc Diehl, Benjamin Terrier, David Smadja, Valerie Taly, David Veyer, Hélène Péré. ***Circulating ubiquitous RNA, a highly predictive and prognostic biomarker in hospitalized COVID-19 patients.*** *Clinical Infectious Diseases.* 2021.1. pp. 410–e417.

Table of Contents

Abbreviations

CRC	Colorectal Cancer
TME	Tumor Micro-Environment
ITH	Intra-Tumoral Heterogeneity
NGS	Next-Generation Sequencing
MSI	Micro-Satellite Instability
MMR	Mis-Match Repair
EMT	Epithelial-Mesenchymal Transition
MSS	Micro-Satellite Stable
CMS	Consensus Molecular Subgroups
KRAS	Kirsten Rat Sarcoma viral oncogene homologue
BRAF	v-raf murine sarcoma viral oncogene homolog B1
TP53	Tumor Protein p53
WNT	WNT/β-catenin
MYC	BHLH Transcription Factor
CSC	Cancer Stem Cells
PTEN	Phosphatase and Tensin Homologue
EGFR	Epidermal Growth Factor Receptor
VEGF	Vascular Endothelial Growth Factor
5-FU	5-Fluorouracil
5FUMP	5-Fluoro-Uridine-Mono-Phosphate
5FdUMP	5-Fluorodeoxyouridine-Mono-Phosphate
PD-1	Programmed Death receptor-1
IC50	Half-maximal Inhibitory Concentration
CM	Conditioned Medium
2D	Two-Dimensional
3D	Three-Dimensional
MCTS	Multi-Cellular Tumor Spheroid
LC	Liquid Chromatograph
LC/MS	Liquid Chromatography Mass Spectrometry
miRNA	MicroRNA

PTEN	Phosphatase and Tensin homolog deleted on chromosome ten
TCA	Tri-Carboxylic Acid
DSCCs	Drug Sensitive Cancer Cells
DRCCs	Drug Resistant Cancer Cells
FBS	Fetal Bovine Serum
EV	Extracellular Vesicle
NTA	Nanoparticle Tracking Analysis
TEM	Transmission Electron Microscopy
PDMS	Polydimethylsiloxane
LncRNA	Long non-coding RNA
VMT	Vascularized Micro-Tumor
PI	Propidium Iodide

Chapter 1

General introduction

i. Cancer

As one of the leading causes of death worldwide, cancer is one of the largest health concerns of modern times accounting for nearly 10 million deaths in 2020 (1). There are more than 200 different forms of cancer, each one has its unique biological features that requires specific therapeutic approaches (2). Normally cell growth and survival are tightly regulated processes. However during the conversion of a cell from a non-malignant state to a malignant state, the cell has undergone genetic changes referred to as "*driver mutations*" (3). Driver mutations are characterized by the acquisition of genetic mutations in specific areas within the genome. They have the ability to convert normal genes into oncogenes which works by altering gene function or amplification of gene expression leading to changes in way the cells proliferate and grow (4). However most mutations that occur in cancer are actually "*passenger mutations"* that provide no growth advantages (5).

Even though many of these mutations are well characterized, taken individually they are often not enough for the cell to turn malignant (6). In 2000, Hanahan and Weinberg proposed six hallmarks for understanding the diversity of neoplastic diseases (7). These were comprised of six biological characteristics that include sustaining proliferative signalling, evading growth suppressors, activating invasion and metastasis, enabling replicative immortality, inducing angiogenesis and resisting cell death (Figure 1.1). Taken together, these traits encompass the biological capabilities that cells acquire during the development of cancers which allows them to form malignant tumors (7)(8). In 2022, Hanahan confirmed that two additional hallmarks have been validated, as research in the two past decades have largely confirmed the importance of reprogramming of cellular metabolism and avoiding immune destruction (9).

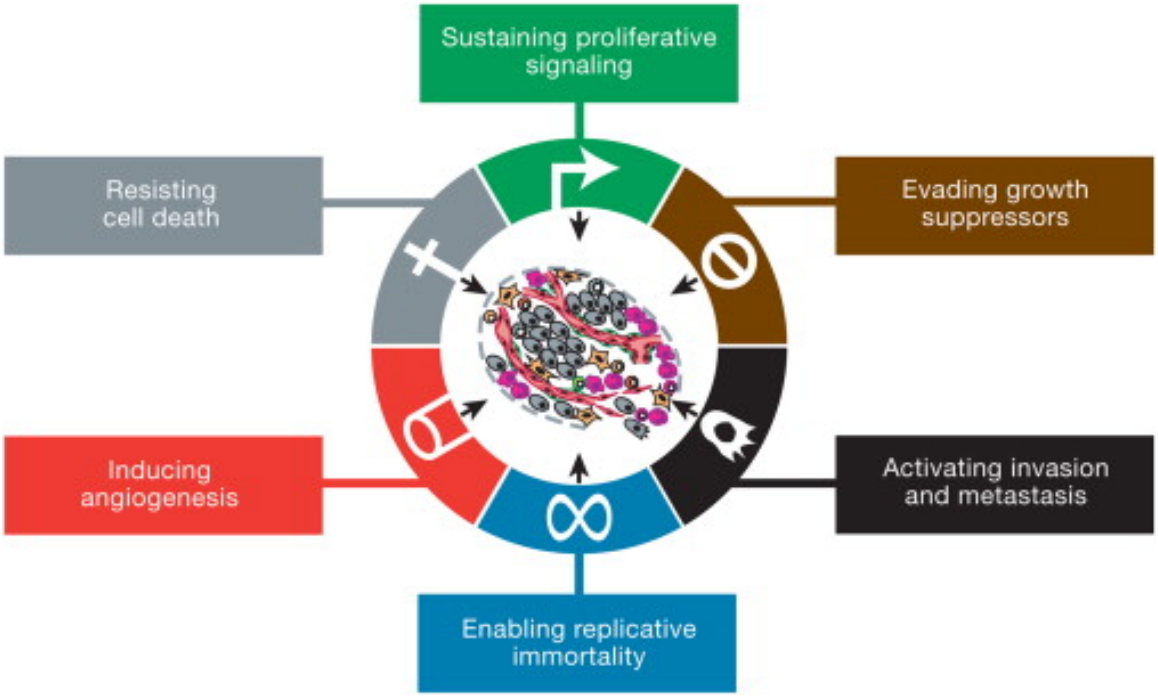

Figure 1.1. The original hallmarks of cancer

The original hallmarks of cancer consists of six biological characterisations include sustaining proliferative signalling, evading growth suppressors, activating invasion and metastasis, enabling replicative immortality, inducing angiogenesis and resisting cell death. Taken from Hanahan and Weinberg (8).

ii. Colorectal cancer

Colorectal cancer (CRC) is one of the most frequent cancer, with the third highest mortality rate of all cancers world-wide (Figure 1.2) (10) (11). Despite many advances in screening and treatment, it remains a major public health issue (12). Even though industrialized countries have made large progress in screening, early removal of tumors and personalized treatments, a large proportion of patients still experience tumor relapse and/or develop drug resistance (10). Environmental and heredity factors play important roles in the development of CRC. A substantial risk factor for CRC development is familial history accounting for approximately 5 to 6 % of all CRC cases. In these cases germline mutations have been detected that lead to an inherited predisposition to CRC (13).

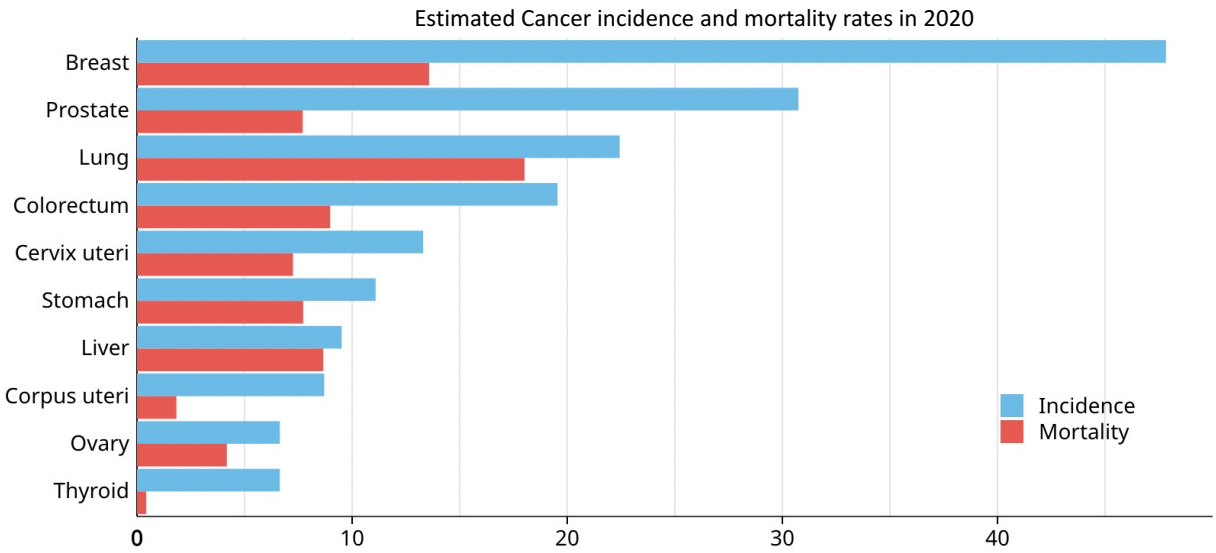

Figure 1.2. Estimated world incidence and mortality rate

The estimated age-standardized incidence rate (blue) and mortality (red) rates for all cancer in 2020. GLOBOCAN estimation project, 2020. Reprinted from WHO (1).

CRC is not a single disease, but rather a heterogeneous group of malignancies originating from cells within the gastrointestinal tract (14). There are five stages of CRC: Stage 0 and stages I through IV. In stage 0 the cancer cells can only be found in the inner mucosa lining of the bowel. The cells are not located in the epithelium or in the mucosal connective tissue layer. In stage I the cancer has continued to grow into the connective tissue layer the submucosa or into the thick outer muscle layer of the colon or rectum, the muscularis propria. In stage II colon cancer, the cancer has spread to nearby tissue or organs which are next to the bowel, but it has not yet spread to the lymph nodes or other distant parts of the body. In stage III, CRC cells have spread to one or more nearby lymph nodes, but they have not grown beyond the lymph nodes and colon wall to other parts of the body. Stage IV colon cancers have spread from the colon to distant organs and tissues. Colon cancer most often spreads to the liver, but it can also spread to other places such as the lungs, brain, peritoneum or to distant lymph nodes.

iii. Understanding tumor progression

There are several key factors that influence the way the cancer progresses. The tumor heterogeneity and its surrounding microenvironment are key factors that play large parts in how the cancer evolves.

Tumor microenvironment

The Tumor Micro-Environment (TME) is the environment surrounding the tumor which consists of a diverse mixture of cancer associated fibroblasts, endothelial cells, immune cells and other non-tumor cells all in constant interplay with the tumor (Figure 1.3) (15). This complex cellular environment has multiple functions, it is responsible for regulating tumor cells proliferation, maintain tumor stemness and controlling immune surveillance. The TME is a dynamic environment that evolves in response to changing environmental conditions and oncogenic signals from the growing tumour (16). For example, various immune cells are present within the TME which interact with the tumor cells via direct contact or through cell secreted molecules such as chemokine and cytokine signalling, which effects the behaviour of the tumor and in turn its response to therapy (17). Other cells such as endothelial cells and pericytes are actively contributing to the formation of new blood vessels that act by supporting the tumor with nutrients which is required for the cancer cells to survive and proliferate (18). The tumor progression is largely influenced by the interaction between the cancer cells and their surrounding microenvironment. Increasing evidence shows that the TME has critical roles in determining blood vessel growth (19), tumor metastasis (15) and function of the infiltrating immune cells (20). Recent studies also demonstrates that the TME is a primary driver of tumor progression which can be used as a potential drug target (15) (21) (22). This highlights the importance of analyzing the influences of the TME on dynamic process such as metastasis and cancer progression.

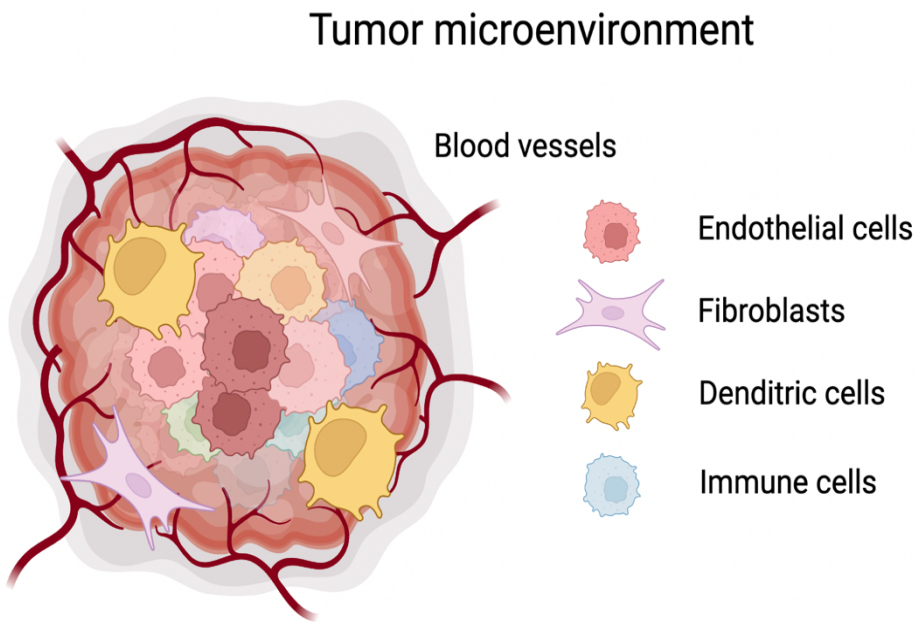

Figure 1.3. Components of the Tumor Micro-Environment

The Tumor Micro-Environment (TME) consists of a great variety of different cell types, some of the more common cells are blood vessels, endothelial cells, fibroblasts, dendritic cells and different immune cells.

Tumor heterogeneity and its impact on cancer progression

It is well established tumors can be composed of a large set of different cell types referred to as tumor heterogeneity (23). Based on morphology, tumor heterogeneity has been observed as early as the 1800s when distinct differences in the tumors regions was observed. There can be differences found between multiple tumors in the body referred to as inter-tumor heterogeneity, or there can be genetic differences found within one tumor are referred to as intra-tumor heterogeneity (Figure 1.4). Intra-tumor heterogeneity can lead to a subset of cells having varying cell proliferation rate, treatment response as well as drug resistance (23). Intra-tumor heterogeneity may originate from different mechanisms including genetic variation, epigenetic alteration, plastic gene expression, and signal transduction.

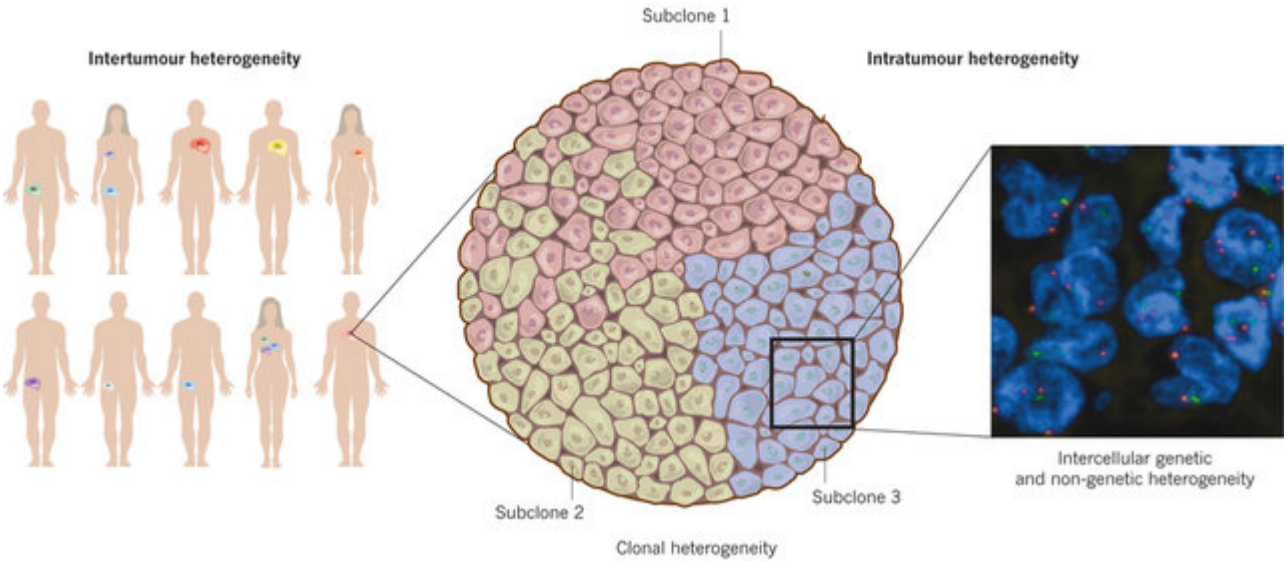

Figure 1.4. Inter-tumor heterogeneity and intra-tumor heterogeneity

The figure illustrates the differences between inter-tumor heterogeneity and intra-tumor heterogeneity. Intertumor heterogeneity refers to differences between and within patients and intratumor heterogeneity refers to genetic differences found in one tumor. The image is taken with permission from Burrel et al. (24).

Analyzing tumour heterogeneity can be crucial issue, where advances in Next-Generation Sequencing (NGS) has detected great heterogeneity between tumors (24). However there are limitations with using such methods because it is unlikely to accurately capture tumor heterogeneity due to biases such as the place the sample is taken and where the cell is in the cell cycle (25). Depending on the place the sample is taken certain cell types may be overrepresented thereby giving a skewed representation of the tumor composition. Furthermore, where the cells are in the cell cycle may also affect the transcriptome profile considering that it only represents a single snapshot in time. However, it is worth noting that dysregulation of the cell cycle is one of the cancer hallmarks and may in addition be used as a biomarker of disease. Because it has been shown that cell-cycle gene expression serves as a tumor signature considerable effort has been made to identify specific genes across the cell cycle (25). The tumor heterogeneity can at times have a clinical value but in other instances drug targeting a driver mutation might only be successful if the mutation is present in the majority of subclones (26).

Consensus molecular subtypes of colorectal cancer

To gain more understandings of the inter-tumor heterogeneity of CRC and its underlying molecular mechanisms, a large focus has been placed on classifying CRC into different subgroups. The previous classification system for CRC was based on molecular analysis, which relied on combinations of molecular features such as Kirsten Rat Sarcoma Viral Oncogene Homologue (*KRAS)*, v-raf murine sarcoma viral oncogene homolog B1 **(***BRAF)*, and Tumor Protein p53 *(TP53)* mutations, Micro-Satellite Instability (MSI), CpG island methylator phenotype, somatic copy number alterations, and activation of various molecular pathways such as WNT/β-catenin (WNT) and MYC Proto-Oncogene BHLH Transcription Factor (MYC). To further develop this, CRC tumors have been classified into molecular subtypes based on transcriptomic analysis from more than 4,000 CRC samples (27). Based on the gene expression pattern four distinct consensus molecular subgroups (CMS1 to CMS4) have been identified that all display different biological signatures (28) . The CMS1 subtype is characterized by high MSI and immune infiltration. CMS2 represents high expression of Mis-Match Repair (MMR) genes, *BRAF* mutated, upregulation of immune cells and proliferation pathways. CMS3 is identified by high frequency of *KRAS* mutations, Micro-Satellite Stable (MSS) and downregulation of pathways involved in Epithelial-Mesenchymal Transition (EMT) transition and immune system. CMS4 has increased presence of mesenchymal and stromal cells (Table 1.1). The CMS classification has prognostic value independent of the stage of the cancer, with CMS4 having a poor clinical outcome, even when treated with chemotherapy (29). (27)

Table 1.1. Consensus molecular subtypes of colorectal cancer as described by Guinney *et al.* (27).

	CMS1	CMS2	CMS3	CMS4
Incidence	14%	37%	13%	23%
Alternative name	Microsatellite instability - Immune	Canonical	Metabolic	Mesenchymal
Transcriptomic pathways	Immune infiltration and activation	WNT and MYC activation	Metabolic dysregulation	Angiogenesis, stromal infiltration
Genomic associations	MSI, high mutation count, low copy number	Chromosomal instability, low/moderate mutation count and copy number	Chromosomal instability, moderate mutation count, low/moderate copy number	Chromosomal instability, low mutation count, high copy number
Associated mutations	*BRAF* mutations		*KRAS* mutations	
Therapy response	No responds to 5-FU. Responds to Immune therapy	Responds to FOLFOX and Cetuximab	Responds to FOLFOX	No response to FOLFOX and Cetuximab. Responds to FOLFIRI

Approximately 55% of the tumors cannot be assigned to one consensus subtype, as they have mixed gene expression signatures (30). Furthermore, the current CMS classification rely on data obtained from bulk sequencing, which by nature lacks the resolution to investigate CRC tumors at the cellular level which is needed for detecting molecular signatures in small yet critical cell populations. Therefore, recent research has been focused on expanding the classification system to create a new system based on single cell data (31). There is yet a lot to learn about the CRC classification system where the ultimate goal of classifying CRC into molecular subtype is to enhance prognosis and diagnosis at

specific stages (32). Furthermore, during tumor progression subtype switching is a reoccurring event where it has been observed that anti-EGFR therapy can triggered an evolutionary shift where certain cell types swich from CMS2 to CMS4 characteristics. This was further linked to the development of secondary treatment resistance in metastatic CRC (33).

iv. Patient treatment strategies

The choice of the treatment for CRC is largely determined by the stage of the cancer. When surgery can be performed, over all 60% of cases are disease-free within five years (34). However, a large portion of patients still needs further treatment with either radiotherapy or systemic therapy (such as chemotherapy or targeted therapies) (34). For stage III patients, adjuvant chemotherapy has been the standard option for the last two decades. Of these, 5-fluorouracil (5-FU) has been used as the main treatment option (35). More recently, focus has instead been placed on targeted therapies. For example, monoclonal antibody therapies such as Dostarlimab, an immune checkpoint inhibitor, have demonstrated remarkable potential in the treatment of CRC. In a recent study it was shown that 100% of stage II or III rectal adenocarcinoma treated patients that had been treated with Dostarlimab were cured from the disease (36). Dostarlimab works by binding to Programmed Death receptor-1 (PD-1) thereby blocking it from binding to its ligands, this in turn triggers the immune system to attack the cancer.

Another treatment option is to treat the cancer in a three-dimensional way focusing on attacking the cancer in a full-scale manner rather than using individually targeted drugs that target single features (37). This multiscale approach can be directed to focus on the cancer hallmarks as targets for a more full-scale treatment where multiple hallmarks can be targeted simultaneously or in a subsequential manner (Figure 1.5). For example, monoclonal antibodies such as Anti-Epidermal Growth Factor Receptor (EGFR) and Anti-Vascular Endothelial Growth Factor (VEGF) that works by reducing the amount of new blood vessels from forming thereby reducing cell proliferation signalling (Figure 1.5) (38).

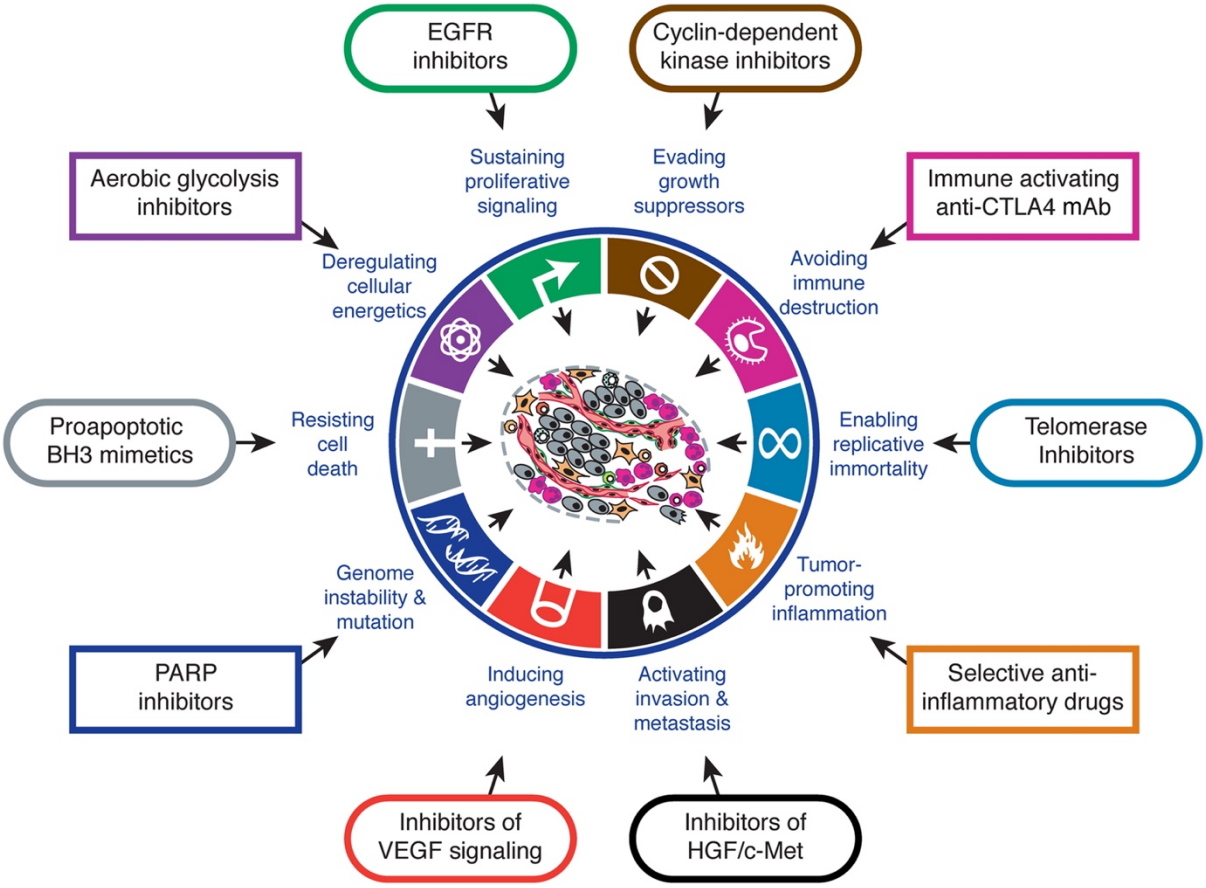

Figure 1.5. The new hallmarks of cancer and their therapeutic targeting

Examples of cancer drugs that interfere with each of the cancer hallmarks (as described by Hanahan et al. in 2022) are indicated. The eight hallmarks currently comprise the acquired capabilities for sustaining proliferative signaling, evading growth suppressors, resisting cell death, enabling replicative immortality, inducing/accessing vasculature, activating invasion and metastasis, reprogramming cellular metabolism, and avoiding immune destruction. Two new "emerging hallmarks" phenotypic plasticity and disrupted differentiation are also illustrated in the figure. The drugs have been shown to target different cancer hallmarks. The examples are drugs that have been developed or are in clinical trials. Taken from Hanahan and Weinberg (8).

v. Drug resistance mechanisms

Despite significant advancements in the treatment of patients, resistance to therapies still remains a major issue (26). Multiple theories have been proposed for how cells develop resistance. An early theory of how drug resistance is developed is called the Goldie-Coldman theory which was made to precisely model cancer progression (39). This

hypothesis states that cancer cells acquire spontaneous mutations that cause drug resistance. The likelihood that the tumor contains drug-resistant cells is dependent on both tumour size and mutation rate. At a given mutation rate the tumor size becomes the most important factor in predicting the prevalence of drug-resistant clones. This theory has given rise to several others, including that resistance mechanisms follows Darwinian evolution where drug resistance can arise from a clonal evolution of the tumor cells where a subset of cells survives the drug treatment (40). These cells can either be present at the start of the tumor development, so called inherent resistance, or there can be new mutations that occur during the treatment, so called acquired resistance. There are several inherent and acquired resistant mechanisms which are present in cells that works to reduce the effectiveness of drug treatments. The cells that remain viable after the treatment may subsequently expand leading to a more severe disease and thereby worse clinical outcome (41). Another theory for how drug resistance is developed is the stem cell theory. The theory states that a small subset of cells can undergo genetic changes similar to stem cells. Cancer Stem Cells (CSCs) have the ability to self-renew and to differentiate into the heterogeneous cells (42). Extensive preclinical evidence has indicates that tumor cells with CSCs features tend to be more resistant to chemotherapy and targeted agents (43). They are believed to be one of the main initiators of cancer relapse after primary treatment (44).

There are many different cellular mechanisms which can cause tumor cells to become drug resistant (41). For example, increased expression of drug efflux pumps, decreased drug uptake, inhibition of cell death, alteration of cell surface receptors, drug inactivation, alteration of the drug target or enhanced and alternative metabolism (45). During chemotherapy treatment a selection pressure is applied to the cells. Many drugs target the DNA or RNA synthesis resulting in a greater genomic instability and thus increasing the potential of developing drug resistance (41). Other drug strategies have instead been developed to target receptors responsible for drug efflux. One example is the ABC transporter superfamily which is primarily responsible for drug efflux via transmembrane transporters. ABCC1, also known as multidrug resistance-associated protein 1, has been linked to the release of a wide range of anticancer agents. Its overexpression has been

linked to resistance in a multiple cancers (46). Other drugs have instead focused on activating the immune response, where certain immune cells are activated to help fight the cancer (47). In recent paper studying the immunotherapy doxorubicin, a cancer drug commonly used for the treatment of malignant tumors, showed that doxorubicin-induced drug resistance through up-regulation of polyamine biosynthesis and D-glutamine metabolism (48).

5-Fluorouracil and its mode of action

5-FU is a chemotherapeutic agent that has been used to treat a variety of cancers since the 1950s including colorectal and breast cancer (Figure 1.6.a) (49). 5-FU is a one of the main drugs used for both adjuvant and metastatic CRC treatment (50). Despite the fact that new chemotherapeutic have shown improvement in metastatic CRC, 5-FU are still used in most treatment regimens.

5-FU is a heterocyclic aromatic compound that show structural resemblance with naturally occurring nucleotides, it is an analogue of uracil with a fluorine atom at the C-5 position instead of hydrogen (Figure 1.6.a). 5-FU enters the cell by facilitated transport using the same mechanism as that of uracil by either non-facilitated diffusion or via the adenine-nucleotide carrier (51). Three different mode of action have been proposed, RNA uptake, DNA uptake or the inhibition of thymidine synthase leading to inhibition of DNA synthesis (50). The exact mechanism has not yet been determined but it is known that the main pathway is inhibiting DNA uptake where most of the 5-FU is being metabolized. There are three ways that cytotoxic nucleotides can be formed by: (i) converting 5-FU to 5-fluoro-uridine-monophosphate (5FUMP) through orotate phosphoribosyl transferase; (ii) sequential conversion of 5-FU to 5FUMP by uridine phosphorylase and uridine kinase; and (iii) sequential conversion of 5-FU to 5-fluorodeoxyouridine-monophosphate (5FdUMP) by thimidine phosphorylase and thymidine kinase (52) (Figure 1.6.b).

a)

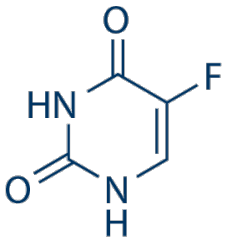

Chemical structure of 5-FU

b)

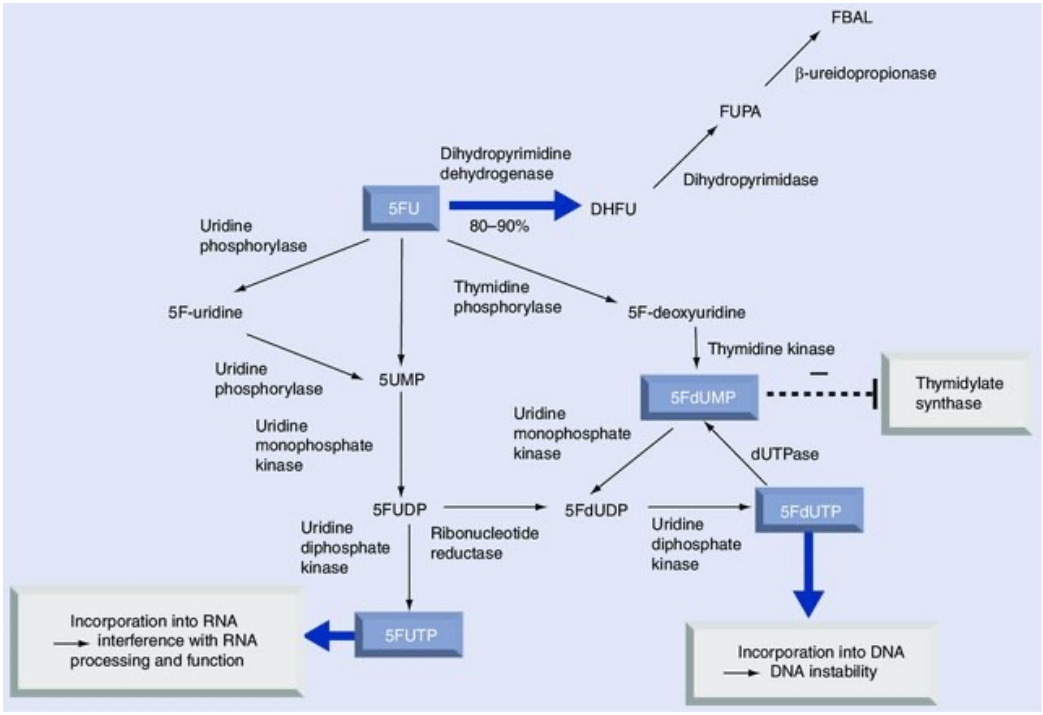

Figure 1.6. 5-fluorouracil and its metabolic pathways

a) Chemical structure of 5-FU. b) Metabolic pathway of 5-FU. The figure illustrates three different mechanisms for 5-FU metabolism inside a cell. Most of the 5-FU is converted to DHFU through dihyddropyrimidine dehydrogenase. The image is modified from Kim et al. (52).

vi. Different types of cancer biomarkers

Biomarkers are measurable and quantifiable biological material, process, or structure through the body that can affect disease outcome. Examples of common biomarkers for oncology are enzymes, protein markers, nucleic acids, genetic markers, EVs or cancer cells themselves (53). Throughout the tumor evolution the expression and/or function of these biological markers can be altered, analysing these changes can thus lead to new insights

into cancer progression and potentially to better treatment management. Ideally a biomarker should have the following characteristics: (1) good consistency; (2) high reproducibility on same biological samples and (3) good classification performance where it is easy to distinguishing disease cases from controls across multiple studies (54).

Genetic biomarkers

Genetic biomarkers are changes in the genome that can lead to an altered gene expression. In CRC, a large fraction of tumors carries mutations such as *KRAS*, *p53*, *SMAD4* and *BRAF*, which can be used to detect the presence of cancer and disease outcome (55). Genetic biomarkers can be studied by using microarrays or next generation sequencing. Microarrays such as cDNA microarrays, RNA immunoprecipitation chips, protein microarrays, protein modification microarray, have been widely used due to its simplicity and cost-effective way of detecting and comparing the levels for hundreds of genes in a single experiment (41). In a typical microarray experiment, cDNA which has been reverse transcribed from a biological sample, can hybridize to a pre-designed complementary DNA placed on an array. When the cDNA is bound to a site on the array it indicates the presence of the gene (53). However, there are several technical limitations. The main problem is that it only profiles predefined transcripts or genes which leads to missing data and may therefore affect the ability to make large conclusions (56).

With the advancement in Next-Generation Sequencing (NGS) technologies, it is now possible to study the genome or transcriptome by direct sequencing of the transcripts. NGS has made it possible for cancer research to accelerate at a much faster speed than previously (57). It has also made it possible to reach a molecular precision where single nucleotide changes can be precisely detected. Projects such as The Cancer Genome Atlas have aimed to create large cellular atlases by genomic characterization of various cancer types. Using such methods large genomic differences could be found within tumors and potentially new biomarkers can be detected (58).

Cancer cell secreted molecules as biomarkers

Cancer cell secreted molecules, also known as the "*cancer cell secretome*" refers to all the molecules secreted by a cancer cell and can be used as potential biomarker for detecting cancer and its progression (59). Direct cell signalling can target a variety of processes such as the creation of gap junctions, tunnelling nanotubes and receptor molecules. Indirect cell signalling mechanisms occurs throughout long distances withing the body, mainly through the blood stream. Some of the key components of the cell secretome are proteins, cytokines, enzymes, mRNA in soluble form or within Extracellular Vesicles (EV). These signalling mechanisms are important for a large variety of cell communications for example endocrine signalling or communication between immune cells (60).

Protein biomarkers

Proteins are complex molecules which are responsible for most cell activities. A wide verity of proteins is being produced by cells which can be used to determine disease outcome (61). The study of the entire set of proteins expressed in a cell or tissue is known as proteomics. With the advances of Liquid Chromatograph (LC) technology, in particular Liquid Chromatograph Mass Spectrometry (LC/MS), large-scale protein analysis that works by fractionating complex samples prior to protein identification has now become widely used (62). Proteomics-based technologies have made it possible to find potential biomarkers and protein expression patterns that can be used to classify tumors, predict their prognosis, and determine which patients could respond to a certain treatment (53). High-throughput proteomics is still an underdeveloped field compared to other omics fields and its contribution to oncology research has probably not yet been fully reached (63).

MicroRNA as a biomarker

MicroRNAs (miRNAs) are short single-stranded non-coding RNAs with a length of 21-25 nucleotides. Their expression levels have been linked to tumor development and progression (64). miRNAs can alter the stability or translational efficiency of targeted messenger RNAs by binding complementary with the 3′ untranslated region of target genes. It is predicted that one miRNA can target hundreds of different genes. Furthermore, MiRNAs are found in blood in a remarkably stable form, and several studies have confirmed

their role as potential minimally invasive circulating biomarkers for the diagnosis and monitoring of various human cancers (65). In CRC it was shown that the levels of miR-1914-3p and miR-1915-3p in plasma from drug resistant patients were lower than in the responders. *In vitro*, these two miRNAs were shown to facilitate cell resistance to 5-FU and oxaliplatin by down regulating the transcription factor NFIX (66).

Extracellular vesicles

Extracellular vesicles (EVs) are small lipid bilayer membrane-enclosed vesicles in a size range of 30 nm–10 μm. EVs are secreted by most, if not all, cell types (67) and released via membrane budding or fusion of multivesicular bodies with the cell membrane leading to subsequent release of intraluminal vesicles (Figure 1.7) (68). EVs are understood to be a general term that refers to cell secreted vesicles, however there are multiple subtypes of EVs including exosomes, microvesicles, ectosomes, oncosomes, and apoptotic bodies (68) (69). It is thought that EVs play complex roles in cell-to-cell communication. They can act by transferring membrane receptors between cells, deliver proteins to target cells, and modify the receiving cells by transfer of genetic information. These functional vehicles can carry a complex composition of proteins, lipids, sugars, and a wide variety of genetic materials, such as DNA, mRNA and non-coding RNAs (70). Due to their substantial roles in cell-to-cell communication they hold considerable diagnostic and therapeutic value in several diseases. For example, EVs which have been released into the bloodstream can be detected and used as diagnostic and prognostic biomarkers (71). In a recent study Hinestrosa *et al.* analyzed EVs taken from blood samples of patients with pancreatic, ovarian, or bladder cancer (72). The study showed that the EV composition from the patient samples were significantly altered compared to the control samples. This method holds promising potential to be used as a screening tool for clinicians to detect cancers at early stages.

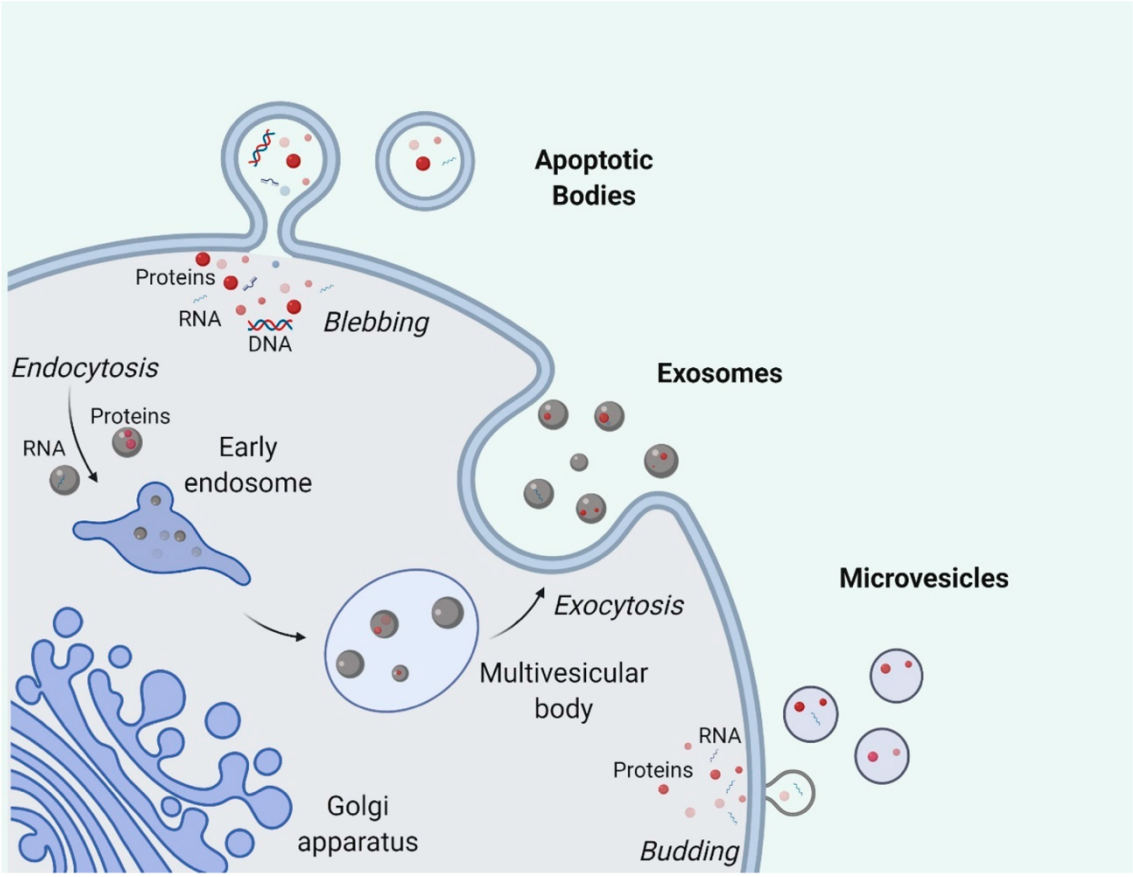

Figure 1.7. Extracellular Vesicles

Image showing how extracellular vesicles are formed and their subtypes termed exosomes, microvesicles and apoptotic bodies. It shows the and potential cargo of the EVs, which can contain proteins, RNA, DNA or a combination of them. Image taken with permission from Dang et al. (69).

vii. Experimental tumor models

Experimental tumor models are used to study biomarkers as well as cancer progression, tumor heterogeneity, metastasis and response to treatment, among other things (73). Some of the current strategies for modelling cancer include *in vivo* models to study disease progression in living organisms and *in vitro* models that mimics the tumor environment as closely as possible in cell culture environments (Table 1.2) (Figure 1.8).

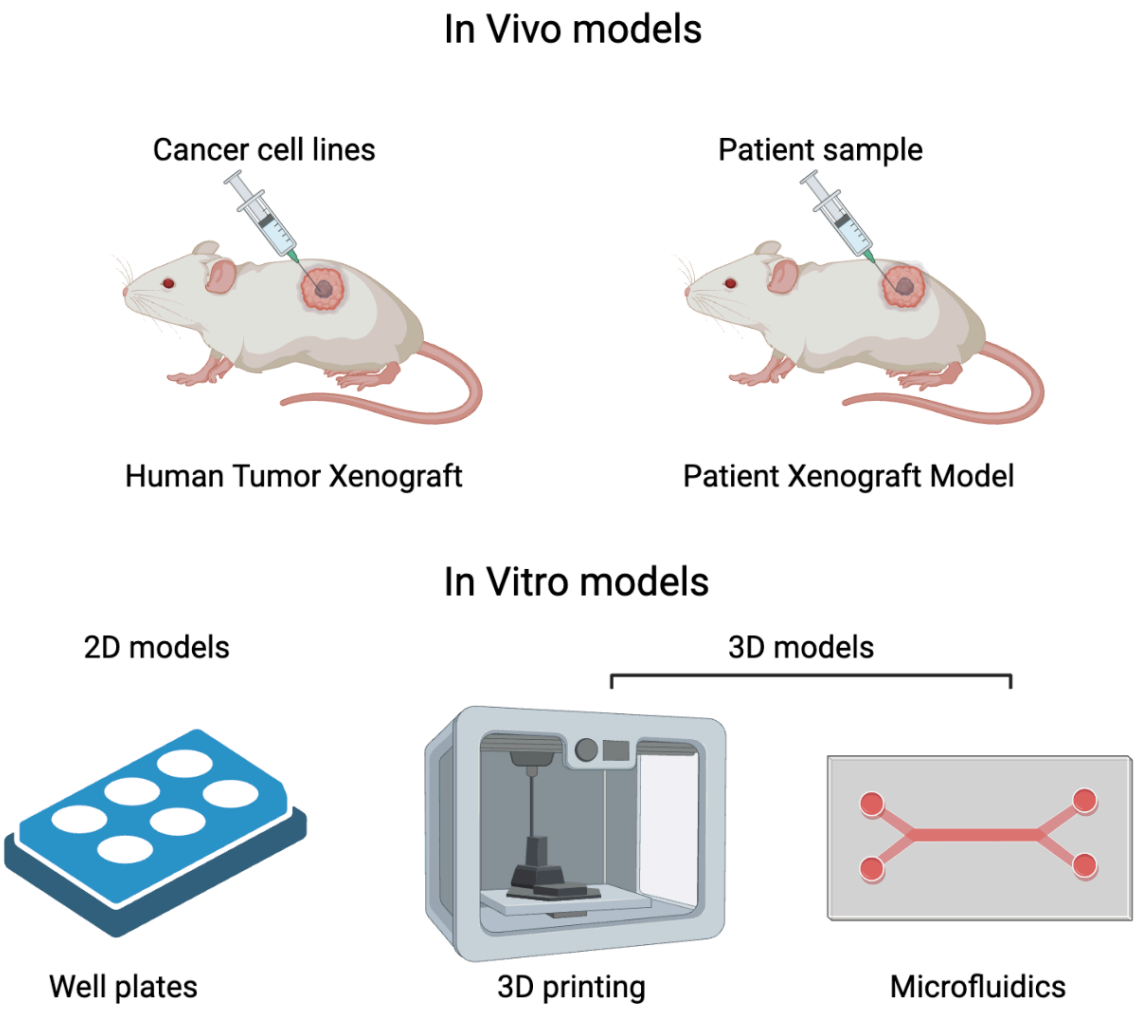

Figure 1.8. Experimental models used to study cancer

The figure displays different in vivo and in vitro models. In this example two in vivo models are displayed, a Human Tumor Xenograft model and a Patient Xenograft Model. 2D in vitro models such as well plates, and 3D models such as 3D printing or Microfluidics are illustrated.

In vivo models

In vivo models are designed to study cancer in living organisms such as drosophila (74), zebrafish (75), monkey (76), dog, mice (77) and rat (78). The most frequently used animal models are rodents such as mice and rat animal models which have been extensively developed to study human cancers as they can precisely mimic the complexity of tumors in a controlled environment. However there are also drawbacks in using animal models as it rases ethical concerns, are expensive, time-consuming, and still have a relatively high degree of error due to the innate differences between animal and human physiology (Table 1.2) (79).

Human tumor xenograft model

One of the most widely used models is the human tumor xenograft model which consists of cells from cancer cells that have been transplanted into immunodeficient mice. Human xenograft models are the gold standard technique for testing the efficacy of novel oncology drugs before they are processed to clinical trials. For example, xenodraft models which are used to study CRC have revealed mechanisms of underly intrinsic resistance to vemurafenib (80). The findings of this study led to the start of a clinical trial in which CRC patients were given a combination therapy targeting both *BRAF*, *V600E* and *EGFR*, demonstrating the advantage of xenograft models in developing novel combinatorial drug treatment strategies (80).

More recently developed are the Patient derived xenografts (PDX) models, which are tumor models where patient derived tumor cells have been implanted into mice (81). This model can accurately simulate tumor development and progression in an environment where it is possible to monitor the disease. Additionally, PDX models have been shown to maintain key characteristics of the parental tumor, including histology, gene expression, and copy number variations (82).

Table 1.2. Advantages and disadvantages of *In vitro* and *In vivo* models.

MODEL	ADVANTAGES	DISADVANTAGES
***IN VITRO* 2D CULTURE**	Simple	Static conditions
	Reproducible	Fail to produce dynamic microenvironment
	Low-cost	Not clinically predictive
	Easy downstream processing	No concentration gradient
***IN VITRO* SPHEROIDS**	More accurate representation of i*n vivo* conditions	Static environment
	Provides 3D environment for direct cell-to-cell interactions	Added expense
	High throughput	Challenges in endpoint measurements
	Reproduce complex tissue structures	More complex culture systems than 2D cultures
XENOGRAFT MODELS	Whole body pharmacokinetics	Does not represent the human microenvironment
	Genetically modifiable	Ethical concerns
	Clinical relevance	Expensive
	Allows study of complex interactions	Time consuming

In vitro models

The use of tissue engineered *in vitro* models has become a good alternative to *in vivo* models due to its low cost, simplicity to use and the fact that it does not rise any ethical concerns (Table 1.2). *In vitro* cancer research has traditionally been performed by culturing cells in well-plate settings in a two-dimensional (2D) environment. However, *in vivo* conditions are dynamic three-dimensional (3D) microstructures (79). As a result, recent research has been shifting more towards 3D cell culture.

Spheroid 3D models

In recent years there has been a significant increase in scientific papers regarding 3D cell cultures such as spheroids, Multicellular tumour cell spheroids (MCTSs) and organoids. Spheroids are *in vitro* models of cells cultured in 3D. MCTSs are created by combining multiple cell lines in 3D. Organoids are 3D tissue cultures derived from stem cells. Culturing cells in 3D environments have demonstrated many advantages over conventional 2D cell culture systems. 3D models more accurately represent the complex *in vivo* microenvironment and mimic cellular behaviour which is closer to natural conditions. Large tumors typically consist of a necrotic core, and a proliferating zone on the outer rim (Figure 1.9.a) (83). This layered structure reflects the differences in cell proliferation rate as well as it mimics the oxygen and nutrient gradients that can be found in *in vivo* tumours (Figure 1.9.b) (84).

An ideal *in vitro* cancer model will indeed consist of a 3D cancer tissue with an environment that closely mimics the TME where various cell types, vascularization, and immune components, as well as biochemical properties such as oxygen and nutrient gradients are included (83). These 3D models can be generated by using nonadherent u-shaped wells, 3D scaffolds, bioprinting or tumor on a chip models (Figure 1.9.c). U-bottom well plates have become the mainstream technology for spheroid formation as it is possible to use standardized cell culture protocol thereby making the transition to this technology the most straightforward of these techniques. In a recent study a 3D model based on CRC was created by combining intestinal fibroblasts, monocytes, and epithelial colon cancer cells (85). The cells in this model were able to successfully simulate tumor features and underwent spatial organization where extracellular matrix was formed. This model provided an insightful prototype to the study the effect of nanotherapeutic drug delivery in CRC.

3D scaffolds

Encapsulating cells in 3D polymer scaffolds is another method for 3D cell culture (Figure 1.9.c). 3D matrixes can be composed of many different polymers that all have a variety of biophysical and biochemical properties. They can be fabricated in a wide ranging of

methods, from simple freeze-drying to bioreactors. Methods like 3D printing, stereolithography, polymer phase separation, lyophilizing and gas foaming can use soluble templates to form well-designed pores or channels (86). Scaffolds used in tissue engineering should be porous to allow for rapid nutrient and oxygen transfer while also providing a 3D microenvironment for the encapsulated cells. 3D matrix environments can be made up of mammalian polymers (such as collagen, hyaluronic acid, gelatine and matrigel), or synthetic polymers (such as polylactide and poly(ethylene glycol)) (87). Biomaterials such as collagen or matrigel have found widespread application in developing a 3D matrix as it closely mimics *in vivo* environments where cells can form cell–matrix interactions however there are large batch to batch variations that may affect the reproducibility. Synthetic polymers such as polylactide and poly(ethylene glycol) have been widely used as they provide great flexibility in the design of the biochemical and biophysical properties. However, some of these polymers have limited biocompatibility and lack the ability to support critical cell–matrix interactions.

Bioprinting

Bioprinting is a manufacturing technique that uses 3D printing methods to print tissues and organs in 3D (88). In bioprinting, the biomaterials typically contain bioactive molecules and/or cells referred to as the bioink. A computer program controls the deposition of the bioink and it leads to the creation of 3D structures. The bioink is processed layer by layer according to preprogramed patterns that can be specifically designed for the purpose. There are multiple different approaches for bioprinting, including inkjet printing (89), extrusion-based printing (90), laser-assisted printing (91), and stereolithography (92). The versatility of biomaterials and printing techniques enabling on-demand fabrication of customized tissue scaffolds and medical device geometries (93). Bioprinting provides a well-constructed microenvironment where individual cell types can be specifically placed making it possible to reproduce the complex cancer microenvironment. When compared to traditional cell culture methods, bioprinting enable significantly improved control of cell distribution within 3D space.

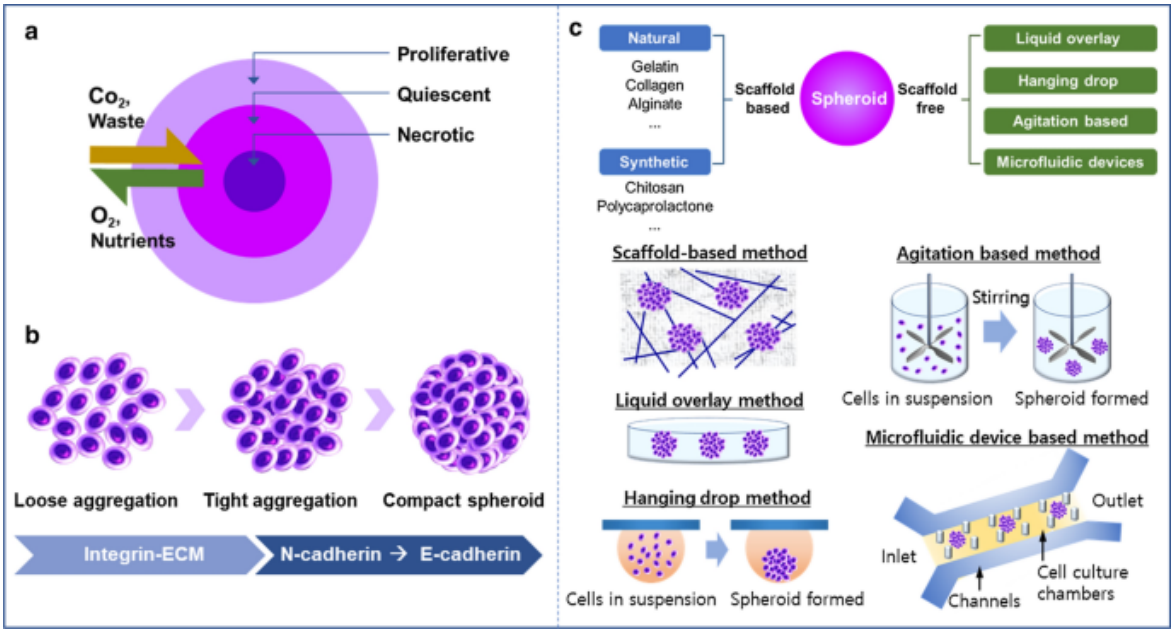

Figure 1.9. Spheroid formation and techniques to make spheroids

a) A MCTS model is ideally composed of three primary layers: a necrotic core, a quiescent inner layer, and a proliferative outer layer. MCTSs should have a gradient in oxygen, carbon dioxide, and nutrients similar to in vivo tumors. b) Spheroid compactness effected by c) Different methods for spheroid production including using scaffolds, hanging drops, microfluidics. Image taken with permission from Han et al. (94).

Microfluidics tumor on chip models

In the last decade organ on chip models have been developed as efficient tools for studying human physiology and pathology at the tissue, cellular and molecular level. Microfluidic devises have the same physical length scale as that of the TME which allows cells to be cultured in conditions similar to in vivo structures (94). Furthermore, it is possible to have high control of physical properties such as precise liquid control, interstitial pressure, soluble factor gradients, and oxygen (83). Cellular and molecular events can be monitored with high resolution using microscopy. When using precious samples, such as clinical samples, microfluidic systems make it possible to use a low sample due to its precise liquids handling capacities (94). The ability to integrate microfluidic 3D spheroid cultures with other elements simply by changing the design of the microfluidic chip makes it possible to combine the spheroid culture with vascular tissue structures to study cancer cell migration (95). Common microfabrication techniques such as photolithography, replica

moulding, and microcontact printing are well-suited to create micron sized structures that can be cast into PDMS or other polymers (96).

viii. Thesis objective

The goal of this thesis was to investigate the key mechanisms that influence CRC tumor development and progression using new tools and methods. A specific focus has been placed on intratumor heterogeneity, where its impact on tumor progression and drug resistance has been studied. The first aim was to investigate the impact of intra-tumor heterogeneity on CRC by focusing on the CMS classification. In this first part of the work, we have aimed to mimicking the tumor heterogeneity of CRC by co-culturing different CMS cell lines.

Furthermore, development of drug resistance is one of the major issues in CRC. The emergence of drug resistance is an evolutionary process since it is associated with a variety of intrinsic and extrinsic biological factors. There are still many key mechanisms that influence drug resistance that are under question where the exact mechanisms are often unknown. Therefore, we aim to investigate the key factors effecting how cells develop resistance by analyzing key mechanisms and pathways which are central in resistance development. To build on this we aimed to focus on the effect of the intra-tumor heterogeneity on tumor resistance and progression, by investigating the effect of co-culturing Drug Sensitive Cancer Cells (DSCCs) and Drug Resistant Cancer Cells (DRCCs). More specifically we were interested in investigating the effects of co-culturing DSCCs and DRCCs and their interactions under chemotherapy treatment. Understanding the molecular basis of chemoresistance will help in identifying new therapeutic targets which eventually will lead to improved treatment for patients.

Chapter 2

Intratumor heterogeneity and cell secretome promote chemotherapy resistance and progression of colorectal cancer

i. Introduction

CRC tumors have been reported to comprise four consensus molecular subtypes (CMS) that have been identified based on whole tumour transcriptional profiles (27). The system has proven useful in understanding CRC tumor biology and is shown to predict prognosis (97). The CMS classification serves as a framework to better understand the inter-tumor heterogeneity of CRC. In most cancers, including in CRC, it has been shown that intra-tumor heterogeneity promotes drug resistance and progression (28). Furthermore, our group has previously shown that over 55% of tumors are composed of mixed CMS which has been associated with worse tumors outcome (30). These findings therefor raise questions of whether intra-tumoral communication between CMS subtypes contributes to tumor progression and therapy resistance in CRC. Here, to mimic the intra-tumor heterogeneity of CRC, we have aimed to create new methods to study tumor progression and resistance mechanisms by generating MCTSs consisting of multiple CMS. This model can serve as a useful system to study cell-to-cell interactions and the effect of these interactions on drug resistance.

Furthermore, the greater complexity in CRC compared to healthy tissue results in CRC having a different molecular signature and an increased activation of signalling pathways. There is a complex cell communication network in tumors that are involved in cell-to-cell communications where our current understandings of these processes have largely been made by modelling interactions between cells in the TME. It is well recognized that cell signalling mechanism can play a significant role in the resistance mechanisms. Because of this, recent research has focused on the cancer cell secretome, to gain new insights in cell-to-cell communication.

Furthermore, the cell secretome can drastically change during chemotherapy treatment where a series of cell signalling mechanisms are initiated, some which might have an impact on the drug resistance. Therefore, the secretome is now being considered as a potential drug target for precision medicine where each component is being dissected to fully understand its many functions. However, the specific mode of action of these mechanisms are generally unknown. Cell signalling mechanisms between tumor cells are largely underexplored and therefor the characterization of these networks can unlock new discoveries that could potentially lead to new therapeutic targets. In this chapter we aim to study cell signalling mechanisms of co-cultured CMS cells and their secretome using tumor models.

Intratumor heterogeneity and cell secretome promote chemotherapy resistance and progression of colorectal cancer

Julia Källberg[1], Alexandra Harrison[1], Valerie March[1], Santa Berzina[1], Ivan Nemazanyy[2], Oliver Kepp[3,4], Guido Kroemer[3-5], Sophie Mouillet-Richard[1], Pierre Laurent-Puig[1,6], and Valérie Taly[1]*, Wenjin Xiao[1]*

[1]Centre de Recherche des Cordeliers, INSERM, CNRS, Université Paris Cité, Sorbonne Université, USPC, Equipe labellisée Ligue Nationale contre le cancer, Paris, France.

[2]Platform for Metabolic Analyses, Structure Fédérative de Recherche Necker, INSERM US24/CNRS UMS 3633, Paris, France.

[3]Equipe labellisée par La Ligue contre le cancer, Université Paris Cité, Sorbonne Université, INSERM UMR1138, Centre de Recherche des Cordeliers, Paris, France.

[4]Metabolomics and Cell Biology Platforms, Gustave Roussy Cancer Center, Villejuif, France.

[5]Institut du Cancer Paris CARPEM, Department of Biology, Hôpital Européen Georges Pompidou, AP-HP, Paris, France.

[6]Institut du Cancer Paris CARPEM, Department of Oncology, Hôpital Européen Georges Pompidou, AP-HP, Paris, France

*Corresponding authors:

Dr Valerie Taly and Dr Wenjin Xiao.

Emails: valerie.taly@parisdescartes.fr, wenjin.xiao@parisdescartes.fr

Abstract

The major underlying cause for the high mortality rate in colorectal cancer (CRC) relies on its drug resistance, to which intratumor heterogeneity (ITH) contributes substantially. CRC tumors have been reported to comprise heterogeneous populations of cancer cells that can be grouped into 4 consensus molecular subtypes (CMS). However, the impact of inter-cellular interaction between these cellular states on the emergence of drug resistance and CRC progression remains elusive. Here, we explored the interaction between cell lines belonging to the CMS1 (HCT116 and LoVo) and the CMS4 (SW620 and MDST8) subtypes in a 3D coculture model, mimicking the ITH of CRC. The spatial distribution of each cell population showed that CMS1 cells had a preference to grow in the center of the spheroids, while CMS4 cells localized at the periphery of the spheroids, in line with observations in tumors from CRC patients. Cocultures of CMS1 and CMS4 cells did not alter cell growth, but significantly sustained the survival of both CMS1 and CMS4 cells in response to the front-line chemotherapeutic agent 5-fluorouracil (5-FU). Mechanistically, the secretome of CMS1 cells exhibited a remarkable protective effect for CMS4 cells against 5-FU treatment, while promoting cellular invasion. Secreted metabolites may be responsible for these effects, as demonstrated by the existence of 5-FU induced metabolomic shifts, as well as by the experimental transfer of the metabolome between CMS1 and CMS4 cells. Overall, our results suggest that the interplay between CMS1 and CMS4 cells stimulates CRC progression and reduces the efficacy of chemotherapy.

Key words:

Colorectal cancer, intratumor heterogeneity, consensus molecular subtype, drug resistance, cell communication, cell secretome, metabolites

Introduction

Colorectal cancer (CRC) is the second most common cancer [1], with metastatic CRC having an extremely low 5-year survival rate of around 15% [2]. Chemotherapeutic drugs such as fluoropyrimidines, especially 5-fluorouracil (5-FU), have been routinely used for the treatment of CRC, alone or in combination with surgery, radiotherapy or targeted treatments [3]. However, chemotherapy resistance represents one of the main obstacles for the effective treatment of CRC [4]. It is therefore important to unravel the molecular mechanisms of drug resistance.

The tumor microenvironment (TME) of CRC is composed of a variety of cell types, including different neoplastic, immune and stromal cells, as well as blood vessels and elements of the extracellular matrix (ECM), which are in constant interplay [5]. The TME is of cardinal importance for tumor progression, metastasis and resistance to therapies [6–8]. In addition to interactions between malignant cells and the TME, intratumor heterogeneity (ITH) has also been suggested to contribute to drug resistance of CRC [9–11]. ITH refers to the coexistence of genetically, epigenetically or phenotypically distinct cancer cells within a tumor. Clonal evolution drives the genetic diversification of cancer cells, generating cancer sub-clones [12,13]. While phenotypic differences between cancer cell types stem from this genomic variation, they can also originate from interactions with the TME, as well as one another [12,13]. Heterogeneous cancer cells display an inherent functional variability in proliferative potential that may be depend on by intercellular communication [10,14,15].

Based on transcriptomics data, a recent subtype concordance analysis by the Colorectal Cancer Subtyping Consortium has yielded 4 transcriptionally driven molecular subgroups of tumors, – termed Consensus Molecular Subtypes (CMS) [16]. CMS1 tumors are defined by microsatellite instable/immune features, while CMS2, CMS3 and CMS4 display canonical, metabolic, and mesenchymal phenotypes, respectively. The CMS classification represents a significant advance in understanding CRC inter-tumor heterogeneity, and may serve as a

prognostic and predictive factor for the efficacy of therapy against CRC and thus are considered as a path to precision medicine [17]. More recently, research following the derivation of CMS subtypes has shown that a tumor can be classified as a mixed CMS, likely reflecting ITH [18–22]. For example, studies on the spatial distribution of CMS in tumors revealed that CMS4 cells are enriched at the tumor 'invasive front', while other CMS classes are more frequently found at the core [18,21]. Intriguingly, our team has observed that more than half of CRC tumors actually correspond to CMS mixtures, highlighting the transcriptional heterogeneity of CRC [22]. Such ITH was associated with dismal prognosis, and this was particularly well documented for tumors composed by CMS1 and CMS4 cells. These findings now raise the question of whether the intratumoral communication between different CMS subtypes underlies tumor progression and therapy resistance in CRC. Nevertheless, to the best of our knowledge, such studies have not yet been reported.

The secretome is an emerging mechanism of cellular interplay in tumors, as it contains protumorigenic factors released by different cell types [23]. Compared to their non-malignant counterparts, cancer cells have an aberrant secretome that can influence every stage of the tumorigenic cascade.[24] Importantly, cancer treatments can alter the composition of the cancer cell secretome. Such therapy-induced changes in the secretome can promote the formation of an immunosuppressive TME and tumor relapse [23,25]. Studies have also shown that the therapy-induced secretome of cancer cells can modulate drug responses in adjacent cells, potentially by stimulating the outgrowth, dissemination and metastasis of other cancer cell populations [14,26,27]. In particular, cells from the core of the tumor can cooperate with those at the invasive front and promote their malignancy by extracellular signals [28]. Thus, research on secretome-dependent mechanisms of cancer cell interplay is essential to expand our current understanding of CRC, from initiation to overcoming therapy resistance.

In this study, we investigated the interaction of human CMS1 and CMS4 cells, and analyzed chemotherapy outcome. We mimicked the ITH of CRC by coculturing CMS 1 and CMS4 cells in a 3D spheroid model. A specific cell distribution pattern was observed in the cocultured spheroids, with CMS1 cells (HCT116 or LoVo) growing at the center, while CMS4 cells (SW620 or MDST8) localizing at the periphery. Although the coculture of CMS1 and CMS4 did not alter the cell growth of either population, CMS1 cells showed a significant drug resistance-promoting effect on their CMS4 counterparts in response to 5-FU, while sustaining their own survival. 5-FU caused CMS1 cells to release factors that stimulated the outgrowth of CMS4 cells. Moreover, such secretome of CMS1 cells supported the invasive capacity of MDST8. Overall, the therapeutic action of 5-FU induced secretome changes of CMS1 cells that promoted 5-FU resistance of tumor spheroids. Of note, we found that secreted metabolites can be responsible for these effects. Altogether, our results provide mechanistic insights into the intercellular communication between CMS1 cells in the tumor spheroid core and edge-located CMS4 cells that may contribute to tumor progression and chemotherapy resistance.

Results

3D tumor spheroid formation of CMS cell lines

HCT116 and LoVo have been classified as CMS1 cells [29], while SW620 and MDST8 have been classified as CMS4 cells.[30] In order to assess the link between CMS subtypes and chemotherapy sensitivity, the half maximal inhibitory concentrations (IC_{50}) of 5-FU acting on these cell lines were determined using viability assays. HCT116 cells exhibited the highest sensitivity to 5-FU with IC_{50}=3.83±0.76 μM for 3 days, whereas SW620 cells were the most resistant with a 32.6-fold higher IC_{50}=124.68±27.09 μM (Supplementary Table S1), in line with the previous observations that CMS4 cells are relatively resistant against chemotherapy [30,31].

Tumor spheroids composed by different CMS cell lines were generated using microwell-based cultures with ultralow attachment surfaces. HCT116 cells formed compact spheroids after two days with a diameter of ~100 μm and grew into ~450 μm structures on day 4, representing a physiologically relevant size (Supplementary Figure S1a) [34]. The cells maintained viability for 4 days in culture and exhibited increased 5-FU resistance with IC_{50}=15.00±3.84 μM (Supplementary Figure S1b) as compared to 2D monolayer cultures, as previously described [35]. This increased drug resistance is believed to be largely due to restriction of 5-FU diffusion into 3D structures, as well as due to the molecular concentration gradients in oxygen, pH, nutrients and cellular metabolites [35,36]. Although LoVo and MDST8 cells also showed the potential to form spheroids, these structures were rather loose resulting in non-spherical shape (Supplementary Figure S2). Indeed, the morphology of LoVo spheroids is suggestive of loosely aggregating structures that fail to organize into organoids. MDST8 cells tended to form aggregates of multiple small sub-spheroids that failed to generate compact, fully integrated spheroids. SW620 cells did not adopt a spheroidal conformation at all (Supplementary Figure S2). Therein, when grown in suspension, distinct CMS cell lines differ in their propensity to generate spheroids.

Spatial distribution of CMS cells in cocultured 3D spheroids

To model the intercellular interactions of CMS populations *in vivo*, 3D cocultured tumor spheroid models that reflect the ITH of CRC were established. 10% of CMS4 cells, which were either SW620 and MDST8 cells labelled with the CMTRA cell tracker (red), were cocultured with 90% of CMS1 cells such as HCT116 labeled with the CMFDA cell tracker (green) or LoVo expressing green fluorescent protein (GFP). We observed that the CMS1/CMS4 cocultures formed spheroidal structures and that CMS1 cells (HCT116 or LoVo) grew at the center of such spheroids, while CMS4 cells (SW620 or MDST8) preferentially localized in the periphery (Figure 2.1.a). Similar spheroid morphologies were observed when coculturing

CMS1 and CMS4 cells at a 1:1 ratio. Collectively, these data suggest that CMS1 cells present a core-like location while CMS4 cells organize at the edges of mixed spheroids.

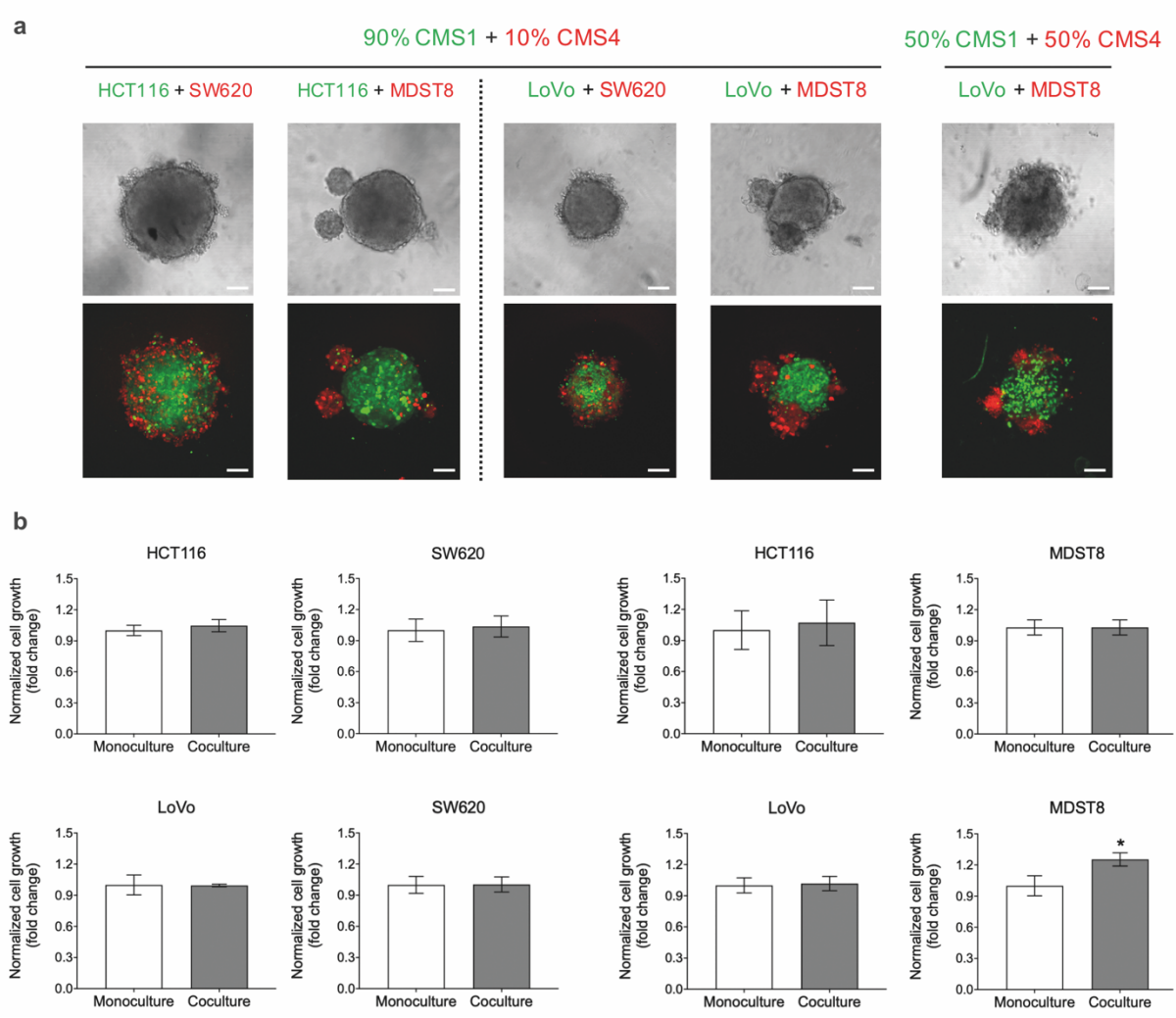

Figure 2.1. CMS1 and CMS4 cells in cocultured 3D spheroids

(**a**) Representative live cell confocal fluorescence microscopy images showing spheroid morphology and cell distribution on day 4 post-seeding. HCT116 cells were stained with cell tracker CMFDA (green), SW620 and MDST8 cells were stained with CMRA (red) fluorescent probes, LoVo cells express GFP. Scale bars=100 µm. (**b**) Cell growth in cocultured 3D spheroids. Cell growth was measured in cocultured tumor spheroids using image analysis on the fluorescent cell trackers after 4 days post-seeding and normalized by the monoculture as a control. The bars represent the average of viability and the error bars represent the standard

deviation (n=3). Statistical significance was calculated using a one-way ANOVA followed by Student's t-test. A p-value of less than 0.05 and 0.01 were considered significant (*) and highly significant (**), respectively.

Cell growth and drug resistance in cocultured 3D spheroids

Next, we explored the effects of CMS interactions on cell growth in cocultured tumor spheroids composed of 10% CMS4 and 90% CMS1 cells. Interestingly, coculture did not appear to exert a strong effect on the cell growth in either population (Figure 2.1.b). To further assess the effect of coculture on drug resistance, spheroids were treated with 5-FU after their initial formation on day 1 post-seeding. The subsequent growth of each cell population was monitored by fluorescence microscopic imaging. When added to cultures comprising HCT116 cells alone, 10-50 μM of 5-FU decreased the volume of spheroids, accompanied by decreased compactness and shape (Figure 2.2.a). In contrast, HCT116 cells cocultured with SW620 cells were protected against 5-FU, resulting in an 18.3% and 32.2% increase in HCT116 survival rate with 10 and 50 μM of 5-FU, respectively (Figure 2.2.b). Moreover, the number of admixed SW620 cells was largely increased, by up to 91% (10 μM of 5-FU), in the coculture compared to that in the monoculture (Figure 2.2b). This suggests that CMS1 cells confer 5-FU resistance to CMS4 cells in coculture conditions and that mixed CMS1/CMS4 spheroid possess a collective survival advantage in adverse conditions. Indeed, MDST8 cells were also conferred 5-FU resistance by HCT116 cells. In these mixed spheroids, MDST8 cells showed an 130% increase in survival rate (50 μM of 5-FU) when compared to those in monocultures (Figure 2.2.b), without being in comprehensive contact with HCT116, but rather forming several small spheroids on their own (Supplementary Figure S3). The overall survival of HCT116 cells was again supported by MDST8 cells (Figure 2.2.b). In addition, coculture with HCT116 cells stimulated outgrowth of CMS4 cells against 5-FU treatments, showing a maximum increase of

36% (5 μM of 5-FU) and 22% (2.5 μM of 5-FU) in cell number for SW620 and MDST8, respectively, when compared to the vehicle-treated control.

Finally, LoVo cells stably expressing GFP were cocultured with either SW620 or MDST8 cells. The resulting spheroids were then exposed to different 5-FU concentrations using the same experimental setup as above (Supplementary Figure S4 and S5). As observed for HCT116 cells, coculture significantly sustained the survival of LoVo and enhanced the resistance of CMS4 cells to 5-FU (Figure 2.2.b). Once again, this effect appeared independent of close contact of one cell population to another (Supplementary Figures S4 and S5). Collectively, these results suggest that CMS1/CMS4 coculture increases 5-FU resistance.

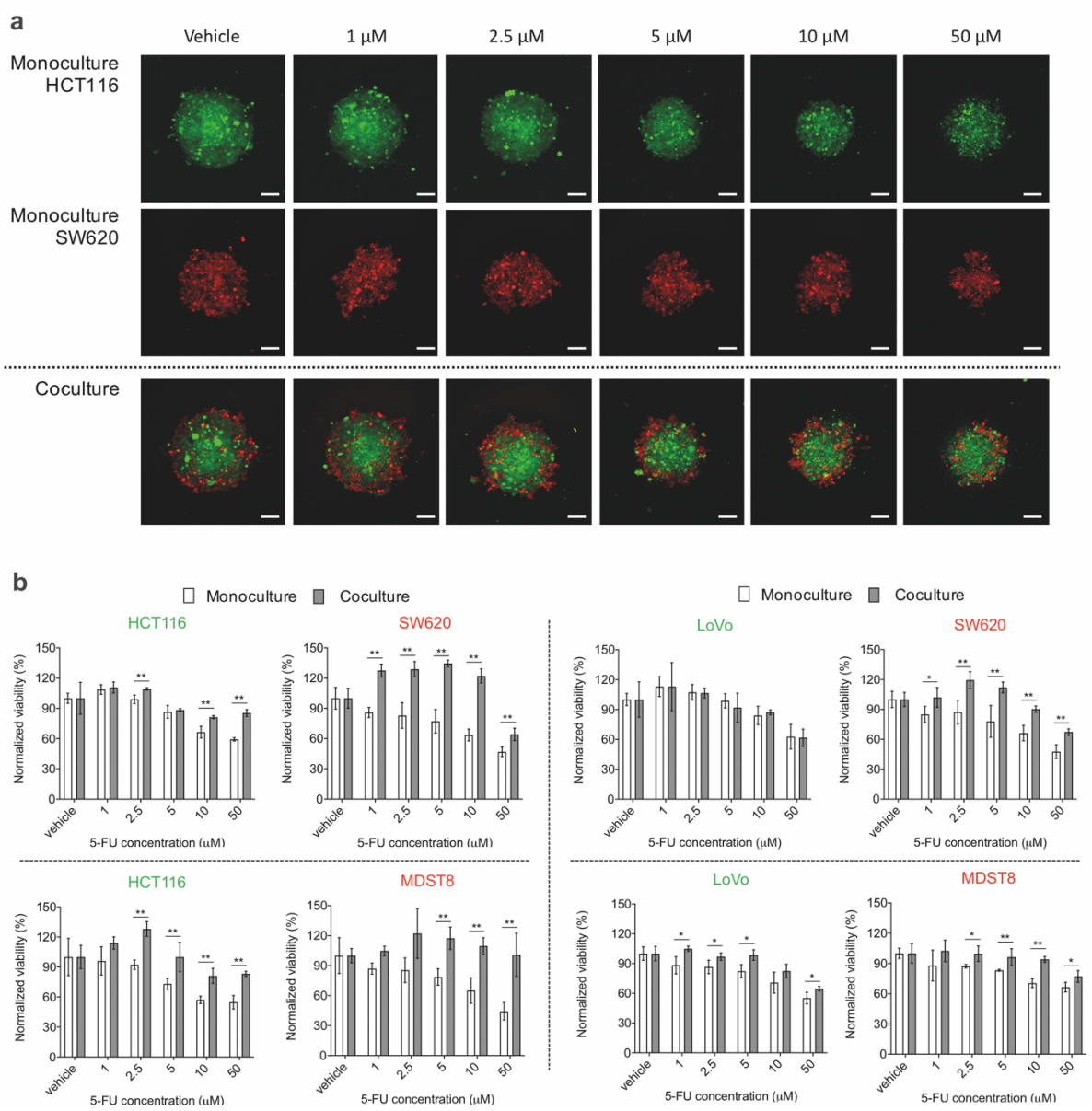

Figure 2.2. Monocultured and cocultured spheroids of CMS1 and CMS4 cells

(**a**) Representative live cell confocal fluorescence microscopy images showing the spheroid morphology of HCT116 and SW620 after 3 days of 5-FU treatment. Cells were stained with either cell tracker CMFDA (green) or CMRA (red) fluorescent probes. Scale bars=100 µm. (**b**) 5-FU response of CMS1 and CMS4 cells in the spheroids. Tumor spheroids were exposed to different concentrations of 5-FU for 3 days. Cell viability was measured using image analysis on the fluorescent cell trackers, and normalized by the vehicle control. The bars represent the average of viability and the error bars represent the standard deviation (n=3). Statistical significance was calculated using a one-way ANOVA followed by Student's t-test. A p-value of less than 0.05 and 0.01 were considered significant (*) and highly significant (**), respectively.

The effect of the CMS1 secretome on CMS4 drug resistance

We next investigated the potential mechanisms involved in the interplay between CMS1 and CMS4 cells. Recently, Bastola and colleagues reported that the secretome from the glioblastoma core promoted malignancy of cells at the tumor edge [28]. Based on this finding, we examined whether the secretome of 5-FU treated CMS1 cells would influence the drug response of CMS4 cells to 5-FU. Conditioned media (CM) were derived from HCT116 cells cultured in the absence (DMSO, CM_vehicle) or presence of 2.5 μM of 5-FU (CM_5-FU) for 3 days. Recipient SW620 cells were then cultured in HCT116 CM and their own culture medium at a 1:1 ratio and exposed to increasing concentrations of 5-FU for 3 days (Figure 2.3.a). Both CM_vehicle and CM_5-FU dramatically reduced the toxic effect of 500 μM 5-FU on SW620, yielding a 3-fold increase in viable cells (Figure 2.3.b). Enhanced resistance to 5-FU used at 30 to 100 μM was also observed with MDST8 received HCT116 CM. In contrast, the drug response of neither HCT116 nor LoVo was altered by HCT116-derived CM. These data suggest that the HCT116 secretome can promote 5-FU resistance of CMS4 cells specifically.

In an attempt to determine whether the secretome of other CMS1 cells could also induce 5-FU resistance, or whether this phenomenon exclusively applies to HCT116, CM were collected from LoVo cells under the same conditions and added to CMS4 cells. LoVo-derived CM significantly sustained the viability of SW620 and MDST8 cells against 5-FU at concentrations from 10 to 500 μM (Figure 2.3.c). LoVo CM_vehicle induced minimal or no increase in viability in these cell lines, suggesting that the observed effect is largely the result of specific secretome changes induced by 5-FU. Unlike SW620 and MDST8 cells, HCT116 and LoVo cells were as insensitive to LoVo CM as they were to HCT116 CM (Figure 2.3.b).

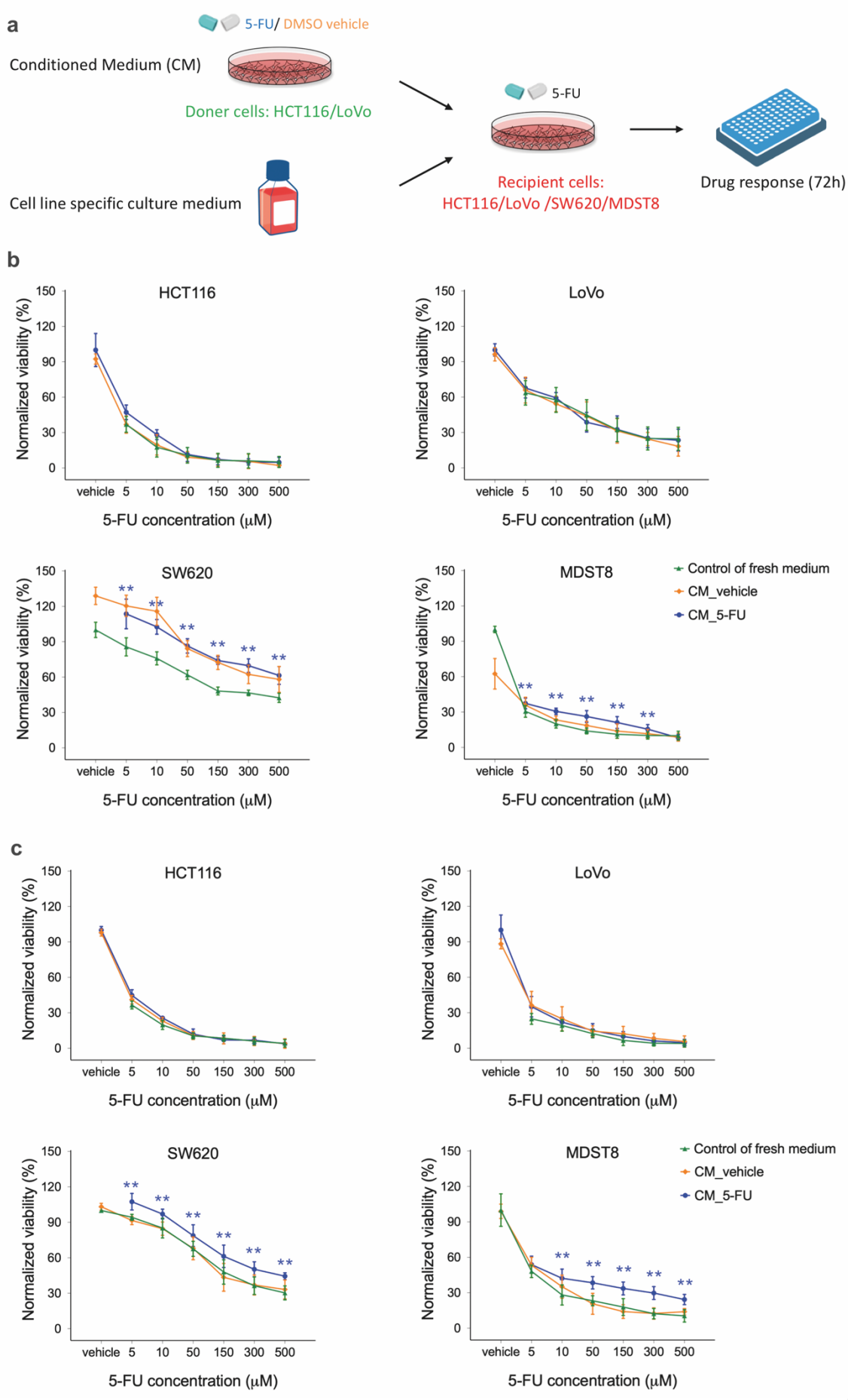
a
5-FU/ DMSO vehicle
Conditioned Medium (CM)
Doner cells: HCT116/LoVo
Cell line specific culture medium
5-FU
Recipient cells:
HCT116/LoVo /SW620/MDST8
Drug response (72h)
b
HCT116
LoVo
SW620
MDST8
Normalized viability (%)
vehicle 5 10 50 150 300 500
5-FU concentration (μM)
Control of fresh medium
CM_vehicle
CM_5-FU
c
HCT116
LoVo
SW620
MDST8
Normalized viability (%)
vehicle 5 10 50 150 300 500
5-FU concentration (μM)
Control of fresh medium
CM_vehicle
CM_5-FU

Figure 2.3. Drug resistance effect of conditioned media (CM) of CMS1 cells

(**a**) Schematic of recipient cells treated with CM of doner cells. Recipient cells were treated with either CM_vehicle or CM_5-FU of (**b**) HCT116 or (**c**) LoVo doner cells, and were exposed to different concentrations of 5-FU for 3 days. Cells treated with media only was taken as a control. Cell viability was measured using MTS assays. The squares, circles and triangles represent the average viability normalized by the vehicle control and the error bars represent the standard deviation (n=3). Statistical significance was calculated using a one-way ANOVA followed by Student's t-test. A p-value of less than 0.05 and 0.01 were considered significant (*) and highly significant (**), respectively, when compared to the control.

The effect of the CMS1 secretome on CMS4 migration and invasion

We next examined the capacity of MDST8 to migrate through the matrix of the basement membrane after exposure to the CMS1 secretome. This was determined using transwell inserts coated with a Matrigel layer onto which MDST8 were cultured. These transwell inserts were then placed on top of HCT116 or LoVo cells. Exposure to soluble signals emanating from HCT116 or LoVo cells modestly increased MDST8 migration through the transwell membrane by 1.15 and 1.23 fold, respectively (Figure 2.4.a, Figure S6). DMSO-treated HCT116 and LoVo cells significantly increased MDST8 invasion rate by 1.64 and 1.45 fold, causing 6.82% and 16.54% MDST8 cells to cross the Matrigel barrier, respectively (Figure 2.4). The invasion capacity of MDST8 was further promoted by addition of 5-FU to the system by 16.53% (in response to HCT116 cells) and 26.53% (in response to Lovo cells) (Figure 2.4). Therefore, we may surmise that, in response to 5-FU, CMS1 cells secrete factors that promote the invasion

capacity of CMS4 cells.

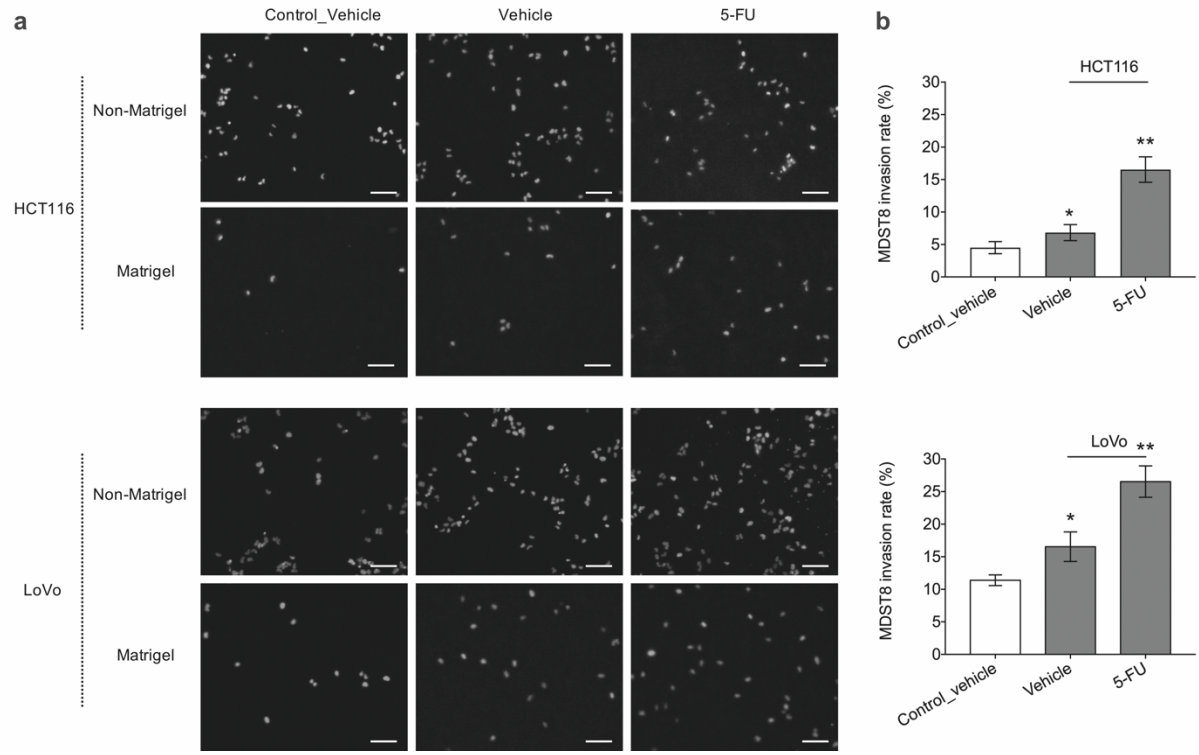

Figure 2.4 MDST8 cell invasion through transwell membrane

(**a**) Representative widefield fluorescence microscopy images showing MDST8 migration and invasion through transwell membrane with and without Matrigel coating after 2 day exposure to HCT116 or LoVo in the bottom wells. MDST8 exposed to only media without cells was taken as a control. Cells were treated with either DMSO vehicle or 2.5 uM of 5-FU. Cell nuclei were stained with Hoechst (blue). Scale bars=100 μm. (**b**) Invasion rate of MDST8 presented as the percentage of cell invasion through Matrigel coated transwell membrane relative to the cell migration through the non-Matrigel coated transwell membrane. The bars represent the average and the error bars represent the standard deviation (n=3). Statistical significance was calculated using a one-way ANOVA followed by Student's t-test. A p-value of less than 0.05 and 0.01 considered significant (*) and highly significant (**), respectively, when compared to the control.

The effect of metabolites on CMS4 drug resistance

During tumor progression and metastasis, tumor cells undergo rapid metabolic adaptations and coordinate with their surroundings to maintain biosynthetic and bioenergetic demands while escaping immunosurveillance or therapeutic interventions, which are now recognized as hallmarks of cancer [37]. Thus, we investigated whether metabolites in the CMS1 secretome are responsible for the observed effects. CM were collected from HCT116 or LoVo cultured in the absence (DMSO, CM_vehicle) or presence of 2.5 μM of 5-FU (CM_5-FU) for 3 days. Metabolites of these CM were dialyzed into fresh media (Metabolite_vehicle, Metabolite_5-FU) using dialysis membranes with a cut-off of 3.5 kDa and applied to CMS4 cell lines as previously. Similar to CM_5-FU, Metabolite_5-FU greatly sustained the viability of both SW620 and MDST8 cells against 5-FU at concentrations from 5 to 300 μM (Figure 2.5a.). The same effect was observed with LoVo metabolites (Figure 2.5.b). These results suggest that dialyzable metabolites (rather than extracellular vesicles or proteaceous factors) are the key communicators in the CMS1 secretome that can promote 5-FU resistance of CMS4 cells.

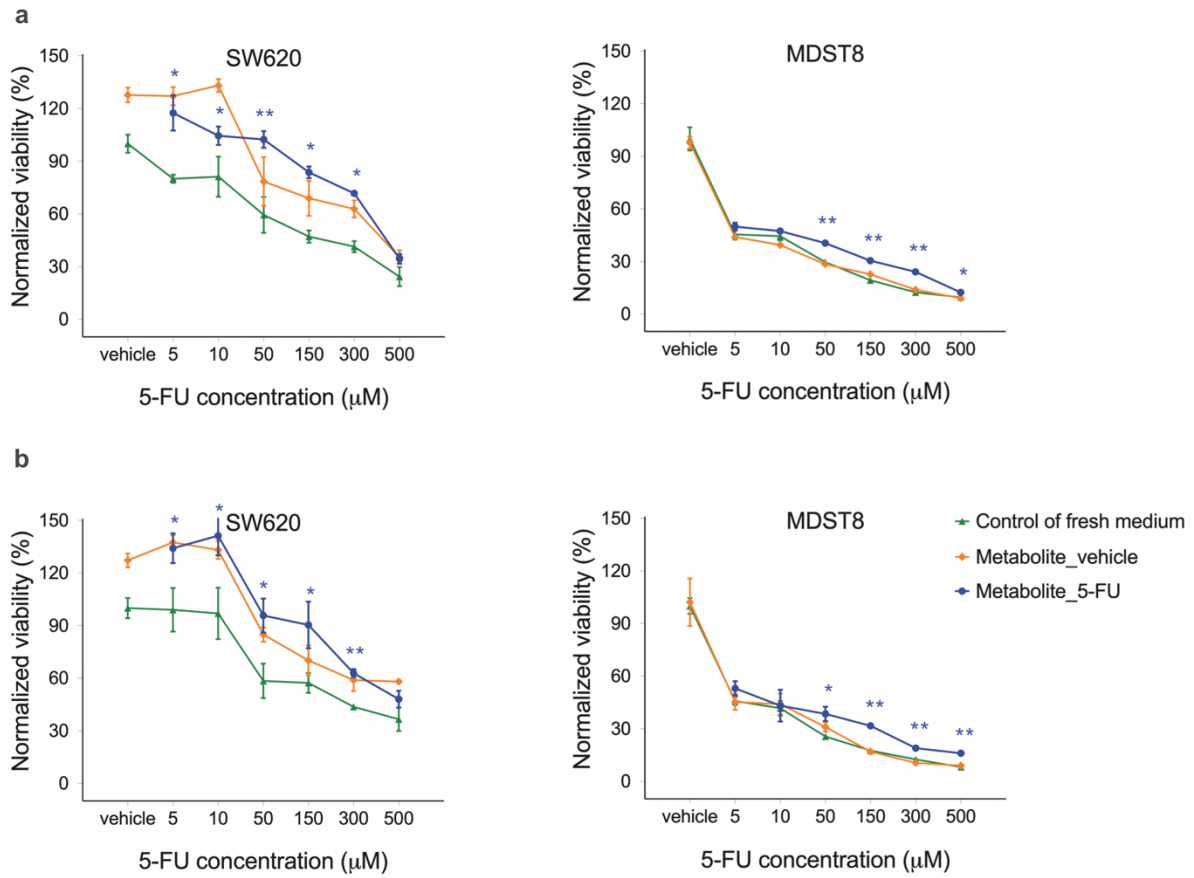

Figure 2.5. Drug resistance effect of metabolites of CMS1 cells

CMS4 cells were treated with either metabolite_vehicle or metabolite_5-FU of (**a**) HCT116 or (**b**) LoVo CMS1 cells, and were exposed to different concentrations of 5-FU for 3 days. Cells treated with media only was taken as a control. Cell viability was measured using MTS assays. The squares, circles and triangles represent the average viability normalized by the control and the error bars represent the standard deviation (n=3). Statistical significance was calculated using a one-way ANOVA followed by Student's t-test. A p-value of less than 0.05 and 0.01 were considered significant (*) and highly significant (**), respectively, when compared to the control.

Table 1. Fold change of metabolite levels in DMSO vehicle treated conditioned media (CM_Vehicle) of HCT116 compared to control media without cells (Control).

Metabolite	log2 (fold change, down-regulated)	Metabolite	log2 (fold change, up-regulated)
Hypoxanthine	-6.49	S-Adenosyl-L-Homocysteine	7.03
Niacin/ Nicotinate	-5.64	Glycerol 3-phosphate	5.94
Linoleic acid	-4.79	Alpha-Ketoglutarate	3.95
Cytidine	-4.69	Orotic acid	3.80
Glutamine	-4.45	Pyruvate	3.25
Adenine	-2.95	Lactate	2.91
Serine	-2.28	N-acetylaspartate	2.85
Taurine	-1.90	Serotonin	1.59
Oleic acid	-1.74	Pyridoxal	1.26
Hexanoylcarnitine	-1.51	Acetyllysine	0.94
Palmitoleic acid	-1.44	Decanoic acid	0.70
Tryptophan	-1.39	Nicotinamide	0.65
Creatine	-1.39	Malate	0.61
Cystine	-1.14	Asparagine	0.57
Leucine	-1.01	Fumarate	0.45
Lysine	-0.99	Urate	0.40
Methionine	-0.94	Glutamate	0.40
Acetylglutamine	-0.92	Glycine	0.34
Ornithine	-0.88	L-Kynurenine	0.24
Valine	-0.84	Fructose	0.20
Threonine	-0.80	Creatinine	0.19
Glucose	-0.69		
Tyrosine	-0.66		
L-Alanine	-0.50		
L-Sarcosine	-0.50		
Histidine	-0.50		
Phenylalanine	-0.49		
Cysteine sulfinic acid	-0.47		
IsoLeucine	-0.46		
Carnitine	-0.45		
Aspartate	-0.36		

Metabolite analyses of CMS1 conditioned media

To evaluate the metabolic adaptation of CMS1 cells in response to 5-FU, as well as to identify the relevant mediators and pathways involved in the reactive secretome, the CM of CMS1 cells were analyzed by liquid chromatography–tandem mass spectrometry (LC-MS/MS). A total of 91 metabolites involved in a broad range of metabolic pathways were quantified, including amino acids, organic acids, nucleotides, and cofactors (Table S2). The relative steady-state levels of 52 metabolites were significantly altered in the CM_vehicle of HCT116 compared to the control media without cells (Supplementary Figure S7 and Table 1). Pathway analysis indicated that the levels of 13 metabolites involved in aminoacyl-tRNA biosynthesis (amino acids) were consumed by HCT116 cells (Supplementary Table S3), representing the highest pathway significance. Of note, phenylalanine, tyrosine and tryptophan biosynthesis as well as linoleic acid metabolism showed the highest pathway impact of 1.0 among down-regulated metabolites. On the other hand, up-regulated metabolites in the HCT116 secretome were mainly involved in alanine, aspartate and glutamate metabolism, including N-acetylaspartate, asparagine, glutamine, fumarate, pyruvate and alpha-ketoglutarate, representing the highest pathway significance. Moreover, D-glutamine and D-glutamate metabolism and vitamin B6 metabolism showed the highest pathway impact of 0.50 and 0.49, respectively. Metabolites were significantly altered in the CM_vehicle of LoVo compared to the control media without cells (Supplementary Figure S8 and Table 2.2.). Similar to HCT116, significantly down-regulated metabolites were involved in the aminoacyl-tRNA biosynthesis, representing the highest pathway significance. Once again, phenylalanine, tyrosine and tryptophan biosynthesis together with linoleic acid metabolism showed the highest pathway impact (Table 2, Supplementary Table S5). Unlike HCT116 cells, upregulated metabolites were mainly involved in citrate cycle (TCA cycle), representing the highest pathway significance (Supplementary Table S6). Riboflavin metabolism, D-glutamine and D-

glutamate metabolism, and vitamin B6 metabolism showed the highest pathway impact of 0.50, 0.50 and 0.49, respectively. Overall, the metabolite profile of LoVo CM_vehicle largely overlaps with that of HCT116 CM_vehicle (Supplementary Table S7).

We next examined the influence of 5-FU on the metabolite composition of CMS1 secretome. A total of 37 soluble metabolites exhibited differential patterns in the secretome induced by 5-FU compared to vehicle for both HCT116 and LoVo (Supplementary Figure S9 and S10, Table S7 and S8). Among these metabolites, we observed a significant overlap of 22 (19 upregulated and 3 downregulated) compounds between HCT116 and LoVo (Table 2.3). Pathway analysis on these up-regulated metabolites revealed that 5-FU treatments impacted several metabolic pathways, including aminoacyl-tRNA biosynthesis, which showed the highest pathway significance. Phenylalanine, tyrosine and tryptophan biosynthesis and linoleic acid metabolism had the highest pathway impact of 1.0 (Supplementary Table S9**)**. These data suggest that such differentially regulated factors in the CMS1 secretome, induced by 5-FU, could stimulate drug resistance, outgrowth, and invasion capacity of CMS4 cells.

Table 2.2. Fold change of metabolite levels in DMSO vehicle treated conditioned media (CM_Vehicle) of LoVo compared to control media without cells (Control).

Metabolite	log2 (fold change, down-regulated)	Metabolite	log2 (fold change, up-regulated)
Docosahexaenoic acid	-6.75	Acetylcysteine	9.11
Niacin/ Nicotinate	-6.73	Orotic acid	6.29
Hypoxanthine	-6.48	Alpha-Ketoglutarate	4.10
Cytidine	-5.38	N-Acetylaspartate	3.54
Glutamine	-4.78	Glycerol 3-phosphate	3.45
Linoleic acid	-2.89	Lactate	2.97
Serine	-2.53	Pyruvate	2.86
Taurine	-2.09	Cysteine	2.23
Tryptophan	-2.05	Butyric acid	2.06
Palmitoleic acid	-1.91	Serotonin	1.99
Creatine	-1.71	Pyridoxal	1.93
Oleic acid	-1.43	Acetyl-lysine	1.67
L-Alanine	-1.32	Cis-aconitate	1.35
L-Sarcosine	-1.32	Nicotinamide	1.02
Methionine	-1.29	Butyryl-carnitine	0.92
Threonine	-0.98	Malate	0.72
Lysine	-0.85	Fumarate	0.53
Tyrosine	-0.85	L-Kynurenine	0.40
Glucose	-0.83	Citrulline	0.33
Cysteinesulfinic acid	-0.76	Riboflavin	0.29
Carnitine	-0.75	Acetylcarnitine	0.28
IsoLeucine	-0.73	Creatinine	0.24
Aspartate	-0.72	Glycine	0.22
Leucine	-0.68	Pantothenate	0.22
Phenylalanine	-0.67	Glutamate	0.22
Histidine	-0.65		

Table 2.3. Overlap of fold change of metabolite levels in 5-FU treated conditioned media (CM_5-FU) of HCT116 and LoVo compared to DMSO vehicle treated conditioned media (CM_Vehicle).

Metabolite	log2 (fold change, down-regulated)		Metabolite	log2 (fold change, up-regulated)	
	HCT116	LoVo		HCT116	LoVo
Lactate	-1.01	-0.93	Glutamine	4.02	4.03
Acetyllysine	-0.53	-0.79	Niacin/ Nicotinate	2.96	1.85
Fructose	-0.20	-0.24	Linoleic acid	2.81	1.78
			Hypoxanthine	2.24	1.65
			Palmitoleic acid	1.74	1.65
			Serine	1.66	1.51
			Oleic acid	1.55	1.49
			Tryptophan	1.18	1.26
			Lysine	0.88	1.26
			Creatine	0.84	1.09
			Pyruvate	0.79	1.05
			Methionine	0.71	0.93
			Threonine	0.56	0.78
			Tyrosine	0.50	0.77
			L-Alanine	0.44	0.76
			L-Sarcosine	0.44	0.70
			Cytidine	0.42	0.55
			Phenylalanine	0.37	0.50
			IsoLeucine	0.33	0.40

Discussion

ITH facilitates therapeutic resistance in CRC. In this study, we demonstrate an impact of the interplay between CMS1 and CMS4 cell lines on CRC drug resistance and progression. Investigation of the intercellular communication between these two cancer cell populations uncovers that the secretome, specifically the metabolites, from CMS1 cells promotes CMS4 chemotherapy resistance, outgrowth and invasion. Our findings provide new evidence that the

inter-clonal communication occurs between CRC cancer cells and such interplay can confer tumor aggressiveness. This work also highlights distinct secretive factors involved in the heterogenous clonal cooperation, which could represent potential targets for preventing tumor progression.

Two mechanisms could underlie the observed increase in the drug resistance of CMS cells: cell interplay and/or direct consequences of 5-FU exposure. The latter may involve the 5-FU - driven selection and proliferation of drug resistant subclones or a 'shielding' effect caused by the preferential 5-FU targeting of CMS1 cells over CMS4 cells [38,39]. Such an effect is more likely for the highly 5-FU-sensitive HCT116 cells rather than LoVo cells. Given the high seeding cell density of HCT116 cells in cocultures, their 5-FU-induced demise could consequently result in an increase in available space and nutrients, prompting the growth of CMS4 cells. However, we did not observe any enhanced drug resistance in monocultures of CMS4 cells without HCT116. Therefore, cell interplay is more likely the cause of the observed increase in resistance.

Cell communication may involve direct physical interactions and/or secreted signaling among different cell types. CRC cells have been reported to secrete certain factors into the extracellular space, allowing their communication with the microenvironment [40]. Here, we proved that secreted signals can also be shuttled from one cancer cell type to another, thus affecting therapy resistance, outgrowth, and invasion. This finding indicates that direct cell-to-cell contact may not be obligatory for such effects [41–43,28]. Secreted signals may also account for previously reported mechanisms, including the paracrine modulation of cellular resistance to chemotherapy-induced cell death [23]. Chemoresistance can also be conferred between tumor cells through the secretome by upregulating the expression of drug efflux pumps and antiapoptotic proteins [23]. Indeed, we found that the composition of the secretome was significantly altered after administration of 5-FU. Components of such therapy-induced

secretome have been reported to allow cancer cells to interact with various non-malignant cell types surrounding them, like immune cells [44], and to promote epithelial-to-mesenchymal transition in pre-malignant and malignant cells [45].

The secretome is a complex network of secreted signals, the major components of which include extracellular vesicles (EVs) and soluble factors, such as cytokines, growth factors, enzymes, and metabolites [23]. By interacting with surrounding cells, cancer cell-derived EVs can promote CRC progression, drug resistance, escape of immune-surveillance, angiogenesis, invasion and metastasis [46-48]. Soluble mediators secreted from cancer cells, such as cytokines, growth factors and enzymes, have also been reported to strongly correlate with tumor recurrence and compromised therapeutic efficacy in various cancers [23]. In the context of raising knowledge on cancer-cell-intrinsic metabolic remodeling, recent studies have begun to explore metabolic communications between tumor cells and TMEs and their effect on therapeutic interventions [49-52]. The release of metabolites, such as saccharides, amino acids, lipids and nucleosides, can induce specific pathways in neighboring non-malignant cells, thereby modulating TMEs. For example, the secreted metabolites of fibrosarcoma cells have been reported to induce vascular tube formation of endothelial cells, resulting in pro-metastatic angiogenesis [53]. However, such metabolic communications between heterogenous populations of cancer cells have remained underexplored. Therefore, as a preliminary study of the cell communication between CMS subtypes of CRC, we examined a limited set of soluble metabolites, selected from a broad range of major pathways. In the future, this investigation should be extended to in-depth examination of the metabolomics that may help to uncover new strategies for alleviating therapy resistance in CRC.

Materials and Methods

Cell culture

Human CRC cell lines were obtained from ATCC or ECACC. All cell lines were maintained in culture flasks (Corning, France) in a humid 5% CO_2 incubator at 37°C. HCT116 (ATCC®CCL-247), LoVo (ATCC®CCL-229), MDST8 (ECACC99011801) and SW620 (ATCC®CCL-227) cells were respectively maintained in McCoy's 5A, F-12K, DMEM, and Leibovitz's L-15(Gibco, France). All culture media were supplemented with 10% (v/v) inactivated FBS (Gibco, France) and 1% (v/v) penicillin-streptomycin (Gibco, France), and were changed every 3 days.

IC50 determination

IC50 values of 5-FU (Sigma, US) were determined for all cell lines. Cells were seeded into 96-well plates and incubated overnight to allow attachment, followed by 5-FU treatments in various concentrations of 0, 0.5, 1.0, 1.5, 2.5, 5,0, 10, 20, 30, 50, 75, 100, and 150 µM for 3 days. Cell viability was assayed using 3-(4,5-dimethylthiazol-2-yl)-5-(3carboxymethoxyphenyl)-2-(4-sulfophenyl)-2H-tetrazolium (MTS) assay (Promega, USA), before being washed once with culture media to remove any drug residue. After a 4 h incubation, the absorbance at 570 nm (600 nm as a reference) was measured using a plate reader (Tecan, France). IC50 values were calculated by using Prism 9.

3D spheroids generation and 5-FU treatments

1 500 cells were seeded into ultralow attachment U-shaped 96-well plates (Corning, France). Cell seeding was followed by an overnight incubation to allow tumor spheroid formation. Spheroids were treated with 0, 1, 2.5, 5, 10, and 50 µM of 5-FU for 3 days. Cell viability was assayed using CellTiter 96® AQueous One Solution Cell Proliferation Assay (MTS; Promega,

France), before being washed once with culture media to remove any drug residue. After a 4 h incubation, the absorbance at 490 nm was measured using a plate reader (Tecan, France).

Live-cell confocal fluorescence imaging and image analyses

A Zeiss LSM710 confocal laser scanning microscope was used for live-cell imaging. Cells were stained with 0.5 µM of either cell tracker CMFDA (green) or CMRA (red) fluorescent probes (Life Technologies, USA), following the manufacturer's instructions. LoVo cells were transduced with LentiBrite Lentiviral Biosensor (Sigma, USA) to express GFP. The excitation filters used were 450-490 nm for cells labeled with CMFDA or expressing GFP and 515-560 nm for CMRA. Images were captured using LSM Zen Black software (Zeiss, Germany) and processed by Fiji software. Area and mean pixel intensity measurements of images were taken on each fluorescence channel with B&W threshold on a dark background. These parameters were used to calculate integrated density indicating cell area.

Cell migration and invasion assay

BioCoat GFR Matrigel invasion inserts (Corning, France) were rehydrated following the manufacturer's instructions. 1x 10^4 cells in culture medium containing 0.1% BSA were seeded into 24-well plates. The rehydrated GFR Matrigel invasion inserts were next transferred to the wells and 1x 10^4 cells were seeded to the inside of these inserts. BioCoat control inserts without GFR Matrigel coating (Corning, France) were taken as controls. Cells were incubated in a humid 5% CO_2 incubator at 37°C for 24 h to allow migration. After incubation, the non-invading cells were removed from the upper surface of the insert membrane following the manufacturer's instructions and then the nuclei of invading cells were stained with Hoechst (Life Technologies, USA). The cells were imaged by using a Zeiss Axio Observer Z1 widefield microscope (Zeiss, Germany) and processed by Fiji software. Cell counting was performed on

obtained images and the number of cells was calculated as a mean average of 9 images per condition. The percent of invading cells were defined as equation 1.

$$\% \text{ Invasion} = \frac{\text{Number of cells invading through GFR Matrigel insert membrane}}{\text{Number of cells migrating throuh control insert membrane}} \times 100 \quad \text{equation 1}$$

Conditioned media (CM) collection

HCT116 or LoVo cells were seeded into T-75 cm^2 flasks and incubated overnight to allow attachment. Media was then replaced with 2.5 µM of 5-FU or DMSO vehicle as a control. After a 3-day incubation, the conditioned media (CM) were collected and centrifuged at 200 rcf for 5 min to remove any cells. The supernatant was then filtered using a syringe and 0.22 µm filters (Sartorius, France), flash-frozen and stored at -80°C.

Conditioned media (CM) treatment

1 500, 10 000, 2 000, and 2 000 cells of HCT116, LoVo, MDST8, and SW620, respectively, were seeded into 96-well plates and left to incubate overnight. The cell treatment was carried out by diluting 5-FU solutions in a 1:1 mixture of cell line specific culture media and HCT116 or LoVo CM. Final 5-FU concentrations were 5, 10, 50, 150, 300 and 500 µM. Cell viability was assayed using MTS (Promega, USA).

Metabolite dialysis and treatment

CM of HCT116 or LoVo cells were collected as previously and centrifuged at 200 rcf for 5 min to remove any cells. Metabolites of the CM were dialyzed into fresh media using 3.5K MWCO cellulose dialysis tubing (ThermoFisher Scientific, France) at 4° C. 2 000 cells of MDST8 and SW620, respectively, were seeded into 96-well plates and left to incubate overnight. The cell treatment was carried out by diluting 5-FU solutions in a 1:1 mixture of cell line specific culture media and HCT116 or LoVo metabolite solution. Final 5-FU

concentrations were 5, 10, 50, 150, 300 and 500 μM. Cell viability was assayed using MTS (Promega, USA).

Targeted metabolites analyses by liquid chromatography–tandem mass spectrometry (LC-MS/MS)

CM metabolites were extracted as previously described.[54] Extraction solution was composed of 50% methanol, 30% ACN, and 20% water. CM samples were diluted 30-fold by adding extraction solution. Samples were vortexed for 5 min at 4°C and then centrifuged at 16 000 rcf for 15 min at 4°C. The supernatants were collected and stored at −80°C until analyses. LC/MS analyses were conducted on a QExactive Plus Orbitrap mass spectrometer equipped with an Ion Max source and a HESI II probe and coupled to a Dionex UltiMate 3000 UPLC system (ThermoFisher Scientific, USA). External mass calibration was performed using the standard calibration mixture every 7 days as recommended by the manufacturer. 5 μL of each sample was injected onto Zic-pHilic (150 mm × 2.1 mm i.d. 5 μm) with the guard column (20 mm × 2.1 mm i.d. 5 μm) (Millipore) for the liquid chromatography separation. Buffer A was 20 mM ammonium carbonate, 0.1% ammonium hydroxide (pH 9.2); buffer B was acetonitrile. The chromatographic gradient was run at a flow rate of 0.200 μL/min as follows: 0-20 min; linear gradient from 80% to 20% B; 20-20.5 min; linear gradient from 20% to 80% B; 20.5-28 min: hold at 80% B.[54] The mass spectrometer was operated in full scan, polarity switching mode with the spray voltage set to 2.5 kV, the heated capillary held at 320°C. The sheath gas flow was set to 20 units, the auxiliary gas flow was set to 5 units, and the sweep gas flow was set to 0 unit. The metabolites were detected across a mass range of 75-1 000 m/z at a resolution of 35 000 (at 200 m/z) with the AGC target at 106, and the maximum injection time at 250 ms. Lock masses were used to ensure mass accuracy below 5 ppm. Data were acquired with Thermo Xcalibur software (ThermoFisher Scientific, USA). The peak areas of metabolites were

determined using Thermo TraceFinder software (ThermoFisher Scientific, USA), identified by the exact mass of each singly charged ion and by known retention time on the HPLC column. Metabolomic data analyses were performed using Metaboanalyst 5.0 software.[55]

Statistical analysis

Statistical significance was determined by a one-way ANOVA followed by two-tailed equal variance Student's t-test. P-values less than 0.05 and 0.01 were considered significant (*) and highly significant (**), respectively.

References

1 Allemani C, Matsuda T, Di Carlo V, Harewood R, Matz M, Nikšić M *et al.* Global surveillance of trends in cancer survival 2000–14 (CONCORD-3): analysis of individual records for 37 513 025 patients diagnosed with one of 18 cancers from 322 population-based registries in 71 countries. *The Lancet* 2018; **391**: 1023–1075.

2 Colorectal Cancer Survival Rates | Colorectal Cancer Prognosis. https://www.cancer.org/cancer/colon-rectal-cancer/detection-diagnosis-staging/survival-rates.html.

3 Carethers JM. Systemic Treatment of Advanced Colorectal Cancer: Tailoring Therapy to the Tumor. *Therap Adv Gastroenterol* 2008; **1**: 33–42.

4 Hammond WA, Swaika A, Mody K. Pharmacologic resistance in colorectal cancer: a review. *Ther Adv Med Oncol* 2016; **8**: 57–84.

5 Bray LJ, Hutmacher DW, Bock N. Addressing Patient Specificity in the Engineering of Tumor Models. *Front Bioeng Biotechnol* 2019; **7**: 217.

6 Polyak K, Haviv I, Campbell IG. Co-evolution of tumor cells and their microenvironment. *Trends in Genetics* 2009; **25**: 30–38.

7 Joyce JA, Pollard JW. Microenvironmental regulation of metastasis. *Nat Rev Cancer* 2009; **9**: 239–252.

8 Turley SJ, Cremasco V, Astarita JL. Immunological hallmarks of stromal cells in the tumour microenvironment. *Nat Rev Immunol* 2015; **15**: 669–682.

9 Saunders NA, Simpson F, Thompson EW, Hill MM, Endo-Munoz L, Leggatt G *et al.* Role of intratumoural heterogeneity in cancer drug resistance: molecular and clinical perspectives. *EMBO Mol Med* 2012; **4**: 675–684.

10 Kreso A, O'Brien CA, Galen P van, Gan OI, Notta F, Brown AMK *et al.* Variable Clonal Repopulation Dynamics Influence Chemotherapy Response in Colorectal Cancer. *Science* 2013; **339**: 543–548.

11 Pribluda A, de la Cruz CC, Jackson EL. Intratumoral Heterogeneity: From Diversity Comes Resistance. *Clin Cancer Res* 2015; **21**: 2916–2923.

12 Marusyk A, Polyak K. Tumor heterogeneity: causes and consequences. *Biochim Biophys Acta* 2010; **1805**: 105.

13 Marusyk A, Janiszewska M, Polyak K. Intratumor Heterogeneity: The Rosetta Stone of Therapy Resistance. *Cancer Cell* 2020; **37**: 471–484.

14 Obenauf AC, Zou Y, Ji AL, Vanharanta S, Shu W, Shi H *et al.* Therapy-induced tumour secretomes promote resistance and tumour progression. *Nature* 2015; **520**: 368–372.

15 Martín-Pardillos A, Valls Chiva Á, Bande Vargas G, Hurtado Blanco P, Piñeiro Cid R, Guijarro PJ *et al.* The role of clonal communication and heterogeneity in breast cancer. *BMC Cancer* 2019; **19**: 666.

16 Guinney J, Dienstmann R, Wang X, De Reyniès A, Schlicker A, Soneson C *et al.* The consensus molecular subtypes of colorectal cancer. *Nat. Med.* 2015; **21**: 1350–1356.

17 Okita A, Takahashi S, Ouchi K, Inoue M, Watanabe M, Endo M *et al.* Consensus molecular subtypes classification of colorectal cancer as a predictive factor for chemotherapeutic efficacy against metastatic colorectal cancer. *Oncotarget* 2018; **9**: 18698–18711.

18 Dunne PD, McArt DG, Bradley CA, O'Reilly PG, Barrett HL, Cummins R *et al.* Challenging the Cancer Molecular Stratification Dogma: Intratumoral Heterogeneity Undermines Consensus Molecular Subtypes and Potential Diagnostic Value in Colorectal Cancer. *Clin Cancer Res* 2016; **22**: 4095–4104.

19 Ubink I, Elias SG, Moelans CB, Laclé MM, van Grevenstein WMU, van Diest PJ *et al.* A Novel Diagnostic Tool for Selecting Patients With Mesenchymal-Type Colon Cancer Reveals Intratumor Subtype Heterogeneity. *J Natl Cancer Inst* 2017; **109**.

20 Alderdice M, Richman SD, Gollins S, Stewart JP, Hurt C, Adams R *et al.* Prospective patient stratification into robust cancer-cell intrinsic subtypes from colorectal cancer biopsies. *J Pathol* 2018; **245**: 19–28.

21 Trinh A, Lädrach C, Dawson HE, ten Hoorn S, Kuppen PJK, Reimers MS *et al.* Tumour budding is associated with the mesenchymal colon cancer subtype and RAS/RAF mutations: a study of 1320 colorectal cancers with Consensus Molecular Subgroup (CMS) data. *Br J Cancer* 2018; **119**: 1244–1251.

22 Marisa L, Blum Y, Taieb J, Ayadi M, Pilati C, Le Malicot K *et al.* Intratumor CMS heterogeneity impacts patient prognosis in localized colorectal cancer. *Clin Cancer Res* 2021; **27**: 4768-4780.

23 Madden EC, Gorman AM, Logue SE, Samali A. Tumour Cell Secretome in Chemoresistance and Tumour Recurrence. *Trends Cancer* 2020; **6**: 489–505.

24 Ritchie S, Reed DA, Pereira BA, Timpson P. The cancer cell secretome drives cooperative manipulation of the tumour microenvironment to accelerate tumourigenesis. *Fac Rep* 2021; **10**: 4.

25 Shnaider PV, Ivanova OM, Malyants IK, Anufrieva KS, Semenov IA, Pavlyukov MS *et al.* New Insights into Therapy-Induced Progression of Cancer. *Int J Mol Sci 2*020; **21**: 7872.

26 Aldonza MBD, Hong J-Y, Lee SK. Paclitaxel-resistant cancer cell-derived secretomes elicit ABCB1-associated docetaxel cross-resistance and escape from apoptosis through FOXO3a-driven glycolytic regulation. *Exp Mol Med* 2017; **49**: e286–e286.

27 Emmink BL, Verheem A, Van Houdt WJ, Steller EJA, Govaert KM, Pham TV *et al.* The secretome of colon cancer stem cells contains drug-metabolizing enzymes. *J Proteomics* 2013; **91**: 84–96.

28 Bastola S, Pavlyukov MS, Yamashita D, Ghosh S, Cho H, Kagaya N *et al.* Glioma-initiating cells at tumor edge gain signals from tumor core cells to promote their malignancy. *Nat Commun* 2020; **11**: 4660.

29 Sveen A, Bruun J, Eide PW, Eilertsen IA, Ramirez L, Murumagi A *et al.* Colorectal cancer consensus molecular subtypes translated to preclinical models uncover potentially targetable cancer cell dependencies. *Clin Cancer Res* 2018; **24**: 794–806.

30 Linnekamp JF, Hooff SR van, Prasetyanti PR, Kandimalla R, Buikhuisen JY, Fessler E *et al.* Consensus molecular subtypes of colorectal cancer are recapitulated in in vitro and in vivo models. *Cell Death Differ* 2018; **25**: 616–633.

31 Deng J, Tian A-L, Pan H, Sauvat A, Leduc M, Liu P *et al.* Everolimus and plicamycin specifically target chemoresistant colorectal cancer cells of the CMS4 subtype. *Cell Death Dis* 2021; **12**: 978.

32 Bao B, Jiang J, Yanase T, Nishi Y, Morgan JR. Connexon-mediated cell adhesion drives microtissue self-assembly. *FASEB* 2011; **25**: 255–264.

33 Stadler M, Scherzer M, Walter S, Holzner S, Pudelko K, Riedl A *et al.* Exclusion from spheroid formation identifies loss of essential cell-cell adhesion molecules in colon cancer cells. *Sci Rep* 2018; **8**: 1151.

34 Advances in establishment and analysis of three-dimensional tumor spheroid-based functional assays for target validation and drug evaluation. *BMC Biol* 2012; **10**: 29.

35 Langhans SA. Three-Dimensional in Vitro Cell Culture Models in Drug Discovery and Drug Repositioning. *Front Pharmacol* 2018; **9**: 6.

36 Virgone-Carlotta A, Lemasson M, Mertani HC, Diaz J-J, Monnier S, Dehoux T *et al.* In-depth phenotypic characterization of multicellular tumor spheroids: Effects of 5-Fluorouracil. *PloS One* 2017; **12**: e0188100.

37 Li F, Simon MC. Cancer Cells Don't Live Alone: Metabolic Communication within Tumor Microenvironments. *Dev Cell* 2020; **54**: 183–195.

38 Holohan C, Van Schaeybroeck S, Longley DB, Johnston PG. Cancer drug resistance: an evolving paradigm. *Nat Rev Cancer* 2013; **13**: 714–726.

39 Cree IA, Charlton P. Molecular chess? Hallmarks of anti-cancer drug resistance. *BMC Cancer* 2017; **17**: 10.

40 Zeng X, Yang P, Chen B, Jin X, Liu Y, Zhao X *et al.* Quantitative secretome analysis reveals the interactions between epithelia and tumor cells by in vitro modulating colon cancer microenvironment. *J Proteomics* 2013; **89**: 51–70.

41 Schaaij-Visser TBM, de Wit M, Lam SW, Jiménez CR. The cancer secretome, current status and opportunities in the lung, breast and colorectal cancer context. *Biochim Biophys Acta* 2013; **1834**: 2242–2258.

42 Fertig EJ, Lee E, Pandey NB, Popel AS. Analysis of gene expression of secreted factors associated with breast cancer metastases in breast cancer subtypes. *Sci Rep* 2015; **5**: 12133.

43 Canto LM do, Cury SS, Barros-Filho MC, Kupper BEC, Begnami MDF de S, Scapulatempo-Neto C *et al.* Locally advanced rectal cancer transcriptomic-based secretome analysis reveals novel biomarkers useful to identify patients according to neoadjuvant chemoradiotherapy response. *Sci Rep* 2019; **9**: 8702.

44 Heeran AB, Dunne MR, Morrissey ME, Buckley CE, Clarke N, Cannon A *et al.* The Protein Secretome Is Altered in Rectal Cancer Tissue Compared to Normal Rectal Tissue, and Alterations in the Secretome Induce Enhanced Innate Immune Responses. *Cancers* 2021; **13**: 571.

45 Tato-Costa J, Casimiro S, Pacheco T, Pires R, Fernandes A, Alho I *et al.* Therapy-Induced Cellular Senescence Induces Epithelial-to-Mesenchymal Transition and Increases Invasiveness in Rectal Cancer. *Clin Colorectal Cancer* 2016; **15**: 170-178.e3.

46 Clerici SP, Peppelenbosch M, Fuhler G, Consonni SR, Ferreira-Halder CV. Colorectal Cancer Cell-Derived Small Extracellular Vesicles Educate Human Fibroblasts to Stimulate Migratory Capacity. *Front Cell Dev Biol* 2021; **9**: 696373.

47 Shao Y, Chen T, Zheng X, Yang S, Xu K, Chen X *et al.* Colorectal cancer-derived small extracellular vesicles establish an inflammatory premetastatic niche in liver metastasis. *Carcinogenesis* 2018; **39**: 1368–1379.

48 Zhang S, Zhang Y, Qu J, Che X, Fan Y, Hou K *et al.* Exosomes promote cetuximab resistance via the PTEN/Akt pathway in colon cancer cells. *Braz J Med Biol Res* 2018; **51**: e6472.

49 Ho P-C, Liu P-S. Metabolic communication in tumors: a new layer of immunoregulation for immune evasion. *J Immunother Cancer* 2016; **4**: 4.

50 Gupta S, Roy A, Dwarakanath BS. Metabolic Cooperation and Competition in the Tumor Microenvironment: Implications for Therapy. *Front Oncol* 2017; **7**.

51 Lyssiotis CA, Kimmelman AC. Metabolic Interactions in the Tumor Microenvironment. *Trends Cell Biol* 2017; **27**: 863–875.

52 Li X, Wenes M, Romero P, Huang SC-C, Fendt S-M, Ho P-C. Navigating metabolic pathways to enhance antitumour immunity and immunotherapy. *Nat Rev Clin Oncol* 2019; **16**: 425–441.

53 Mao MJ, Leonardi DE. Vascular-endothelial response to IDH1 mutant fibrosarcoma secretome and metabolite: implications on cancer microenvironment. *Nat Rev Clin Oncol* 2019; 16, 425–441.

54 Mackay GM, Zheng L, van den Broek NJF, Gottlieb E. Chapter Five - Analysis of Cell Metabolism Using LC-MS and Isotope Tracers. In: Metallo CM (ed). *Methods Enzymol*. 2015; 561: 171–196.

55 Hahn C, Schwartz MA. Mechanotransduction in vascular physiology and atherogenesis. *Nat Rev Mol Cell Biol* 2009; **10**: 53–62.

Acknowledgements

The authors thank the CRC core facilities for the technical and methodological help, assistance and support. Image acquisition was done at the "Histology, cell Imaging and flow Cytometry Center (CHIC)". JK is funded by the European Union's Horizon 2020 research and innovation program under the Marie Skłodowska-Curie grant agreement No 813786. AH was supported by EUR G.E.N.E. (reference #ANR-17-EURE-0013), part of the Université de Paris IdEx #ANR-18-IDEX-0001 funded by the French Government through its "Investments for the Future" program. SB was funded by Campus France scholarship. This work was supported by the Ministère de l'Enseignement Supérieur et de la Recherche, the Université Paris-Descartes, the Centre National de la Recherche Scientifique (CNRS), the Institut National de la Santé et de la Recherche Médicale (INSERM), the National Cancer Institute, the Ministry of Solidarity and Health, the SIRIC CARPEM (CAncer Research and PErsonalized Medicine, funding and fellowship for W.X.; no. INCa-DGOS-Inserm_12561), the Ligue Nationale Contre le Cancer (LNCC, Program "Equipe labelisée LIGUE"; no. EL2016.LNCC/VaT) and Canceropole Ile-de-France. This work was supported by ITMO Cancer AVIESAN (Alliance Nationale pour les Sciences de la Vie et de la Santé, National Alliance for Life Sciences and Health; N◦19CS006-

00, COCAHEMSICLE) within the framework of the Cancer Plan, and by Institut National du Cancer (INCa) with the program Heterogeneity of tumors and ecosystem (HTE program) within the sub program “deciphering the heterogeneous genome-microenvironment interplay in colon and hepatocellular carcinomas (HETCOLI). GK is supported by the Ligue contre le Cancer (équipe labellisée); Agence National de la Recherche (ANR)—Projets blancs; ANR under the frame of E-Rare-2, the ERA-Net for Research on Rare Diseases; Association pour la recherche sur le cancer (ARC); Cancéropôle Ile-de-France; Chancellerie des universités de Paris (Legs Poix), Fondation pour la Recherche Médicale (FRM); a donation by Elior; European Research Area Network on Cardiovascular Diseases (ERA-CVD, MINOTAUR); Gustave Roussy Odyssea, the European Union Horizon 2020 Project Oncobiome; Fondation Carrefour; High-end Foreign Expert Program in China (GDW20171100085 and GDW20181100051), Institut National du Cancer (INCa); Inserm (HTE); Institut Universitaire de France; LeDucq Foundation; the LabEx Immuno-Oncology; the RHU Torino Lumière; the Seerave Foundation; the SIRIC Stratified Oncology Cell DNA Repair and Tumor Immune Elimination (SOCRATE); and the SIRIC Cancer Research and Personalized Medicine (CARPEM). OK is supported by the DIM Elicit and INCA.

Author contributions statement

WX and VT participated to the conception of this work. WX, GK, SMR, PLP and VT participated to the design of the work. WX, JK, AH, VM, SB, IN and OK participated to the data acquisition and analysis. WX, JK, AH, VM, SB, IN, OK, GK, SMR, PLP and VT participated to data interpretation. WX, AH, OK, GK, SMR, PLP and VT participated to the writing and revision of the work. All authors have approved the submitted version and have agreed both to be personally accountable for the author's own contributions and to ensure that questions related to the accuracy or integrity of any part of the work, even ones in which the

author was not personally involved, are appropriately investigated, resolved, and the resolution documented in the literature.

Competing interests

The authors do not have competing interest in the work presented here.

Data Availability Statement

The datasets generated during and/or analyzed during the current study are available from the corresponding author on reasonable request.

Appendix

Table S1 IC_{50} of colorectal cancer cell lines to 5-FU

Colorectal cancer (CRC) cell lines were treated with different concentrations of 5-FU and cell viability was measured using MTS assays. The average and the standard deviation were calculated using cells from 3 different passages (n=3). Statistical significance was calculated using a two-tailed Student's t-test. A p-value of less than 0.05 and 0.01 considered significant (*) and highly significant (**), respectively.

Cell line	IC_{50} (μM) of 72h
HCT116	3.83 ± 0.76
LoVo	18.85 ± 3.65
MDST8	8.53 ± 1.60
SW620	124.68 ± 27.09

Table S3. Pathway analysis on down-regulated metabolites in DMSO vehicle treated conditioned media (CM_Vehicle) of HCT116 compared to control media without cells (Control).

The Total is the total number of compounds in the pathway; the Hits is the actually matched number from the user uploaded data; the Raw p is the original p value calculated from the enrichment analysis; the Holm p is the p value adjusted by Holm-Bonferroni method; the FDR p is the p value adjusted using False Discovery Rate; the Impact is the pathway impact value calculated from pathway topology analysis.

	Total	Expected	Hits	Raw p	-log10(p)	Holm adjust	FDR	Impact
Aminoacyl-tRNA biosynthesis	48	0.59	9	8.85E-10	9.05E+00	7.43E-08	7.43E-08	0.00
Glycine, serine and threonine metabolism	33	0.40	4	5.28E-04	3.28E+00	4.38E-02	2.22E-02	0.09
Phenylalanine, tyrosine and tryptophan biosynthesis	4	0.05	2	8.42E-04	3.07E+00	6.91E-02	2.36E-02	1.00
Valine, leucine and isoleucine biosynthesis	8	0.10	2	3.82E-03	2.42E+00	3.09E-01	7.09E-02	0.00
Alanine, aspartate and glutamate metabolism	28	0.34	3	4.22E-03	2.37E+00	3.37E-01	7.09E-02	0.11
Phenylalanine metabolism	10	0.12	2	6.04E-03	2.22E+00	4.78E-01	8.46E-02	0.36
Glyoxylate and dicarboxylate metabolism	32	0.39	2	5.68E-02	1.25E+00	1.00E+00	4.84E-01	0.00
Linoleic acid metabolism	5	0.06	1	5.99E-02	1.22E+00	1.00E+00	4.84E-01	1.00
Cysteine and methionine metabolism	33	0.40	2	6.00E-02	1.22E+00	1.00E+00	4.84E-01	0.10
Biosynthesis of unsaturated fatty acids	36	0.44	2	7.00E-02	1.15E+00	1.00E+00	4.84E-01	0.00
D-Glutamine and D-glutamate metabolism	6	0.07	1	7.14E-02	1.15E+00	1.00E+00	4.84E-01	0.00
Nitrogen metabolism	6	0.07	1	7.14E-02	1.15E+00	1.00E+00	4.84E-01	0.00
Arginine and proline metabolism	38	0.47	2	7.70E-02	1.11E+00	1.00E+00	4.84E-01	0.01
Pyrimidine metabolism	39	0.48	2	8.06E-02	1.09E+00	1.00E+00	4.84E-01	0.01
Tyrosine metabolism	42	0.51	2	9.17E-02	1.04E+00	1.00E+00	5.13E-01	0.14
Ubiquinone and other terpenoid-quinone biosynthesis	9	0.11	1	1.05E-01	9.77E-01	1.00E+00	5.53E-01	0.00
Biotin metabolism	10	0.12	1	1.16E-01	9.34E-01	1.00E+00	5.75E-01	0.00
Arginine biosynthesis	14	0.17	1	1.59E-01	7.98E-01	1.00E+00	7.43E-01	0.00
Nicotinate and nicotinamide metabolism	15	0.18	1	1.70E-01	7.71E-01	1.00E+00	7.50E-01	0.00
Purine metabolism	65	0.80	2	1.88E-01	7.26E-01	1.00E+00	7.89E-01	0.02
Selenocompound metabolism	20	0.25	1	2.20E-01	6.58E-01	1.00E+00	8.39E-01	0.00
Citrate cycle (TCA cycle)	20	0.25	1	2.20E-01	6.58E-01	1.00E+00	8.39E-01	0.05
Pyruvate metabolism	22	0.27	1	2.39E-01	6.21E-01	1.00E+00	8.73E-01	0.21
Lysine degradation	25	0.31	1	2.67E-01	5.73E-01	1.00E+00	9.28E-01	0.00
Glycolysis / Gluconeogenesis	26	0.32	1	2.76E-01	5.59E-01	1.00E+00	9.28E-01	0.10
Valine, leucine and isoleucine degradation	40	0.49	1	3.93E-01	4.05E-01	1.00E+00	1.00E+00	0.00
Tryptophan metabolism	41	0.50	1	4.01E-01	3.97E-01	1.00E+00	1.00E+00	0.14

Table S4. Pathway analysis on up-regulated metabolites in DMSO vehicle treated conditioned media (CM_Vehicle) of HCT116 compared to control media without cells (Control).

The Total is the total number of compounds in the pathway; the Hits is the actually matched number from the user uploaded data; the Raw p is the original p value calculated from the enrichment analysis; the Holm p is the p value adjusted by Holm-Bonferroni method; the FDR p is the p value adjusted using False Discovery Rate; the Impact is the pathway impact value calculated from pathway topology analysis.

	Total	Expected	Hits	Raw p	-log10(p)	Holm adjust	FDR	Impact
Alanine, aspartate and glutamate metabolism	28	0.38	6	8.91E-07	6.05E+00	7.48E-05	7.48E-05	0.33
Citrate cycle (TCA cycle)	20	0.27	4	1.05E-04	3.98E+00	8.72E-03	4.36E-03	0.18
Pyruvate metabolism	22	0.30	4	1.56E-04	3.81E+00	1.28E-02	4.36E-03	0.24
Glyoxylate and dicarboxylate metabolism	32	0.43	4	7.01E-04	3.15E+00	5.68E-02	1.19E-02	0.11
Arginine biosynthesis	14	0.19	3	7.10E-04	3.15E+00	5.68E-02	1.19E-02	0.12
D-Glutamine and D-glutamate metabolism	6	0.08	2	2.54E-03	2.60E+00	2.01E-01	3.55E-02	0.50
Butanoate metabolism	15	0.20	2	1.65E-02	1.78E+00	1.00E+00	1.98E-01	0.00
Aminoacyl-tRNA biosynthesis	48	0.65	3	2.51E-02	1.60E+00	1.00E+00	2.63E-01	0.00
Glycolysis / Gluconeogenesis	26	0.35	2	4.67E-02	1.33E+00	1.00E+00	4.36E-01	0.10
Glutathione metabolism	28	0.38	2	5.35E-02	1.27E+00	1.00E+00	4.49E-01	0.11
Porphyrin and chlorophyll metabolism	30	0.41	2	6.06E-02	1.22E+00	1.00E+00	4.63E-01	0.00
Cysteine and methionine metabolism	33	0.45	2	7.18E-02	1.14E+00	1.00E+00	4.64E-01	0.03
Glycine, serine and threonine metabolism	33	0.45	2	7.18E-02	1.14E+00	1.00E+00	4.64E-01	0.25
Nitrogen metabolism	6	0.08	1	7.87E-02	1.10E+00	1.00E+00	4.72E-01	0.00
Arginine and proline metabolism	38	0.51	2	9.18E-02	1.04E+00	1.00E+00	5.14E-01	0.09
Tryptophan metabolism	41	0.56	2	1.04E-01	9.81E-01	1.00E+00	5.38E-01	0.20
Tyrosine metabolism	42	0.57	2	1.09E-01	9.63E-01	1.00E+00	5.38E-01	0.02
Vitamin B6 metabolism	9	0.12	1	1.16E-01	9.36E-01	1.00E+00	5.40E-01	0.49
Nicotinate and nicotinamide metabolism	15	0.20	1	1.86E-01	7.31E-01	1.00E+00	7.88E-01	0.19
Histidine metabolism	16	0.22	1	1.97E-01	7.06E-01	1.00E+00	7.88E-01	0.00
Glycerolipid metabolism	16	0.22	1	1.97E-01	7.06E-01	1.00E+00	7.88E-01	0.04
Glycerophospholipid metabolism	36	0.49	1	3.91E-01	4.07E-01	1.00E+00	1.00E+00	0.08
Amino sugar and nucleotide sugar metabolism	37	0.50	1	4.00E-01	3.98E-01	1.00E+00	1.00E+00	0.00
Pyrimidine metabolism	39	0.53	1	4.16E-01	3.80E-01	1.00E+00	1.00E+00	0.05
Primary bile acid biosynthesis	46	0.62	1	4.71E-01	3.27E-01	1.00E+00	1.00E+00	0.01
Fatty acid biosynthesis	47	0.64	1	4.78E-01	3.20E-01	1.00E+00	1.00E+00	0.00
Purine metabolism	65	0.88	1	5.96E-01	2.25E-01	1.00E+00	1.00E+00	0.00

Table S5. Pathway analysis on down-regulated metabolites in DMSO vehicle treated conditioned media (CM_Vehicle) of LoVo compared to control media without cells (Control).

The Total is the total number of compounds in the pathway; the Hits is the actually matched number from the user uploaded data; the Raw p is the original p value calculated from the enrichment analysis; the Holm p is the p value adjusted by Holm-Bonferroni method; the FDR p is the p value adjusted using False Discovery Rate; the Impact is the pathway impact value calculated from pathway topology analysis.

	Total	Expected	Hits	Raw p	-log10(p)	Holm adjust	FDR	Impact
Aminoacyl-tRNA biosynthesis	48	0.81	12	1.29E-12	1.19E+01	1.08E-10	1.08E-10	0.00
Valine, leucine and isoleucine biosynthesis	8	0.13	3	2.22E-04	3.65E+00	1.84E-02	9.33E-03	0.00
Phenylalanine, tyrosine and tryptophan biosynthesis	4	0.07	2	1.59E-03	2.80E+00	1.30E-01	4.45E-02	1.00
Taurine and hypotaurine metabolism	8	0.13	2	7.12E-03	2.15E+00	5.77E-01	1.50E-01	0.71
Alanine, aspartate and glutamate metabolism	28	0.47	3	1.04E-02	1.98E+00	8.32E-01	1.57E-01	0.34
Phenylalanine metabolism	10	0.17	2	1.12E-02	1.95E+00	8.86E-01	1.57E-01	0.36
Glycine, serine and threonine metabolism	33	0.55	3	1.64E-02	1.79E+00	1.00E+00	1.97E-01	0.09
Biosynthesis of unsaturated fatty acids	36	0.60	3	2.07E-02	1.68E+00	1.00E+00	2.03E-01	0.00
Arginine biosynthesis	14	0.23	2	2.18E-02	1.66E+00	1.00E+00	2.03E-01	0.00
Nicotinate and nicotinamide metabolism	15	0.25	2	2.49E-02	1.60E+00	1.00E+00	2.09E-01	0.00
Histidine metabolism	16	0.27	2	2.81E-02	1.55E+00	1.00E+00	2.15E-01	0.22
beta-Alanine metabolism	21	0.35	2	4.67E-02	1.33E+00	1.00E+00	3.27E-01	0.00
Linoleic acid metabolism	5	0.08	1	8.12E-02	1.09E+00	1.00E+00	5.25E-01	1.00
D-Glutamine and D-glutamate metabolism	6	0.10	1	9.67E-02	1.01E+00	1.00E+00	5.41E-01	0.00
Nitrogen metabolism	6	0.10	1	9.67E-02	1.01E+00	1.00E+00	5.41E-01	0.00
Cysteine and methionine metabolism	33	0.55	2	1.04E-01	9.83E-01	1.00E+00	5.46E-01	0.13
Pyrimidine metabolism	39	0.65	2	1.37E-01	8.62E-01	1.00E+00	6.33E-01	0.01
Ubiquinone and other terpenoid-quinone biosynthesis	9	0.15	1	1.42E-01	8.49E-01	1.00E+00	6.33E-01	0.00
Valine, leucine and isoleucine degradation	40	0.67	2	1.43E-01	8.44E-01	1.00E+00	6.33E-01	0.00
Biotin metabolism	10	0.17	1	1.56E-01	8.07E-01	1.00E+00	6.55E-01	0.00
Pantothenate and CoA biosynthesis	19	0.32	1	2.76E-01	5.59E-01	1.00E+00	1.00E+00	0.00
Selenocompound metabolism	20	0.34	1	2.89E-01	5.40E-01	1.00E+00	1.00E+00	0.00
Purine metabolism	65	1.09	2	2.98E-01	5.25E-01	1.00E+00	1.00E+00	0.02
Lysine degradation	25	0.42	1	3.47E-01	4.60E-01	1.00E+00	1.00E+00	0.00
Glycolysis / Gluconeogenesis	26	0.44	1	3.58E-01	4.46E-01	1.00E+00	1.00E+00	0.00
Glyoxylate and dicarboxylate metabolism	32	0.54	1	4.21E-01	3.75E-01	1.00E+00	1.00E+00	0.00
Arginine and proline metabolism	38	0.64	1	4.78E-01	3.20E-01	1.00E+00	1.00E+00	0.01
Tryptophan metabolism	41	0.69	1	5.05E-01	2.97E-01	1.00E+00	1.00E+00	0.14
Tyrosine metabolism	42	0.70	1	5.13E-01	2.90E-01	1.00E+00	1.00E+00	0.14
Primary bile acid biosynthesis	46	0.77	1	5.46E-01	2.63E-01	1.00E+00	1.00E+00	0.01

Table S6. Pathway analysis on up-regulated metabolites in DMSO vehicle treated conditioned media (CM_Vehicle) of LoVo compared to control media without cells (Control).

The Total is the total number of compounds in the pathway; the Hits is the actually matched number from the user uploaded data; the Raw p is the original p value calculated from the enrichment analysis; the Holm p is the p value adjusted by Holm-Bonferroni method; the FDR p is the p value adjusted using False Discovery Rate; the Impact is the pathway impact value calculated from pathway topology analysis.

	Total	Expected	Hits	Raw p	-log10(p)	Holm adjust	FDR	Impact
Citrate cycle (TCA cycle)	20	0.32	5	9.45E-06	5.02E+00	7.94E-04	7.94E-04	0.23
Arginine biosynthesis	14	0.23	4	4.74E-05	4.32E+00	3.93E-03	1.54E-03	0.35
Alanine, aspartate and glutamate metabolism	28	0.45	5	5.49E-05	4.26E+00	4.50E-03	1.54E-03	0.33
Glyoxylate and dicarboxylate metabolism	32	0.52	5	1.08E-04	3.97E+00	8.72E-03	2.26E-03	0.13
Pyruvate metabolism	22	0.35	4	3.17E-04	3.50E+00	2.54E-02	5.33E-03	0.24
Butanoate metabolism	15	0.24	3	1.49E-03	2.83E+00	1.17E-01	2.08E-02	0.00
D-Glutamine and D-glutamate metabolism	6	0.10	2	3.60E-03	2.44E+00	2.81E-01	4.32E-02	0.50
Glutathione metabolism	28	0.45	3	9.31E-03	2.03E+00	7.17E-01	9.78E-02	0.11
Glycine, serine and threonine metabolism	33	0.53	3	1.47E-02	1.83E+00	1.00E+00	1.37E-01	0.25
Pantothenate and CoA biosynthesis	19	0.31	2	3.61E-02	1.44E+00	1.00E+00	3.03E-01	0.01
Aminoacyl-tRNA biosynthesis	48	0.77	3	3.97E-02	1.40E+00	1.00E+00	3.03E-01	0.00
Riboflavin metabolism	4	0.06	1	6.30E-02	1.20E+00	1.00E+00	4.14E-01	0.50
Glycolysis / Gluconeogenesis	26	0.42	2	6.41E-02	1.19E+00	1.00E+00	4.14E-01	0.10
Porphyrin and chlorophyll metabolism	30	0.48	2	8.25E-02	1.08E+00	1.00E+00	4.95E-01	0.00
Nitrogen metabolism	6	0.10	1	9.31E-02	1.03E+00	1.00E+00	5.11E-01	0.00
Cysteine and methionine metabolism	33	0.53	2	9.73E-02	1.01E+00	1.00E+00	5.11E-01	0.10
Thiamine metabolism	7	0.11	1	1.08E-01	9.67E-01	1.00E+00	5.33E-01	0.00
Taurine and hypotaurine metabolism	8	0.13	1	1.22E-01	9.13E-01	1.00E+00	5.46E-01	0.00
Arginine and proline metabolism	38	0.61	2	1.23E-01	9.09E-01	1.00E+00	5.46E-01	0.09
Vitamin B6 metabolism	9	0.15	1	1.36E-01	8.65E-01	1.00E+00	5.55E-01	0.49
Tryptophan metabolism	41	0.66	2	1.40E-01	8.54E-01	1.00E+00	5.55E-01	0.20
Tyrosine metabolism	42	0.68	2	1.45E-01	8.37E-01	1.00E+00	5.55E-01	0.02
Nicotinate and nicotinamide metabolism	15	0.24	1	2.17E-01	6.63E-01	1.00E+00	7.73E-01	0.19
Histidine metabolism	16	0.26	1	2.30E-01	6.38E-01	1.00E+00	7.73E-01	0.00
Glycerolipid metabolism	16	0.26	1	2.30E-01	6.38E-01	1.00E+00	7.73E-01	0.04
Glycerophospholipid metabolism	36	0.58	1	4.47E-01	3.50E-01	1.00E+00	1.00E+00	0.08
Pyrimidine metabolism	39	0.63	1	4.74E-01	3.24E-01	1.00E+00	1.00E+00	0.05
Primary bile acid biosynthesis	46	0.74	1	5.32E-01	2.74E-01	1.00E+00	1.00E+00	0.01

Table S7. Overlap of fold change of metabolite levels in DMSO vehicle treated conditioned media (CM_Vehicle) of HCT116 and LoVo compared to control media without cells (Control).

Metabolite	log2 (fold change, down-regulated)		Metabolite	log2 (fold change, up-regulated)	
	HCT116	LoVo		HCT116	LoVo
Hypoxanthine	-6.49	-6.48	Glycerol 3-phosphate	5.94	3.45
Niacin / nicotinate	-5.64	-6.73	Alpha-Ketoglutarate	3.95	4.10
Linoleic acid	-4.79	-2.89	Orotic acid	3.80	6.29
Cytidine	-4.69	-5.38	Pyruvate	3.25	2.86
Glutamine	-4.45	-4.78	Lactate	2.91	2.97
Serine	-2.28	-2.53	N-acetylaspartate	2.85	3.54
Taurine	-1.90	-2.09	Serotonin	1.59	1.99
Oleic acid	-1.74	-1.43	pyridoxal	1.26	1.93
Palmitoleic acid	-1.44	-1.91	acetyllysine	0.94	1.67
Tryptophan	-1.39	-2.05	Malate	0.61	0.72
Creatine	-1.39	-1.71	Fumarate	0.45	0.53
Leucine	-1.01	-0.68	glutamate	0.40	0.22
Lysine	-0.99	-0.85	Glycine	0.34	0.22
Methionine	-0.94	-1.29	L-Kynurenine	0.24	0.40
Threonine	-0.80	-0.98	Creatinine	0.19	0.24
Glucose	-0.69	-0.83			
Tyrosine	-0.66	-0.85			
L-Alanine	-0.50	-1.32			
L-Sarcosine	-0.50	-1.32			
Histidine	-0.50	-0.65			
Phenylalanine	-0.49	-0.67			
Cysteine sulfinic acid	-0.47	-0.76			
IsoLeucine	-0.46	-0.73			
carnitine	-0.45	-0.75			
Aspartate	-0.36	-0.72			

Table S8. Fold change of metabolite levels in 5-FU treated conditioned media (CM_5-FU) of HCT116 compared to DMSO vehicle treated conditioned media (CM_Vehicle).

Metabolite	log2 (fold change, down-regulated)	Metabolite	log2 (fold change, up-regulated)
Orotic acid	-1.84	Glutamine	4.02
Glycerol 3-phosphate	-1.02	Niacin/ Nicotinate	2.96
Lactate	-1.01	Hypoxanthine	2.24
Acetyllysine	-0.53	Octanoyl-carnitine	2.21
Asparagine	-0.51	Palmitoleic acid	1.74
Alpha-Ketoglutarate	-0.46	Serine	1.66
N-acetylaspartate	-0.25	Oleic acid	1.55
Fructose	-0.20	Taurine	1.55
Glutamate	-0.18	Tryptophan	1.18
Creatinine	-0.17	Lysine	0.88
		Creatine	0.84
		Ornithine	0.83
		Pyruvate	0.79
		Methionine	0.71
		Leucine	0.69
		Valine	0.64
		Cystine	0.57
		Threonine	0.56
		Tyrosine	0.50
		L-Alanine	0.44
		L-Sarcosine	0.44
		Cytidine	0.42
		Glucose	0.39
		Histidine	0.38
		Phenylalanine	0.37
		IsoLeucine	0.33
		Carnitine	0.24

Table S9. Fold change of metabolite levels in 5-FU treated conditioned media (CM_5-FU) of LoVo compared to DMSO vehicle treated conditioned media (CM_Vehicle).

Metabolite	log2 (fold change, down-regulated)	Metabolite	log2 (fold change, up-regulated)
Cysteine	-1.46	Docosahexaenoic acid	4.59
Butyric acid	-1.08	Glutamine	4.03
Acetyllysine	-0.93	Niacin/ Nicotinate	1.85
Lactate	-0.79	Oxoadipate	1.78
Serine	-0.77	Threonine	1.65
Folate	-0.67	Pyruvate	1.65
Cis-aconitate	-0.57	Hypoxanthine	1.51
Acetylcysteine	-0.45	Cytidine	1.49
L-Kynurenine	-0.35	Dodecanoic acid/Lauric acid	1.35
Citrulline	-0.34	L-Alanine	1.26
Carnosine	-0.25	L-Sarcosine	1.26
Fructose	-0.24	Creatine	1.09
Hexanoic acid	-0.24	Phenylalanine	1.05
Betaine	-0.22	Methionine	0.93
		Linoleic acid	0.78
		Lysine	0.77
		Oleic acid	0.76
		Serotonin	0.70
		Myristic acid	0.60
		Tryptophan	0.55
		Palmitoleic acid	0.50
		IsoLeucine	0.40
		Aspartate	0.32

Table S10. Pathway analysis on the overlap of metabolites in 5-FU treated conditioned media (CM_5-FU) of HCT116 and LoVo compared to DMSO vehicle treated conditioned media (CM_Vehicle).

The Total is the total number of compounds in the pathway; the Hits is the actually matched number from the user uploaded data; the Raw p is the original p value calculated from the enrichment analysis; the Holm p is the p value adjusted by Holm-Bonferroni method; the FDR p is the p value adjusted using False Discovery Rate; the Impact is the pathway impact value calculated from pathway topology analysis (maximum importance of each pathway is 1.0).

	Total	Expected	Hits	Raw p	-log10(p)	Holm adjust	FDR	Impact
Aminoacyl-tRNA biosynthesis	48	0.59	9	8.85E-10	9.05E+00	7.43E-08	7.43E-08	0.00
Glycine, serine and threonine metabolism	33	0.40	4	5.28E-04	3.28E+00	4.38E-02	2.22E-02	0.09
Phenylalanine, tyrosine and tryptophan biosynthesis	4	0.05	2	8.42E-04	3.07E+00	6.91E-02	2.36E-02	1.00
Valine, leucine and isoleucine biosynthesis	8	0.10	2	3.82E-03	2.42E+00	3.09E-01	7.09E-02	0.00
Alanine, aspartate and glutamate metabolism	28	0.34	3	4.22E-03	2.37E+00	3.37E-01	7.09E-02	0.11
Phenylalanine metabolism	10	0.12	2	6.04E-03	2.22E+00	4.78E-01	8.46E-02	0.36
Glyoxylate and dicarboxylate metabolism	32	0.39	2	5.68E-02	1.25E+00	1.00E+00	4.84E-01	0.00
Linoleic acid metabolism	5	0.06	1	5.99E-02	1.22E+00	1.00E+00	4.84E-01	1.00
Cysteine and methionine metabolism	33	0.40	2	6.00E-02	1.22E+00	1.00E+00	4.84E-01	0.10
Biosynthesis of unsaturated fatty acids	36	0.44	2	7.00E-02	1.15E+00	1.00E+00	4.84E-01	0.00
D-Glutamine and D-glutamate metabolism	6	0.07	1	7.14E-02	1.15E+00	1.00E+00	4.84E-01	0.00
Nitrogen metabolism	6	0.07	1	7.14E-02	1.15E+00	1.00E+00	4.84E-01	0.00
Arginine and proline metabolism	38	0.47	2	7.70E-02	1.11E+00	1.00E+00	4.84E-01	0.01
Pyrimidine metabolism	39	0.48	2	8.06E-02	1.09E+00	1.00E+00	4.84E-01	0.01
Tyrosine metabolism	42	0.51	2	9.17E-02	1.04E+00	1.00E+00	5.13E-01	0.14
Ubiquinone and other terpenoid-quinone biosynthesis	9	0.11	1	1.05E-01	9.77E-01	1.00E+00	5.53E-01	0.00
Biotin metabolism	10	0.12	1	1.16E-01	9.34E-01	1.00E+00	5.75E-01	0.00
Arginine biosynthesis	14	0.17	1	1.59E-01	7.98E-01	1.00E+00	7.43E-01	0.00
Nicotinate and nicotinamide metabolism	15	0.18	1	1.70E-01	7.71E-01	1.00E+00	7.50E-01	0.00
Purine metabolism	65	0.80	2	1.88E-01	7.26E-01	1.00E+00	7.89E-01	0.02
Selenocompound metabolism	20	0.25	1	2.20E-01	6.58E-01	1.00E+00	8.39E-01	0.00
Citrate cycle (TCA cycle)	20	0.25	1	2.20E-01	6.58E-01	1.00E+00	8.39E-01	0.05
Pyruvate metabolism	22	0.27	1	2.39E-01	6.21E-01	1.00E+00	8.73E-01	0.21
Lysine degradation	25	0.31	1	2.67E-01	5.73E-01	1.00E+00	9.28E-01	0.00
Glycolysis / Gluconeogenesis	26	0.32	1	2.76E-01	5.59E-01	1.00E+00	9.28E-01	0.10
Valine, leucine and isoleucine degradation	40	0.49	1	3.93E-01	4.05E-01	1.00E+00	1.00E+00	0.00
Tryptophan metabolism	41	0.50	1	4.01E-01	3.97E-01	1.00E+00	1.00E+00	0.14

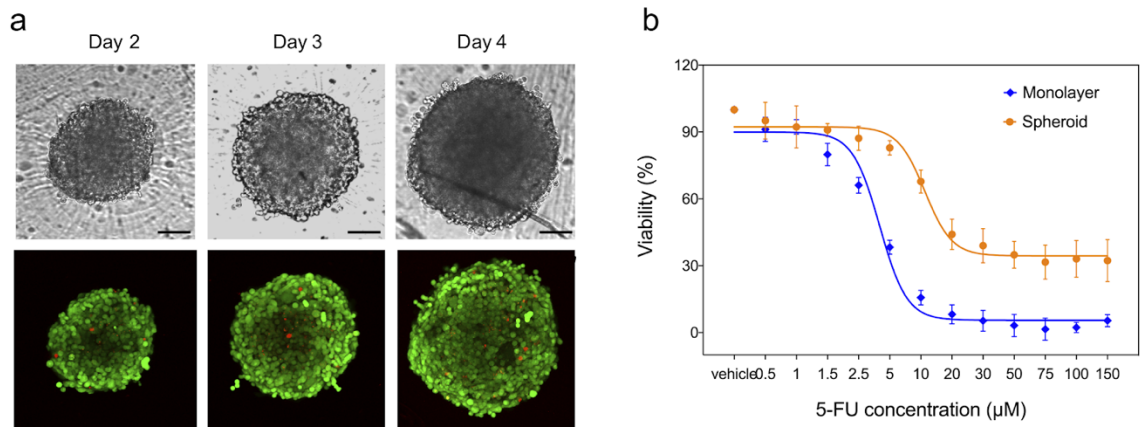

Figure S1 3D tumor spheroid formation of HCT116 and drug responses to 5-FU

(**a**) Representative live cell confocal fluorescence microscopy images showing HCT116 spheroid formation from day 2 to day 4 post seeding. Cell viability was assessed by live/dead staining using Calcein (green) and PI (red). Scale bars=100 μm. (**b**). Dose responses of HCT116 cells to 5-FU. Cells were treated with different concentrations of 5-FU and cell viability was measured using MTS assays. The squares, circles and triangles represent measured viability normalized by the vehicle control, while the solid lines represent dose response curves. The symbols represent the average and the error bars represent the standard deviation (n=3).

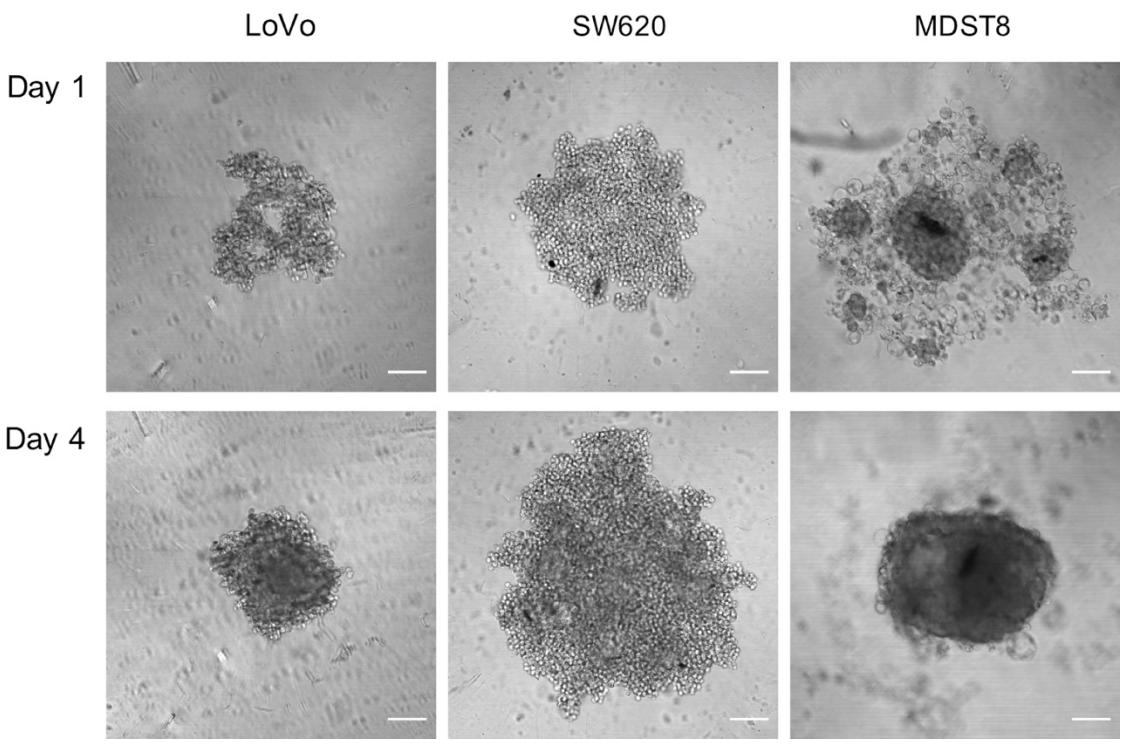

Figure S2 3D tumor spheroid formation of CMS cell lines

Representative bright field microscopy images showing LoVo, SW620 and MDST8 spheroid formation on day 1 and day 4 post seeding. Scale bars=100 µm.

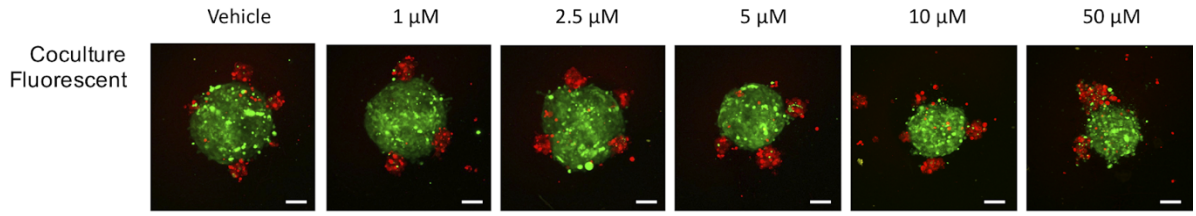

Figure S3 Monocultured and cocultured spheroids of HCT116 and MDST8

Representative live cell confocal fluorescence microscopy images showing spheroid morphology after 3 days of 5-FU treatment. Cells stained with either cell tracker CMFDA (green) or CMRA (red) fluorescent probes. Scale bars=100 µm.

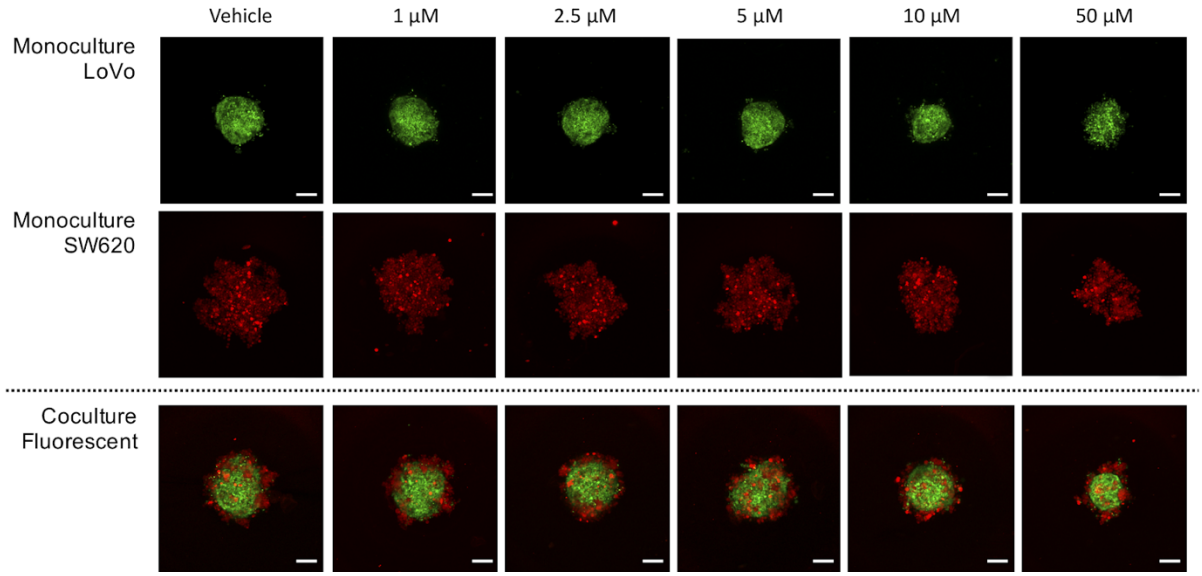

Figure S4 Monocultured and cocultured spheroids of LoVo and SW620

Representative live cell confocal fluorescence microscopy images showing spheroid morphology after 3 days of 5-FU treatment. LoVo cells expressed a GFP reporter (green) and SW620 cells were stained with cell tracker CMRA (red) fluorescent probes. Scale bars=100 μm.

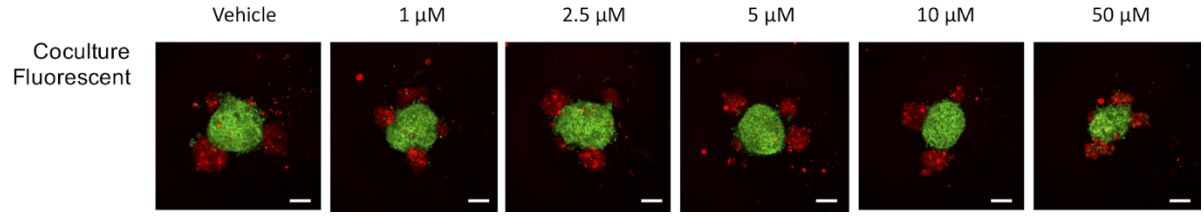

Figure S5 Cocultured spheroids of LoVo and MDST8

Representative live cell confocal fluorescence microscopy images showing spheroid formation morphology after 3 days of 5-FU treatment. LoVo cells expressed a GFP reporter (green) and

MDST8 cells were stained with cell tracker CMRA (red) fluorescent probes. Scale bars=100 μm.

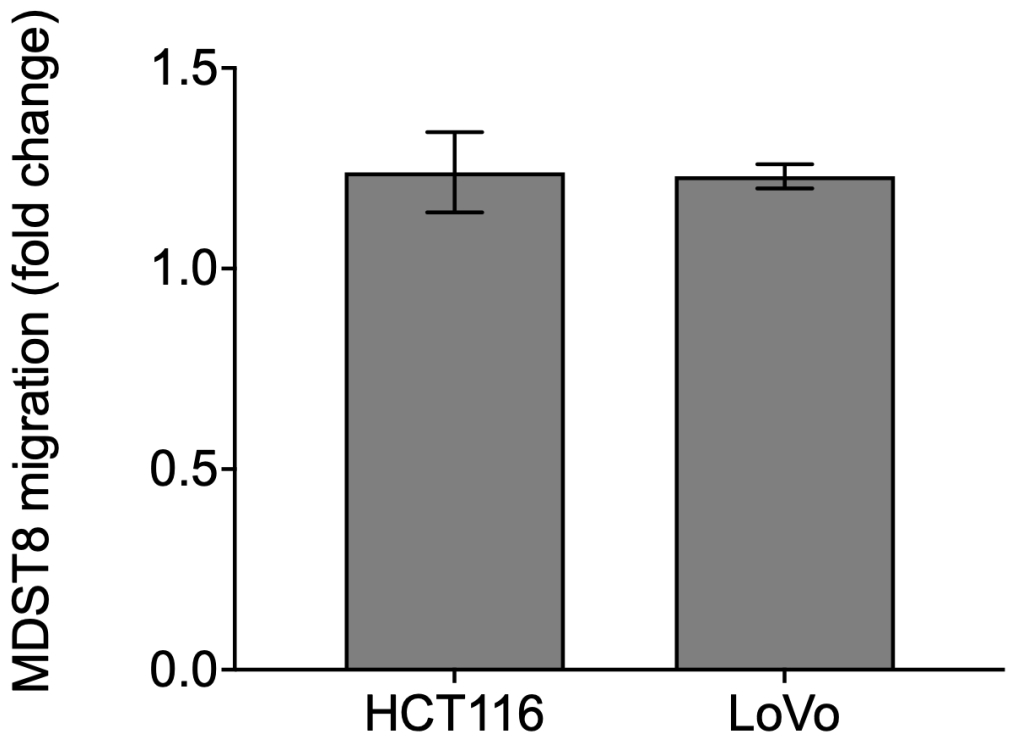

Figure S6 MDST8 cell migration through transwell membrane

Fold change of MDST8 migration through non-Matrigel coated transwell membrane when exposed to HCT116 or LoVo in the bottom wells. MDST8 exposed to only media without cells was taken as a control. Cells were treated with DMSO vehicle. The bars represent the average and the error bars represent the standard deviation (n=3). Statistical significance was calculated using a one-way ANOVA followed by Student's t-test. A p-value of less than 0.05 and 0.01 were considered significant (*) and highly significant (**), respectively.

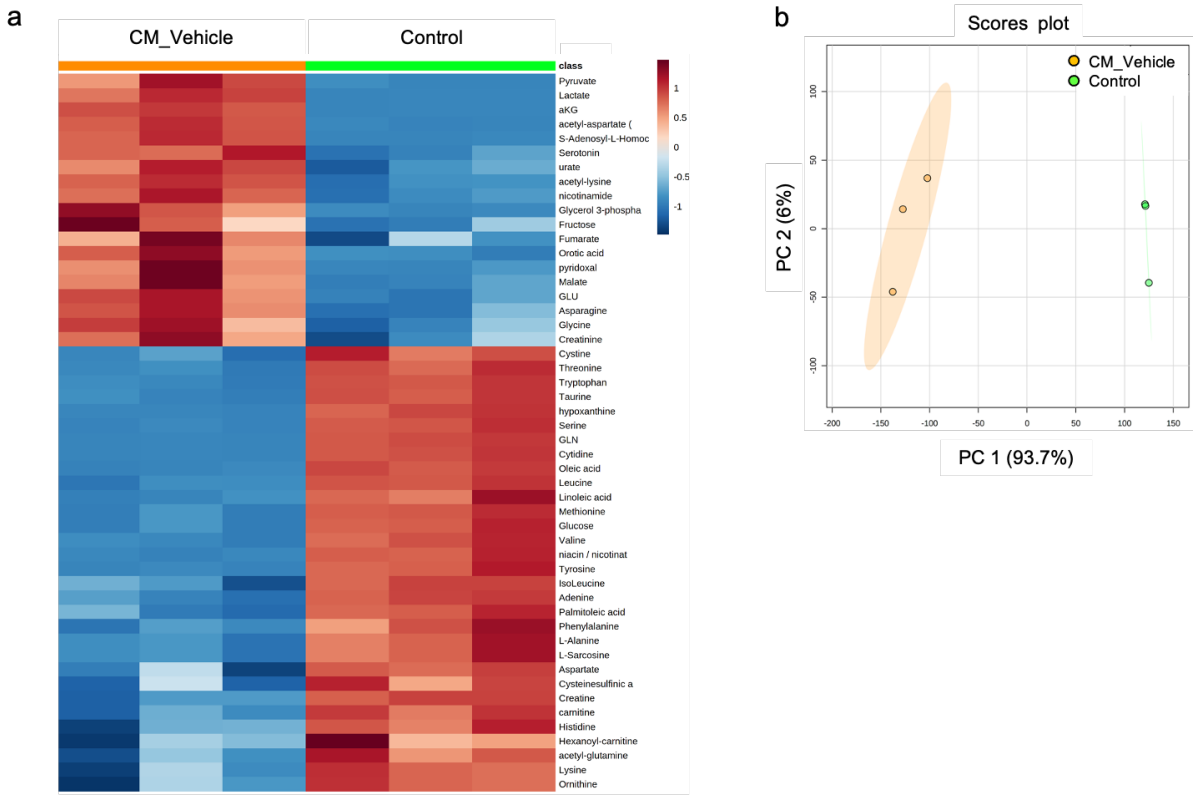

Figure S7 Metabolite analyses of HCT116 conditioned media

(**a**) Metabolomics profile of vehicle treated conditioned media (CM_Vehicle, orange) of HCT116 compared to control media without cells (Control, green), presented as a heatmap visualization and hierarchical clustering analysis. Rows are metabolites and columns are samples (n=3). The color key indicates the metabolite expression value (blue, lowest; red, highest). (**b**) Principal component analysis (PCA) plotting showing clusters of samples based on their similarity. Statistical significance was calculated using a one-way ANOVA followed by Student's t-test ($p<0.05$).

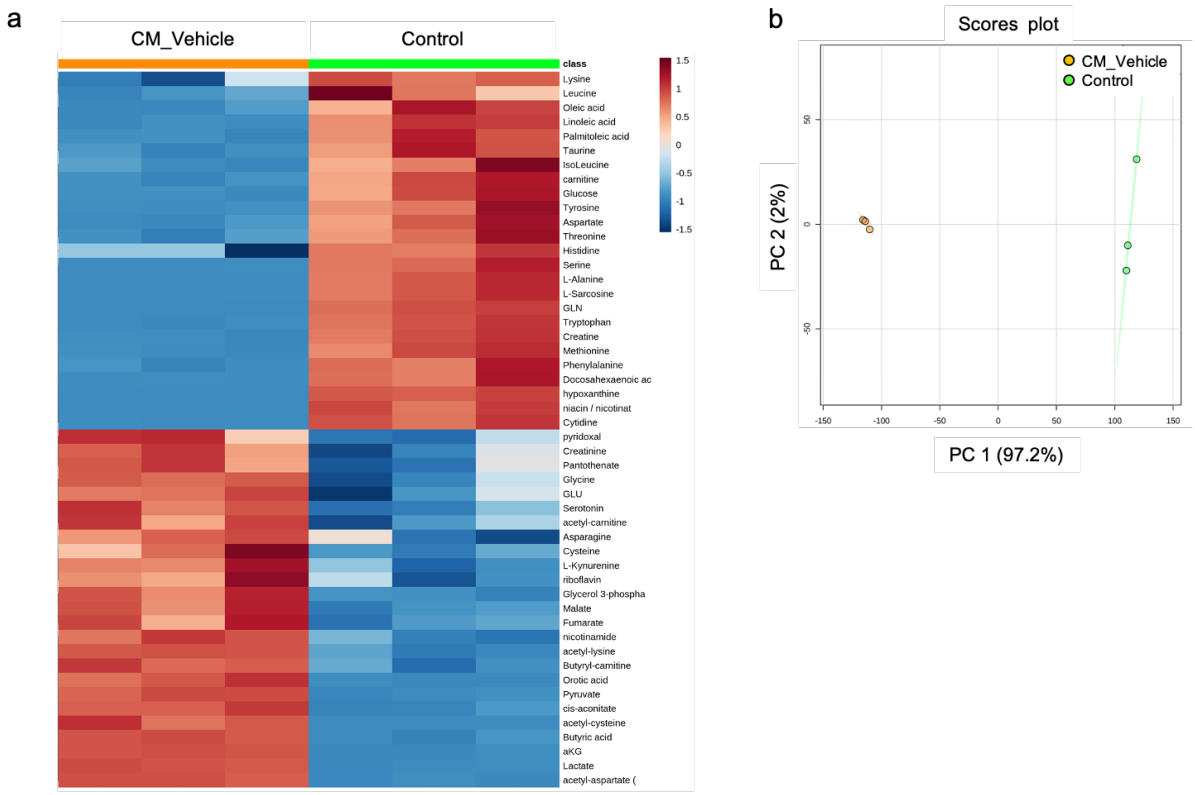

Figure S8 Metabolite analyses of DMSO vehicle treated conditioned media of LoVo

(**a**) Metabolomics profile of DMSO vehicle treated conditioned media (CM_Vehicle, orange) of LoVo compared to control media without cells (Control, green), presented as a heatmap visualization and hierarchical clustering analysis. Rows are metabolites and columns are samples (n=3). The color key indicates the metabolite expression value (blue, lowest; red, highest). (**b**) Principal component analysis (PCA) plotting showing clusters of samples based on their similarity. Statistical significance was calculated using a one-way ANOVA followed by Student's t-test ($p<0.05$).

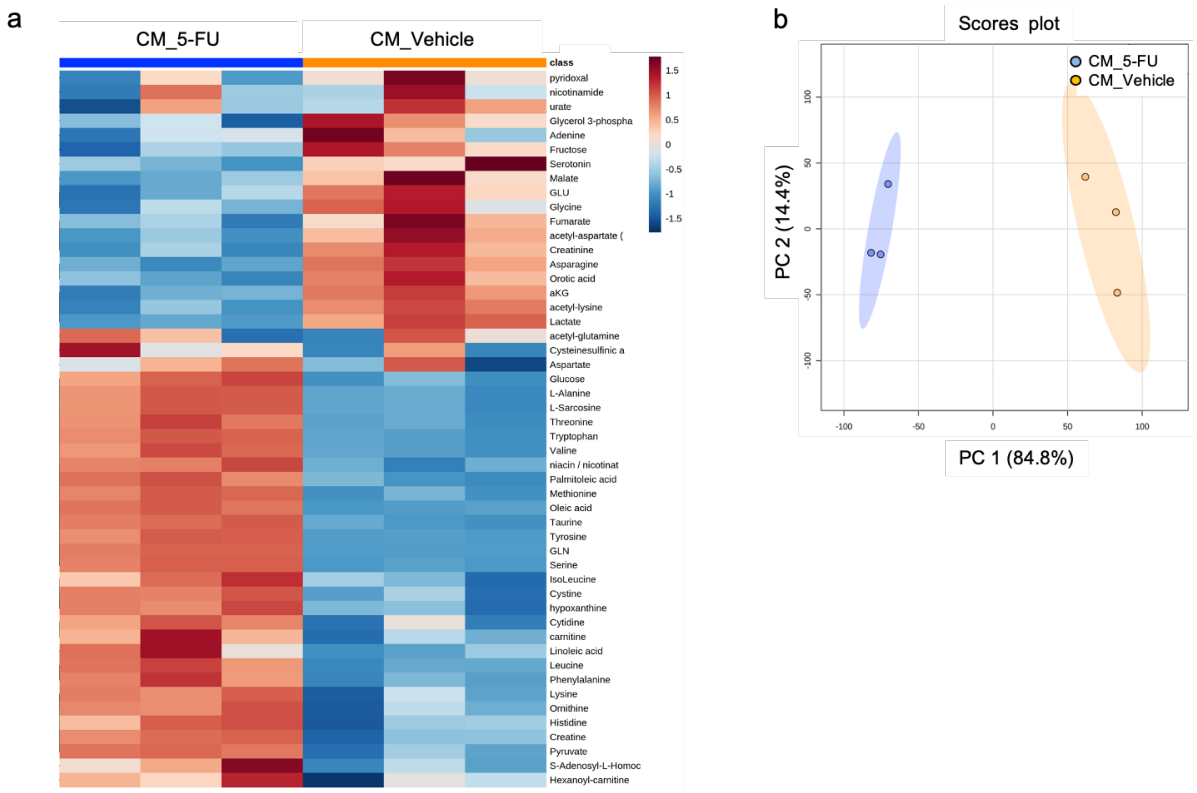

Figure S9 Metabolite analyses of 5-FU treated conditioned media of HCT116

(**a**) Metabolomics profile of 5-FU treated conditioned media (CM_5-FU, blue) of HCT116 compared to DMSO vehicle treated conditioned media (CM_Vehicle, orange), presented as a heatmap visualization and hierarchical clustering analysis. Rows are metabolites and columns are samples (n=3). The color key indicates the metabolite expression value (blue, lowest; red, highest). (**b**) Principal component analysis (PCA) plotting showing clusters of samples based on their similarity. Statistical significance was calculated using a one-way ANOVA followed by Student's t-test ($p<0.05$).

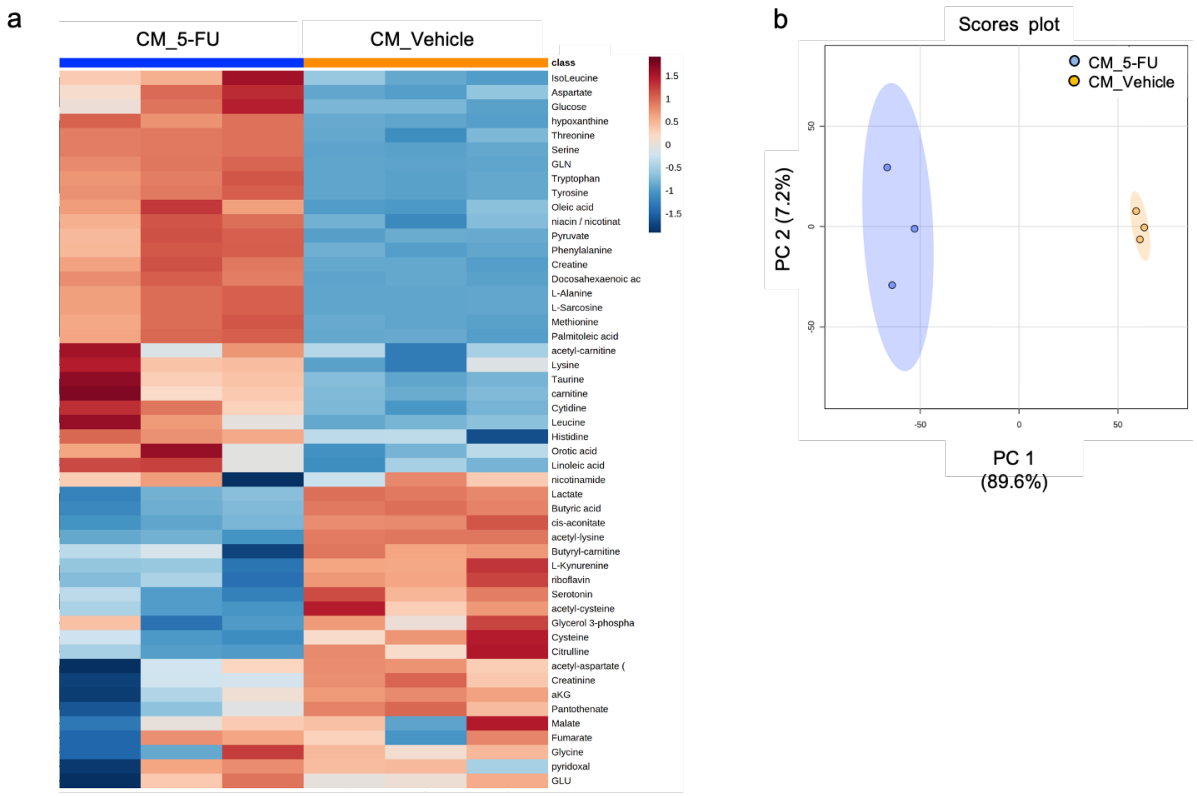

Figure S10 Metabolite analyses of 5-FU treated conditioned media of LoVo

(**a**) Metabolomics profile of 5-FU treated conditioned media (CM_5-FU, blue) of LoVo compared to DMSO vehicle treated conditioned media (CM_Vehicle, orange), presented as a heatmap visualization and hierarchical clustering analysis. Rows are metabolites and columns are samples from 3 independent experiments (n=3). The color key indicates the metabolite expression value (blue, lowest; red, highest). (**b**) Principal component analysis (PCA) plotting showing clusters of samples based on their similarity. Statistical significance was calculated using a one-way ANOVA followed by Student's t-test ($p<0.05$).

ii. Discussion

Tumor spheroid models of CMS cells

The CMS classification currently represent the best description of CRC heterogeneity at the gene-expression level. In previous studies, the CRC cell lines HCT116 and LoVo have been categorized as CMS1 cells, while SW620 and MDST8 have been classified as CMS4 cells (98). We have attempted to mimic the intratumor heterogeneity of CRC by co-culturing cell lines belonging to different CMS. The CRC cell lines have been co-cultured as MCTSs which closely resemble the 3D architecture of *in vivo* tumors (Figure 2.2). Depending on the compactness of the spheroid the MCTSs can be classified into three types: compact spheroids, tight aggregates, and loose cell aggregates (99). Here we saw that the MCTSs started to form after one day of cell culture in the u-shaped wells. MCTS models of LoVo and MDST8 formed loose cell aggregates while HCT116 formed compact spheroid structures (Figure 2.1). The compactness of the spheroid can be dependent on the initial aggregation of cells which is initiated by weak integrin-ECM linkages, and then they come into close proximity as a result of interactions between N- and E-cadherin (94). The compactness of the spheroid might have an effect of the drug response, as loose spheroids have more surface per square area compared to compact spheroids and therefor the compact spheroids will therefore have less drug penetration and thereby a different drug response.

Following that, we observed similarities between monocultured spheroids compared to co-cultured MCTS models were the cell growth, size and shape where similar in the two conditions. Next, we were interested the effects of 5-FU treatment on the spheroid models. In previous studies Karlsson *et al.* cultured HCT116 spheroids and monitored the drug dose response towards standard colon cancer drugs such as 5-FU, oxaliplatin and irinotecan, melphalan, topoisomerase inhibitors, acriflavine, and VLX50 (100). The spheroids were incubated with drug concentrations for 72 hours whereby it was revealed that spheroids cultured for three days were more resistant to four standard drugs compared to monolayered cells. Furthermore, spheroids at day six were almost completely resistant to these drugs. The fact that the cells cultured in 3D systems were more resistant

to these drugs could be linked to genetic and/or phenotypic changes caused by spheroid formation. In this study we observe similar effects where the spheroid shows more drug tolerance compared to 2D cell culture (Figure S1). The increased drug tolerance observed in the spheroids could be linked to the compactness of the cell structure. In spheroids the administered drugs have less surface area thereby effecting the drug penetration, as seen in the loose spheroids compared to the compact spheroids.

Next, we sought to analyze the effect the 5-FU treatment on the CMS cells within the MCTS models using confocal imaging. By using confocal imaging precise determination of the cell distribution withing the spheroids can be monitored. From this analysis, an increased cell survival during drug treatment was observed in the CMS4 cells when they were co-cultured together with the CMS1 (Figure 2.3). We can thus conclude that an increased drug resistance had been mediated from the CMS1 to the CMS4 cells.

Drug resistance effect of conditioned media

To further investigate this, we have cultured the cells indirectly to see if these effects are mediated by direct cell-to-cell contact or through cell secreted molecules. This has been done by applying CM from CMS1 to CMS4 cells whereby an increased cell survival was observed in the CMS4 cells when treated with 5-FU. This data agree with the previous results from the MCTS models were outgrowth of CMS4 cells was observed in the co-culture (CMS1-CMS4) during 5-FU treatment. The results from the CM experiments show that the CMS1 cell secretome have a huge impact in the overall tumor survival. Furthermore, the results lead us to believe that these mechanisms are in fact mediated through cell secreted molecules.

Drug induced cell migration

Next, we aimed to investigate the migratory capacity of cells during drug treatment. Through a multi-step procedure known as the metastatic cascade, tumor cells can migrate from the primary affected organ to a distant site. This process begins in the primary tumor with the release of soluble substances into the bloodstream (101). Certain signals released

by cells are thought to prepare the tissues at the new metastatic sites to support new tumor lesions. By culturing cell in transwells we aim to mimic this process. Using transwells makes it possible to study cell migration in co-culture systems during drug treatment. By culturing the cells in chambers which are separated by a membrane the cell can secret cell signalling molecules in response to each other or the drug treatment. After the drug treatment the relative number of cells that migrate from the upper chamber (primary site) to the lower chamber (secondary site) can be determined. It was observed that the CMS4 cells had an increased migratory tendency when exposed to the CMS1 secretome. This effect was most prominent during 5-FU exposure, indicating that the chemotherapy induces cell secreted molecules from the CMS1 cells which influence the migration of CMS4 cells (Figure 2.4).

Metabolic analysis

To get deeper understandings of these mechanisms, the potential key mediators that can be involved in these processes have been analyzed. The metabolites from CMS1 cell secretome was analyzed by chromatography–tandem mass spectrometry (LC-MS/MS). The analysis focused on detecting cell secreted metabolites whereby 91 metabolites were detected, including amino acids, organic acids, nucleotides and cofactors (Table S2). All of which are involved in a wide range of metabolic pathways. When compared to the control media without cells, 52 metabolites were significantly altered in the HCT116 CM_DMSO (Supplementary Figure S7) (Table 1.1).

To determine if the metabolites were involved in any potential pathways, pathway analysis has been performed. The results obtained from the analysis showed that the levels of 13 metabolites involved in aminoacyl-tRNA biosynthesis (amino acids) were consumed by HCT116 cells. Notably, among the down-regulated metabolites, phenylalanine, tyrosine, and tryptophan production as well as linoleic acid metabolism displayed the highest pathway effect of 1.0 (Table 2, Supplementary Table S5). The highest pathway relevance was found in up-regulated metabolites in the HCT116 secretome, which primarily involved alanine, aspartate, and glutamate metabolism. These include n-acetylaspartate, asparagine,

glutamine, fumarate, pyruvate and alpha-ketoglutarate, representing the highest pathway significance.

Overall, there was a significant overlap between the metabolite profiles of HCT116 CM_DMSO and LoVo CM_DMSO. When the LoVo CM was compared to the control media without cells, 52 metabolite levels in the CM_DMSO of LoVo cells were substantially altered (Supplementary Figure S8) (Table 2.2). As observed in the HCT116 CM, the aminoacyl-tRNA biosynthesis represents the highest pathway significance. Once more, the largest pathway impact was demonstrated by the production of phenylalanine, tyrosine, and tryptophan as well as the metabolism of linoleic acid. In contrast to HCT116 cells, elevated metabolites were primarily connected to the tricarboxylic acid cycle (TCA cycle), which was the most significant pathway (Supplementary Table S6). The highest pathway impact values were for the metabolism of riboflavin, D-glutamine and D-glutamate, and vitamin B6 with values of 0.50, 0.50, and 0.49, respectively.

To continue our investigation, we wanted to see if there were any direct effects of the metabolites on the cells. This was done by collecting CM_DMSO and CM_5-FU from CMS1 cells and extracting the metabolites via dialysis. By culturing the cells together with the metabolites, it was observed that the HCT116 CM_5-FU metabolites significantly increased the viability of the CMS4 cells when treated with 5-FU at doses ranging from 5 to 300 μM (Figure 2.5). Similar results were seen when cells were treated with the LoVo metabolites (Figure 2.5). These findings confirm that metabolites are important messengers in the CMS1 secretome increasing the CMS4 cells resistance capacity to 5-FU.

i. Chapter conclusion and perspective

It is well established that intra-tumor heterogeneity plays a significant role in drug resistance mechanisms in various cancers, where the cell heterogeneity contributes to the tumors drug resistance. Here we have mimicked the intra-tumor heterogeneity of CRC through the co-culture of different CMS cells. It was observed that CMS co-culture systems

had an increased drug tolerance compared to cells cultured as monoculture control. This demonstrated that the interplay between CMS1 and CMS4 have a large impact on the drug resistance of the cells. To further investigate these mechanisms CM from CMS1 cells applied to CMS4 whereby it was shown that the cell secretome of CMS1 cells increased CMS4 tolerance to 5-FU chemotherapy. Further experiments demonstrated that the CMS1 secretome increased the migratory tendency of CMS4 cells during chemotherapy drug treatment. This led to the investigation of the CMS1 cell secretome where key metabolites were analysed to detect specific pathways that were involved in these mechanisms. In this study, we show that the cell secretome have an impact on cell proliferation and spheroid progression.

Here, we studied how intra-tumor heterogeneity affected CRC; however, to further understand the impact of the entire Tumor Micro-Environment (TME) future research should examine the overall effect of the TME on tumor progression and drug resistance. This can be done by co-culturing CMS cell with immune cells or endothelial cells to then gain a better understanding of the overall TMEs effect. Future research could also focus on performing deeper analysis of the CMS1 cell secretome, to more precisely determine key pathways and metabolites which are responsible for the increased drug resistance observed in the CMS4 cells.

Chapter 3

The role of cell-cell cross talk in drug resistance

i. Introduction

The development of drug resistant cells brought on by therapeutic pressure is one of the largest issues in the treatment of CRC. After long term exposure, most treatment plans will result in drug resistance development (102). The cause of this resistance has been suggested to be due to both intrinsic and extrinsic biological causes. Some of the biological factors include the clonal evolution of tumors (103), the development of CSC (42), altered expression of drug efflux pumps (104), modulation of ion channels (105) or altered drug metabolism (106). Over the past decades, several molecular resistance mechanisms have been unravelled, but there are still many questions that are unknown regarding resistance mechanisms and the potential changes that result in drug resistant cells are underexplored.

In our previous observations we have mimicked the intra-tumor heterogeneity of CRC by co-culturing different CMS cells as MCTS. We observed that co-culture systems affected the tumor progression via cell secreted molecules. It is known that tumors are often composed of both drug resistant and sensitive cells (24). Furthermore, it has also previously been shown that Drug Resistant Cancer Cells (DRCC) can alter the behaviour of Drug Sensitive Cancer Cells (DSCC) through cell secreted molecules eventually leading to an increased drug resistance. A less studied drug resistance path involves DSCCs altering the behaviour of DRCCs leading to tumor progression, observed in melanoma (107). These findings now raise the question if similar effects could be detected in in other cancers. Here, we aim to look closer at resistance mechanisms, we present our investigation of DSCC-DRCCs crosstalk in CRC and its underlying chemotherapy resistance mechanisms.

Recently, another method of resistance development has been suggested where the resistance appears through cellular communications withing the tumor. This can happen through cell signalling mechanisms such as proteins, RNA, DNA or Extracellular Vesicles (EV). Crosstalk between cells occurs through cell secreted molecules that can travel far

distances within the body. Tumor cells interact with each other through multiple different cell-signalling mechanisms. Several studies have shown that EVs are the key mediators involved in cell-to-cell crosstalk that lead to tumor progression (108) (90), metastasis (109) and an changing the TME structure (110) (111) (61). But their role in communication between DSSSs and DRCCs has not yet been explored. Therefore, we were interested in analyzing the effects of EVs in DSCCs and DRCCs.

The role of EVs in cell communication

Given the variety of cellular processes that take place, it can be challenging to determine through which processes certain cell-to-cell interactions occur. It has been demonstrated that tumors cells secret a greater number of EVs compared to normal cells (112). Furthermore, the tumors may contribute the heterogeneity of EVs that are secreted, and the proportion of tumor-derived vesicles will increase as the disease progresses. Therefore, to investigate the cell-to-cell crosstalk involved in cancer progression EVs can be a good path to begin this investigation (113).

EVs are available in a wide variety of sizes and shapes (see Chapter 1 Introduction). Additionally, while EV composition and characteristics are similar to those of other biological material, fluorescent markers may not be an effective way to label EVs (114). Therefore, it can be difficult to distinguish the EVs from other biological material. To detect if EVs are present in the sample it is therefore necessary to perform multiple characterization techniques to ensure their presence as well as detecting the total number of EVs. Therefore, we sought out to determine if EVs could be detected in the samples using nanoparticle tracking analysis (NTA) and transmission electron microscopy (TEM) and flow cytometry. These methods work in complementary to each other to determine the chape, size and number of EVs.

ii. Motive

Drug resistance development is a leading cause of treatment failure. There are many different mechanisms that can cause drug resistance, including clonal variations where certain cell types have different sensitivity to chemotherapy drugs. The initial drug

treatment might only be efficient on a portion of the tumor cells and the more resistant cells could clonally expand and survive the treatment. There is currently a lack of knowledge regarding what governs these processes, as well as how subpopulations of cells interact with each other. Therefore, in this part, we are interested in investigating how cells develop drug resistance. Furthermore, we have previously observed cell-to-cell crosstalk in cells with varying CMS classification (see Chapter 2). We observed that tumor models of co-culture cells had increased drug resistance compared to the monocultured cells. To continue our investigation on the impact of intra-tumor heterogeneity on CRC we aim to study the effects of cell co-culture systems consisting of DSCCs and DRCCs. To start this investigation, we want to identify CRC cell lines which are DSCCs. Thereafter we aim to develop DRCCs from the original DSCC population. After creating the DRCCs we want to investigate key mechanism and pathways that converts the cells from a drug sensitive state to a drug resistant state. We further aim to co-culture the DSCCs and the DRCCs to investigate potential cell-to-cell interactions under drug treatment. Lastly, we aim to investigate what mechanisms are involved in cell-to-cell crosstalk between DSCCs and DRCCs.

iii. Methods

Cell culture

HCT116 (ATCC®CCL-247) cells were purchased from ATCC (American Type Culture Collection, USA). HCT116 cells were cultured in McCoy's 5A Medium (Gibco, France) according to ATCC guidelines. The medium was supplemented with 10% Fetal Bovine Serum (FBS) (Gibco, France) and 5% Penicillin-Streptomycin (Gibco, France). Cells were maintained in T-75 cm^2 culture flasks (Corning, France) and the cell culture medium was replaced every three days. Once the confluency had reached 90 percent, the cells were passed into new culture flasks. All cells were maintained in a humidified incubator at 37 °C and 5% CO^2.

To prepare a cell solution the reagents PBS, cell culture media, and trypsin-EDTA (0.05%) were placed in the water bath for 15 minutes in a 37°C water bath. The medium was removed from the cell culture flasks and the cells were washed with PBS. 3 mL trypsin

was added to a T-75 culture flask and placed in the incubator for 3 minutes. Once the cells had detached from the culture flask 7 mL of medium was added before transferring the solution to a falcon tube. Cells were centrifuged for 5 minutes at 300 rcf. The supernatant was removed, and pelted cells were resuspended in 1 mL media. The cells were stained with trypan blue and the total number of cells were counted using the Countess machine (ThermoFisher Scientific, USA). The desired number of cells were added to new T-75 culture flasks.

IC50 determination

Cells were seeded into 96-well plates and incubated overnight, after 24 hours cells were treated with 5-FU (Sigma Aldrich, USA) at increasing concentrations ranging from 0, 5,0, 10, 50, 150, 300 and 500 μM. After three days the cell viability was determined using MTS assay (CellTiter 96® AQ_{ueous} One Solution Reagent Promega). The MTS assay was performed by washing the cells with culture media, to remove any drug residue. Thereafter 100 μL of cell medium together with 20 μL MTS working solution was added to each well. After incubating the cells for 4 hours, the absorbance was measured at 490 nm using a plate reader (Tecan, France). Dose response curves and IC50 values were calculated by using Graph Pad Prism software (USA). Statistical significance was determined by student's T-test.

RNA extraction

The samples were prepared by seeding 0.4 million HCT116 and HCT116-R cells in 24 well plates (see protocol for cell culture). The cells were cultured for 72 hours in standard culture conditions. Thereafter, the RNA extraction was prepared by following manufacturer's RNeasy kit from Qiagen protocol, briefly, cells were lysed by adding 700 μL Buffer RLT (1 % v/v) and 10 μL β-mercaptoethanol (Sigma Aldrich, France). Cell scrapers were used to scrape the bottom of the well plate to make sure all cells were lysed. Thereafter, 700 μL of 70% ethanol was added to the lysate. 700 μL of the sample was transferred to RNeasy Mini spin columns and placed in 2 mL collection tubes. The samples were centrifuged for 15 seconds at 8000 g and the flow-through was discarded. 350 μL

Buffer RW1 was added to RNeasy columns and centrifuged for 15 seconds at 10,000 rpm and the flow-through was discarded. 10 µL DNase I stock solution was added to 70 µL Buffer RDD. 80 µL DNase I incubation mix was added directly to the RNeasy column membrane and incubated at room temperature for 15 minutes. 350 µL BufferRW1 was added to the RNeasy column and centrifuged for 15 seconds 8000 g, flow-through was discarded. 500 µL Buffer RPE was added to the RNeasy spin column and centrifuged for 15 seconds 8000 g, flow-through was discarded. 500 µL Buffer RPE was added to the RNeasy spin column and centrifuge for 2 minutes at 8000g. The RNeasy spin column was placed in new 2 mL collection tubes. Whereafter the tubes were centrifuged at full speed for 1 minute to dry the spin column membrane. The RNeasy spin column was placed in new 1.5 mL collection tubes. 30 µL RNase-free water was added directly to the spin column membrane and centrifuged for 1 minute at 8000 g to elute the RNA.

Library preparation

The library preparation was performed by following the manufacturer's recommendations, (QuantSeq 3' mRNA-Seq Library Prep Kit FWD for Illumina from LEXOGEN). Briefly, the RNA samples were thawed on ice and centrifuged to make sure all RNA was suspended. The 3' ligation reagent mixture was prepared on ice by adding: 1 µL QIAseq miRNA 3' Adapter, 1 µL QIAseq miRNA RI, 1 µL QIAseq miRNA 3' Ligase, 2 µL QIAseq miRNA 3' Buffer, 10 µL Ligation Activator, and 2 µL Nuclease-free Water. Template RNA was added to each tube which already contained the 3' ligation Master Mix. Tubes were centrifuged and mixed by pipetting up and down approximately 20 times. Samples were incubated for one hour at 28°C thereafter 20 minutes at 65°C, followed by a 4°C incubation for 5 minutes. The 5' Ligation reaction was prepared on ice by mixing: 20 µL 3' ligation reaction, 15 µL Nuclease-free water, 1 µL QIAseq miRNA 5' Adapter, 1 µL QIAseq miRNA 5' Ligase, 2 µL QIAseq miRNA 5' Buffer and 1 µL QIAseq miRNA RI. Samples were incubated as follows: 1 hour at 28°C, followed by 20 minutes at 65°C, lastly, at 4°C for 5 minutes. Thereafter, 2 µL QIAseq miRNA RT initiator was added to each tube. The thermal cycler was programmed to 75°C 2 minutes, 70°C 2 minutes, 65°C 2 minutes, 60°C 2 minutes, 55°C 5 minutes, 37°C 5 minutes 25°C and kept at 4°C. The reverse 5' ligation reaction was

prepared by mixing: 42 µL 5' ligation reaction together with QIAseq miRNA RT Initiator, 2 µL QIAseq miRNA RT Primer, 2 µL Nuclease-free Water, 12 µL QIAseq miRNA RT Buffer, 1 µL QIAseq miRNA RI and 1 µL QIAseq miRNA RT Enzyme. Samples were incubated as follows: 1 hour at 50°C thereafter 15 minutes at 70°C followed by a 4°C incubation for 5 minutes. Thereafter the library amplification was prepared using QIAseq miRNA 96 Index. The library amplification reaction was prepared on ice by adding: 15 µL QIAseq miRNA Library Buffer, 8 µL HotStarTaq DNA Polymerase, 1.5 µL QIAseq miRNA 96 Indexes IL Auto (from plate), 14.5 µL Nuclease-free Water. The thermal cycler was programmed to 15 minutes at 95°C, 15 seconds 60°C, 30 seconds 72°C, 15 seconds, 2 minutes 72°C and kept at 4°C. 40 µL of the library amplification reactions was centrifuged. 37.5 µL of QMN Beads was added to the plates containing the cDNA reactions and vortexed for three seconds. Samples were then incubated for five minutes at room temperature and the plates were placed on a magnet stand until the beads had migrated. Supernatant was kept and transferred to new plates. Plates containing the beads were discarded. 65 µL of QMN Beads was added to the supernatant and vortexed for three seconds followed by a five-minute incubation at room temperature. Plates were placed on a magnet stand until the beads have fully migrated. Supernatant was discarded and beads kept whereafter 200 µL of 80% ethanol was added. The washing step was repeated by adding 200 µL of 80% ethanol (Sigma Aldrich, USA). Samples with beads still placed on the magnetic stand were air-dried at room temperature for ten minutes. The DNA was eluted by adding 17 µL of nuclease free water to the plates and the plates were removed from the magnetic stand. Samples were carefully pipetted up and down until all beads were thoroughly resuspended, lastly the sample was incubated at room temperature for two minutes.

Transcriptomic analysis

The Quality of raw data was evaluated using FastQC. Poor quality sequences and adapters were trimmed or removed with fastp, to retain only good quality paired reads. Illumina DRAGEN bio-IT Platform (v3.8.4) was used for mapping on hg38 reference genome and quantification with Gencode v37 annotation gtf file. Library orientation, library composition and coverage along transcripts were checked with Picard tools. Following

analysis were conducted with R software. Data were normalized with DESeq2 (v1.30) bioconductor package, prior to differential analysis with DESeq2 workflow. Multiple hypothesis adjusted p-values were calculated with the Benjamini-Hochberg procedure to control FDR. Finally, enrichment analysis was conducted with clusterProfiler R package (v3.18.0) with Gene Set Enrichment Analysis, on Hallmark pathways, Gene Ontology database, KEGG pathways from MSigDB collections.

MCTS formation and confocal imaging

The cells were stained using the cell tracker by removing the cell medium and washing with PBS (2 mL). 1 µL of CMFDA green cell tracker dye (1 µM) fluorescent probes (Life Technologies, USA) were added to the HCT116 cells, while the orange cell tracker dye CMRA (1 µM) fluorescent probes (Life Technologies, USA) was added to the HCT116-R cells and incubated for 30 minutes. The cell culture medium was removed from the stained cells and washed with PBS (2 mL). Cell solutions were mixed at 90 % CHT116 and 10 % CHT116-R cells. Controls were made where monoculture of each cell line was cultured under the same culture conditions. 1500 cells per well was added in the ultra-low attachment u shaped wells (Corning, France). After 24 hours, when the cells had sedimented, the cell treatment was carried out by adding 5-FU drug concentration raining from 1 µM to 50 µM for 72 hours.

At the end point the relative number of each cell line was determined by analyzing the number of cells stained with green cell tracker compared to the number of cells stained with orange cell tracker. To determine this, whole MCTSs were imaged using confocal laser scanning microscope (Zeiss LSM710). The images were transferred to Fiji (ImageJ) where Fluorescence intensity was analyzed by merging the z-stacks to obtain one image per condition. The z-stack image was used to detect the relative amount of each cell line. The mean fluorescent intensity of each spheroid was obtained and normalized to the DMSO control.

Conditioned Medium

CM was prepared by seeding 0.5 and 1 HCT116 million cells in T-75 flasks for treatment with DMSO and 5-FU, respectively (see cell culture protocol for how to prepare the cell solution). After 24 hours the cells were treated with the corresponding treatment, DMSO and 2.5 µM 5-FU. After 72 hours of treatment, the medium was collected and centrifuged for five minutes at 350 rcf, whereby the pellet was discarded. Lastly, the medium was filtered through a 0.2-micron syringe filter (Sartorius, France) and aliquots were made and flash frozen using liquid nitrogen, samples were stored at -80°C (Figure 3.1).

Conditioned Medium (CM) treatment

Cell solutions of HCT116 and HCT116-R were prepared and 1500, each respective cell line was seeded into 96-well plates and incubated in a humidified incubator at 37 °C and 5% CO^2 (see cell culture protocol for how to prepare the cell solutions). After 24 hours of cell culture, the cell culture medium was removed by aspiration and 100 µL of each drug concentration was added to the wells together with 100 µL of each corresponding medium, including cell culture media, CM_DMSO and CM_5-FU, respectively. Cells were incubated for 72 hours for the treatment to occur. The alamarBlue™ (ThermoFisher Scientific, France) assay was performed as followed to assess cell viability. The medium was removed, and cells were washed with cell culture medium. 80 µL of cell culture medium was added to each well together with 20 µL alamarBlue™ solution. The plate was incubated for 4 hours, and the absorbance was read at 570 nm (600 nm as a reference) using a plate reader (Tecan, France). Data analysis was performed using Prism 9 (USA). Statistical significance was calculated using a two-tailed Student's t-test. A p-value of less than 0.05 and 0.01 was considered significant (*) and highly significant (**), respectively.

Isolation of Extracellular Vesicles (EVs) by ultracentrifugation

The CM was centrifuge for five minutes at 350 x g. The pellet was discarded, and the supernatant was kept and filtered using 40 µm syringe filters. Several centrifugation steps followed, 20 minutes at 2,000 × g at 4°C. The supernatant was kept and transferred to polyallomer tubes. 32 minutes at 10,000 × g at 4°C, supernatant was transferred to ultracentrifugation tubes. 70 minutes at 100,000 × g at 4°C, the supernatant was removed,

and the pellet was resuspended in 700 µL PBS. 10 mL PBS was added and centrifuged one hour at 100,000 × g at 4°C. Supernatant was removed and 50 µL of PBS was added to resuspend the pelleted EVs.

Nanoparticle Tracking Analysis (NTA) method

EV sizes and concentrations were determined according to the manufacturer's instructions (Particle Metrix). The instrument (ZetaView QUATT, Particle Metrix, Germany) was equipped with a 488 nm laser. The calibration beads and biological samples were diluted in PBS to a final volume of 1 mL, to obtain an optimal particle concentration range for the measurement. Calibration was done for light scattering and fluorescent measurements. Capture settings were set at: sensitivity 65, shutter 100, minimum trace length 10. Scatter was recorded and measured at sensitivity 80, shutter 100, and minimum trace length 15. Triplicates were measured for each sample. A washing step was done between each measurement using distillated water. Capture was done at medium video setting, corresponding to 30 frames per position. ZetaView software 8.5.10 was used to analyze the recorded videos. For each sample, 11 different locations were recorded during which temperature was kept at 25°C. Immediately prior to the measurement EV aggregates were broken up by pushing the sample through a 29G needle gently.

Imaging Extracellular Vesicles (EVs) using TEM

The EV solution was resuspended in 50 µL of 2% PFA (Sigma Aldrich, USA) by pipetting. The extracellular vesicles were fixed on electron-microscope grids by depositing 5 µL of the resuspended pellets on Formvar-carbon coated EM grids (Biovalley, France). Three replicates were prepared for each EV sample. The membranes were covered and incubated for 20 minutes in room temperature. 100 µL drops of PBS (Biovalley, France) were placed on sheets of Parafilm. The grids with the membrane side down were transferred to drops of PBS using clean forceps to wash. The grids were moved to 50 µL droplets containing 1% glutaraldehyde (Biovalley, France) and incubated at room temperature for five minutes. The membranes were transferred to 100 µL drops of distilled water and incubated for two minutes. This step was repeated seven times for a total of eight water

washes. The grids were transferred to 50 µL drops of methyl cellulose-UA (Biovalley, France) and incubated on ice for 10 minutes. The grids were transferred with stainless steel loops and excess fluid was blotted off by gently pushing the loop sideways on whatman filter paper (Sigma Aldrich, USA), so that a thin film was left behind over the EV side of the grids. The gris were left to air dry for 10 minutes while still on the stainless-steel loop. The prepared specimen was observed under the Transmission Electron Microscope (Tecnai 12) at 80 kV equipped with a CCD camera (Gatan MSC794).

Detecting Extracellular Vesicles (EVs) using flow cytometry

The magnetic beads were vortexed for 30 seconds and 20 µL of bead solution was transferred to an eppendorf tube. The beads were washed by adding 200 µL of PBS to the tube and placing it next to a magnet for one minute and discarding the supernatant. The tube was removed from the magnet and the EV-sample was titrated with an Isolation Buffer to a final volume of 100 µL to the magnetic beads. 50 µL of the pre-enriched EV solution, EV_DMSO and EV_5-FU, was added to 50 µL of Isolation Buffer. The sample was incubated overnight at 4°C on a sample mixer. After the overnight incubation the tubes were centrifuge for 5 seconds to collect the sample at the bottom of each tube. 300 µL of Isolation Buffer was added to the bead-bound EVs to wash them, the sample was mixed gently by pipetting. The tube was placed on the magnet for 1 minute and the supernatant was discarded. The tube was removed from the magnet and 400 µL of Isolation Buffer was added, the sample was mixed gently by pipetting. The tube was placed on the magnet for one minute and the supernatant discarded. The bead-bound EVs were resuspend in 300 µL Isolation Buffer. 300 µL of the resuspended EVs was added to 1 µL of the CD81 antibodies. The sample was incubated for 45 minutes at room temperature protected from light on a sample shaker (~1000 rpm). 300 µL of Isolation Buffer was added to wash the bead-bound EVs the sample was mixed by pipetting. The tube was placed on the magnet for one minute and the supernatant was discarded. The washing step was repeated once, and the sample was resuspended in 300 µL of Isolation Buffer for detection using flow cytometry (BD FACSAria).

Cells treated with EVs

HCT116 cells were seeded at 1500 cells per well (see cell culture protocol) cells were cultured for 24 hours (Figure 3.1). The medium was removed from the cells by aspiration and 100 µL of each drug dilution was added to the empty wells. The cell treatment was carried out by diluting 5-FU solutions in a 1:1 mixture of cell culture media containing 3 µL of fresh media, EV_DMSO and EV_5-FU respectively. Cells were incubated for 72 hours at normal cell culture conditions. To determine the cell viability at the end point, the MTS

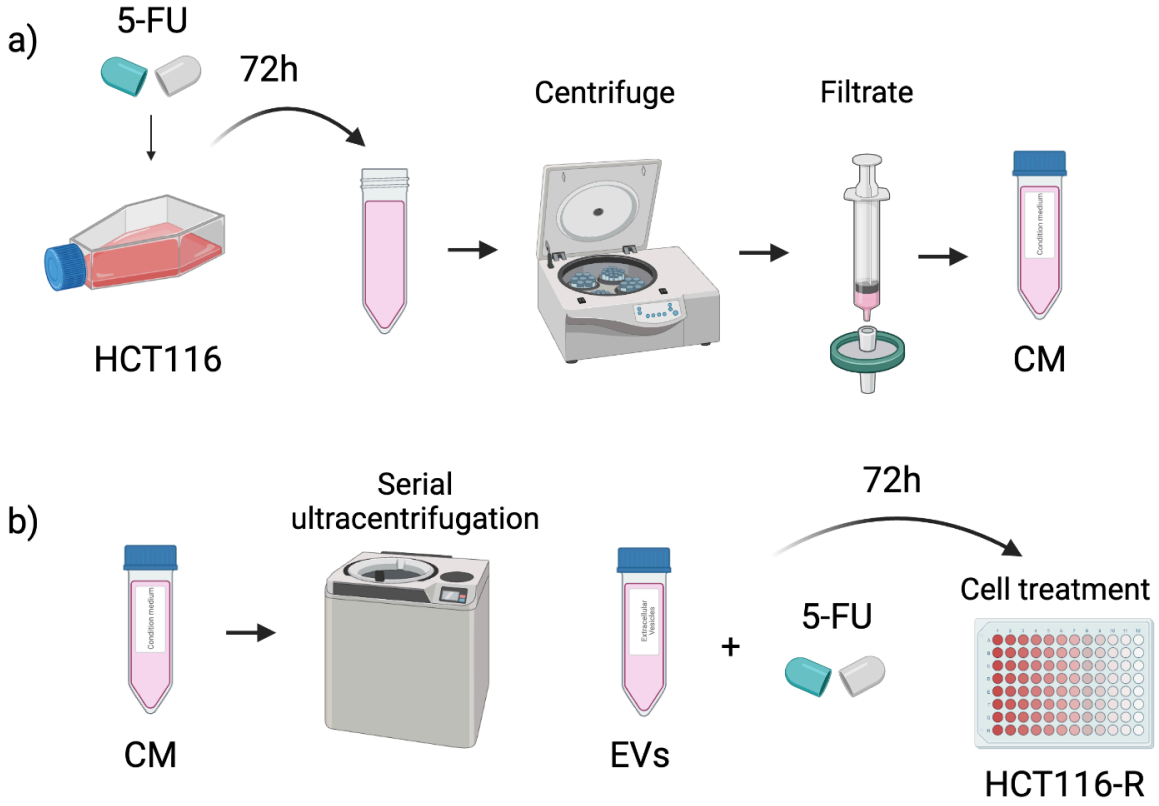

Figure 3.1. Illustration of the experimental protocol

Illustration of the experimental protocol for a) generation of CM by treating the HCT116 cells with 2.5 µM 5-FU or DMSO as a control for 72 hours. After the treatment the cell culture medium was collected and centrifuged whereafter the supernatant was collected. Lastly the CM were filtered. b) Treatment of cells with EVs extracted from CM. To extract the EVs the CM is subjected to a series of ultracentrifugation steps. After the EVs have been extracted they can be used to treat the cells at different drug dilutions.

assay was performed as described previously (see section IC50 determination).

iv. Results

To start our investigation of chemotherapy resistance mechanisms, Drug Sensitive Cancer Cells (DSCCs) and Drug Resistant Cancer Cells (DRCCs) lines have been identified. The drug sensitivity of different CRC cell lines was identified by comparing half-maximal Inhibitory Concentrations (IC50), meaning the concentration that kills 50% of the cells when treated with the drug (Figure 3.2). Cells were treated with increasing 5-fluorouracil (5-FU) and the cell lines that had an IC50 below 5 µM were classified as DSCCs and those with an IC50 above 5 µM above were classified as DRCCs. The IC50 values of HCT116: 3.7 µM ; LoVo: 19.5 µM ; Colo320: 5.1 µM ; MDST8: 7.5 µM ; NCI-H716: 150 µM and SW620: 117.2

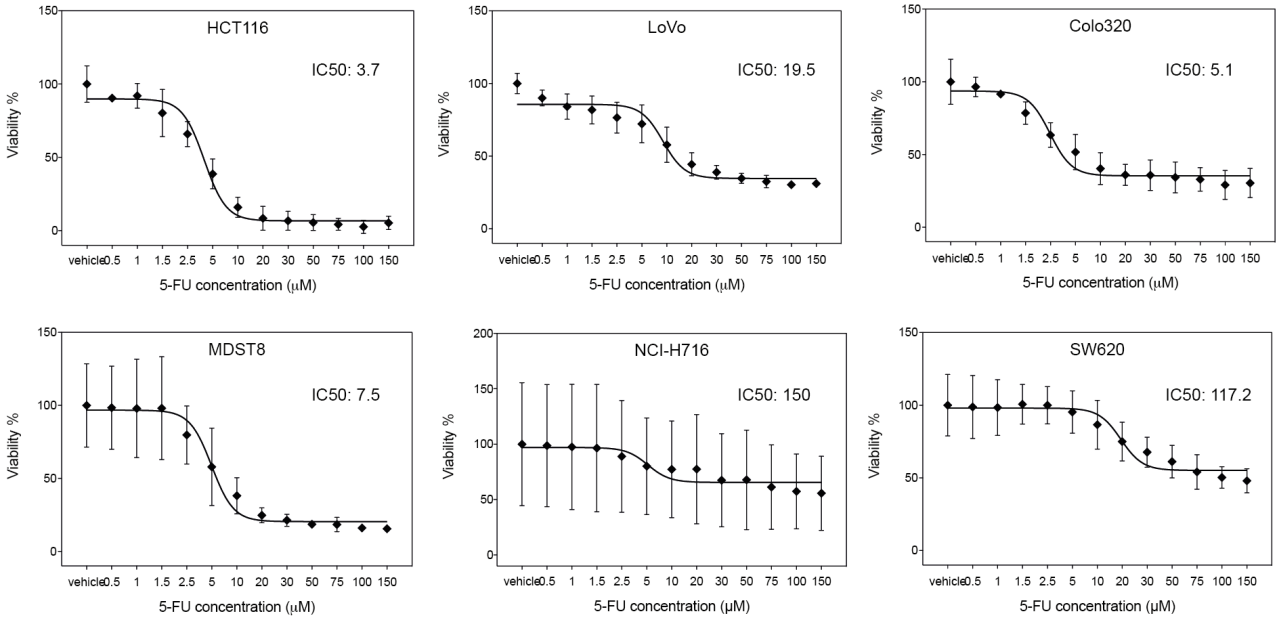

Figure 3.2. Dose response curves from different CRC lines

Dose response curves of CRC cell lines treated with different concentrations of 5-FU. Y-axis shows cell viability measured using alamar blue assay and x-axis shows 5-FU concentration in µM. The symbols represent the average, and the error bars represent the standard deviation (n=3). HCT116 IC50 = 3.7 µM, LoVo IC50 = 19.5 µM, Colo320 IC50 = 5.1 µM, MDST8 IC50 = 7.5 µM, NCI-H716 IC50 = 150 µM and SW620 IC50 = 117.2 µM.

μM. Only one cell line, HCT116, was classified as DSCCs towards 5-FU with a IC50 of 3.7 μM.

Development of HCT116-Resistant cells

To study the relationship between DSCCs and DRCCs the drug sensitive cell line HCT116 was treated with long term exposure of 5-FU during several months to develop a DRCCs cell line from the parental HCT116 cell line. After several rounds of chemotherapy exposure, drug resistance was analysed by making new dose-response curves and determining the IC50 value. The HCT116 cell line that had been exposed to long term 5-FU treatment (HCT116-R) showed an increase in the IC50 value when treated with 5-FU compared to that of the untreated HCT116 (Figure 3.3). IC50 value of HCT116 and HCT116-R were 3.9 and 6.2 μM, respectively.

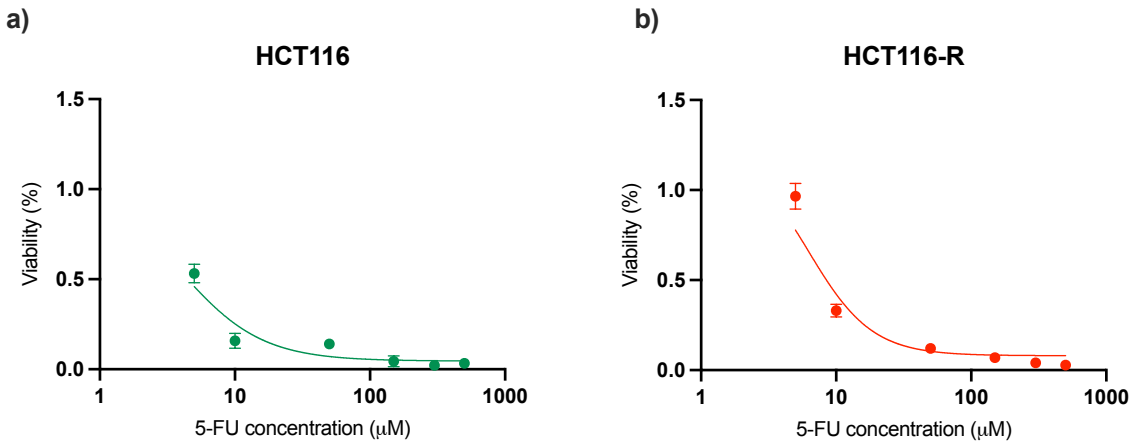

Figure 3.3. IC50 determination of HCT116 and HCT116-R cells

Dose-response curves of a) HCT116 cells b) HCT116-R cells treated with different 5-FU concentrations. X-axis showing increasing 5-FU concentrations at 0, 2.5, 5, 10, 50 and 150 μM. Y-axis showing cell viability measured using MTS assay and normalized to the control. IC50 values of HCT116 and HCT116-R were 0.74 and 4.9 μM, respectively. Error bars represent the standard error of mean. Dose-response curves and IC50 values were calculated by using Graph Pad Prism.

Transcriptomic analysis of HCT116 and HCT116-R cells

Transcriptomic analysis was performed to detect possible genetic changes that could occur after the emergence of resistance. The transcriptome refers to the complete set of mRNAs found in a cell. RNA sequencing was performed on HCT116 and HCT116-R samples to identify the differentially expressed genes. Each sample was composed of a large starting material of approximately 10^4 cells, thereby minimizing potential errors that can occurs in samples with a low genetic material. To compare the total transcriptome of the two groups principal component analysis (PCA) was plotted. The main purpose of Principal Component Analysis plots is to visualize the major source of variation in the data and to identify potential outliers. Here we observe that that the triplicate of HCT116 cell samples clusters together in the upper right corner. The HCT116-R samples have a larger difference in the gene expression between the samples (Figure 3.4). The third HCT116-R sample had a lower genetic starting material which may be the cause of its divergence from the other two samples.

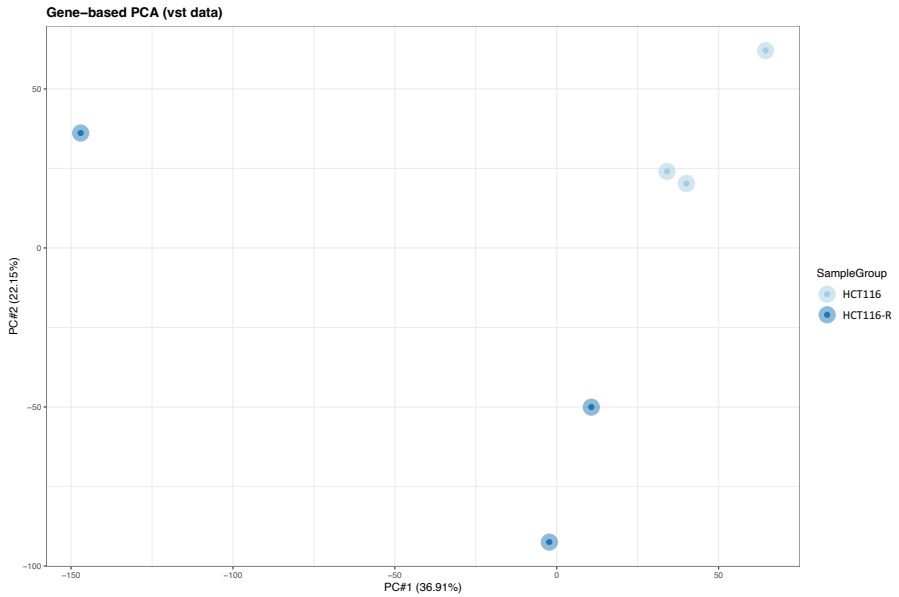

Figure 3.4. Principal Component Analysis (PCA) of the transcriptomic data from HCT116 and HCT116-R cells

Clustering of the transcriptomic data from the two cell lines HCT116 and HCT116-R by principal component analysis (PCA). The PCA compares the total transcriptome of the cells. The symbols represent the average of the two samples, HCT116 (light blue) HCT116-R (dark blue). The number of replicates were three (n=3).

The heatmap displays genes that have been differentially expressed between HCT116 and HCT116-R cells. Over expressed genes (red) and under expressed genes (blue) are shown. The HCT116 and HCT116-R samples have two significantly different gene expression profiles where the triplicate samples show similar gene expression (Figure 3.5). Significant difference can be observed between the two groups where HCT116-R has an upregulation of multiple genes. In total, 12 716 genes were sequenced where most genes, 12 591, showed no changes in their expression level. When comparing the expression level of HCT116-R compared to HCT116 cells 83 genes were upregulated and 42 were downregulated. The heatmap shows the genes with the largest difference in their expression level with the log2 fold-change threshold set at 2. All samples were made in triplicates.

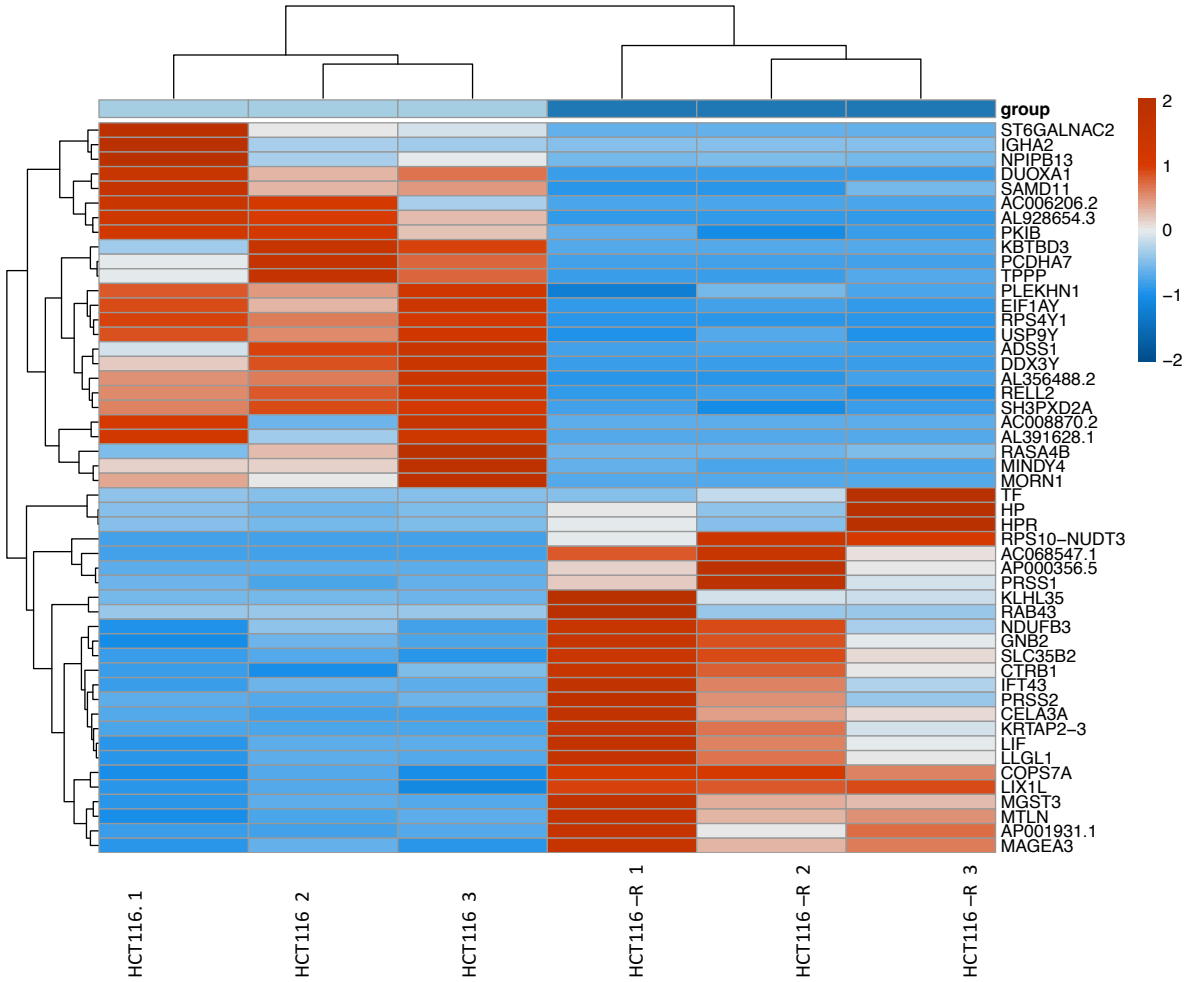

Figure 3.5. Gene expression profiles of HCT116 cells and HCT116-R cells

Heatmap of the gene expression profiles in HCT116 and HCT116-R cells showing differentially expressed genes in HCT116-R compared to HCT116. The genes in the heatmap are ranked by its expression values with the log2 fold-change threshold set at 2. Red displaying upregulated genes, blue showing down regulated. The darker colour represents the gene with the highest expression. Rows are genes and columns are samples (n=3). The name of each gene is displayed to the right.

To better visualize how much the genes were regulated a vulcano plot was made were genes that have been up or downregulated in the HCT116 cells compared to the HCT116-R cells can be observed (Figure 3.6). In this plot we can observe the genes that has the highest significance in its up or down regulation. *RPS4Y1*, *DDX3Y* and *AL928654.3* has been

downregulated in the HCT116-R cells (Figure 3.6). *RPS4Y1* is a ribosomal protein, loss of function of RPS4Y1 have been associated with increased risk of cancer and could possibly be used as a cancer biomarker in the future (115). *DDX3Y* have been associated with poor outcome in CRC (116). *AL928654.3* is a Long non-coding RNAs (LncRNAs), a large RNAs without protein coding ability. LncRNA plays a key role in gene regulation, competing endogenous RNAs (ceRNAs) in many kinds of cancers, by blocking miRNAs and reducing inhibition of their target messenger RNAs (mRNAs). Studies suggested that other LncRNAs inhibited the progression of colon cancer through the miR-93-5p/17-5p/NHLRC3 axis, which in turn could be a potential therapeutic targets for colon cancer (117).

Genes that have been upregulated are *RSP10-NUD3*, *AC069547.1* and *RAB43* (Figure 3.6). It has been shown that several RAB members have been reported to promote tumorigenesis in many types of cancers. In a recent study it was shown that overexpression of *RAB43* promoted proliferation and metastasis in gliomas (118). Furthermore patients with tumors positive for *RAB43* had worse overall survival than patients with *RAB43*-negative tumors (119). There is little found in the literature regarding the genes *RSP10-NUD3* and *AC069547.1.*

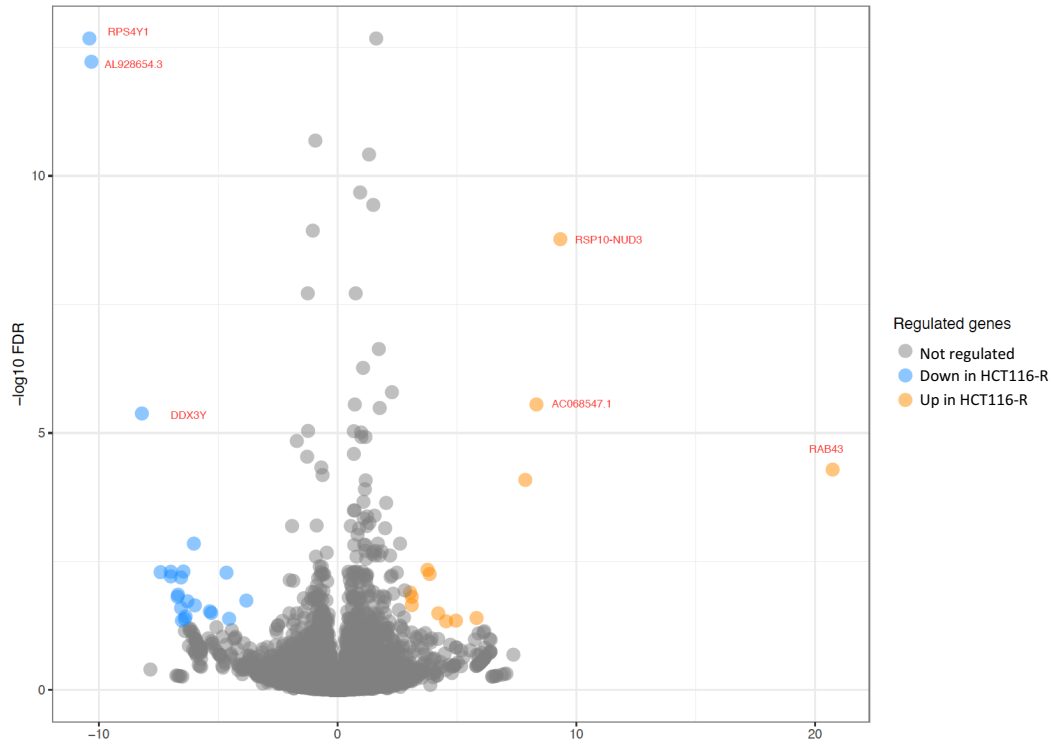

Figure 3.6. Volcano plot of differentially expressed genes

The vulcano plot shows up and down regulated genes in HCT116 cells compared to HCT116-R cells. Blue dots show downregulated genes and yellow dots show upregulated genes. Genes that have been upregulated are RSP10-NUD3, AC069547.1 and RAB43. Genes that have been downregulated are RPS4Y1, AL928654.3 and DD3Y. Number of replicates were 3 (n=3).

To identify the specific genes and pathways that have been differently expressed, pathway analysis was performed whereby a "oncogenes" filter was applied to select for genes related to oncology. Significant difference was observed in the PTEN, PIGF, p53, KRAS.LUNGBREAST, CSR and CAMP pathways (Figure 3.7) (Table 3.1). The phosphatase and tensin homologue (PTEN) is a tumor suppressor on chromosome 10 that signal cells to stop dividing (via AKT Serine/Threonine Kinase 1) and trigger cell death via apoptosis (120). Through the dephosphorylation of protein substrates, PTEN controls cell migration, cell adherence to surrounding tissues, and the formation of new blood vessels (121). Evidence also suggests that PTEN helps control insulin secretion which lead to increases tumor metabolism and growth (122).

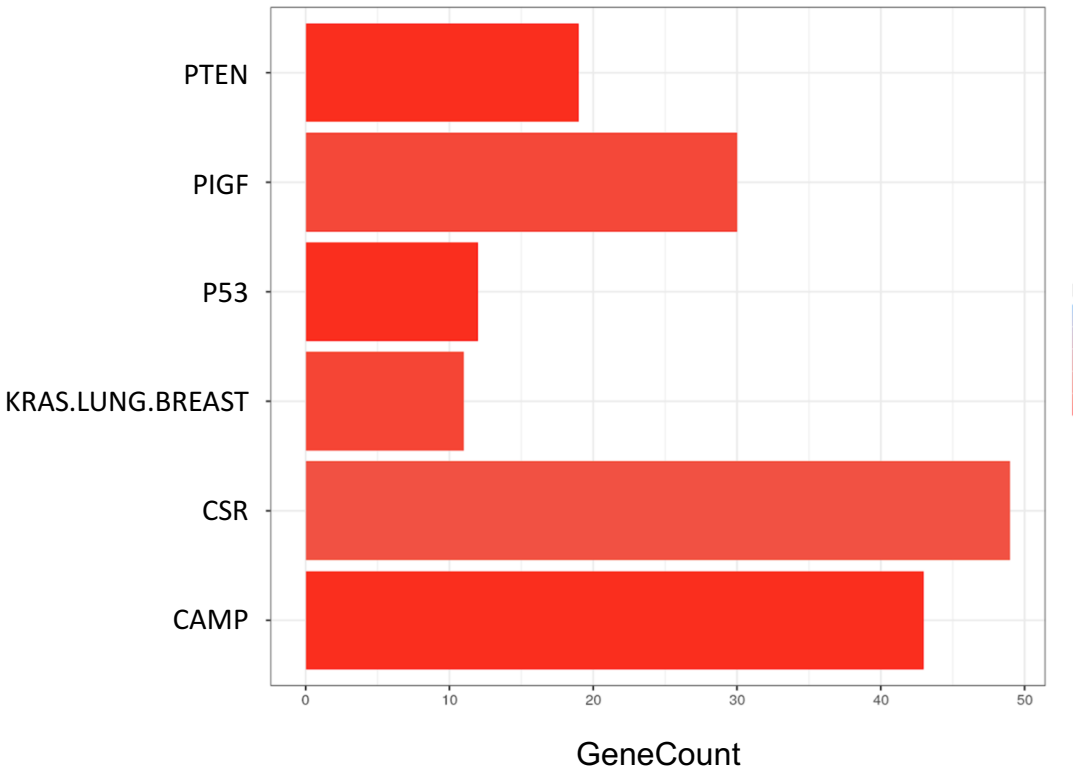

Figure 3.7. Upregulated pathways in HCT116-R cells

Upregulated pathways that are related to chemotherapy drug resistance. Significant difference was observed in the pathways PTEN, PIGF, p53, KRAS, CSR and CAMP pathways. Statistical significance was calculated using students t-test.

The tumor suppressor protein p53 is a part of the p53 pathway composed of a network of genes involved in DNA repair and stopping cells with mutated or damaged DNA from dividing. However, mutations in p53 are found in most cancers, and so contribute to the complex network of molecular events leading to tumor formation (123). The tumor suppressor protein p53 have prognostic relevance for many human tumor types where mutated p53 is often connected to drug resistance (123). The CSR genes pathway are involved in important processes in wound healing and angiogenesis, processes that are involved in contributing to cancer invasion and metastasis. Expression of the CSR signature predicted poor overall survival in several common epithelial tumors such as breast, lung, and gastric cancers.

Table 3.1. Pathways that have been identified to be up or down regulated in HCT116 compared HCT116-R cells and their effects.

PATHWAY	EFFECT	P-VALUE	REF
PTEN	PTEN regulates cell migration, cell adhesion to surrounding tissues, and formation of new blood vessel via dephosphorylation of protein substrates	0.00021	(122)
P53	P53 is a direct transcriptional target gene of CTCF which in turn promotes colorectal cancer cell proliferation and chemotherapy resistance to 5-FU via the P53-Hedgehog axis	0.00024	(124)
CAMP	Oncogenic signature gene sets	0.00033	(125)
KRAS.LUNG.BREAST_	Genes up-regulated in epithelial lung and breast cancer cell lines over-expressing an oncogenic form of KRAS	0.00090	(126)
PIGF	Plasental Growth Factor involved in wound healing immune regulation and angiogenesis	0.00033	(127)

Co-culture of HCT116 and HCT116-R cells as MCTSs

After inducing drug resistance in HCT116 cells and creating a drug resistant cell line (HCT116-R) we were interested in observing the effects of co-culturing the cells. By culturing cells as MCTSs more physiologically relevant models are provided that closely mimicking *in vivo* conditions. Therefore, to investigate the potential cooperative effect between DSCCs (HCT116) and DRCCs (HCT116-R) the cells have been co-cultured as MCTSs (Figure 3.8). After two days of culture the cells form compact spheroids. The co-culture spheroids had a uniform spherical shape with a diameter around 200 µm at day four. The cell distribution within the spheroids showed a homogeneous distribution of the DSCCs and DRCCs cells throughout the MCTSs (Figure 3.8), this cell distribution is likely due to similar cell surface markers. To distinguish each respective cell line, the cells were pre-stained with green cell tracker and orange, respectively. The relative number of each cell line could later be detected using confocal imaging.

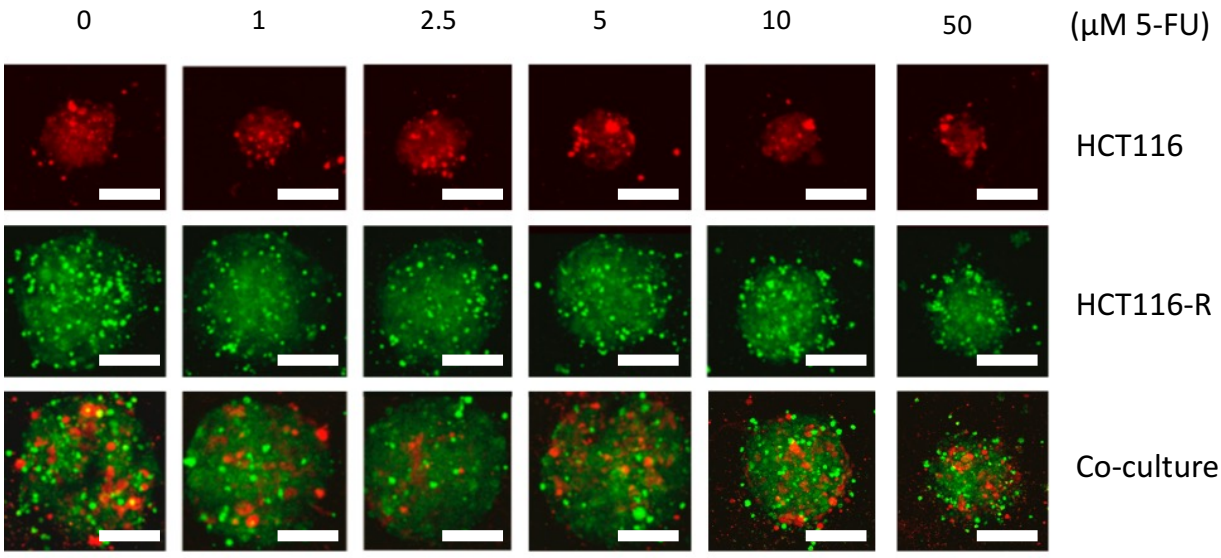

Figure 3.8. HCT116 and HCT116-R cultured as Multi-Cellular Tumor Spheroids (MCTSs)

HCT116 and HCT116-R cells cultured as monoculture and as co-cultured spheroids. The cells were stained with green cell tracker and orange cell trackers, respectively. The images were taken at day four of cell culture. They display z-stacks of merged images of whole spheroids obtained from confocal imaging. Spheroids were treated with 0, 1, 2.5, 5, 10, and 50 µM of 5-FU for 3 days. The scale bar in white represents 200 µm.

The figure 3.9 illustrates three separate experiments where DSCCs (HCT116) and DRCCs (HCT116-R) were cultured as MCTSs. As a control the cells were cultured as monoculture spheroids. a-c) HCT116 cells cultured as monoculture (grey bar) and co-cultured MCTSs (green bars). d-f) HCT116-R cells cultured as monoculture (grey bar) and co-cultured MCTSs (red bars). In the MCTS model, consisting of co-cultured DSCCs (HCT116) and DRCCs (HCT116-R), an increased cell survival was observed of both cell lines when the cells were co-culture compared to the monocultured cells at different drug concentrations (Figure 3.9). Both the DRCCs (red bars) and DSCCs (green bars) have an increase drug resistance in the co-culture systems compared to cells cultured as monocultured (the grey bars). This suggests that the cells have the capacity to mediate 5-FU resistance to each other in co-culture conditions. This could be due to crosstalk between the cells in response to 5-FU drug treatment, leading to increased cell proliferation.

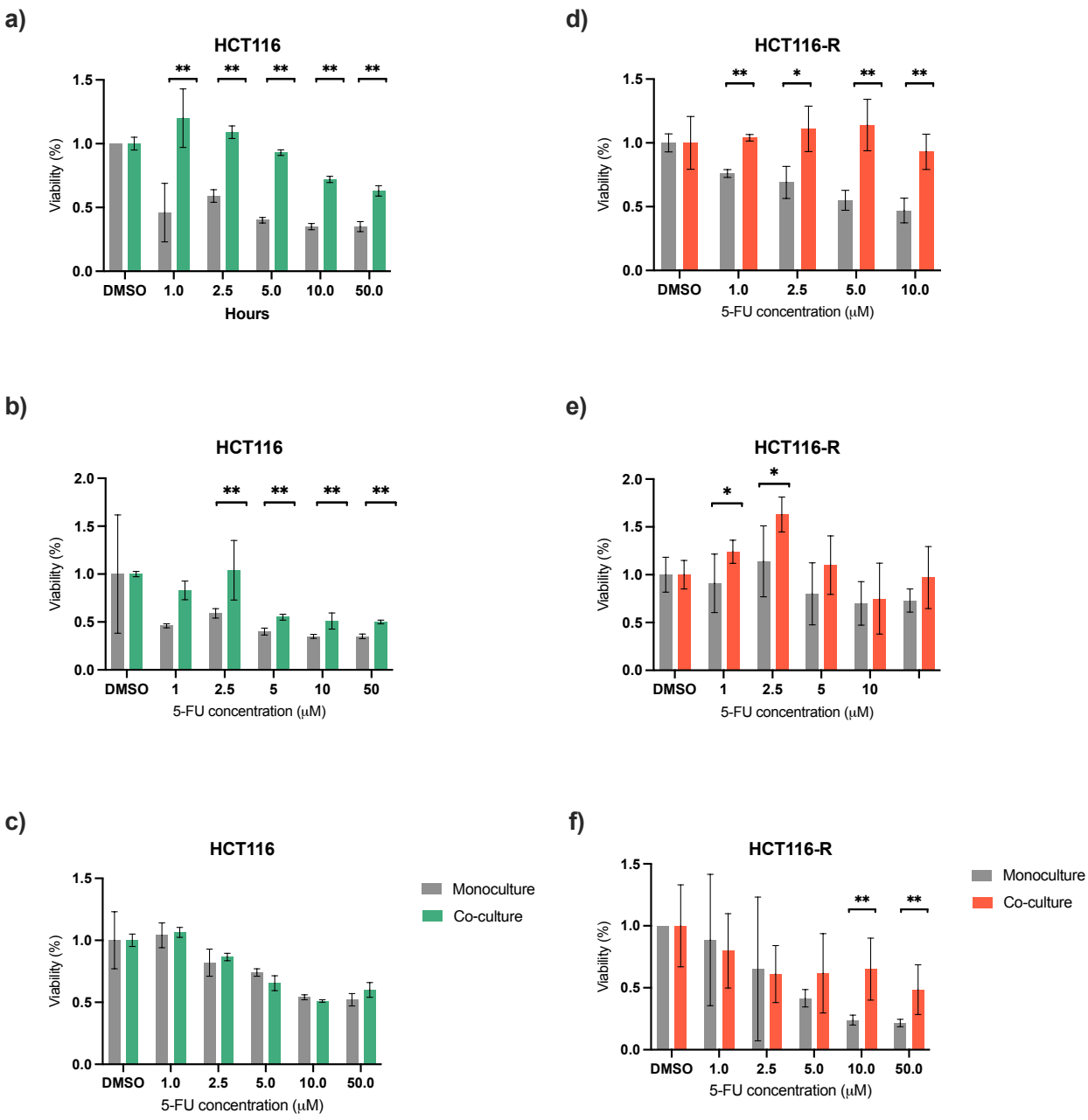

Figure 3.9. Cell viability of monocultured cells compared to Multi-Cellular Tumor Spheroids (MCTSs)

Three separate experiments of HCT116 and HCT116-R co-cultured as MCTSs after 72 drug treatment. a-c) HCT116 cells cultured as monoculture (grey bar) and co-cultured MCTSs (green bars). d-f) HCT116-R cells cultured as monoculture (grey bar) and co-cultured MCTSs (red bars). Cells were stained with tracker CMFDA green and CMFDA orange cell trackers, respectively. The X-axis shows the amount of 5-FU ranging from 1 to 50 μM. Y-axis shows the cell viability normalized to the DMSO control. The error bars represent the standard deviation calculated using cells from four different samples. Statistical significance was calculated using a two-tailed Student's t-test. A p-value of less than 0.05 and 0.01 was considered significant (*) and highly significant (**), respectively.

To analyze if the observed effects of increased drug resistance previously observed in the MCTS models were due to indirect effects CM from HCT116 cells were generated. The CM was made by treating HCT116 with 2.5uM 5-FU (CM_5-FU) or DMSO (CM_DMSO). The CM_DMSO was made as a control to compare if the effects were drug induced. Both the DSCCs and DRCCs were treated with the CM_5-FU and CM_DMSO. The DSCCs showed no effect on cell viability when treated with its own CM (Figure 3.10.a). However, when the DRCCs were treated with the CM_5-FU an increased cell viability was observed (Figure 3.10.b-d). The increased cell viability was only present in cells treated with CM_5-FU indicating that the CM from DSCCs is changed in response to the 5-FU treatment. It is likely that the DSCCs secrets molecules that help in the viability of DRCCs when treated with 5-FU (Figure 3.10).

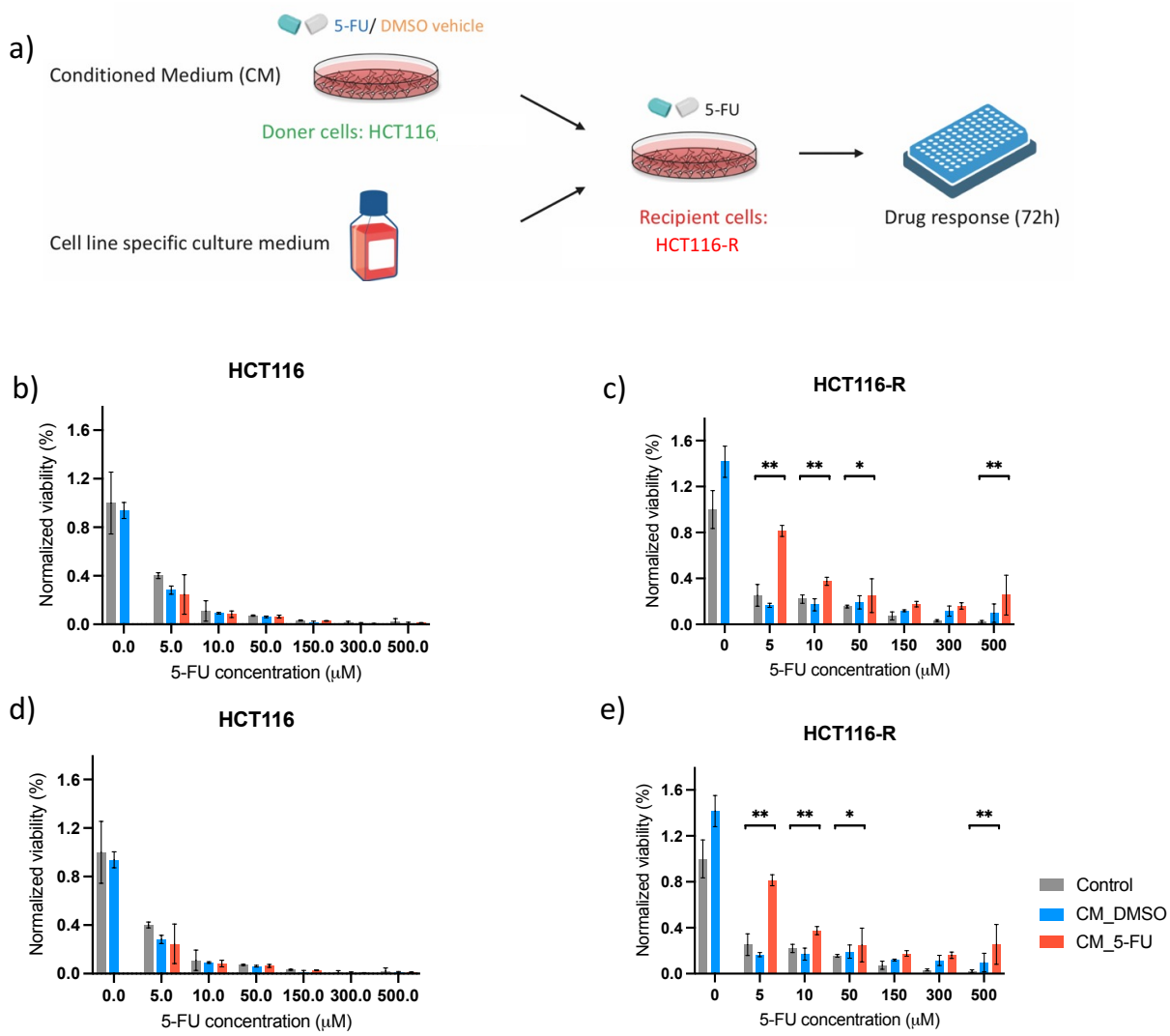

Figure 3.10. HCT116 and HCT116-R treated with Conditioned Medium (CM)

a) Schematic of cells treated with CM of HCT116 cells. Recipient cells were treated with either CM_vehicle or CM_5-FU. b) HCT116 cells treated with their own CM c-e) HCT116-R cells treated with HCT116 CM. The bar graph illustrates cells treated with; control (grey), CM_DMSO (blue) and CM_5-FU (red). X-axis shows the amount of chemotherapy 5-FU at increasing concentration ranging from 5 to 500 μM. Y-axis shows the cell viability normalized to the control. Cell viability was measured using MTS assays and the error bars represent the standard error of mean. Statistical significance was calculated using a one-way ANOVA followed by two-tailed equal variance Student's t-test. A p-value of less than 0.05 and 0.01 were considered significant (*) and highly significant (**), respectively, when compared to the control.

Characterisation of EVs

When cells were not cultured in direct contact with each other, increased drug resistance was observed; thus, these observed mechanisms were thought to be mediated by cell secreted molecules. It is known that tumor cells interact with each other through multiple different cell-signalling mechanisms. Several studies have shown that EVs are the key mediators involved in cell-to-cell crosstalk that led to tumor progression. To determine if EVs were precent in the sample NTA, flow cytometry and TEM was therefore performed.

NTA can be used to characterize nanoparticles in suspension in the size range of 10 – 2000 nm. EVs are between 30 nm–10 μm which makes it possible to detect using NTA. NTA is a method for measuring the EV concentration and size distribution where both light scattering and Brownian motion are used to detect particles in the nm-range. Using NTA both the size of individual particles and their total concentration can be determined with a dark field microscope, the laser shines through the sample which scatters when it encounters a particle. Individual EVs can be identified by measuring the way that the light scatters through the sample, after which their Brownian motion is tracked. Using the Stokes-Einstein equation the velocity of the particle can thereafter be used to calculate the particle size. (128). The NTA analysis was performed on EV_DMSO and EV_5-FU samples whereby the mean particle concentration was 1,40 x 10^{11} and 8 x 10^{10} particles/mL for each sample respectively. The vesicles were in the size range of around 150 nm for the samples were EVs had been extracted, more specifically EV_DMSO were 156.10 ± 0.14 nm and EV_5-FU were 152.80 ± 5.09 nm. In both samples a distinct peak that can be detected (Figure 3.11).

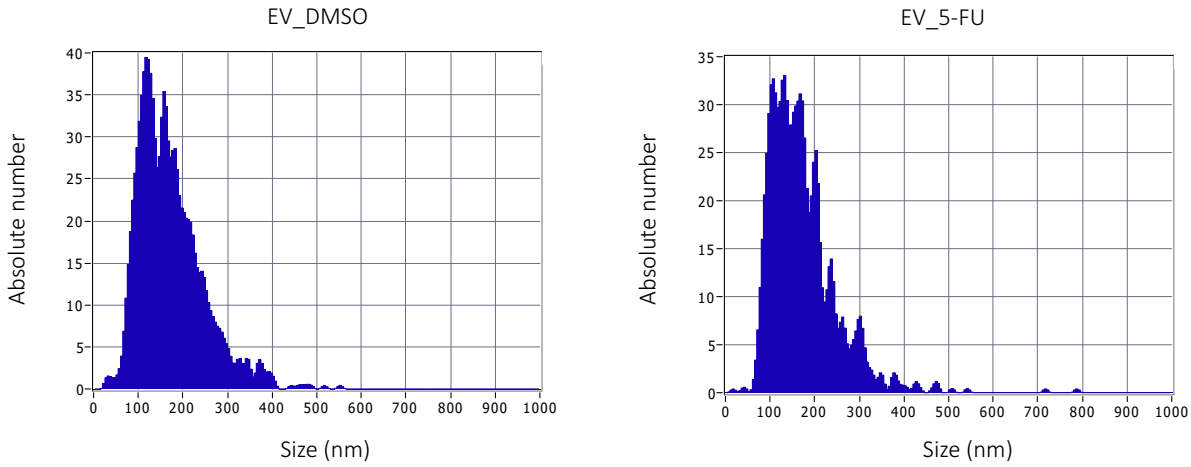

Figure 3.11. Nanoparticle Tracking Analysis of Extracellular Vesicles (EVs)

Nanoparticle Tracking Analysis (NTA) analysis was performed on EV_DMSO and EV_5-FU samples. On the x-axis the size distribution is displayed. On the y-axis the absolute number of particles are shown. For both sample the peaks are at approximately 100 nm.

For further characterization, the EVs were classified into different size and shape categories using TEM. For biological samples, TEM can transmit electrons through samples as thin as 100–200 nm to produce images with a potential subnanometer resolution. To visualize the EVs, the samples were prepared using a standardized procedures whereby the sample containing the EVs was prepared on TEM grids and observed in an electron microscope. Particles from the sample were adhered to carbon-coated formvar grids. To fix the EVs they were treated with paraformaldehyde to preserve their structures as the imaging is carried out in a vacuum. After fixation, the grid was placed on a droplet of contrast agent, uranyl acetate. The sample was thereafter exposed to an electron beam, and images were created based on the detected transmitted electrons. The contrast agent scatters electrons more efficiently thus staining the background and making it appear darker than the EVs. Consequently, the EVs should appear as bright particles on top of a dark background. Representative images were taken at multiple positions on each grid. EVs in the size range of around 100 nm were observed (Figure 3.12). Notably, EVs observed by TEM often appear as cup shaped because of dehydration during sample preparation which can be seen in the sample named "Standard" in Figure 3.12. This sample was prepared from HCT116 EVs that had been purchased dehydrated to be used as a control. Which is why

the shape might be different because the EVs had been dehydrated. In the EV sample from HCT116 cells, we instead observe a double membrane structure (Figure 3.12).

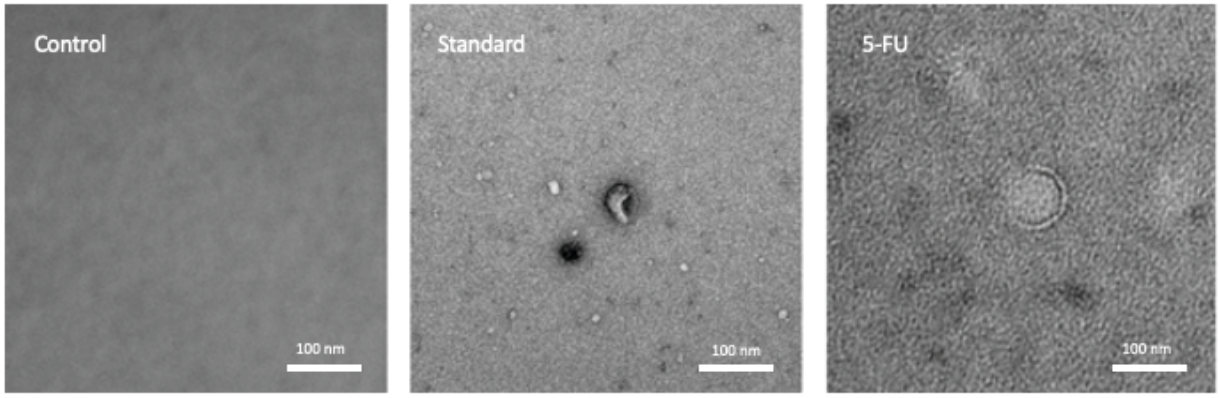

Figure 3.12. Transmission Electron Microscopy (TEM) images of Extracellular Vesicles (EVs)

Extracellular Vesicless (EVs) were imaged using Transmission Electron Microscopy (TEM). Control sample represents PBS alone, Standard represents EVs from HCT116 cells and 5-FU represents EVs from HCT116 CM_5-FU. Scale bar shows 100 nm.

Thereafter flow cytometry was performed to determine presence of EVs. EVs cannot be detected alone using regular flow cytometers because the sensitivity is too low, therefore polystyrene beads with a larger diameter of 4.5 μm were used (68). The beads were coated with antiCD63, a common EV marker, so that the EVs can attach to the beads. Beads alone were used as a control. To obtain a fluorescent peak that can be distinguished from the beads, the EVs were stained with red fluorescently labelled CD81 antibodies, another common EV surface marker. Ideally a large fluorescent shift between the two peeks should be observed, then the beads are fully saturated with EVs. Then it can be certain there is a large amount of EVs in the sample. In this experiment we observe a slight shift to the right in the EVs sample, indicating that a low number of EVs are present in the sample (Figure 3.13.b).

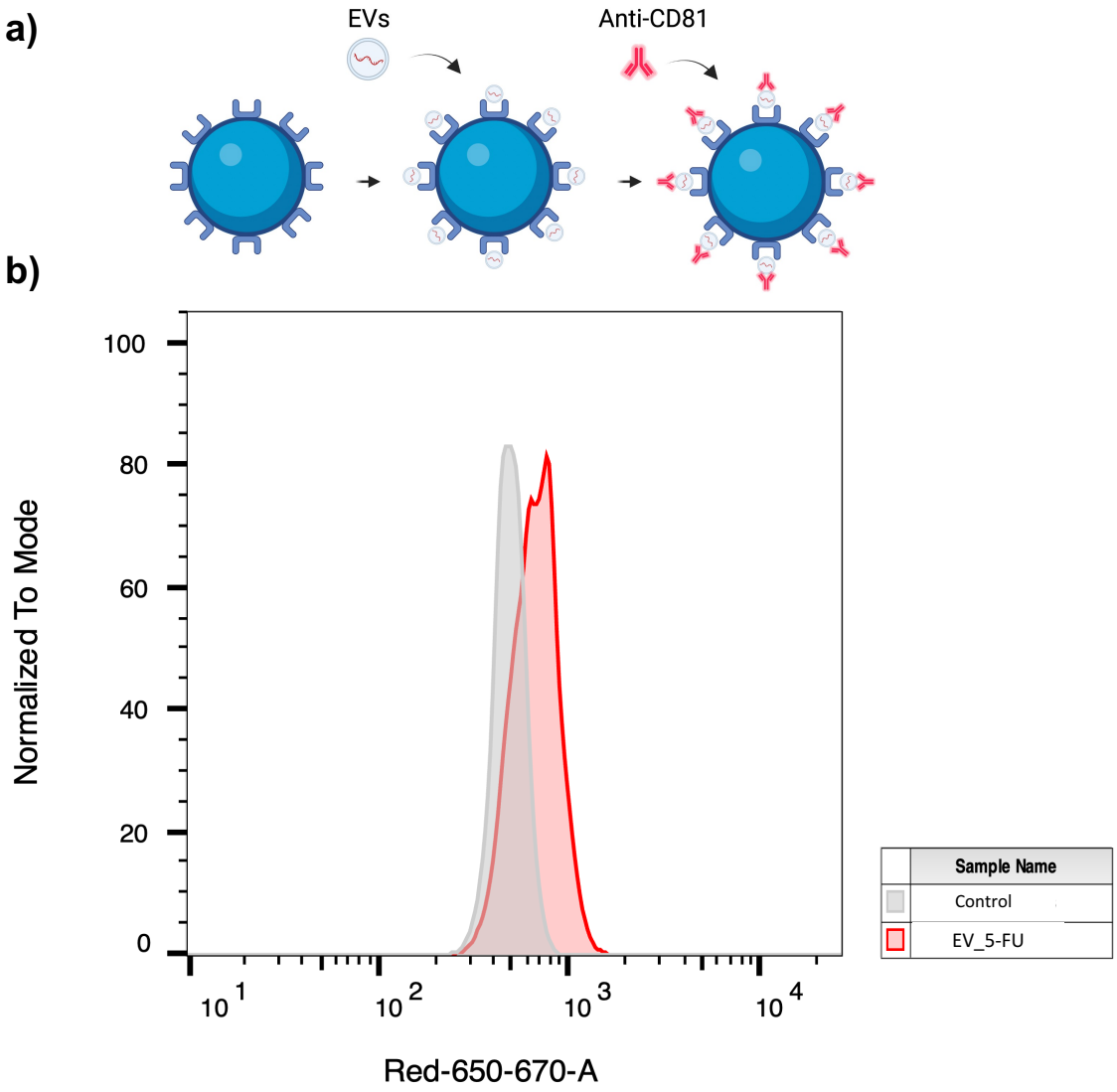

Figure 3.13. Flow cytometry of bead-bound Extracellular Vesicles (EVs)

Flow cytometry performed on bead-bound EVs. a) EVs carrying the antigen (CD63) will be captured on the beads whereafter the red fluorescently labelled AntiCD81 can be attached to the EVs. b) The peaks show the PBS control (grey) and EV_5-FU (red) samples.

Effects of EVs on cells

EVs were extracted from the HCT116 CM_DMSO and CM_5-FU by using a standardized ultracentrifugation protocol. Then, we performed the same drug gradient experiments as previously, however in this experiment EVs were also directly added to the cells. The cells were treated with medium, EV_DMSO and EV_5-FU whereafter the cell viability was determined. The DSCCs treated with their own EVs did not show any significant effect

from the treatment (Figure 3.14.a-b). However, at 5 µM 5-FU there was a significant effect of the EV treatment. This could be due to errors in the manipulation when the experiment was performed. The DRCCs treated with the DSCCs EVs showed significant difference in the EV treatment at 0, 5 and 300 µM (Figure 3.14.c). This however did not seem to be reproducible as seen in the second experiment (Figure 3.14.d) where little effect was observed due to the EV treatment.

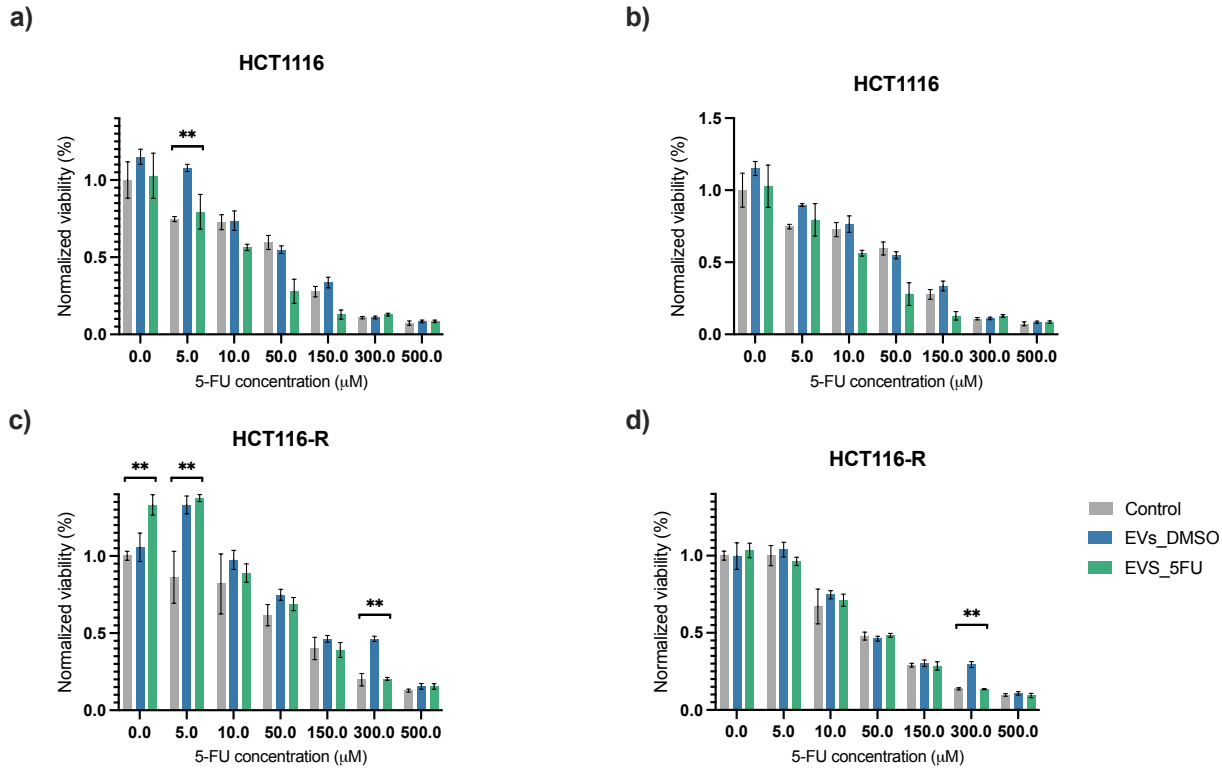

Figure 3.14. Cells treated with Extracellular Vesicles (EVs)

Cells treated with EVs extracted from CM. a-b) HCT116 cells treated with their own EVs. c-d) HCT116-R cells treated with the HCT116 EVs. EVs extracted from CM_DMSO (blue boxes) and CM_5-FU (green boxes), medium was used as a control (grey boxes). X-axis showing increasing 5-FU concentrations and Y-axis showing cell viability measured using MTS assay. The bars represent the average and the error bars represent the standard deviation (n=3). Statistical significance was calculated using a one-way ANOVA followed by two-tailed equal variance Student's t-test. A p-value of less than 0.05 and 0.01 were considered significant (*) and highly significant (**), respectively, when compared to the control.

v. Discussion

We started by identifying CRC cell lines that we classified as Drug Sensitive Cancer Cells (DSCCs) and Drug Resistant Cancer Cells (DRCCs) towards 5-FU (Figure 3.2). HCT116 was the only cell line that was identified as DSCCs. Consequently, to analyze the potential effects of co-culturing DSCCs and DRCCs a drug resistant HCT116 cell line (HCT116-R) was created from the parental HCT116 cells.

Development of drug resistant cells

In this study, we generated a 5-FU-resistant cell lines from HCT116 cells. The HCT116-R cell line showed approximately 1.5 times higher IC50 value compared to the parental HCT116 cell line (Figure 3.3). To further confirm these results as well as identify potential pathways which are involved in resistance mechanisms HCT116 and HCT116-R transcriptome have been sequenced. A significant difference was observed in the gene expression profiles and regulated pathways between the two cell lines (Figure 3.5) (Figure 3.7). Some of the genes that have been downregulated in the DRCCs are *RPS4Y1*, *DDX3Y* and *AL928654.3.* Some of the genes that have been upregulated are *RSP10-NUD3*, *AC069547.1* and *RAB43* (Figure 3.6). Some of these genes have previously been shown to be involved in drug resistance mechanisms as well as in cancer development (see results for a more detailed description). The specific pathways and mechanisms involved needs to be further analysed to gain deeper insights in specific processes that are at play. The epigenetic changes that account for the differences between DSCCs and DRCCs are only beginning to be uncovered. By identifying specific genes and pathways that differ in the DRCCs we aim to identify changes that can be useful in gaining new insights in how cells develop resistance, which in the future could be useful in developing new treatment strategies (41). This provides a tool to investigate the molecular pathways and detailed mechanisms that may be associated with drug resistance in CRC.

In the pathway analysis we observe a significant change in the PTEN, PIGF, p53, KRAS.LUNGBREAST, CSR and CAMP pathways (Figure 3.7) (Table 1.3). Some of these pathways have been shown to be contributing factors in drug resistance mechanisms and

tumor progression. However, an important point to consider is how long the resistant state lasts. Recently it has been suggested that drug resistance might be a transient state where cancer cells undergo phenotypic switching, in which the cells change from a more drug sensitive state to a drug resistant state (129). This is due to certain genes being activated or disactivated during drug treatment. The fraction of cancer cells that can transit reversibly between the different stages and the proportion that remains unchanged should be identified to develop more effective treatment strategies. It has been further hypothesized that cancer stem cells (CSCs) can play a key role in cell plasticity as CSCs as they have many of the key properties for phenotypic switching (130). The molecular mechanisms underlying these dynamic changes is of fundamental importance to gain more information in the quest to understand how cells develop resistance.

Cooperative effect of drug resistant cells

To investigate the potential cooperative effect between the DSCCs and DRCCs the cells where cultured as MCTSs. As a control, each respective cell line where cultured as monocultured spheroids under the same culture conditions. When comparing the monocultured spheroids to the MCTSs models, it was shown that the MCTS model had an increased cell survival during drug treatment. In particular, the DRCCs showed highest impact of the co-culture in all experiments (Figure 3.9). To further investigate this effect, CM from the DSCCs (CM_DMSO and CM_5-FU) was applied to the DRCCs. Cell viability was monitored by using a viability assay whereby it was shown that DRCCs treated with DSCCs CM stimulated the outgrowth of the DRCCs (Figure 3.9). The CM of the DSCCs did not show an effect on themselves, but the cell survival of the cells was sustained by the CM. These combined effects indicate that the DSCCs influences the DRCCs proliferation. As the cell communication is observed in the CM it is believed that these effects are due to cell secreted molecules of DSCCs that induce the survival of the DRCCs.

Characterisation of EVs and their effect on cell proliferation

We observe both direct cell-to-cell interactions, as seen in the MCTS models, and indirect cell communication via CM. It was therefore believed that the crosstalk could be mediated

through cell secreted molecules. Within the TME, EV mediated crosstalk plays a key role in heterogeneous cell populations where in a previous study it has been shown that tumor EVs have complex interactions with nearby stromal cells like fibroblasts and endothelial cells (108). Glioblastoma-derived EVs containing mRNA, miRNA, and angiogenic proteins have been taken up by recipient cells which promoted tumor growth and endothelial cell proliferation. Based on this we were interested in investigating the roles of EVs in the drug resistance we had observed, were DSCCs increased drug resistance in DRCC.

EVs can contain a great amount of genetic information that could be transferred to other cells, thereby promoting tumors progression in cancer patients (131). To obtain a complete picture of EVs and their role in cell communication, we decided to characterize the EVs in terms of size distribution, load, and quantification of the number. NTA, flow cytometry, and TEM are some of the go-to methods for confirming the presence of EVs in samples (128). First, to analyze if EVs could be detected in the cell secretome, we used standardized ultracentrifugation protocols to up concentrate the EVs in the sample. EVs detected from the NTA analysis had a size range of 150 nm and were detected in a mean particle concentration of 1,40 x 10^{11} and 8 x 10^{10} particles/mL for the EV_DMSO and EV_5-FU samples respectively (Figure 3.11). Using TEM it is possible to detect the shape of EVs and their size. We observed EVs in a size range of around 100 nm with a double membrane spherical shape in the EV_5-FU sample (Figure 3.12). Flow cytometry is used to detect the presence of EVs in the sample, we could observe a slight florescent shift in the EV sample compared to the control (Figure 3.13.b). These results combined strongly suggests there are EVs in the cell secretome of cells treated with chemotherapy 5-FU.

It has been shown that EVs secreted from mutated HCT116 cells were involved in the crosstalk between immune cells. EVs containing miR-1246 were release form the malignant cells leading to an altered TME composition, and an increasing abundance of tumor supporting macrophages (132). In future studies we aim to get a more comprehensive picture of the EVs and their roles in promoting drug resistance. By analyzing their cargo it is possible to find specific pathways that can have key roles in promoting drug resistance.

We analysed if the EVs had any potential direct effect on the cells by applying the EVs to cells at different 5-FU concentrations. DSCCs treated with their own EVs showed no significant effect from the treatment except for cells treated at 5 µM 5-FU (Figure 3.14.a-b). However, when DRCCs were treated with the EVs an increased cell viability was observed at 0, 5 and 300 µM 5-FU (Figure 3.14.c). This experiment was not reproducible as the follow up experiment did not show any effects of the EV treatment (Figure 3.14.d). Therefore, to get further insights in these mechanisms analyzing the EV cargo could provide deeper understandings in what molecular processes are occurring. EVs carries a complex molecular composition where there is great variation between each vesicle. This could explain why an increased cell viability was observed in some samples while in others no effects were observed.

vi. Chapter conclusion and perspective

One of the major challenges in the treatment of CRC is the development of drug resistant cells. However, there is currently a lack of the understandings of the mechanisms behind drug resistance development as well as understanding the role of DRCCs within the tumor. Therefore, assays that closely study these mechanisms are crucial to unravel the mechanisms by which tumor cells grow and metastasize. In this chapter we investigate the evolution of chemotherapy resistance in cancer by analyzing cell behaviour such as proliferation, death, and migration in response to drug treatment. Here we have begun to study the mechanism of resistance development as well as studying the cooperative effect between DSCCs and DRCCs. This has been studied by co-culturing DSCCs and DRCCs as MCTSs whereby we could observe an increased cell survival of the DRCCs under drug treatment. In the future we are interested in further analyzing if similar effects could be found in other CRC cell lines.

To further study these mechanisms and determine if they are due to cell secreted molecules CM from DSCCs were applied to DRCCs. Under 5-FU drug treatment, an increased cell survival was observed when the DRCCs was treated with CM from DSCCs. These observed

results suggest that the DSCCs can have a large impact in the overall tumor development and progression. The developed strategies could constitute innovative and pertinent tools that could give pertinent elements for our understanding on how cells develop resistance towards cancer drugs.

By developing new strategies for the co-cultures of CMS cells, we have identified potential mechanisms involved in the crosstalk between these cells. We started by studying the potential interactions between various molecules found in the cell secretome of HCT116 CM_5-FU and CM_DMSO by analysing the cell metabolites (see Chapter 2). Thereafter we continued our investigation of the HCT116 CM by detecting and characterizing their EVs. In future studies, we hope to learn more about these mechanisms and their effect on the tumor progression to gain a better understanding of how drug resistance is developed. Therefore, we are interested in separating the soluble metabolites from the EVs to investigate the contribution of the different components within the cell secretome. Once this has been identified Next Generation Sequencing (NGS) can be performed on the substrates and potentially specific pathways can be untangled.

Here we have performed transcriptomic sequencing of HCT116 and HCT116-R cells. We have compared the transcriptome profile of the two cell lines to identify potential key genes or pathways which may be involved in resistance mechanisms. However, when performing transcriptome sequencing, there might be genomic differences that are dependent on where the cells are in the cell cycle. Considering that the transcriptomic profiles only represent a single snapshot in time. Therefore, to get deeper knowledge of these mechanisms, it is of interest to repeat these experiments with other cell lines (or primary tumor tissue) to see if similar mechanisms could be detected.

Chapter 4

Spheroids on chip approaches for studying resistance mechanisms and cell to cell interplay

i. Introduction

Microfluidics are miniaturized systems that which are used to manipulate fluids at nano-liter to micro-liter scale. Microfluidic research date back to the early 1980s (133) (134) and is currently advancing at a rapid pace. It is a multidisciplinary field that combines chemistry, engineering, physics, nanotechnology, and biotechnology. Microfluidic systems present important tools to study reactions and mechanisms at sub-micron scale (135). Because of the small length scale of the system, factors such as surface tension, energy dissipation, and fluidic resistance starts to dominate the system and thereby fluid behaviour varies substantially at the microscopic scale compared to the macroscopic scale. There are many advantages in using microfluidics, it provides precise liquid handling capacities, flexibility in chip design, uses low volumes of liquid thereby lowering the cost. It can be tailored to suit a wide range of experimental approaches. Common uses of microfluidics range from applications in physics to study fluid behaviour to chemical applications studying chemical reactions or biological applications include organ on a chip models and single cell assays (136).

One of the more common applications of microfluidics are organ-on-chip systems where whole organs have been mimicked at a microscale (137). From this, tumor-on-chip models have been made which have largely been based on pre-existing on organ-on-chip models. Microfluidic tumor spheroid models stand out for their ability to automatically develop hundreds of spheroids in parallel and reduced the sample volume as liquids can be precisely controlled. Microfluidics also offers precise control of the physical scale down to tens to hundreds of micrometres that matches that of the TME. Furthermore, microscopy can be used to monitor events in real time with high spatiotemporal resolution (138). All these properties combined makes microfluidic platforms ideal for *in vitro* spheroid cultures.

Tumor spheroids have been developed using micro patterning (139), u-shaped microwells (140) and digital acoustofluidics (141). Droplet methods are attractive tools since they can provide a scalable way of producing single compartments for spheroids to be produced while also offering a broad range of manipulation tools. Lee *et al.* developed a platform for spheroid generation using gellinated droplets (142). This platform allowed a high throughput of 42,000 spheroids per experiment, but the manipulation and analysis of the spheroids were limited. In the group of Charles Baroud, Sart *et al.* have described a microfluidic approach for spheroid culture on chip (143). This method is based on droplet microfluidics where cells are encapsulated in droplets that can be trapped on the chip in anchored droplet traps (Figure 4.1.a). Using this method hundreds of spheroids could be produced in a relatively short time frame. The method used traps which allowed the spheroids to be confined on the microchip thereby precise image could be performed in real time. This made it possible to monitor the cell distribution within the spheroids over time. To expand from this Tomasi *et al.* altered some of the design features on the microchip which allowed for easy trapping of secondary droplets (144). Secondary droplets can be used to add new cell culture media to spheroids, allowing for longer cell culture on chip (Figure 4.1.b). It is also useful for drug screening, as drugs mixed with fluorescent dye can be added to the droplets, thereby allowing different drugs and drug concentrations to be analysed on the same chip (Figure 4.1.c). Using this method Tomasi *et al.* could perform high-throughput drug screening where individual spheroids could be monitored in real time. These combined results led up to the creation of a company called Okumera which specializes in the creation of microfluidic platforms for spheroids culture. In this study we aim to use their platform for co-culturing HCT116 and HCT116-R cells as MCTSs.

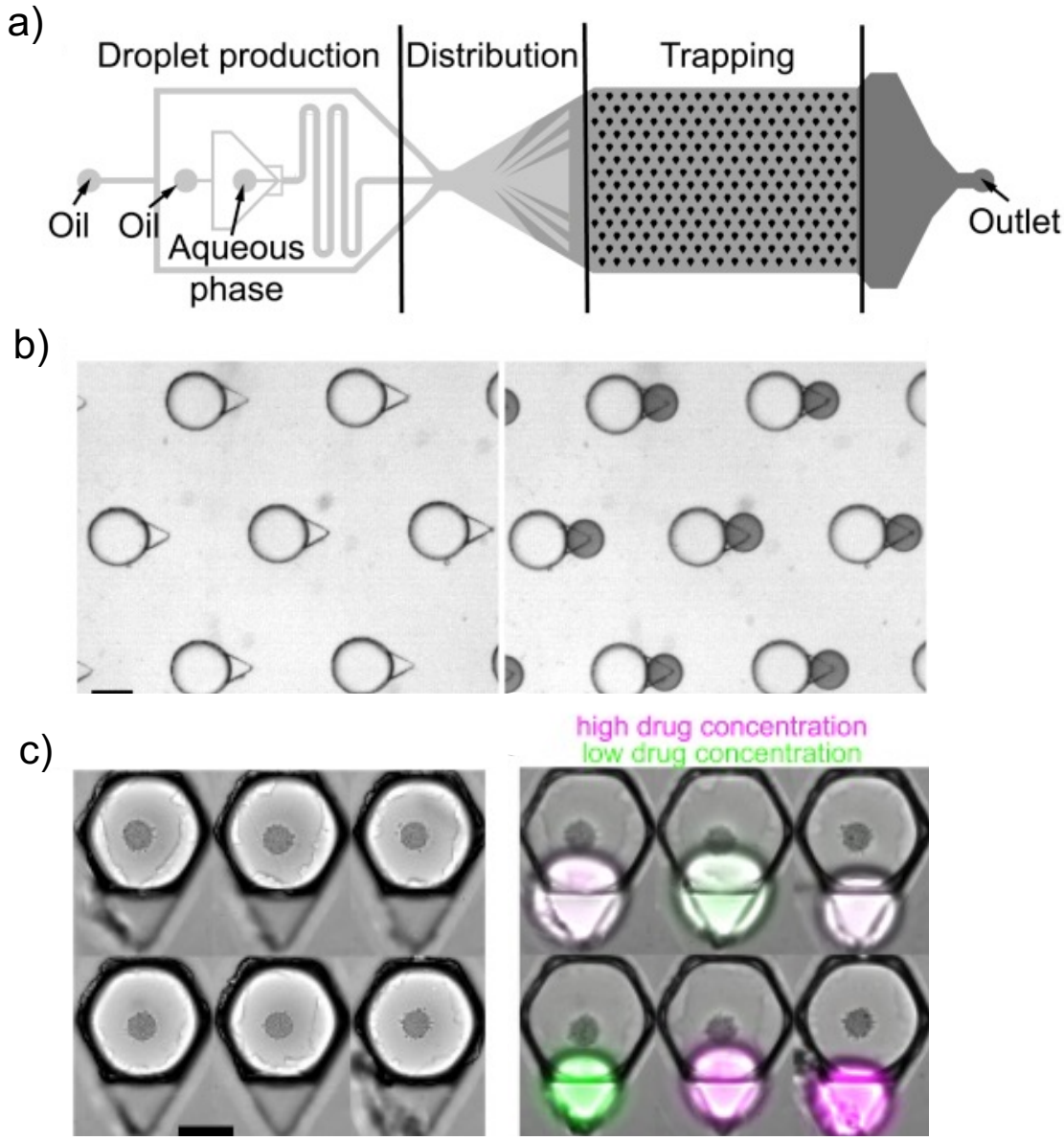

Figure 4.1. Microfluidic chip design

a) The design of the microfluidic chip showing the droplet production, distribution and trapping. b) On the image to the left, droplets have been injected on the chip and each trap has been filled with a droplet. On the image to the right, small droplets (dark dye) have been trapped on the triangle part of each anchor. Scale bar is 100 µm. c) The image to the left show spheroids on chip and the image to the right display secondary droplets with varying drug dilutions that has been trapped on the triangle part of the anchor. The drugs have been labelled with florescent dye and thereby multiple drugs can be loaded on the same chip. Scale bar is 100 µm. The image is modified and taken with permission from Tomasi et al. (144).

Droplet formation and manipulation

Droplet-based microfluidics is a high throughput method that uses an immiscible fluid phase combined with an aqueous phase to create independent micro reactors in form of nano-liter to pico-liter droplets (Figure 4.2.a) (145). Each droplet acts as an individual compartment and can be used to compartmentalize single cells in a high throughput manner. Large numbers of droplets can be generated at astonishingly high rates (>10^7/s) (146). One of the major advantages with using droplet-based microfluidics relies on its high throughput screening capabilities, making it possible to analyze a large set of cells from complex and heterogeneous populations in a relatively short time frame (147).

Traditionally, droplets have been produced using T-junction (Figure 4.2.a), flow-focusing (Figure 4.2.e) and coaxial focusing structures. Once droplets have been made there are multiple techniques readily available to manipulate the droplets. By for example placing an electrical field over the droplet, the surface tension is temporarily broken making it possible to perform multiple different manipulations. These include droplet splitting (Figure 4.2.c) (148), droplet merging (Figure 4.2.f) (149) and pico-injection (Figure 4.2.g) (150). Droplet splitting is a useful technique that can be performed to detect multiple analytes from the same droplet. Droplet merging and pico-injection can be performed to inject something into the droplet, this can include a cell assay. To keep the droplets on the microfluidic chip they can be trapped in different geometric constrains that can be placed on the chip. This way multiple reaction chambers can be placed on chip and reactions can take place in parallel and be monitored in real time.

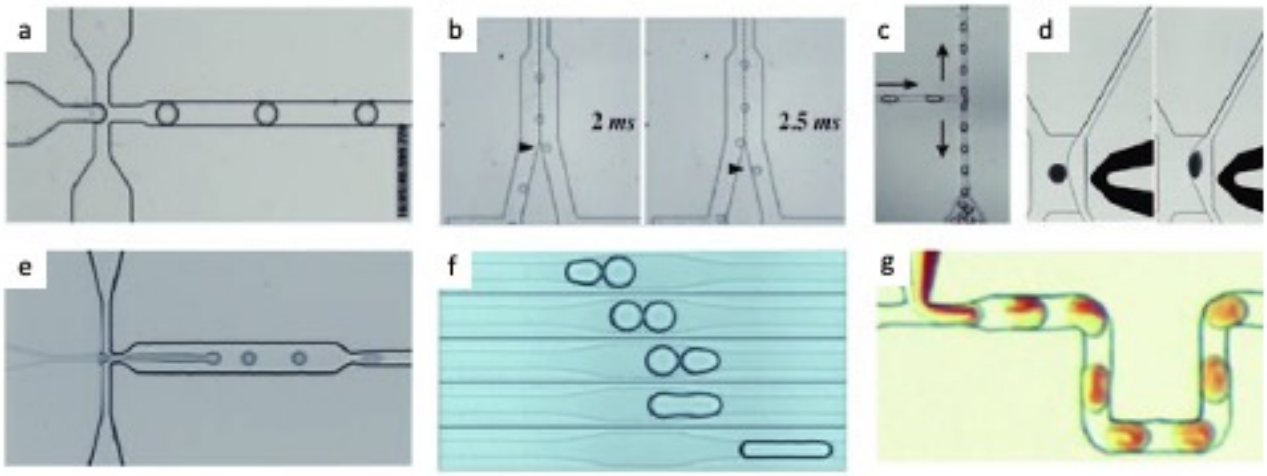

Figure 4.2. Droplet microfluidic and its manipulation tools

a) Droplet production using a T-junktion. b) Droplet sorting. c) Droplet splitting d) Droplet fusion by electro coalescence e) Droplet formation from jetting in a flow-focusing device f) droplet merging and g) Pico-injection. Image modified from Theberge et al. (151).

ii. Motive

We began with a proof-of-concept study where DSCCs and DRCCs were co-cultures as MCTSs using nonadherent u-shaped well plates. In the co-culture systems, crosstalk was observed between the cells upon 5-FU drug treatment. We discovered that the secretome of DSCCs increased the proliferation of DRCCs (see chapter 3). To build on this, we have aimed to use the microfluidic platforms from the company Okumera to create hundreds of uniform spheroids in a relatively short time frame. Their platform enables real time monitoring of the cell distribution within the spheroids. This is particularly interesting as we can study the cell distribution of DRCCs and DSCCs in the co-culture systems. Thereby we could monitor how the cells grow within the spheroids as well as the interactions between the DRCCs and the DSCCs. Furthermore, their platform enables fast drug screening thereby multiple drug concentrations and mixtures can be administered to the cells in an automatic way and the cell viability can be analyses.

iii. Methods

Microfluidic chip fabrication

The silicon wafers were placed on a 95 °C hotplate for five minutes to remove any potential humidity or water residue from the wafer. Photoresist (SU-8 3010) was spin coated on the silicon wafer and cross-linked in the pattern of the microfluidic device using photomasks and UV light exposure. The spin-coated wafer was pre-baked by placing it on a 65 °C hot plate for one minute. Polydimethylsiloxane (PDMS) replica molds were made by mixing 10:1 ratio of PDMS to curing agent (Sylgard 184, Dow Chemical, MI, USA) and heated at 80°C for two hours.

For the fabrication of the bottom part of the chip, the molds for the chambers were covered with PDMS. Then, above the anchored chamber traps, a glass slide was placed on the uncured PDMS. Finally, the mold was heated for 15 minutes on a hot plate at 180 °C. The device was then bonded to seal the top and the bottom sides using oxygen plasma treatment (Harrick, Ithaca, USA). Thereafter the surface of the microfluidic channels was treated by filled the channels three times with Novec Surface Modifier (3 M, Paris, France), a fluoropolymer coating agent for placed on a hot plate for 30 minutes at 110 °C.

Cell loading on chip

All experiments were carried out using FC40 fluorinated oil (3M) combined with a biocompatible FluoroSurfactant (Ran Biotechnologies). The solutions were loaded in syringes made of either glass (SGE) or plastic (Terumo). PTFE tubing (Adtech) was used to connect the syringes to the PDMS chips. The solutions and corresponding flow rate were operated by syringe pumps that were computer controlled (neMESYS, Cetoni). The experiment started by preparing a cell solution (see Chapter 3 Methods) containing 1 µM GFP cell tracker and 3 µM Pi (ThermoFisher Scientific, USA). The cells were loaded on to the chip in one inlet while another inlet was loaded with the oil solution. The flow rates were kept at 40 µl/min and droplets were produced at the T-junction. After the droplets have been created, they are able to attach to the anchored traps. Once the droplets have

been trapped the cells were left to settle down and to organize as spheroids for 24-48 hours in the CO^2 incubator.

Droplets with varying cell densities were created to determine the number of HCT116 and HCT116-R cells that can be cultured as spheroids on the chip. For the small traps 20 and 50 cells were used. For the larger trap 75 and 150 cells were used. The experiments were carried out for eight days during which the spheroids imaged every day using widefield fluorescence microscopy (Zeiss Axio Observer Z1) at 10X magnification. Using the acquired images, the spheroid diameter could be measured using Fiji (ImageJ) software. For the co-culture experiments, the cells were further imaged at day two and four using confocal laser scanning microscope (Zeiss LSM710) to determine the relative number of each respective cell line.

Drug treatment

Drug treatment was performed by adding a secondary droplet that can get trapped in the triangle part of the anchor and thereafter merged with the existing trapped droplet that is located in the trapping chamber. The trapping chamber is constantly kept filled with FC40 fluorinated oil (3M). Droplet merging is performed by changing the oil and filling the trapping chamber with a 20% (v/v) 1H,1H,2H,2H-perfluoro-1-octanol (Sigma Aldrich USA) solution dissolved in 3 M Novec™-7500 Engineered Fluid. The surface tension of 1H,1H,2H,2H-perfluoro-1-octanol is lower compared to the FC40 fluorinated oil thereby enabling droplet merging.

The to enable the secondary droplet to attach to the triangle part of the anchor, the secondary droplet needs to be 30 times smaller compared to the trapped droplet. Therefore, to have a final 5-FU concentration of approximately 2.5 μM, the secondary droplet must contain 30 times higher 5-FU concentration. To determine the 5-FU concentration within the spheroid traps the 5-FU was mixed with 1 μM Flouro dye 647 (ThermoFisher Scientific, USA).

iv. Results

Previously we have cultured DRCCs and DSCCRs as MCTSs in u-shaped wells whereby an increased drug resistance was observed in the co-culture systems (see Chapter 3). Here we have cultured the same cell lines using a microfluidic platform. Using well plates, the cells form compact spheroids after one days of cell culture (see Chapter 3). On the microfluidic platform, it took approximately two days for the cells to form compact spheroids (Figure 4.3). Using the microfluidic platform, the cells have less access medium as compared to well plate settings. This might cause the cells to grow slower and thereby the time for spheroid formation is longer.

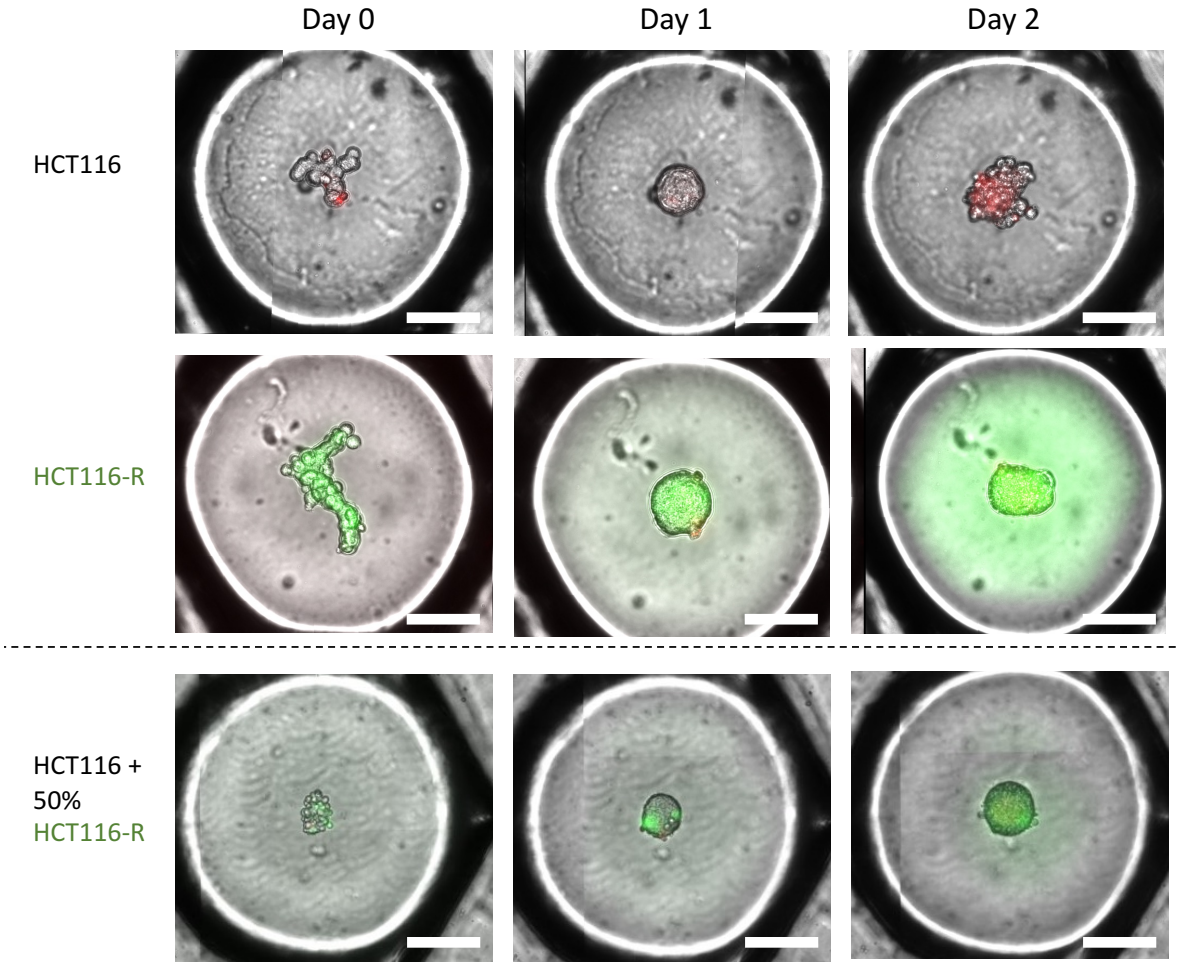

Figure 4.3. Spheroid formation over time

Cells cultured as spheroids using microfluidic droplet traps. Representative live cell confocal fluorescence microscopy images showing HCT116 spheroid formation from day zero to day two post seeding. The pictures illustrate how spheroids are formed after approximately two days of cell culture. Monoculture of HCT116 and HCT116-R cells, respectively. MCTSs of HCT116 + HCT116-R at (50/50%). HCT116-R is stained with CMFDA green cell tracker. PI is added to all droplets staining necrotic cells in red. Scale bars=30 µm.

Furthermore, to analyze the cell growth on chip the spheroid diameter was measured every day using microscopy. It was observed that the diameter increased slightly over time (Figure 4.4). As the spheroids grow, it can be expected that the spheroid diameter also increases. Here we can only observe a slight increase in the spheroid diameter. When looking at Figure 4.4 it is observed that one of the spheroids (BT80 co-culture) increase its diameter drastically over time. This is the only spheroid cultured in the big trap, which

could be an indication that the larger traps are better suited for long term cell culture. In the big traps the droplet size is larger and thereby the cells have more cell culture medium. However, as the spheroids mature with each day, the compactness also increases. Thereby the spheroid diameter might not be the best way to determine cell growth within the spheroids.

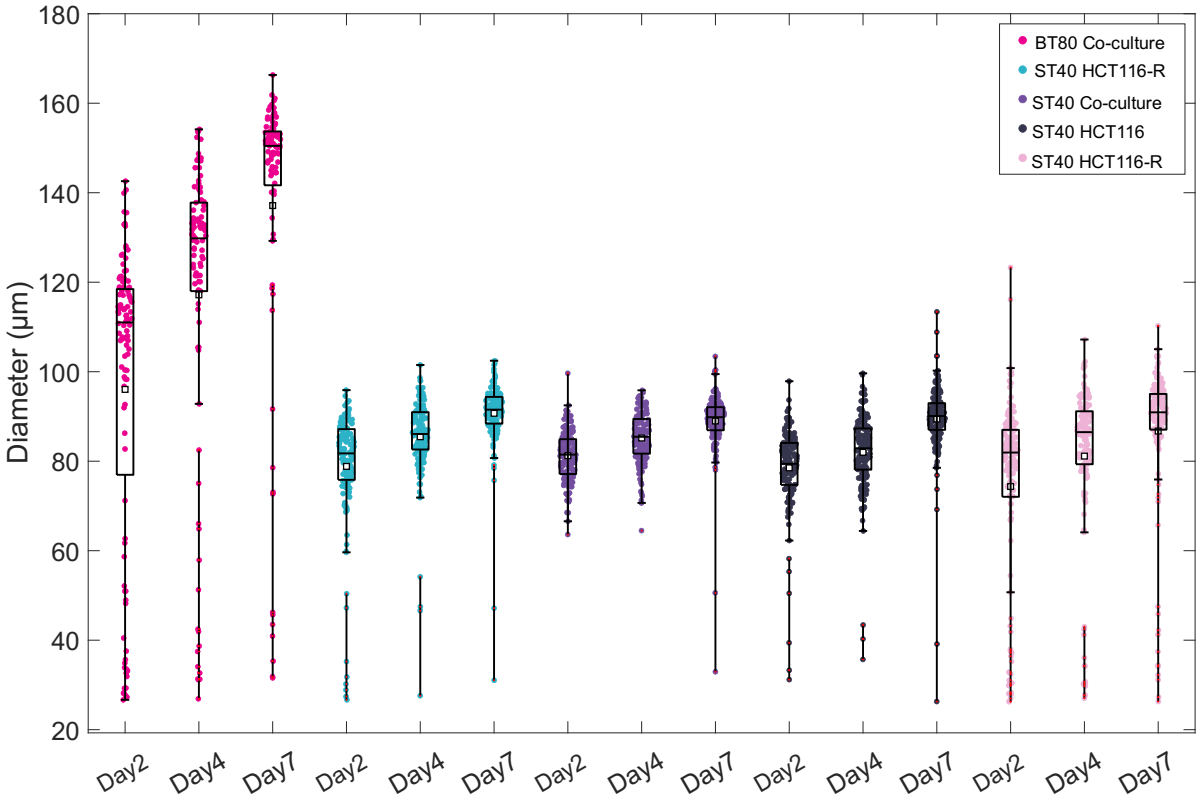

Figure 4.4. Spheroid diameter measured over time

The box plot shows the diameter of each individual spheroid at day 2, 4 and 7. The small trap (ST) was 400 µm in diameter and the big trap (BT) was 800 µm in diameter. ST was seeded with 40 cells and BT was seeded with 80 cells. The co-culture of HCT116 and HCT116-R cells was at (80/20 %) of each respective cell line. HCT116 and HCT116-R were monoculture as a control.

Thereafter cell viability was determined by adding PI to the droplets on day 0 and counting the number of red fluorescent cells. PI has an excitation maximum near 500 nm and an emission maximum at 625 nm in the absence of cells. Binding of PI to DNA causes a red

shift of the excitation maximum to 540 nm and the emission maximum to 640 nm, with a two- to threefold increase in fluorescence intensity. Once the cell has entered cell death, PI can access the chromosomes which thereafter starts to emit a bright red fluorescent colour. Because the PI remains stable over time, it is possible to count the number of cells that died each day. It can be observed that the cell viability is stabile over time. At day four the cell viability remains high, however at day seven it starts to decrease slightly from a viability at 1 to 0.8 (Figure 4.5).

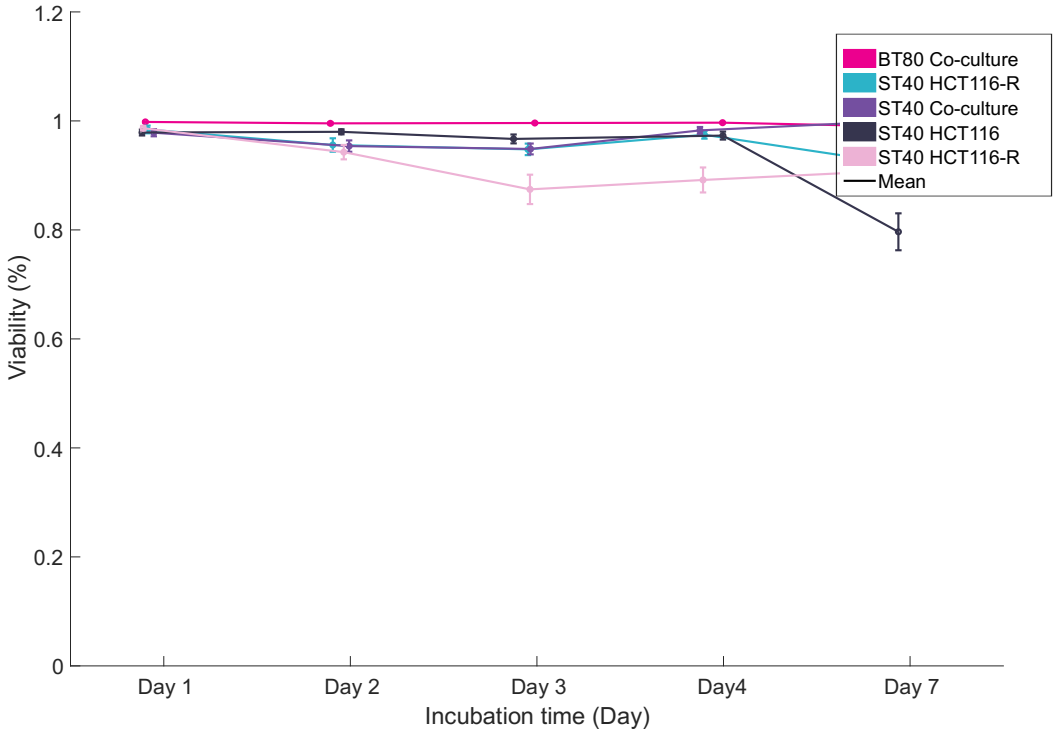

Figure 4.5. Cell viability measured over time

Cell viability was measured by adding PI at day 0 and then detecting the number of cells stained that were stained with PI over time. All cells stained with PI are non-viable cells. The small trap (ST) was 400 µm in diameter and the large trap (LT) was 800 µm in diameter. Viability ranges from 0 (all cells stained with PI, corresponding to a situation with no viable cell) to 1 (no cell stained with PI, thus corresponding to a situation with all cells alive). The number of cells are indicated in the box (ie. 40 or 80 cells). Cells are either co-culture of HCT116 and HCT116-R cells (80/20%) or monocultured HCT116 and HCT116-R. The standard deviation is based on over 100 replicates.

The box plot shows the spheroids viability for each individual spheroid over time. Most spheroids display high cell viability over time (Figure 4.6), however the spheroids displaying low cell viability can be removed from the experiment using computational methods. At day two and day four the spheroids have a high cell viability. At day seven the cell viability starts to decrease (Figure 4.4). Most of the dead cells that are located on the outside of the spheroid (Figure 4.7). This could be because the PI cannot efficiently penetrate the spheroid and thereby the cells in the spheroid core are not stained. Or the more likely option might be that the spheroid is shedding the necrotic cells leaving them on the outside of the spheroid, as observed in a previous study where HCT116 cells were cultured as spheroids (152).

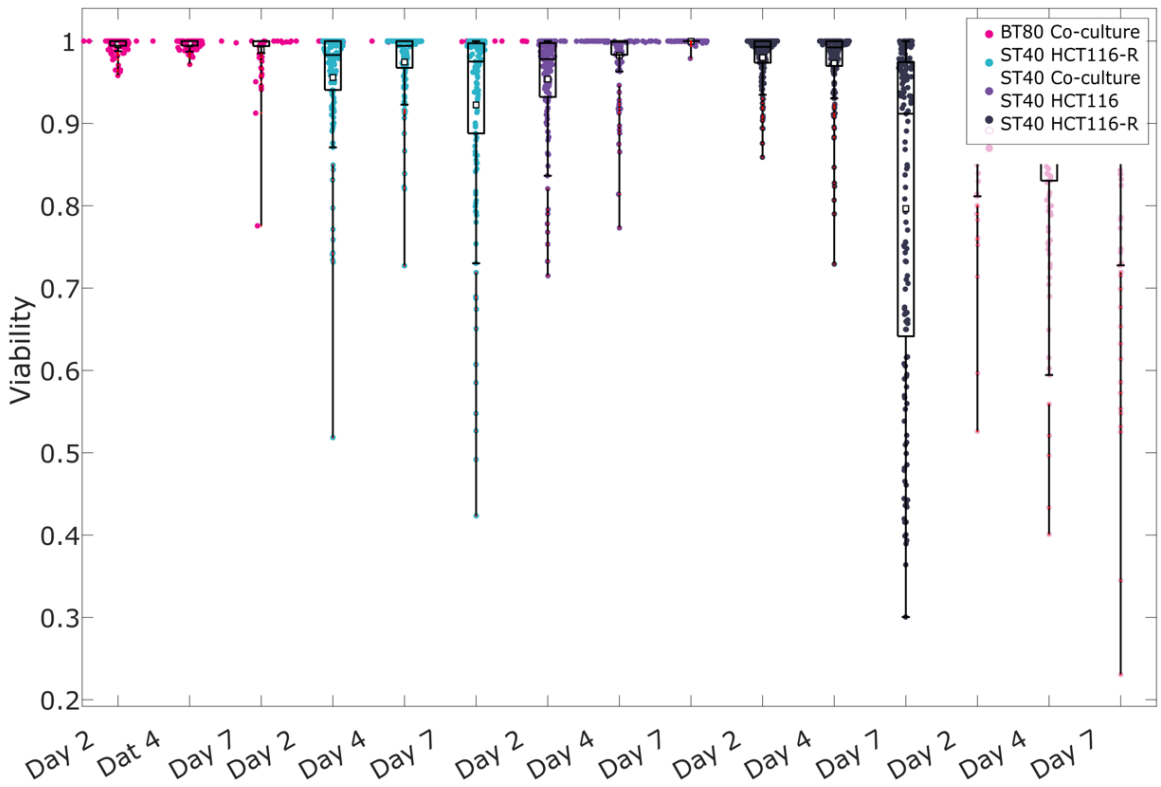

Figure 4.6. Box plot showing cell viability in each spheroid trap

The box plot shows cell viability in each spheroid trap measured at day 2, 4 and 7. Cell viability was analyzed by detecting the number of cells stained with Pi using florescent microscope. The small trap (ST) was 400 µm in diameter and the big trap (BT) was 800 µm in diameter. ST was seeded with 40 cells and BT was seeded with 80 cells. The co-culture of HCT116 and HCT116-R cells was at (80/20 %) of each respective cell line. HCT116 and HCT116-R were monoculture as a control.

Previous we have observed that co-culture systems consisting of HCT116 and HCT116-R cells cultured as MCTSs in u-shaped well plates displayed an increased cell viability in the co-culture systems compared to the monoculture (see Chapter 3). Therefore, we wanted to analyze if similar affects could be observed on microfluidic platforms. Here we have co-cultured HCT116 and HCT116-R cells as MCTSs on a microfluidic platform (Figure 4.7). We are currently analyzing the acquired images to see if we can detect similar results on the microfluidic platform. Preliminary results suggests that DRCCs sustain the proliferation of DSCCs.

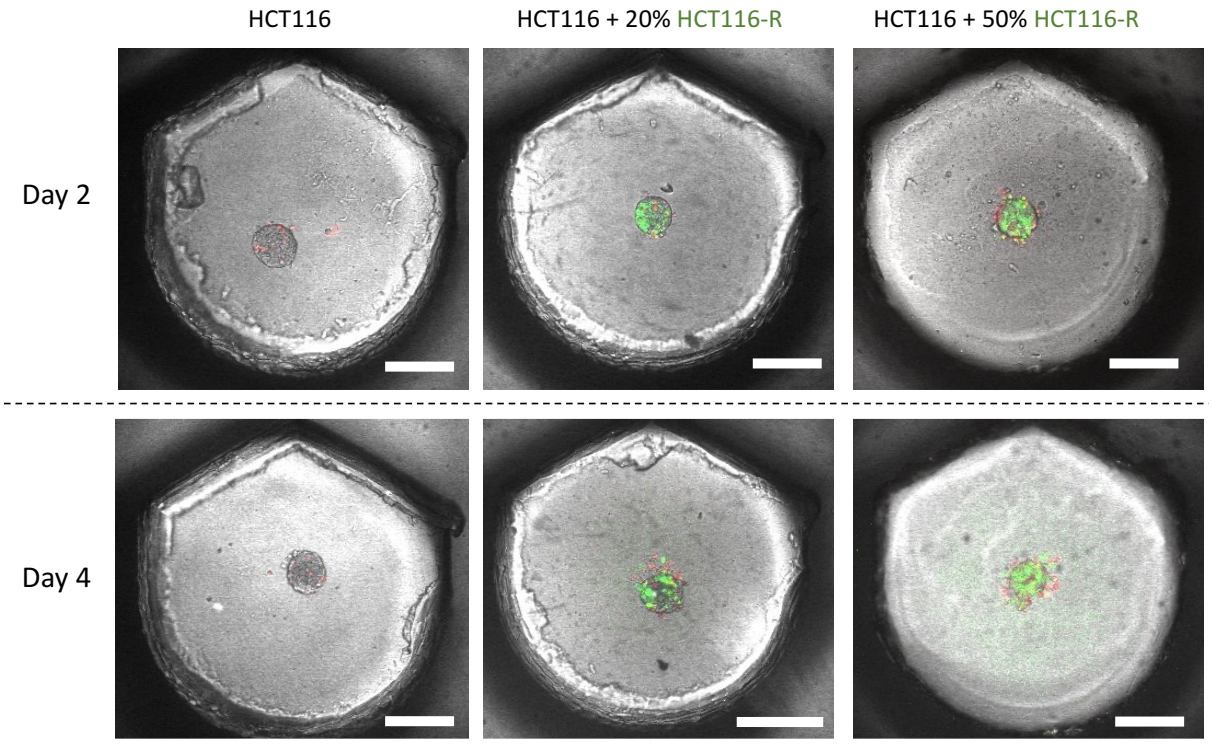

Figure 4.7. Co-culture of HCT116 and HCT116-R

Representative live cell fluorescence microscopy images showing spheroid at day two and day four post seeding. Scale bars=100 µm. Monoculture of HCT116 and co-culture of HCT116 and HCT116-R at 20% and 50% of HCT116-R, respectively. The HCT116-R cells were stained with cell tracker green. PI was added to all traps staining necrotic cells in red. Scale bars=100 µm.

v. Discussion

Using microfluidic platforms for culturing spheroids enables high throughout and precise manipulation of fluids. Since the liquids inside the microchip can be accurately controlled, it is possible to significantly lower the volume of reagents and, as a result, the total number of cells needed. This is ideal for clinical samples which are precious where amount of tissue taken from the patient can be very low, resulting in only a few viable cells. Another advantage is that the loading time is reduced as the sample can be injected directly on to the chip and droplets can automatically be produced thereby reducing the shear stress that can otherwise be placed on the cells. However, a disadvantage might be that the

exchange of liquids is more troublesome leading to an accumulation of toxic cell metabolites thereby affecting the cell viability. To circumvent this Tomasi *et al.* developed a droplet trap platform where multiple droplets can be trapped after each other, enabling better exchange of liquids (144).

Here to generate spheroids on the microchip we used a technique called "anchored droplets" (143) (144). The microfluidic device was composed of a droplet generating part, followed by a trapping chamber that consists of 247 chambers traps were the droplets were trapped (Figure 4.1). Two different designs of the traps were used, small traps (400 μm in diameter) and big traps (800 μm in diameter). Droplets were created with a similar size as the trapping chambers, this allows the droplets to be trapped once it passes a chamber trap. Once the droplet is trapped inside the chamber it will form a u-shape with the help of gravity. The u-shape enables the cells to be positioned close to each other thus facilitating spheroid formation. Here we show generation of homogeneous spheroids of DRCCs and DSCCs using this platform. Cell viability and spheroid diameter was measured over time where it was observed that the cells maintained a high viability over time. Time-laps imaging showed that after eight days of cell culture the cell viability remains high (Figure 4.4, Figure 4.5). The diameter of the cells cultured in the small traps the did not increase as much as could be expected. However, the cells cultured in the big spheroid traps did show an increase in diameter. This is most likely because the cells have access to enough nutrients and oxygen to grow continuously without producing high levels of waste products which can accumulate in the surrounding liquid. This is because one of the limiting factors for maintaining high cell viability within the spheroid is the cell culture medium. If the cells start to lack nutrients or oxygen due to the limited cell culture media medium that is inside the droplet, the cells start to enter cell death. This is because in the cell culture medium there are nutrients needed for cells to proliferate and grow. If there are not enough nutrients the cell proliferation will slow down or stop completely. Furthermore, as the cells grow they produce toxic waste products. When there is an accumulation of waste products, the cells in the spheroids start to enter cell death.

Previous microfluidic CRC tumor models have allowed researchers to investigate different cellular processes including how angiogenesis occurs in the TME and its impact on tumor progression (153), crosstalk between cell in the TME (154) (155) and studying the invasive potential of CRC tumor cells by recapitulates aspects of colon cancer biology (156). For example, HCT116 cell line was cultured as Vascularized Micro-Tumors (VMT) on a microfluidic platform. It was shown that the VMT model captures tumor cell heterogeneity, vascular disruption, and tumor-microenvironment interactions. By further analyzing the transcript of the VMT and comparing it to standardized xenograft models it was shown that the two models closely resembled each other when compared to 2D cell cultures (157). All these models are promising systems for studying tumors *in vitro* at a detailed level.

vi. Chapter conclusion and perspective

Microfluidic offers many advantages for spheroid culture. It enables generation of homogeneous spheroids in an automatic way; precise control of liquids thus minimizing sample volume; closely resembling the TME; enabling real time visualization using microscopy. All these factors combined makes microfluidics systems attractive in both research purposes as well as in clinical settings. In the future these platforms could be implemented in drug trials as more reliable methods compared so standardized 2D systems. Moreover, using this platform drug screening can be performed in a fast and automatic way. Therefore, we plan to perform further drug screening tests on the MCTSs on chip to determine if we can observe cell-to-cell crosstalk as previously observed in well plate settings (see Chapter 3). In the future, the platform could be integrated with other microfluidic chips for spheroid dissociation and eventually analyzis of cells at a single cell level. It would also be possible to collect the cell medium and analyze its content on separate microfluidic or non-microfluidic platforms. These types of platforms can serve as a useful tool to analyze tumor progression and cell-to-cell interactions in real time.

References

1. Cancer [Internet]. [cited 2022 Aug 10]. Available from: https://www.who.int/news-room/fact-sheets/detail/cancer

2. Shaikh MA, Hussain S, Gilhotra R, Singh SK, Rawat S, Singh Y, et al. Chapter 1 - Introduction to cancer cell biology. In: Dua K, Mehta M, de Jesus Andreoli Pinto T, Pont LG, Williams KA, Rathbone MJ, editors. Advanced Drug Delivery Systems in the Management of Cancer [Internet]. Academic Press; 2021 [cited 2022 Nov 8]. p. 1–7. Available from: https://www.sciencedirect.com/science/article/pii/B9780323855037000134

3. Sever R, Brugge JS. Signal Transduction in Cancer. Cold Spring Harb Perspect Med. 2015 Apr;5(4):a006098.

4. Martínez-Jiménez F, Muiños F, Sentís I, Deu-Pons J, Reyes-Salazar I, Arnedo-Pac C, et al. A compendium of mutational cancer driver genes. Nat Rev Cancer. 2020 Oct;20(10):555–72.

5. Elliott K, Larsson E. Non-coding driver mutations in human cancer. Nat Rev Cancer. 2021 Aug;21(8):500–9.

6. Levine AJ, Jenkins NA, Copeland NG. The Roles of Initiating Truncal Mutations in Human Cancers: The Order of Mutations and Tumor Cell Type Matters. Cancer Cell. 2019 Jan 14;35(1):10–5.

7. Hanahan D, Weinberg RA. The Hallmarks of Cancer. Cell. 2000 Jan 7;100(1):57–70.

8. Hanahan D, Weinberg RA. Hallmarks of Cancer: The Next Generation. Cell. 2011 Mar 4;144(5):646–74.

9. Hanahan D. Hallmarks of Cancer: New Dimensions. Cancer Discov. 2022 Jan 12;12(1):31–46.

10. Guren MG. The global challenge of colorectal cancer. Lancet Gastroenterol Hepatol. 2019 Dec;4(12):894–5.

11. Xi Y, Xu P. Global colorectal cancer burden in 2020 and projections to 2040. Transl Oncol. 2021 Jul 6;14(10):101174.

12. Chen K, Collins G, Wang H, Toh JWT. Pathological Features and Prognostication in Colorectal Cancer. Curr Oncol. 2021 Dec 13;28(6):5356–83.

13. Stoffel EM, Mangu PB, Gruber SB, Hamilton SR, Kalady MF, Lau MWY, et al. Hereditary Colorectal Cancer Syndromes: American Society of Clinical Oncology Clinical Practice Guideline Endorsement of the Familial Risk–Colorectal Cancer: European Society for Medical Oncology Clinical Practice Guidelines. J Clin Oncol. 2015 Jan 10;33(2):209–17.

14. Keum N, Giovannucci E. Global burden of colorectal cancer: emerging trends, risk factors and prevention strategies. Nat Rev Gastroenterol Hepatol. 2019 Dec;16(12):713–32.

15. Neophytou CM, Panagi M, Stylianopoulos T, Papageorgis P. The Role of Tumor Microenvironment in Cancer Metastasis: Molecular Mechanisms and Therapeutic Opportunities. Cancers. 2021 Apr 23;13(9):2053.

16. Je B, K V, Jc R. Targeting Metabolism to Improve the Tumor Microenvironment for Cancer Immunotherapy. Mol Cell [Internet]. 2020 Jun 18 [cited 2022 Nov 9];78(6). Available from: https://pubmed.ncbi.nlm.nih.gov/32559423/

17. Bule P, Aguiar SI, Aires-Da-Silva F, Dias JNR. Chemokine-Directed Tumor Microenvironment Modulation in Cancer Immunotherapy. Int J Mol Sci. 2021 Sep 10;22(18):9804.

18. Varn FS, Wang Y, Mullins DW, Fiering S, Cheng C. Systematic pan-cancer analysis reveals immune cell interactions in the tumor microenvironment. Cancer Res. 2017 Mar 15;77(6):1271–82.

19. Kim HJ, Ji YR, Lee YM. Crosstalk between angiogenesis and immune regulation in the tumor microenvironment. Arch Pharm Res. 2022 Jun 1;45(6):401–16.

20. Buck MD, O'Sullivan D, Pearce EL. T cell metabolism drives immunity. J Exp Med. 2015 Aug 24;212(9):1345–60.

21. Altorki NK, Markowitz GJ, Gao D, Port JL, Saxena A, Stiles B, et al. The lung microenvironment: an important regulator of tumour growth and metastasis. Nat Rev Cancer. 2019 Jan;19(1):9–31.

22. Grivennikov SI, Greten FR, Karin M. Immunity, Inflammation, and Cancer. Cell. 2010 Mar 19;140(6):883–99.

23. Swanton C. Intratumour Heterogeneity: Evolution through Space and Time. Cancer Res. 2012 Oct 1;72(19):4875–82.

24. Burrell RA, McGranahan N, Bartek J, Swanton C. The causes and consequences of genetic heterogeneity in cancer evolution. Nature. 2013 Sep;501(7467):338–45.

25. Liu Y, Chen S, Wang S, Soares F, Fischer M, Meng F, et al. Transcriptional landscape of the human cell cycle. Proc Natl Acad Sci. 2017 Mar 28;114(13):3473–8.

26. Vasan N, Baselga J, Hyman DM. A view on drug resistance in cancer. Nature. 2019 Nov;575(7782):299–309.

27. Guinney J, Dienstmann R, Wang X, de Reyniès A, Schlicker A, Soneson C, et al. The consensus molecular subtypes of colorectal cancer. Nat Med. 2015 Nov;21(11):1350–6.

28. Buikhuisen JY, Torang A, Medema JP. Exploring and modelling colon cancer inter-tumour heterogeneity: opportunities and challenges. Oncogenesis. 2020 Jul 9;9(7):1–15.

29. Song N, Pogue-Geile KL, Gavin PG, Yothers G, Kim SR, Johnson NL, et al. Clinical Outcome From Oxaliplatin Treatment in Stage II/III Colon Cancer According to Intrinsic Subtypes: Secondary Analysis of NSABP C-07/NRG Oncology Randomized Clinical Trial. JAMA Oncol. 2016 Sep 1;2(9):1162–9.

30. Marisa L, Blum Y, Taieb J, Ayadi M, Pilati C, Le Malicot K, et al. Intratumor CMS Heterogeneity Impacts Patient Prognosis in Localized Colon Cancer. Clin Cancer Res. 2021 Sep 1;27(17):4768–80.

31. Lee HO, Hong Y, Etlioglu HE, Cho YB, Pomella V, Van den Bosch B, et al. Lineage-dependent gene expression programs influence the immune landscape of colorectal cancer. Nat Genet. 2020 Jun;52(6):594–603.

32. Dienstmann R, Vermeulen L, Guinney J, Kopetz S, Tejpar S, Tabernero J. Consensus molecular subtypes and the evolution of precision medicine in colorectal cancer. Nat Rev Cancer. 2017 Feb;17(2):79–92.

33. Woolston A, Khan K, Spain G, Barber LJ, Griffiths B, Gonzalez-Exposito R, et al. Genomic and Transcriptomic Determinants of Therapy Resistance and Immune Landscape Evolution during Anti-EGFR Treatment in Colorectal Cancer. Cancer Cell. 2019 Jul 8;36(1):35-50.e9.

34. Fan A, Wang B, Wang X, Nie Y, Fan D, Zhao X, et al. Immunotherapy in colorectal cancer: current achievements and future perspective. Int J Biol Sci. 2021 Sep 3;17(14):3837–49.

35. André T, Meyerhardt J, Iveson T, Sobrero A, Yoshino T, Souglakos I, et al. Effect of duration of adjuvant chemotherapy for patients with stage III colon cancer (IDEA collaboration): final results from a prospective, pooled analysis of six randomised, phase 3 trials. Lancet Oncol. 2020 Dec;21(12):1620–9.

36. Cercek A, Lumish M, Sinopoli J, Weiss J, Shia J, Lamendola-Essel M, et al. PD-1 Blockade in Mismatch Repair–Deficient, Locally Advanced Rectal Cancer. N Engl J Med. 2022 Jun 23;386(25):2363–76.

37. Hanahan D. Rethinking the war on cancer. The Lancet. 2014 Feb 8;383(9916):558–63.

38. Kong DH, Kim MR, Jang JH, Na HJ, Lee S. A Review of Anti-Angiogenic Targets for Monoclonal Antibody Cancer Therapy. Int J Mol Sci. 2017 Aug 17;18(8):1786.

39. GOODMAN LS, WINTROBE MM, DAMESHEK W, GOODMAN MJ, GILMAN A, McLENNAN MT. NITROGEN MUSTARD THERAPY: Use of Methyl-Bis(Beta-Chloroethyl)amine Hydrochloride and Tris(Beta-Chloroethyl)amine Hydrochloride for

Hodgkin's Disease, Lymphosarcoma, Leukemia and Certain Allied and Miscellaneous Disorders. J Am Med Assoc. 1946 Sep 21;132(3):126–32.

40. McGranahan N, Swanton C. Clonal Heterogeneity and Tumor Evolution: Past, Present, and the Future. Cell. 2017 Feb 9;168(4):613–28.

41. Emran TB, Shahriar A, Mahmud AR, Rahman T, Abir MH, Siddiquee MohdFR, et al. Multidrug Resistance in Cancer: Understanding Molecular Mechanisms, Immunoprevention and Therapeutic Approaches. Front Oncol. 2022 Jun 23;12:891652.

42. Walcher L, Kistenmacher AK, Suo H, Kitte R, Dluczek S, Strauß A, et al. Cancer Stem Cells-Origins and Biomarkers: Perspectives for Targeted Personalized Therapies. Front Immunol. 2020;11:1280.

43. Yang L, Shi P, Zhao G, Xu J, Peng W, Zhang J, et al. Targeting cancer stem cell pathways for cancer therapy. Signal Transduct Target Ther. 2020 Feb 7;5(1):1–35.

44. Reddy KB. Stem Cells: Current Status and Therapeutic Implications. Genes. 2020 Nov 20;11(11):1372.

45. Sun T, Zhao Q, Zhang C, Cao L, Song M, Maimela NR, et al. Screening common signaling pathways associated with drug resistance in non-small cell lung cancer via gene expression profile analysis. Cancer Med. 2019 Apr 25;8(6):3059–71.

46. Chen XY, Yang Y, Wang JQ, Wu ZX, Li J, Chen ZS. Overexpression of ABCC1 Confers Drug Resistance to Betulin. Front Oncol. 2021;11:640656.

47. Waldman AD, Fritz JM, Lenardo MJ. A guide to cancer immunotherapy: from T cell basic science to clinical practice. Nat Rev Immunol. 2020 Nov;20(11):651–68.

48. Zhang N, Gao M, Wang Z, Zhang J, Cui W, Li J, et al. Curcumin reverses doxorubicin resistance in colon cancer cells at the metabolic level. J Pharm Biomed Anal. 2021 Jul 15;201:114129.

49. Zoetemelk M, Ramzy GM, Rausch M, Nowak-Sliwinska P. Drug-Drug Interactions of Irinotecan, 5-Fluorouracil, Folinic Acid and Oxaliplatin and Its Activity in Colorectal Carcinoma Treatment. Molecules. 2020 Jun 4;25(11):2614.

50. Suetsugu T, Mori R, Futamura M, Fukada M, Tanaka H, Yasufuku I, et al. Mechanism of acquired 5FU resistance and strategy for overcoming 5FU resistance focusing on 5FU metabolism in colon cancer cell lines. Oncol Rep. 2021 Apr 1;45(4):1–8.

51. Peters GJ, Lankelma J, Kok RM, Noordhuis P, van Groeningen CJ, van der Wilt CL, et al. Prolonged retention of high concentrations of 5-fluorouracil in human and murine tumors as compared with plasma. Cancer Chemother Pharmacol. 1993 Jul 1;31(4):269–76.

52. Kim YI. Role of the *MTHFR* polymorphisms in cancer risk modification and treatment. Future Oncol. 2009 May;5(4):523–42.

53. Sawyers CL. The cancer biomarker problem. Nature. 2008 Apr 3;452(7187):548–52.

54. Karimi P, Shahrokni A, Nezami Ranjbar MR. Implementation of Proteomics for Cancer Research: Past, Present, and Future. Asian Pac J Cancer Prev. 2014;15(6):2433–8.

55. Youssef ASED, Abdel-Fattah MA, Lotfy MM, Nassar A, Abouelhoda M, Touny AO, et al. Multigene Panel Sequencing Reveals Cancer-Specific and Common Somatic Mutations in Colorectal Cancer Patients: An Egyptian Experience. Curr Issues Mol Biol. 2022 Mar 18;44(3):1332–52.

56. Rao MS, Van Vleet TR, Ciurlionis R, Buck WR, Mittelstadt SW, Blomme EAG, et al. Comparison of RNA-Seq and Microarray Gene Expression Platforms for the Toxicogenomic Evaluation of Liver From Short-Term Rat Toxicity Studies. Front Genet. 2018;9:636.

57. Tuna M, Amos CI. Genomic sequencing in cancer. Cancer Lett. 2013 Nov 1;340(2):161–70.

58. Peng X, Chen Z, Farshidfar F, Xu X, Lorenzi PL, Wang Y, et al. Molecular Characterization and Clinical Relevance of Metabolic Expression Subtypes in Human Cancers. Cell Rep. 2018 Apr 3;23(1):255-269.e4.

59. Madden EC, Gorman AM, Logue SE, Samali A. Tumour Cell Secretome in Chemoresistance and Tumour Recurrence. Trends Cancer. 2020 Jun 1;6(6):489–505.

60. Dominiak A, Chełstowska B, Olejarz W, Nowicka G. Communication in the Cancer Microenvironment as a Target for Therapeutic Interventions. Cancers. 2020 May;12(5):1232.

61. Paltridge JL, Belle L, Khew-Goodall Y. The secretome in cancer progression. Biochim Biophys Acta BBA - Proteins Proteomics. 2013 Nov 1;1834(11):2233–41.

62. Boschetti E, D'Amato A, Candiano G, Righetti PG. Protein biomarkers for early detection of diseases: The decisive contribution of combinatorial peptide ligand libraries. J Proteomics. 2018 Sep 30;188:1–14.

63. Johansson HJ, Socciarelli F, Vacanti NM, Haugen MH, Zhu Y, Siavelis I, et al. Breast cancer quantitative proteome and proteogenomic landscape. Nat Commun. 2019 Apr 8;10(1):1600.

64. Zanutto S, Ciniselli CM, Belfiore A, Lecchi M, Masci E, Delconte G, et al. Plasma miRNA-based signatures in CRC screening programs. Int J Cancer. 2020;146(4):1164–73.

65. Verma AM, Patel M, Aslam MI, Jameson J, Pringle JH, Wurm P, et al. Circulating plasma microRNAs as a screening method for detection of colorectal adenomas. The Lancet. 2015 Feb 26;385:S100.

66. Hu J, Cai G, Xu Y, Cai S. The Plasma microRNA miR-1914* and -1915 Suppresses Chemoresistant in Colorectal Cancer Patients by Down-regulating NFIX. Curr Mol Med. 2016 Jan 1;16(1):70–82.

67. Yáñez-Mó M, Siljander PRM, Andreu Z, Bedina Zavec A, Borràs FE, Buzas EI, et al. Biological properties of extracellular vesicles and their physiological functions. J Extracell Vesicles. 2015 Jan 1;4(1):27066.

68. Zaborowski MP, Balaj L, Breakefield XO, Lai CP. Extracellular Vesicles: Composition, Biological Relevance, and Methods of Study. Bioscience. 2015 Aug 1;65(8):783–97.

69. Dang XTT, Kavishka JM, Zhang DX, Pirisinu M, Le MTN. Extracellular Vesicles as an Efficient and Versatile System for Drug Delivery. Cells. 2020 Oct;9(10):2191.

70. Tkach M, Théry C. Communication by Extracellular Vesicles: Where We Are and Where We Need to Go. Cell. 2016 Mar 10;164(6):1226–32.

71. Daly R, O'Driscoll L. Extracellular vesicles in blood: are they viable as diagnostic and predictive tools in breast cancer? Drug Discov Today. 2021 Mar 1;26(3):778–85.

72. Hinestrosa JP, Kurzrock R, Lewis JM, Schork NJ, Schroeder G, Kamat AM, et al. Early-stage multi-cancer detection using an extracellular vesicle protein-based blood test. Commun Med. 2022 Mar 17;2(1):1–9.

73. Sajjad H, Imtiaz S, Noor T, Siddiqui YH, Sajjad A, Zia M. Cancer models in preclinical research: A chronicle review of advancement in effective cancer research. Anim Models Exp Med. 2021 Jun;4(2):87–103.

74. McGurk L, Berson A, Bonini NM. Drosophila as an In Vivo Model for Human Neurodegenerative Disease. Genetics. 2015 Oct;201(2):377–402.

75. MacRae CA, Peterson RT. Zebrafish as tools for drug discovery. Nat Rev Drug Discov. 2015 Oct;14(10):721–31.

76. Goto A, Sakamoto K, Hagiwara-Nagasawa M, Kambayashi R, Chiba K, Nunoi Y, et al. Utilization of the chronic atrioventricular block cynomolgus monkey as an in vivo model to evaluate drug interaction-associated torsade de pointes. J Pharmacol Sci. 2020 Apr;142(4):172–5.

77. Holen I, Speirs V, Morrissey B, Blyth K. In vivo models in breast cancer research: progress, challenges and future directions. Dis Model Mech. 2017 Apr 1;10(4):359–71.

78. Krause P, Flikweert H, Monin M, Seif Amir Hosseini A, Helms G, Cantanhede G, et al. Increased growth of colorectal liver metastasis following partial hepatectomy. Clin Exp Metastasis. 2013 Jun 1;30(5):681–93.

79. Ingber DE. Human organs-on-chips for disease modelling, drug development and personalized medicine. Nat Rev Genet. 2022 Aug;23(8):467–91.

80. Prahallad A, Sun C, Huang S, Di Nicolantonio F, Salazar R, Zecchin D, et al. Unresponsiveness of colon cancer to BRAF(V600E) inhibition through feedback activation of EGFR. Nature. 2012 Mar;483(7387):100–3.

81. Bhimani J, Ball K, Stebbing J. Patient-derived xenograft models—the future of personalised cancer treatment. Br J Cancer. 2020 Mar;122(5):601–2.

82. DeRose YS, Wang G, Lin YC, Bernard PS, Buys SS, Ebbert MTW, et al. Tumor grafts derived from women with breast cancer authentically reflect tumor pathology, growth, metastasis and disease outcomes. Nat Med. 2011 Oct 23;17(11):1514–20.

83. Białkowska K, Komorowski P, Bryszewska M, Miłowska K. Spheroids as a Type of Three-Dimensional Cell Cultures—Examples of Methods of Preparation and the Most Important Application. Int J Mol Sci. 2020 Aug 28;21(17):6225.

84. Bredholt G, Mannelqvist M, Stefansson IM, Birkeland E, Bø TH, Øyan AM, et al. Tumor necrosis is an important hallmark of aggressive endometrial cancer and associates with hypoxia, angiogenesis and inflammation responses. Oncotarget. 2015 Oct 14;6(37):39676–91.

85. Bauleth-Ramos T, Feijão T, Gonçalves A, Shahbazi MA, Liu Z, Barrias C, et al. Colorectal cancer triple co-culture spheroid model to assess the biocompatibility and anticancer properties of polymeric nanoparticles. J Control Release Off J Control Release Soc. 2020 Jul 10;323:398–411.

86. Hwang CM, Sant S, Masaeli M, Kachouie NN, Zamanian B, Lee SH, et al. Fabrication of three-dimensional porous cell-laden hydrogel for tissue engineering. Biofabrication. 2010 Sep;2(3):035003.

87. Hughes CS, Postovit LM, Lajoie GA. Matrigel: A complex protein mixture required for optimal growth of cell culture. PROTEOMICS. 2010;10(9):1886–90.

88. Kang Y, Datta P, Shanmughapriya S, Ozbolat IT. 3D Bioprinting of Tumor Models for Cancer Research. ACS Appl Bio Mater. 2020 Sep 21;3(9):5552–73.

89. Boland T, Xu T, Damon B, Cui X. Application of inkjet printing to tissue engineering. Biotechnol J. 2006;1(9):910–7.

90. Chang CC, Boland ED, Williams SK, Hoying JB. Direct-write bioprinting three-dimensional biohybrid systems for future regenerative therapies. J Biomed Mater Res B Appl Biomater. 2011;98B(1):160–70.

91. Gaebel R, Ma N, Liu J, Guan J, Koch L, Klopsch C, et al. Patterning human stem cells and endothelial cells with laser printing for cardiac regeneration. Biomaterials. 2011 Dec;32(35):9218–30.

92. Gauvin R, Chen YC, Lee JW, Soman P, Zorlutuna P, Nichol JW, et al. Microfabrication of complex porous tissue engineering scaffolds using 3D projection stereolithography. Biomaterials. 2012 May 1;33(15):3824–34.

93. Jose RR, Rodriguez MJ, Dixon TA, Omenetto F, Kaplan DL. Evolution of Bioinks and Additive Manufacturing Technologies for 3D Bioprinting. ACS Biomater Sci Eng. 2016 Oct 10;2(10):1662–78.

94. Han SJ, Kwon S, Kim KS. Challenges of applying multicellular tumor spheroids in preclinical phase. Cancer Cell Int. 2021 Mar 4;21(1):152.

95. Mehta P, Rahman Z, ten Dijke P, Boukany PE. Microfluidics meets 3D cancer cell migration. Trends Cancer. 2022 Aug 1;8(8):683–97.

96. Scott SM, Ali Z. Fabrication Methods for Microfluidic Devices: An Overview. Micromachines. 2021 Mar 18;12(3):319.

97. ten Hoorn S, de Back TR, Sommeijer DW, Vermeulen L. Clinical Value of Consensus Molecular Subtypes in Colorectal Cancer: A Systematic Review and Meta-Analysis. JNCI J Natl Cancer Inst. 2022 Apr 1;114(4):503–16.

98. Sveen A, Bruun J, Eide PW, Eilertsen IA, Ramirez L, Murumägi A, et al. Colorectal Cancer Consensus Molecular Subtypes Translated to Preclinical Models Uncover Potentially Targetable Cancer Cell Dependencies. Clin Cancer Res Off J Am Assoc Cancer Res. 2018 Feb 15;24(4):794–806.

99. Ivanov DP, Grabowska AM. Spheroid arrays for high-throughput single-cell analysis of spatial patterns and biomarker expression in 3D. Sci Rep. 2017 Jan 30;7(1):41160.

100. Karlsson H, Fryknäs M, Larsson R, Nygren P. Loss of cancer drug activity in colon cancer HCT-116 cells during spheroid formation in a new 3-D spheroid cell culture system. Exp Cell Res. 2012 Aug 1;318(13):1577–85.

101. Forder A, Hsing CY, Trejo Vazquez J, Garnis C. Emerging Role of Extracellular Vesicles and Cellular Communication in Metastasis. Cells. 2021 Dec 6;10(12):3429.

102. Leary M, Heerboth S, Lapinska K, Sarkar S. Sensitization of Drug Resistant Cancer Cells: A Matter of Combination Therapy. Cancers. 2018 Dec 4;10(12):483.

103. O'Leary B, Cutts RJ, Liu Y, Hrebien S, Huang X, Fenwick K, et al. The Genetic Landscape and Clonal Evolution of Breast Cancer Resistance to Palbociclib plus Fulvestrant in the PALOMA-3 Trial. Cancer Discov. 2018 Nov 1;8(11):1390–403.

104. Gao X, Aguanno D, Board M, Callaghan R. Exploiting the metabolic energy demands of drug efflux pumps provides a strategy to overcome multidrug

resistance in cancer. Biochim Biophys Acta BBA - Gen Subj. 2021 Aug 1;1865(8):129915.

105. Zhao J, Li M, Xu J, Cheng W. The modulation of ion channels in cancer chemo-resistance. Front Oncol. 2022;12:945896.

106. Zaal EA, Berkers CR. The Influence of Metabolism on Drug Response in Cancer. Front Oncol. 2018 Nov 2;8:500.

107. Obenauf AC, Zou Y, Ji AL, Vanharanta S, Shu W, Shi H, et al. Therapy-induced tumour secretomes promote resistance and tumour progression. Nature. 2015 Apr 16;520(7547):368–72.

108. Skog J, Würdinger T, van Rijn S, Meijer DH, Gainche L, Curry WT, et al. Glioblastoma microvesicles transport RNA and proteins that promote tumour growth and provide diagnostic biomarkers. Nat Cell Biol. 2008 Dec;10(12):1470–6.

109. Kogure A, Yoshioka Y, Ochiya T. Extracellular Vesicles in Cancer Metastasis: Potential as Therapeutic Targets and Materials. Int J Mol Sci. 2020 Jun 23;21(12):4463.

110. Cavallari C, Camussi G, Brizzi MF. Extracellular Vesicles in the Tumour Microenvironment: Eclectic Supervisors. Int J Mol Sci. 2020 Sep 15;21(18):E6768.

111. Becker A, Thakur BK, Weiss JM, Kim HS, Peinado H, Lyden D. Extracellular vesicles in cancer: cell-to-cell mediators of metastasis. Cancer Cell. 2016 Dec 12;30(6):836–48.

112. Whiteside TL. Tumor-derived exosomes and their role in cancer progression. Adv Clin Chem. 2016;74:103–41.

113. Carollo E, Paris B, Samuel P, Pantazi P, Bartelli TF, Dias-Neto E, et al. Detecting ovarian cancer using extracellular vesicles: progress and possibilities. Biochem Soc Trans. 2019 Feb 28;47(1):295–304.

114. Melling GE, Conlon R, Pantazi P, Dellar ER, Samuel P, Baena-Lopez LA, et al. Confocal microscopy analysis reveals that only a small proportion of extracellular vesicles are successfully labelled with commonly utilised staining methods. Sci Rep. 2022 Jan 7;12(1):262.

115. Burki TK. Association between extreme down-regulation of chromosome Y and cancer risk. Lancet Oncol. 2020 Feb 1;21(2):e72.

116. Lin TC. DDX3X Multifunctionally Modulates Tumor Progression and Serves as a Prognostic Indicator to Predict Cancer Outcomes. Int J Mol Sci. 2019 Dec 31;21(1):281.

117. Yang L, Yang T, Wang H, Dou T, Fang X, Shi L, et al. DNMBP-AS1 Regulates NHLRC3 Expression by Sponging miR-93-5p/17-5p to Inhibit Colon Cancer Progression. Front Oncol. 2022;12:765163.

118. Han MZ, Huang B, Chen AJ, Zhang X, Xu R, Wang J, et al. High expression of RAB43 predicts poor prognosis and is associated with epithelial-mesenchymal transition in gliomas. Oncol Rep. 2017 Feb 1;37(2):903–12.

119. Huang Z, Liang H, Chen L. RAB43 Promotes Gastric Cancer Cell Proliferation and Metastasis via Regulating the PI3K/AKT Signaling Pathway. OncoTargets Ther. 2020 Mar 11;13:2193–202.

120. Wang J, Li Y, Wan CM, Gan ZJ, Gan LL, He BC, et al. PTEN inhibition leads to the development of resistance to novel isoquinoline derivative TNBG-5602 in human liver cancer cells. Am J Cancer Res. 2021 Sep 15;11(9):4515–27.

121. Salvatore L, Calegari MA, Loupakis F, Fassan M, Di Stefano B, Bensi M, et al. PTEN in Colorectal Cancer: Shedding Light on Its Role as Predictor and Target. Cancers. 2019 Nov 9;11(11):1765.

122. Chen CY, Chen J, He L, Stiles BL. PTEN: Tumor Suppressor and Metabolic Regulator. Front Endocrinol. 2018 Jul 9;9:338.

123. Gnanapradeepan K, Basu S, Barnoud T, Budina-Kolomets A, Kung CP, Murphy ME. The p53 Tumor Suppressor in the Control of Metabolism and Ferroptosis. Front Endocrinol. 2018 Apr 11;9:124.

124. Lai Q, Li Q, He C, Fang Y, Lin S, Cai J, et al. CTCF promotes colorectal cancer cell proliferation and chemotherapy resistance to 5-FU via the P53-Hedgehog axis. Aging. 2020 Jul 20;12(16):16270–93.

125. van Staveren WCG, Solís DW, Delys L, Venet D, Cappello M, Andry G, et al. Gene expression in human thyrocytes and autonomous adenomas reveals suppression of negative feedbacks in tumorigenesis. Proc Natl Acad Sci U S A. 2006 Jan 10;103(2):413–8.

126. Till JE, Yoon C, Kim BJ, Roby K, Addai P, Jonokuchi E, et al. Oncogenic KRAS and p53 loss drive gastric tumorigenesis in mice that can be attenuated by E-cadherin expression. Cancer Res. 2017 Oct 1;77(19):5349–59.

127. Albonici L, Giganti MG, Modesti A, Manzari V, Bei R. Multifaceted Role of the Placental Growth Factor (PlGF) in the Antitumor Immune Response and Cancer Progression. Int J Mol Sci. 2019 Jan;20(12):2970.

128. Théry C, Amigorena S, Raposo G, Clayton A. Isolation and characterization of exosomes from cell culture supernatants and biological fluids. Curr Protoc Cell Biol. 2006 Apr;Chapter 3:Unit 3.22.

129. Pisco AO, Huang S. Non-genetic cancer cell plasticity and therapy-induced stemness in tumour relapse: 'What does not kill me strengthens me.' Br J Cancer. 2015 May;112(11):1725–32.

130. Qin S, Jiang J, Lu Y, Nice EC, Huang C, Zhang J, et al. Emerging role of tumor cell plasticity in modifying therapeutic response. Signal Transduct Target Ther. 2020 Oct 7;5(1):1–36.

131. Sunkara V, Woo HK, Cho YK. Emerging techniques in the isolation and characterization of extracellular vesicles and their roles in cancer diagnostics and prognostics. Analyst. 2016 Jan 4;141(2):371–81.

132. Cooks T, Pateras IS, Jenkins LM, Patel KM, Robles AI, Morris J, et al. Mutant p53 cancers reprogram macrophages to tumor supporting macrophages via exosomal miR-1246. Nat Commun. 2018 Feb 22;9(1):771.

133. Terry SC, Jerman JH, Angell JB. A gas chromatographic air analyzer fabricated on a silicon wafer. IEEE Trans Electron Devices. 1979 Dec;26(12):1880–6.

134. Manz A, Graber N, Widmer HM. Miniaturized total chemical analysis systems: A novel concept for chemical sensing. Sens Actuators B Chem. 1990 Jan 1;1(1):244–8.

135. Whitesides GM. The origins and the future of microfluidics. Nature. 2006 Jul;442(7101):368–73.

136. Regmi S, Poudel C, Adhikari R, Luo KQ. Applications of Microfluidics and Organ-on-a-Chip in Cancer Research. Biosensors. 2022 Jun 27;12(7):459.

137. Leung CM, de Haan P, Ronaldson-Bouchard K, Kim GA, Ko J, Rho HS, et al. A guide to the organ-on-a-chip. Nat Rev Methods Primer. 2022 May 12;2(1):1–29.

138. Azizipour N, Avazpour R, Rosenzweig DH, Sawan M, Ajji A. Evolution of Biochip Technology: A Review from Lab-on-a-Chip to Organ-on-a-Chip. Micromachines. 2020 Jun 18;11(6):599.

139. Kuo CT, Chiang CL, Yun-Ju Huang R, Lee H, Wo AM. Configurable 2D and 3D spheroid tissue cultures on bioengineered surfaces with acquisition of epithelial–mesenchymal transition characteristics. NPG Asia Mater. 2012 Sep;4(9):e27–e27.

140. Liu W, Wang JC, Wang J. Controllable organization and high throughput production of recoverable 3D tumors using pneumatic microfluidics. Lab Chip. 2015 Feb 3;15(4):1195–204.

141. Cai H, Wu Z, Ao Z, Nunez A, Chen B, Jiang L, et al. Trapping cell spheroids and organoids using digital acoustofluidics. Biofabrication. 2020 Jul;12(3):035025.

142. Lee JM, Choi JW, Ahrberg CD, Choi HW, Ha JH, Mun SG, et al. Generation of tumor spheroids using a droplet-based microfluidic device for photothermal therapy. Microsyst Nanoeng. 2020 Jun 29;6(1):1–10.

143. Sart S, Tomasi RFX, Amselem G, Baroud CN. Multiscale cytometry and regulation of 3D cell cultures on a chip. Nat Commun. 2017 Sep 7;8(1):469.

144. Tomasi RFX, Sart S, Champetier T, Baroud CN. Individual Control and Quantification of 3D Spheroids in a High-Density Microfluidic Droplet Array. Cell Rep. 2020 May 26;31(8):107670.

145. Liu D, Sun M, Zhang J, Hu R, Fu W, Xuanyuan T, et al. Single-cell droplet microfluidics for biomedical applications. Analyst. 2022 May 30;147(11):2294–316.

146. Garstecki P, J. Fuerstman M, A. Stone H, M. Whitesides G. Formation of droplets and bubbles in a microfluidic T-junction—scaling and mechanism of break-up. Lab Chip. 2006;6(3):437–46.

147. Baret JC, Miller OJ, Taly V, Ryckelynck M, El-Harrak A, Frenz L, et al. Fluorescence-activated droplet sorting (FADS): efficient microfluidic cell sorting based on enzymatic activity. Lab Chip. 2009 Jul 7;9(13):1850–8.

148. Link DR, Anna SL, Weitz DA, Stone HA. Geometrically Mediated Breakup of Drops in Microfluidic Devices. Phys Rev Lett. 2004 Feb 6;92(5):054503.

149. Priest C, Herminghaus S, Seemann R. Controlled electrocoalescence in microfluidics: Targeting a single lamella. Appl Phys Lett. 2006 Sep 25;89(13):134101.

150. Abate AR, Hung T, Mary P, Agresti JJ, Weitz DA. High-throughput injection with microfluidics using picoinjectors. Proc Natl Acad Sci U S A. 2010 Nov 9;107(45):19163–6.

151. Theberge AB, Courtois F, Schaerli Y, Fischlechner M, Abell C, Hollfelder F, et al. Mikrotröpfchen in Mikrofluidiksystemen: eine Technik für Entdeckungen in der Chemie und Biologie. Angew Chem. 2010;122(34):5982–6005.

152. Brüningk SC, Rivens I, Box C, Oelfke U, ter Haar G. 3D tumour spheroids for the prediction of the effects of radiation and hyperthermia treatments. Sci Rep. 2020 Feb 3;10(1):1653.

153. Chung M, Ahn J, Son K, Kim S, Jeon NL. Biomimetic Model of Tumor Microenvironment on Microfluidic Platform. Adv Healthc Mater. 2017;6(15):1700196.

154. Jeong SY, Lee JH, Shin Y, Chung S, Kuh HJ. Co-Culture of Tumor Spheroids and Fibroblasts in a Collagen Matrix-Incorporated Microfluidic Chip Mimics Reciprocal Activation in Solid Tumor Microenvironment. PLOS ONE. 2016 Jul 8;11(7):e0159013.

155. Bi Y, Shirure VS, Liu R, Cunningham C, Ding L, Meacham JM, et al. Tumor-on-a-chip platform to interrogate the role of macrophages in tumor progression. Integr Biol. 2020 Sep 30;12(9):221–32.

156. Strelez C, Chilakala S, Ghaffarian K, Lau R, Spiller E, Ung N, et al. Human colorectal cancer-on-chip model to study the microenvironmental influence on early metastatic spread. iScience. 2021 May 21;24(5):102509.

157. Hachey SJ, Movsesyan S, Nguyen QH, Burton-Sojo G, Tankazyan A, Wu J, et al. An in vitro vascularized micro-tumor model of human colorectal cancer recapitulates in vivo responses to standard-of-care therapy. Lab Chip. 2021 Apr 8;21(7):1333–51.

Lab on a Chip

PERSPECTIVE

View Article Online
View Journal | View Issue

Check for updates

Cite this: *Lab Chip*, 2022, **22**, 2403

Frontiers in single cell analysis: multimodal technologies and their clinical perspectives

Julia Källberg,[a] Wenjin Xiao,[a] David Van Assche,[b] Jean-Christophe Baret *[bc] and Valerie Taly *[a]

Single cell multimodal analysis is at the frontier of single cell research: it defines the roles and functions of distinct cell types through simultaneous analysis to provide unprecedented insight into cellular processes. Current single cell approaches are rapidly moving toward multimodal characterizations. It replaces one-dimensional single cell analysis, for example by allowing for simultaneous measurement of transcription and post-transcriptional regulation, epigenetic modifications and/or surface protein expression. By providing deeper insights into single cell processes, multimodal single cell analyses paves the way to new understandings in various cellular processes such as cell fate decisions, physiological heterogeneity or genotype–phenotype linkages. At the forefront of this, microfluidics is key for high-throughput single cell analysis. Here, we present an overview of the recent multimodal microfluidic platforms having a potential in biomedical research, with a specific focus on their potential clinical applications.

Received 8th March 2022,
Accepted 31st May 2022

DOI: 10.1039/d2lc00220e

rsc.li/loc

1. Introduction

Untangling the complexity of cellular processes is a major challenge in biomedical research. This quest is fed by the technological development that have enabled analysis at the single cell level in fields including genomics,[1–3] epigenomics,[4] transcriptomics,[5] metabolomics[6] and proteomics.[7,8] Collectively, these assays are capable of analysing all the major stages in the central dogma of molecular biology, from DNA and RNA sequencing to protein detection, thereby providing detailed insights into cellular processes. Over the past decade, further technical advances have allowed for the simultaneous measurement of multiple cellular parameters at the single cell level. Multimodal single cell analysis (MSCA) paves the way to gaining deep insights into cell heterogeneity to discover of new sub-categories of cells.[9] Such analysis supports mechanistic understanding of genotype–phenotype relationships through a detailed descriptions of cell fitness and intermediate cell phenotypes.[10] Large cellular atlases displaying cell lineage trajectories and molecular changes could thus be generated.

Microfluidics has recently been shown to be particularly promising as a technical platform for MSCA. Beyond the ability to miniaturize conventional assays, microfluidics offers advantages of precise automated liquid handling and high throughput capability. It is compatible with a diverse set of analytical measuring systems including fluorescence microscopy,[11] imaging,[12] Raman spectroscopy,[13] chromatography and mass spectrometry.[14] All these aspects are highly important for analysis of small sample volumes, handling scarce samples and achieving the necessary precision associated with such single cell measurements. Flow cytometry has long been considered the "gold standard" for cell-based analysis. Despite its widespread use, flow cytometry has several limitations, mainly its ability to measure only cellular proteins and the requirement for a relatively large starting number of cells.[15] Therefore, the development of new microfluidic technologies is a crucial endeavor with great possibility to unlock the potential of MSCA.

In this review, we focus on the recent progress of microfluidics for MSCA, which represents the ability to simultaneously measure multiple parameters in one experiment. The examples discussed relate to the analysis of genotype–phenotype relationships, the development of chemotherapy resistance in cancer therapies, and cell heterogeneity in oncology, immunology and neurology. A specific focus is placed on the potential clinical applications of the technologies (Fig. 1) and potential technological developments.

[a] *Centre de Recherche des Cordeliers, INSERM, CNRS, Université Paris Cité, Sorbonne Université, USPC, Equipe labellisée Ligue Nationale contre le cancer, Paris, France. E-mail: valerie.taly@parisdescartes.fr*
[b] *University of Bordeaux, CNRS, Centre de Recherche Paul Pascal, UMR 5031, Pessac 33600, France. E-mail: jean-christophe.baret@u-bordeaux.fr*
[c] *Institut Universitaire de France, Paris 75005, France*

2. Key strategies in multimodal analysis

Several key aspects should be considered when performing MSCA. In this section, we provide a short overview of

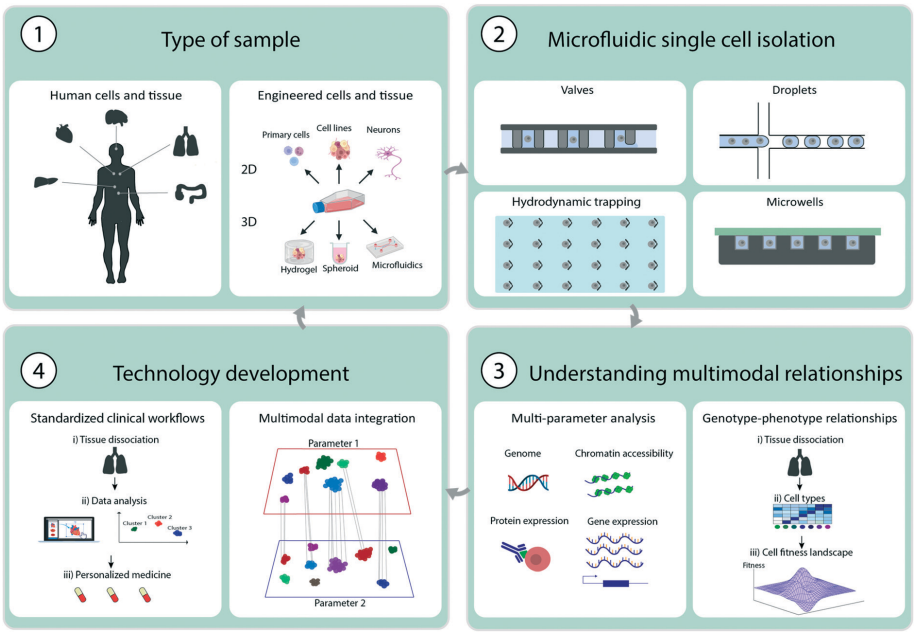

Fig. 1 Illustration of multimodal single cell analysis methodology and technical advancements. 1. Illustration of sample types derived from primary tissue cells or engineered cells or tissues. 2. Different microfluidic single cell isolation techniques using valves, droplets, hydrodynamic trapping or microwells. 3. Understanding multimodal relationships by measure multiple single cell parameters for example genome, chromatin accessibility, protein or gene expression and understand genotype-phenotype relationships 4. Technological development by standardizing clinical workflows and data integration of multiple parameters to understand multimodal relationships.

experimental methods specifically designed for MSCA starting from sample preparation to microfluidic single cell isolation and manipulation techniques. We also provide an overview of strategies for multimodal analysis and commercial microfluidic platforms that are suitable for this analysis.

2.1 Sample preparation

Sample preparation is the first step of MSCA. Depending on the sample type and analytical method the preparation varies greatly. Enrichment of certain cell types may be necessary before the analysis: blood samples may need non-relevant cell types to be removed through density gradient separation or enrichment of the cells of interest with magnetic beads coupled to antibodies.[15]

For tissue samples, a key step is tissue dissociation. Primary aspects to consider include ensuring a homogeneous cell solution while maintaining high cell viability. Dissociation protocols must generally be optimized for each tissue type, because the composition of the extracellular matrix can substantially vary. Some cell types are sensitive to harsh dissociation protocols, and therefore gentle dissociation is required to maintain an accurate representation of the whole cell population. Furthermore, sample handling should be rapid, to avoid unwanted transcriptomic changes or overexpression of stress-response-related genes.[16] Performing pertinent quality control at the bulk level is therefore highly recommended to ensure high quality of the samples for subsequent single cell analysis.[17]

Another concern is the presence of non-viable cells in the cell solution and leaching of cell components into the solution, which may result in compartmentalization of non-relevant cellular content together with single cells. To overcome these challenges, computational methods have recently been used to account for such biases, with a focus on transcriptomic analysis.[18]

2.2 Microfluidic single cell isolation

Several microfluidic approaches for single cell isolation have been developed in recent years. Because these techniques have been extensively reviewed elsewhere,[19,20] they are summarized in Table 1, and only a brief overview is presented here.

First, one approach relies on valve-based systems, as introduced by S. Quake and colleagues,[21,22] who developed pressure controlled valves in a multilayer microfluidic

Table 1 Comparison of different microfluidic single cell isolation techniques illustrating valves, microwells, droplets or hydrodynamic trapping

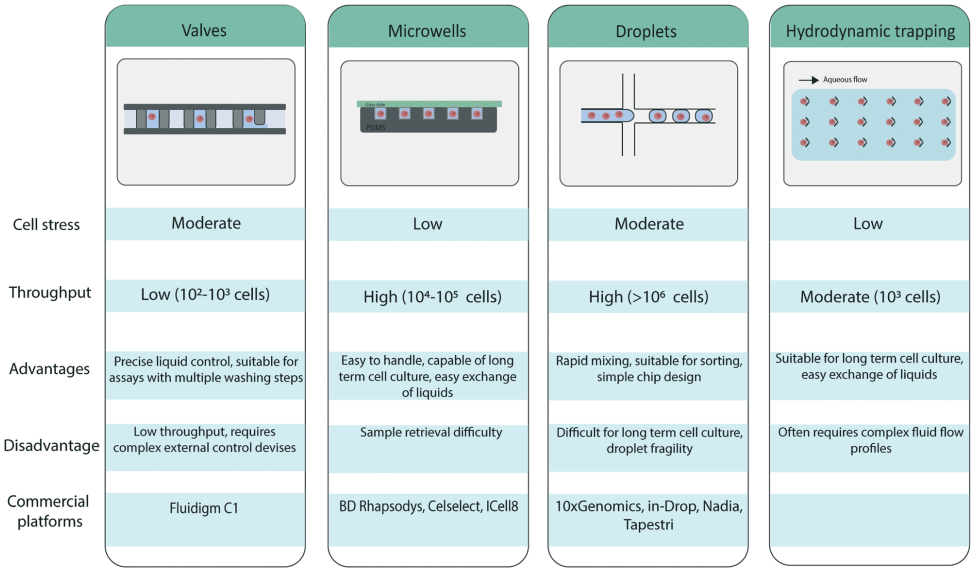

channel to control and direct the flow. The valves create a chamber allowing for single cell isolation and precise control of reagent flow. Because of the high control over the pressure system, these units can be parallelized and can enable a fully integrated workflow. However, these systems tend to be fairly complex in fabrication and design.

Second, well-based systems rely on microwells for single cell isolation. Microwells are loaded with cells through cell sedimentation when a cell suspension is flowed through the device.[23] The actual number of cells seeded in a microwell array is generally Poisson distributed. The Poisson statistics holds true as long as the assumption remains valid that the spatial position of a cell is not affected by other cells, *i.e.*, cells are distributed in the initial sample with a uniform distribution. A low density cell suspension is used to ensure that one cell is present per well. The wells can be subsequently sealed for cell compartmentalization. This method enables high-throughput analysis and is attractive because of its simplicity,[24] but it does not support complex workflows.

A third approach for single cell isolation relates to the field of droplet-based microfluidics. Using droplet-based microfluidics, nL to fL aqueous droplets can be generated in an inert oil phase[25] with high throughput and reproducible sizes. Through emulsification of a cell suspension, droplets are loaded with single cells. Similarly to microcompartment based approaches, such single cell encapsulation/isolation is achieved by using low cell density suspensions so that most droplets contain at most one cell following Poisson distribution.[26] Each droplet serves as a compartment for the analysis of a single cell, because the oil phase serves as a physical barrier and limits cross-contamination between droplets. Perfluorinated oils are usually used as continuous phase to create droplets for biological applications, because they have two interesting properties: (i) the solubility of organic molecules in these oils is considered low, thus restricting leakage of the droplet contents and restricting cross-talk between droplets,[27] and (ii) the high solubility of respiratory gasses in perfluorinated oils which ensure cell survival in droplets.[28] The use of perfluorinated oils has resulted in the commercial development of several fluorinated surfactants that allows for efficient droplet stabilization. Specific efforts have also be placed on ensuring biocompatibility of these compounds.[29] Furthermore, after droplets are formed, the droplet content can be manipulated by injection of another aqueous phase in the droplet through picoinjection[30] or droplet merging,[31] or the droplet can be divided into smaller subunits with droplet splitting.[32] Once the droplet is generated they can be sorted based on fluorescence.[33] Advantages of such approaches thus rely both on its high throughput but also on the flexibility of operations that is given, permitting the efficient implementation of complex and multi-step workflows.

The approaches that have been introduced above compartmentalize single cells. In contrast, microfluidic cell trapping does not establish a physical barrier between single

cells. Trapping-based systems form arrays of trapped cells in a microfluidic device when a cell suspension is flowed through the device. Individual cells have been passively trapped by means of a microfabricated physical geometry.[34]

However, in recent years, further integration of microfluidic devices has given rise to non-contact methods for active trapping of single cells. These methods rely on a physical contrast (*e.g.*, permittivity, refraction index, density and compressibility) between the cells and their suspension medium. Trapping based on dielectrophoresis[35] or optical methods[36] has been developed. Both methods rely on the dielectric properties of the cell to generate a force, which holds the cell in place. For dielectrophoresis this is usually done by designing microelectrodes, while optical trapping relies on a highly focused laser beam with a steep intensity gradient. Furthermore, Collins *et al.* have illustrated the trapping of an array of single cells in acoustic traps.[37] Through the use of standing surface acoustic waves, single cells can be trapped in pressure nodes and individually visualized.

2.3 Microfluidic single cell manipulation

After single cells are isolated, the cells are then incubated to enable long-term cell culture. Incubation in traps or wells is relatively straightforward, because these flow-through systems enable exchange of the medium and metabolites. However, cell incubation in droplets may be constrained by the limited amount of nutrients that the drop contains and the limited accessibility to oxygen. To circumvent these issues cells can instead be encapsulated in large droplets providing sufficient nutrients for long term cell culture[38,39] or cultured in hydrogel droplets allowing for easy exchange of medium.[40] Another aspect to consider is that dynamic droplet incubation may be required to provide homogeneous oxygen accessibility.[41]

Another critical step in multiomic cell analysis is cell lysis, because it is essential for efficient extraction and analysis of intracellular material. Lysis should not interfere with the rest of the microfluidic workflow, to ensure the pertinence of subsequent analysis. Most lysis methods have been developed for bulk suspensions. Therefore, transitioning these methods to microfluidic workflows might need adjustment and new methods dedicated to microfluidic single cell assays should also probably be developed. Most microfluidic platforms use chemical lysis, which can easily be integrated in microfluidic systems. Other options include electrical lysis[42,43] or optical lysis.[44] For chemical lysis, lytic agents can be added by controlling the microfluidic valves, or by flowing of the lytic agents through well-based systems. When droplets are used, the lytic agents can be encapsulated the cell when drops are produced, or afterward through droplet fusion or picoinjection.[30] However, chemical cell lysis in trapping-based systems is more challenging. In general, extensive cell analysis, apart from microscopy, is challenging in trapped cells, because the traps do not provide a physical barrier against the diffusion of intracellular components. Marie *et al.* have, however, recently described the extraction of genetic information from single cells with hydrodynamic trapping in a narrow channel. Once the cell is trapped, the flow through the narrow channel is decreased to avoid inflow of other cells in the same channel and a chemical lysis agent is flushed to the cell. Each individual cell lysate is then extracted, with a parallelisation capability limited to 8 cells.[45]

2.4 Strategies for multimodal analysis

Most MSCA strategies have focused on either the combination of two omic methods or combining omic analysis and microscopy. The difficulty in combining omic analysis and microscopy relies on the efficient link of both measurements. By linking omic analysis with phenotypic analysis, such as cell shape, that can be observed in microscopy it is possible to highlight new genotype–phenotype relationships that has yet to be discovered. By barcoding cells with unique nucleic acid sequences different omic measurements can be analysed separately and linked together. Typically, cell imaging is performed first, and then a barcoded primer or bead is added to the cell, which can be identified during sequencing. The microfluidic chip can be prepared with different barcoded primers or oligonucleotides beforehand, so that sequencing can be associated with spatial coordinates on the microfluidic chip.[46–48] Alternatively, in microwells, oligonucleotide barcodes can be added after single cell imaging, and the sequence of the barcodes can then be optically decoded through several rounds of fluorescent hybridization.[49]

A critical challenge in single cell omic analysis is performing high sensitivity analysis, given that single cells contain small amounts of protein and genomic material.[50] Analysis is particularly challenging with MSCA, because preserving all information within a single cell is essential when more than one cellular parameter is detected. Common problems addressed include sample loss,[51] incompatibility of protocols leading to molecular degradation,[52] or insufficient sensitivity of available methods to ensure accurate detection of the analytes.

To circumvent these issues two main approaches have been considered to perform multiomic analysis. In the first approach, a single cells are split in two, and separate analyses are performed on each aliquot.[53] Droplet splitting in droplet-based microfluidics[54] and the operation of valve-based systems are two microfluidic methods enabling such analysis. Before splitting the sample, a pre-amplification of the analytes can be performed when the sample remains intact, to improve the sensitivity of analyses for genetic measurements.[55]

The second approach is based on simultaneous detection of the analytes to link the cell parameters. This process generally uses beads that bind the different targeted analytes.[56] A molecular barcode on the bead tags cellular material, thereby enabling the clustering of data originating

from the same single cell after analysis in bulk. This method does not require any washing steps or removal of liquids, thus limiting the risk of sample loss. Efficient co-compartmentalization of single cells and beads is essential in this approach. As described previously, in droplet microfluidics, the compartmentalization process follows a Poisson distribution, because the sample is sufficiently diluted to avoid multiple cells or beads per compartment, thereby resulting in only a small fraction of the droplets containing both analytes, because the two loading processes are independent.[25,55] Such issues could dramatically reduce experimental throughput. However it can be circumvented by different means such as close packing when deformable beads are encapsulated,[57] loading the sample by inertial ordering of the particles at high flow velocity[38] or hydrodynamic trapping of particles before droplet production.[39]

2.5 Commercial microfluidic platforms for single cell analysis

Commercial microfluidic platforms are an essential part of medical research and are available in clinical research settings (Table 2). Platforms available to date include the Fluidigm C1 (Fluidigm), Rhapsody platform (BD Biosciences), Chromium single cell platform (10× Genomics) and the Tapestri system (Mission Bio). The specific performances of these platforms for single cell isolation, throughput and cell parameters are compared in the following section.

The fluidigm C1 Single-Cell Auto Prep system entered the market in 2013 and has since been applied in various single-cell omic studies. Fluidigm subsequently released another workflow called C1 REAP-seq, which is specifically designed for multiomic analysis of scRNA-seq and surface markers.[58,59] The platform uses a valve-based system to execute a complex workflow. It uses a reservoir to capture, image, and perform cell lysis, reverse transcription and initial PCR reactions. The throughput of the platform is approximately 100 cells per run, thereby limiting the application scope of the workflow to low throughput analysis.[60]

The BD Rhapsody platform uses microwells. By pairing one cell with a barcoded bead in the well, scRNA-seq analysis can be combined with protein expression to achieve a throughput as high as 20 000 cells per experiment. The transparent microfluidic chip enables visualization and imaging during the workflow.

The 10× chromium single cell platform has been widely used for scRNA-seq experiments. This droplet-based platform encapsulates a cell and barcoded bead in a droplet and can achieve a throughput of approximately 10 000 cells per run. This platform has been used primarily for scRNA-seq analysis but now also offers a solution for measuring transcriptome and open chromatin regions with chromium single cell multiome ATAC.

Similarly, the Tapestri system (Mission Bio) uses droplet-based microfluidics to co-encapsulate cells and barcoded beads. The platform works by performing cell lysis, protease digestion, cell barcoding and targeted amplification with multiplex PCR within the droplets. scDNA-seq can be combined with surface protein detection with this platform.[61] Information on copy number variations and single nucleotide variants can also be obtained.

3. Single cell multiomic analysis using microfluidics

Since the initial single cell transcriptomic study in 2009, many single cell RNA sequencing (scRNA-Seq) technologies have been developed.[62] The throughput capability has significantly grown, and analysis of 2 million single cells has recently been reported.[63] Transcriptomic analyses have paved the way to revealing cell heterogeneity, and unraveling previously unknown cell types and states in complex biological samples.[64] scRNA-Seq assays have now been commercialized and are widely available.[65] In combination with other molecular characterizations, scRNA-seq has been included in most single cell multiomics studies. Such measurements can provide data whose value exceeds that of the sum of its parts, particularly in revealing cell functions, discovering relationships across different omics and

Table 2 Comparison of commercial microfluidic platforms performing single cell multimodal analysis

Name	Company	Parameter 1	Parameter 2	Cell isolation method	Advantages	Disadvantages	Throughput (per run)
BD rhapsody	BD biosciences	Transcriptomics	Surface proteins	Nano/micro wells	Easy data management and visualization, customize panels	Requires fresh sample, high starting number of cells needed	20 000 cells
C1 REAP-seq	Fluidigm	Transcriptomics	Surface proteins	Valve-based system	Multiple applications, flexible use, well established platform	Limited throughput	96 cells
Chromium platform	10× genomics	Transcriptomics	Surface proteins/chromatin accessibility	Droplets	High throughput, flexible use	Requires fresh sample, high starting number of cells needed	>10 000 cells
Tapestri	Mission bio	Genomics	Surface proteins	Droplets	Capable of DNA-sequencing, customize panels	High starting number of cells needed	~5000 cells

Table 3 Summary of multiomic single cell analysis technologies using microfluidic platforms

Parameter 1	Parameter 2	Method	Microfluidic platform	Biological model	Throughput (number of cells)	Max, number of analytes (per run)	Applications	Ref.
Chromatin accessibility	Transcriptomics	ASTAR-Seq	Fluidigm C1 microfluidic chip	K562, JK1, BJ, and Jurkat human cell lines, mESCs, primary cord blood cells	96	K562: 142886 chromatin accessibility sites and 4182 transcripts	Identification of cell states and upstream regulatory networks	58
Chromatin accessibility	Transcriptomics	SNARE-seq	10× chromium droplet platform	Mixtures of BJ, H1 hESC, K562 and GM12878 human cell lines, neonatal and adult mouse cerebral cortex	~10 000	1332 of transcripts and 2583 chromatin accessibility sites	Identification of cell types, discovery of lineage-specific accessible sites, and connection of the dynamics of promoter accessibility with transcription level during neurogenesis	56
Chromatin accessibility	CRISPR perturbations	Perturb-ATAC	Fluidigm C1 microfluidic chip	Human B lymphocytes GM12878 cells and primary human keratinocytes	96		Analysing the role of different chromatin regultory factors to get insights in cell fate decisions	68
Genomics	Transcriptomics		Valve based microfluidics	Human myelogenous leukemia cell line K562	3	14 transcripts and 12 DNA target sequences	Investigate the gene expression patterns and genomic alterations	53
Genomics	Transcriptomics		Hydrodynamic trapping	Mouse lymphocyte cell line A20	100		Simulatinious quantification of absolute amount of RNA and relative quantification of DNA	43
Genomics	Transcriptomics		Hydrodynamic trapping	Mouse lymphocyte cell line A20	12 cells per hour		On chip single cell lysing, extraction, fractionation, and recovery of purified cytoplasmic RNA *versus* gDNA	69
Nuclear RNA	Cytoplasmic RNA	SINC-seq	Hydrodynamic trapping	Human myelogenous leukemia cell line K562	12 cells per hour	6200 and 5600 genes per cytRNA and nucRNA	Detection of nuclear RNA and cytoplasmic RNA from single cells to analyse their correlation	70
Gene expression	DNA methylation	sc-GEM	Fluidigm C1 microfluidic chip	Human BJ cells, iPSCs, ESCs and lung adenocarcinoma NSCLC sample	96	50 methylated gene sites	Assessment of primary lung adenocarcinomas and human fibroblasts reprogramming	59
Enzymatic activities	Transcriptomics	sc-haircut	10× chromium droplet platform	PBMCs, haploid human UNG^{ko} and $RNASEH2C^{ko}$ cells	1000–10 000		Identification of cell-type-specific DNA repair phenotypes in human lymphocytes	71
Targeted genomic regions	Transcriptomics	CORTAD-seq	Fluidigm C1 microfluidic chip	Lung cancer cell line PC9	96	6000 transcripts, EGFR exons 19, 20, and 21	Study on lung cancer resistance to a targeted therapy	72

Table 3 *(continued)*

Parameter 1	Parameter 2	Method	Microfluidic platform	Biological model	Throughput (number of cells)	Max, number of analytes (per run)	Applications	Ref.
Surface proteins	Transcriptomics	REAP-seq	10× chromium droplet platform	PBMCs	1000–10 000	82 surface proteins and >20 000 RNA transcripts	Assessment of immune response modulation, identification of unknown cell types	73
Surface proteins	Transcriptomics	CITE-seq	Drop-seq platform, 10× genomics droplet platform	Human HeLa cells, mouse 4 T1 cells, PMBCs, and CBMCs	1000–10 000	13 surface proteins and 400 RNA transcripts	Integrated measurment of scRNA-seq along with surface proteins	74
TCRs, surface proteins, sample identity by hashtags, and sgRNAs	Transcriptomics	ECCITE-seq	10× chromium droplet platform	A cell mixture of human PBMCs, T-cell lymphoma lines MyLa and Sez4, and mouse NIH-3 T3, PBMCs	1000–10 000	49 surface proteins, ~5000 ECCITE-seq genes, ~4000 10× standard run, two TCRs (TCR α/β and TCR γ/δ), 7 hashing antibodies, CRISPR turbilations and 10 sgRNAs	Multimodal CRISPR screens, clonotype-aware phenotyping of cancer samples	76
Surface proteins	Transcriptomics	One-SENSE	Nanowell-based, BD rhapsody platform	PBMCs	>20 000 cells	>40 surface proteins and >400 transcripts	Identification of T cell subsets	77
Surface proteins	Transcriptomics	CITE-seq	10× chromium droplet platform	BMMCs and PBMCs from healthy and from patients with mixed-phenotype acute leukemia (MPAL)	~10 000	2370 transcripts and 4 surface protein markers	Investigation of molecular features of MPAL from normal development	78
Intracellular proteins	Transcriptomics		Valve-based microfluidics	HEK and U87MG human cell lines	9 cells	~2000 RNA transcripts and 3 proteins	Identification of cell type specific signatures	80
Cytokines	Transcriptomics		Nanowells-based splitable microchip	Mouse macrophage cells	20	5 cytokines and ~4900 genes	Study on inflammatory immune responses	81
Protein	Transcriptomics		FACS and microfluidic devices	Patient-derived glioblastoma cell line U3035MG	210 cells	~96 proteins and transcripts	Study on the effect of therapeutic agent BMP4 in glioblastoma	83
Intracellular proteins	Transcriptomics		Fluidigm C1 microfluidic chip	MCF7 human cell line	96	38 intracellular proteins and 96 transcripts	Study on the responses of breast adenocarcinoma to a chemical perturbation	84
Protein	Transcriptomics		Fluidigm C1 microfluidic chip	A549, SKBR3 and K562 human cell lines	96	84 protein assays and 40 transcripts	A comparison of mRNA and protein levels in single nanoliter reactions	85

recording dynamic biological events. The multiomic single cell platforms available to date are introduced in the following sections and are compared in terms of throughput, analysis sensitivity and ability to detect multiple analytes (Table 3).

3.1 Combining transcriptomic and chromatin accessibility analysis

Many single cell assays are currently available to access open chromatin regions and subsequently reveal information on

regulatory genes and gene activities. Most assays rely on enzyme-mediated modulation of chromatin, thus resulting in different degrees of openness to the chromatin landscape. Assay for transposase-accessible chromatin using sequencing (ATAC-seq) was developed to access open chromatin regions in single cells with the enzyme Tn5 transposase.[66] Several studies have recently expanded on this analysis. Cao *et al.* have performed simultaneous profiling of RNA transcripts and accessible chromatin regions in the adult mouse kidney, and demonstrated the potential of this method by showing the transcriptional state of cells which gave new insights into the upstream regulatory landscape.[67] Cell mixing experiments in combined murine and human cells have revealed that 99% of cells can be distinguished in terms of both scRNA-seq and sc-ATAC-seq profiles.

Another example of using ATAC-seq in combination with other cell parameters is a method called assay for single-cell transcriptome and accessibility regions (ASTAR-Seq) which

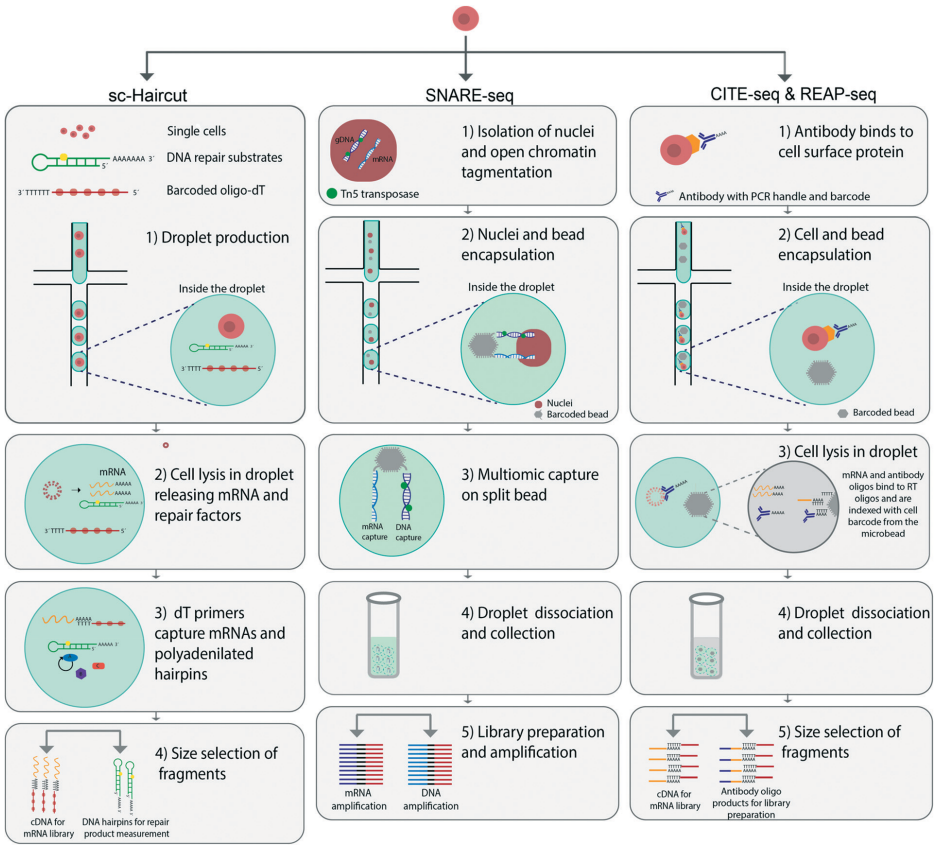

Fig. 2 Comparison of different droplet microfluidic methods for MSCA analysis. The illustration comprises an overview of the workflow of Sc-haircut, SNARE-seq and CITE-seq/REAP-seq. Sc-haircut (left panel) performs parallel analysis of single cell DNA repair mechanisms and gene expression. 1) Droplet production and compartmentalisation of single cells, DNA repair substrates and barcoded oligo-DTs. 2) In drop cell lysis to release mRNA and repair factors. 3) dT primers bind to mRNA and polyadenylated hairpins. 4) Repair products and mRNAs are converted to cDNA with barcoded oligo-dT primers and separated based on size to prepare for library preparation. SNARE-seq (middle panel) 1) isolation of nuclei and DNA tagmentation using the enzyme Tn5 transposase to access the open chromatin regions 2) co-encapsulation of nuclei and beads 3) the split bead binds to both mRNA and DNA linking both modalities together. 4) Droplets are collected and merged, the beads can be harvested and washed 5) library preparation by PCR amplification of mRNA and DNA. CITE-seq /REAP-seq workflow (right panel): 1) preparing antibody-derived tags (ADTs) by oligonucleotide antibody binding to surface proteins on cells in bulk. 2) Co-compartmentalisation of single cells and barcoded beads in droplets using drop-seq 10× Genomics. 3) Cell lysis in droplets to release bound ADTs and mRNA. ADTs and mRNA are thereafter converted to cDNA and amplified using PCR. 4) Droplets are collected and merged 5) PCR for fragment amplification whereby fragments are separated by size.

labels open chromatin regions and performs reverse transcription of mRNA with the valve based fluidigm C1 platform. With this method, human B lymphocyte differentiation from umbilical cord blood has been analysed. By harvesting and analysing single cells at different time points of *in vitro* cell culturing, the authors have observed a correlation with time and cell differentiation were cells transition into a more mature cell state wherein they begin to express *HBA2*, a hemoglobin gene.[58] Another droplet microfluidic platform allows for characterization of single-nucleus chromatin accessibility and mRNA expression sequencing (SNARE-seq) linking a cell's transcriptome with its accessible chromatin regions. In this method, ATAC-seq is used to analyse open chromatin regions, and RNA-seq is used for mRNA detection. Beads and nuclei are co-compartmentalized in droplets. The oligonucleotide split beads enable hybridization of DNA and mRNA to the same bead, thus linking the two parameters[56] (Fig. 2). This method has provided new insights into the regulatory mechanisms between open chromatin regions and RNA transcripts. SNARE-seq has enabled reconstruction of the transcriptomic and epigenomic landscapes in rare cell types, thereby uncovering lineage specific accessible sites.

Moreover, Rubin *et al.* developed Perturb-ATAC, a method in which sequencing of chromatin accessibility using ATAC-seq and CRISPR single guide RNA (sgRNA) are combined to study DNA regulatory factors and regulatory mechanisms affecting cell fate decisions in human B lymphocytes.[68] Collectively, these methods provide novel strategies to study the epigenetic changes and dynamic gene expression in single cells.

3.2 Combining transcriptomic and genomic analysis

The use of microfluidics to physically separate aliquots from an initial droplet that contains a single cell, offers the possibility of measuring multiple cellular parameters simultaneously. One early example was presented in 2014 by Han *et al.*, who used microfluidics to isolate and lyse single cells, whereby the cell content was aliquoted and analysis could be performed on the two cell aliquots. The team used a valve-based microfluidic platform for separating gDNA and cytosolic mRNA, thus enabling their simultaneous detection through separate amplification of the genome and transcriptome.[53] However, the throughput was limited to three cells per microfluidic chip. Similar approaches have since been developed with automated cell handling capacity and increased throughput.[43,69] Using the same underlying approach for separate analyses of cell aliquots, Abdelmoez *et al.* have developed a method called single-cell integrated nucRNA and cytRNA-sequencing (SINC-seq).[70] The method relies on an electric field to separate the nucleus from the cytoplasm, thereby allowing for separate analysis. Through the use of this method, new insights into the regulatory relationship between nuclear RNA and cytoplasmic RNA have been discovered.

To characterize the heterogeneity of DNA repair cellular activities, Richer *et al.* have performed simultaneous measurement of mRNA transcripts and DNA repair mechanisms.[71] They have developed a technique called single-cell haircut (sc-haircut), to compartmentalize single cells with barcoded oligo-dTs and enzymatic substrates for DNA repair using droplet microfluidics (Fig. 2). Enzymatic DNA repair mechanisms at defined positions are detected with synthetic damaged DNA hairpins. The repaired DNA hairpins and mRNAs are subsequently converted to cDNAs for separate analyses. Then, the amount of enzymatic DNA repair is quantified and associated with its gene expression. In this case, DNA lesions repaired by cellular enzymes produce a product that can be analysed by DNA sequencing.

To analyse cancer heterogeneity and drug resistance, a method called concurrent sequencing of the transcriptome and targeted genomic regions (CORTAD-seq) was developed by Kong *et al.*[72] With the Fluidigm C1 platform, cells are first lysed, and both gDNA and cDNA are then subjected to PCR with primers specific to the regions of interest. The gDNA and cDNA are then physically separated for analyses. CORTAD-seq has been used to investigate acquired gefitinib drug resistance in PC9 cells, a lung cancer cell line, and observed that the transcriptome of the lung cancer cells undergoing a T790M mutation in the EGFR (epidermal growth factor receptor) commonly acquired in drug resistant lung epithelial cells.

3.3 Combining transcriptomic and protein analysis

The use of non-destructive assays before sequencing can link surface protein levels to cellular transcriptomes. Cellular Indexing of Transcriptomes and Epitopes by Sequencing (CITE-seq) and RNA Expression and Protein sequencing (REAP-seq) are two similar techniques that use droplet microfluidics for multimodal detection of surface proteins and mRNA transcripts.[73,74] The first step in these techniques is attaching antibody-derived tags to cell surface proteins. Single cells are then co-encapsulated with barcoded beads with the commercial 10× Chromium platform. Thereafter cells are lysed inside the droplets to release both the antibody-derived tags and mRNAs, which then hybridize to the beads. The barcoded beads are composed of a PCR-handle, an antibody barcode and a poly A-tail, thus enabling the mRNA bound to beads to be transcribed and also linking the two parameters (Fig. 2). The difference between CITE-seq and REAP-seq is based on how the DNA barcode is conjugated with the antibody.[73,74] The antibody used for CITE-seq is non-covalently conjugated to streptavidin attached to the DNA barcode, whereas the bonds are covalent in REAP-seq. In both methods, the number of proteins that can be simultaneously measured surpasses the number measurable by cytometry; this number is mainly limited by the number of barcode labeled antibodies as well as possible steric hindrance between the antibody and the cells. In REAP-seq, antibodies are conjugated with DNA barcodes of

66 bp divided into a unique sequence for each antibody (8 bp) and a primer sequence for amplification and subsequent sequencing. CITE-seq has been performed with 228 individual antibodies in a study constructing a multimodal reference atlas of the human PBMC.[75]

Mimitou *et al.* have expanded the CITE-seq platform to develop Expanded CRISPR compatible Cellular Indexing of Transcriptomes and Epitopes by sequencing (ECCITE-seq) in combination with the 10× Chromium platform, reaching a throughput of approximately 10 000 cells per run.[76] ECCITE-seq can simultaneously detect at least five parameters in a single cell, including transcriptomics, surface proteins, sample identity by hashtags, T cell receptors (TCR α/β and TCR γ/δ) and sgRNA. Combining these parameters has enabled specific clonotype features of malignant tumor cells to be deciphered. This multiplex single-cell system can be combined in various ways and may be used in broad biomedical and clinical applications.

Mair *et al.* have presented a platform called one-dimensional soli expression by nonlinear stochastic embedding (One-SENSE) wherein the use of antibody-derived tags and mRNA-seq is similar to that in CITE-seq and REAP-seq.[77] The major differences are that One-SENSE focuses on the selected targets at minimal read depth to minimize the cost, and it uses BD Rhapsody nanowells to achieve a higher throughput of more than 20 000 cells per run. The One-SENSE platform has been used to decipher immune cell heterogeneity in cells that were previously thought to be identical by simultaneously interrogating 492 immune-related genes and 41 surface proteins commonly used for immunophenotyping.

To analyse malignant features in acute leukemia, Granja *et al.* have performed integrated analyses combining CITE-seq for multiplexed protein quantification and transcriptomic profiling, and ATAC-seq for chromatin accessibility in single cells.[78] Through analysis of blood and spinal fluid samples from diseased and healthy donors, specific malignant features have been detected despite widespread epigenetic heterogeneity in the patient cohort.

Measurements of both transcriptomic and intracellular proteins are necessary to obtain a complete description of the cell state. This information can shed light on the complex relationships among various cell types or states, and different disease conditions. Technologies for single cell proteomic analysis remain in their infancy. Commonly used methods for bulk analysis, such liquid chromatography-mass spectrometry, require a relatively large amount of input material, thereby making these analytes difficult to detect at the single cell level.[79] Furthermore, proteins cannot be amplified similarly to RNA or DNA; therefore, the number of proteins that can be measured with single cell proteomics is limited. In the following sections, we present methods that have been used to circumvent these issues.

Xu *et al.* have developed a microfluidic system for investigating cell specific transcripts and proteins. Cells and sequencing beads are loaded onto a chip with a series of microchambers.[80] Intracellular proteins are then subjected to a fluorescence sandwich immunoassay inside the microchambers while the barcoded beads are isolated for cDNA library generation before sequencing. The fluorescence sandwich immunoassay requires a series of washing steps; thus, the use of microfluidic valves plays a key role in adding and removing liquids. However, the throughput is limited to the number of available microchambers.

To understand and analyse single cell features of heterogeneous immune cells, George and Wang have performed cytokine profiling of murine macrophages.[81] Their system is based on multiplex protein and transcriptomic analysis from the same cell with a Splittable Microchip. The Splittable Microchip consists of a polydimethylsiloxane nanowell array coated with cytokine specific antibodies. Secreted cytokines then bind the antibody array; this is followed by incubation with a fluorescent secondary antibody that can be detected with a fluorescence scanner. RNA sequences have been simultaneously analysed, thereby linking the secretome with the transcriptome. Another method for simultaneous detection of proteins and transcriptomes in single cells is proximity extension assays (PEA)[83] together with RNA detection.[50] PEA is an immunoassay in which proteins are quantified with oligonucleotides associated with antibodies. The antibodies bind different epitopes and form a DNA duplex, which is quantified by real-time qPCR. One such method has been presented by Genshaft *et al.*, who have focused on the correlation and expression of proteins and the transcriptome over time by using the Fluidigm C1 platform.[84] The authors have detected as many as 27 different intracellular proteins in MCF7 cells, a breast cancer cell line. Similarly, Gong *et al.* have used PEA for simultaneous detection of 31 intracellular proteins and transcriptome profiling with the Fluidigm C1 platform.[85] Their scatter plot analysis has shown a significant correlation between protein and mRNA levels for several genes.

3.4 Combining genomic and chromatin accessibility

Satpathy *et al.* have reported combined targeted genomic sequencing and chromatin expression. Using ATAC-seq (ATAC-seq) for chromatin accessibility combined with sequencing of genes encoding for the T-cell receptor, the authors have identified T cell heterogeneity in in populations that may appear identical according to surface markers.[82]

In another study, Cheow *et al.* have used the fluidigm C1 platform for single-cell genotype, expression and methylation (sc-GEM) analysis at different stages of primary lung adenocarcinomas and human fibroblast reprogramming. The authors have measured gene expression profiles with single cell RT-qPCR, and DNA methylation changes with the single cell restriction analysis of methylation (SCRAM) assay.[59]

4. Single cell multimodal analysis using microfluidics

Recently, the wave of multimodal measurements has further propagated beyond the omics view. The field is moving

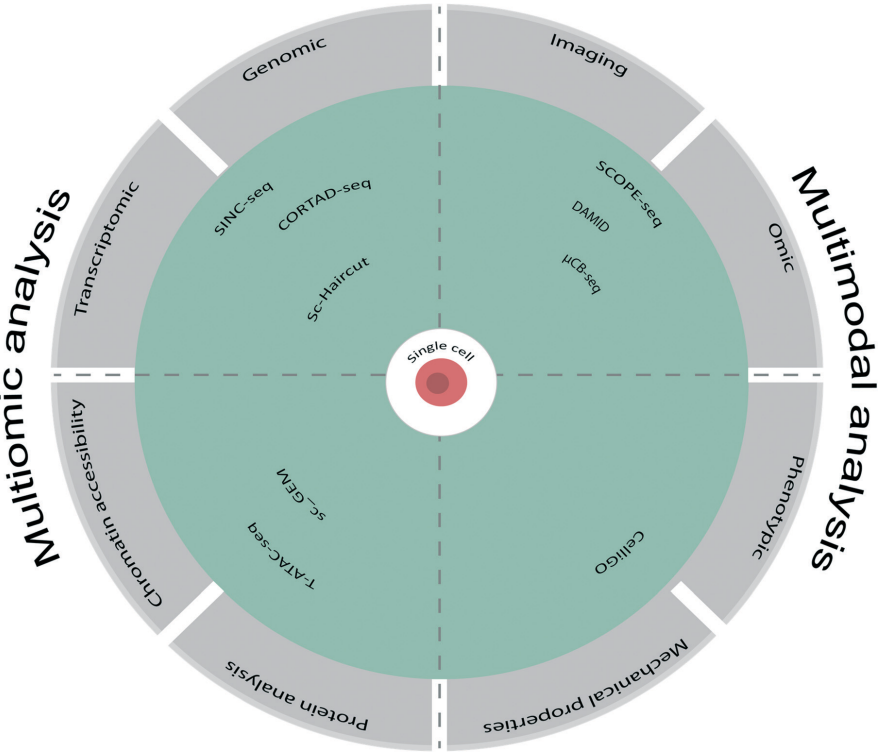

Fig. 3 Schematic overview of multiomic analysis encompassing protein analysis, chromatin accessibility, transcriptomic and genomic analysis. Multimodal analysis has a broader meaning, encompassing other cell characteristics such as cell phenotypic analysis, imaging and cell mechanical properties. Specific examples of the techniques using such analysis are described below each section.

toward combining phenotypic analysis and omic measurements to obtain a more comprehensive picture of cell states and cell types (Fig. 3). In this section, we present currently available multimodal single cell platforms and compare them in terms of throughput, detection capability and field of application in Table 4.

4.1 Combining omics and imaging

Fluorescence imaging is a widely used method for phenotypic analysis of cell morphology and cell specific molecules. One approach to obtaining single cell multimodal data involves coupling live-cell imaging to transcriptomic data. Yuan *et al.* demonstrated this by using dual-barcoded beads. After single-cell imaging in microwells, the dual-barcoded beads are added (Fig. 4). The dual barcode consists of commercially available drop-seq beads for scRNA-seq, to which additional oligonucleotides are added to serve as a second "optical" barcode. The sequence of the additional oligonucleotides can be optically decoded through several rounds of hybridization and fluorescence imaging of the beads. This process allows for spatially locating the beads and cells in the microwell array; thereby single cell imaging can be associated with sequencing data.[49]

In another approach to study genotype–phenotype relationships, Zhang *et al.* have performed parallel optical phenotyping and transcriptomic analysis.[46] The platform combines droplet microfluidics with a nano-well array and has achieved a throughput of 10 000 cells. Cells and beads are co-encapsulated in droplets for RNA-seq. However, the fluorescence intensity of the droplet is interrogated beforehand. Droplets of interest are then dispensed at indexed locations on a nanowell array. The array is indexed by an oligobarcode that allows downstream RNA-seq to be linked to the fluorescence measurements.

Similarly, Chen *et al.* have reported microfluidic cell barcoding and sequencing (μCB-seq) to pair high-resolution imaging and scRNA-seq. μCB-seq consists of parallel valves fabricated by combining multilayer soft lithography and DNA array printing. The valves can be pre-loaded with barcoded

Table 4 Summary of multimodal single cell analysis technologies using microfluidic platforms

Parameter 1	Parameter 2	Method	Microfluidic platform	Biological model	Throughput (number of cells)	Max, number of analytes (per run)	Applications	Ref.
Optical phenotype	Transcriptomics	SCOPE-Seq	Microwell-based microfluidics	A mix of human cell U87 line and mouse cell line 3 T3	30 500	~3600 transcripts, 19 imaging features	Simultaneous detection of live cell imaging and scRNA-seq	49
Optical phenotype	Transcriptomics		Droplet and nanowell-based microfluidics	Human PBMCs, Jurkat and HEK293 human cell lines and 3 T3 mouse cell line	~10 000	17 500 and 15 200 transcripts from mouse and human cells	Identification of cell states and subsets	46
Optical phenotype	Transcriptomics	µCB-seq	Valve-based microfluidics	Human embryonic kidney cells HEK293T and human adipocyte precursor cells (preadipocytes)	10	3008 transcripts	High-resolution imaging and scRNA-seq	47
Live-cell imaging	Transcriptomics		Fluidigm C1 microfluidic chip	Macrophage-like cell line RAW264.7	96	~400 000 reads per cell	Live cell imaging combined with scRNA-seq to correlate NF-κB activation with the transcriptome	48
Live-cell imaging	Genomics	DamID	Valve-based microfluidics	Embryonic kidney cells Hek293t	10		Analyse protein and DNA interactions	86
Cell imaging	Proteomics	Chip-DIA	Hydrodynamic trapping	Non-small-cell lung cancer PC-9 cells and chronic B cell leukemia cells	10–100	~1500 protein groups	Streamlined platform for sensitive single cell protein detection	87
Calcium imaging	Transcriptomics		Fluidigm C1 microfluidic chip	Human neocortex sample and mouse embryonic cortical cells	~500	~3118 transcripts	Study on the cell type specificity and neurotransmitter signaling in the developing human neocortex	88
Cellular mass, growth rate	Transcriptomics	sSMR	Micochannel-based microfluidics	Primary T cells, L1210, FL5.12 human cell lines and a patient-derived glioblastoma cell line BT159	120 cells per hour	>4000 transcripts	Identification of cancer cell heterogeneity in response to drugs	89
CD47 immunofluorescence imaging	Transcriptomics	DISCO	Electrode- and droplet- based digital microfluidics	Murine melanoma B16 cell line, human glioblastoma U87 cell line, CRISPR-modified HAP1 cells	Hundreds of cell contents per hour	Immunofluorescence of CD47 expression, NGS and sanger sequencing	Identification of genetic mutations in CD47 gene	44
IgG activity	Paired antibody V gene sequencing	CelliGO	Droplet-based microfluidics	Primary mouse spleen B cells	Hundreds of thousands of cells per hour		Investigation of IgG repertoire by screening IgG-secreting cells in terms of antibody activity and sequence in response to both soluble and membrane-bound antigens	91
Electrical	Mechanical			SUM159PT breast cancer cell lines	Hundreds of thousands of cells per hour		Real time measurements on biophysical parameters of single cells.	92

primers for capturing reverse-transcribed cDNA. When the fluidic valves are closed, the cells are imaged and sorted to enable the enrichment of cells of interest.[47]

In another study, parallel measurements of transcriptome and proteome have been analysed using live cell confocal imaging to display cell size and shape as well as NF-κB expression levels after LPS stimulation in RAW 264-7 cells.[48]

Because of the vast use of scRNA-seq technologies in recent years, many multimodal approaches have involved this technique. However, several studies have instead focused on other analyses to branch out from this context. For example, Altemose *et al.* have investigated protein and DNA interactions by combining image analysis with sequencing. By using a DNA adenine methyltransferase enzyme, the authors have spatially localized histone modifications and obtained insights into the regulatory relationship between the DNA and specific histone modifications.[86] In another recent approach Gebreyesus *et al.* have developed a platform for single cell counting, imaging and proteomic processing.[87] This platform is capable of distinguishing different cell types based on size as well as sensitive protein detection using all-in-one proteomic sample preparation and data- independent acquisition (DIA) mass spectrometry (MS) for proteomic analysis.

4.2 Combining omics and phenotypic analysis

Cells from various tissues within an organism display phenotypic heterogeneity, owing to both genetic and epigenetic factors. Mayer *et al.* have reported cell diversity in the developing human neocortex with a microfluidic integrated fluidic circuit consisting of flow and control channels, valves, multiplexors and logic devices. This method detects physiological responsiveness by using intracellular calcium as a stimulus to analyse series of neurotransmitter receptor agonists that are later correlated with scRNA-seq data. Physiological reactions to calcium stimuli associate with the molecular identity, thereby allowing new sub-populations of cells to be detected that could otherwise not be identified (Fig. 4).[88]

Kimmerling *et al.* have presented a method for analysing cellular mass and growth in single cells to investigate the link between cell fitness and responses to a drug treatment.[89] By using small fluidic channels, cells are separated with respect to buoyancy, and the cell mass is measured with a sensor array. The cells can be analysed gradually by simply turning on and off the flow. The phenotypic data are later associated with scRNA-seq from the same cell.

Microfluidic chips can be integrated with electronic circuits to allow for easy manipulation of liquids.[90] Recently, Lamanna *et al.* have performed phenotypic and omic analyses by using digital microfluidics of single cells for -omics (DISCO) capture. Cells can be easily manipulated and lysed by laser capture microdissection inside the digital microfluidic chip. CD47 CRISPR-modified HAP1 cells have been analyse for phenotypic changes in CD47 expression, combined with genomics, transcriptomics or proteomics.[44]

4.3 Other multimodal analysis

Other studies have analysed cells for multiple parameters simultaneously without including omic analysis. Gérard *et al.* have presented an efficient and flexible system that combines screening for IgG activity with sequencing of paired antibody V genes through droplet-based microfluidic techniques.[91] The droplets containing antibodies of interest are sorted with a sandwich immune assay based on fluorescent and magnetic beads. The sorted droplets are then barcoded with hydrogel beads bearing primers for IgHV and VL genes tagged with unique barcodes, and the barcoded V genes are sequenced and analysed (Fig. 4). The analyses have been applied in a murine setting but could easily be adapted to humans. For example, by enriching human circulating B cells from peripheral blood, the platform can facilitate analysis of the human immune V gene repertoire in diseased and healthy humans and thus may have diagnostic potential.

Another recent approach for detecting biophysical properties of single cells was developed by Rezard *et al.*[92] By using micro-electro mechanical systems (MEMS) cells could be trapped and analysed for mechanical and electrical properties in real time during continuous flow.

5. Technological developments and clinical transitions

Despite its numerous achievements, MSCA is still in its infancy, with many challenges to overcome. The improvement needed for MSCA include both assay development as well as technological development. Challenges in assay development include reaching limit of detection due to the limited sample volume, low genomic coverage and low sensitivity of analytical methods.

Technological development faces challenges such as correct data alignment of multiple cellular parameters, accounting for high degrees of missing data and inherent assay noise. Recently developed techniques, such as Cobolt,[93] MOFA+[94] and weighted-nearest neighbour,[75] are capable of analysing multimodal datasets. Another recent method, bridge integration, offers supervised mapping that utilize well-known cellular atlases such as the human cell atlas as a reference.[95] By mapping datasets to these reference data points, potential errors can easily be adjusted for and datasets across different cell parameters can easily be compared.

5.1 Technological developments for MSCA

With new technologies being constantly developed, multimodal analysis is exploding. However, there are multiple different cellular properties that are yet to be integrated with multimodal measurements. As a perspective, we highlight here the analysis of biophysical properties of

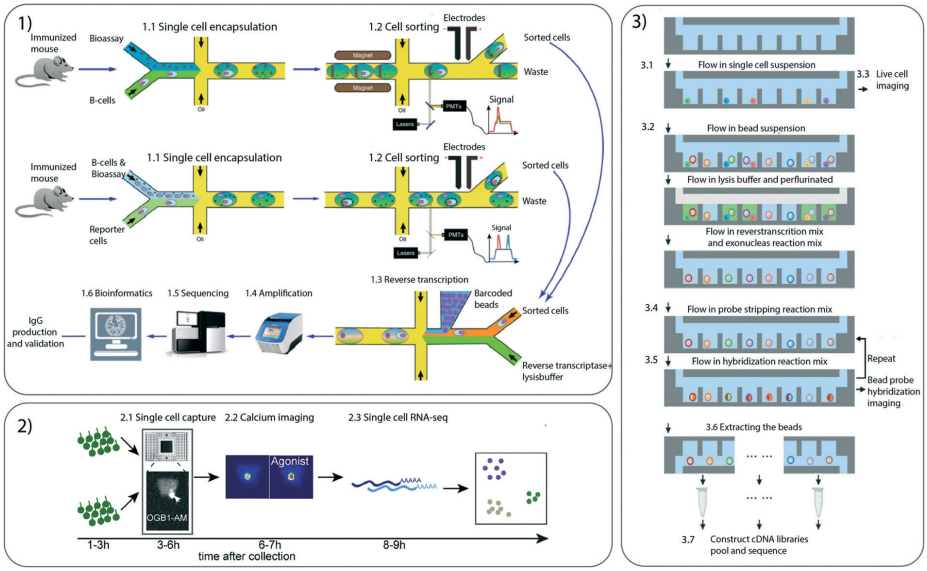

Fig. 4 Different microfluidic multimodal single cell techniques 1) Droplet microfluidic platform for screening of IgG-secreting single cells and to characterize antibody binding to both membrane-bound and secreted antigens. 1.1) Droplet production 1.2) cell sorting 1.3) reverse transcription 1.4) amplification 1.5) sequencing 1.6) bioinformatics. 2) Microfluidic integrated chip for separating single cells and perform calcium imaging 2.1) single cell capture 2.2) calcium imaging 2.3) scRNA-seq. 3) SCOPE-seq platform developed to analyse phenotype and scRNA-seq using a microwell approach. 3.1) Loading of the cell suspension placing a single cell in a well 3.2) bead solution is added 3.3) cell imaging 3.4) Adding of probe stripping reaction mix 3.5) adding of probe hybridization reaction mix 3.6) beads are extracted and cDNA libraries are constructed. Images taken with permission from Gérard *et al.*, Mayer *et al.* and Yuan *et al.*

the cells, yet to be better implemented with other techniques for multimodal analysis.[96] Those biophysical properties are of relevance as they have been associated with the progression of cell differentiation and diseases.

Mechanical measurements of cell stiffness and physical resistance to external forcing have been demonstrated using various actuation modes. Pipette aspiration[97] with a low throughput capacity or parallel arrays of constrictions in microchannels[98,99] with a larger throughput capacity have been used to explore the mechanics of the cell and even the response of the nucleus. The use of soft compartments also proved a powerful tool to relate mechanical stresses on cells to increased motility, of relevance to study the dynamics of tumor evolution,[100] and new microfluidic devices have been developed to investigate the effect of compressive stress on cell growth.[101]

Optical and magnetic tweezers have been developed for mechanical phenotyping.[102,103] Both approaches require a dielectric or magnetic bead to be attached to the cell. By applying a controlled oscillating field, by the use of a tightly focused laser or a magnetic field, the bead is moved in response to the field. The oscillatory motion of the bead causes cell deformation. The resistance against this deformation is determined by the mechanical properties of the cell: the viscoelastic moduli of entangled actin networks were measured,[104] and cytoskeletal changes for prostate cancer cells under hypoxic stress were observed.[105] A more recent development based on the magnetic tweezers is a method named magnetic twisting cytometry.[106] Here the applied magnetic field move and rotate the bead around different axes to determine the mechanical properties of the cell. Another mechanical single cell study was performed by precise microfabrication of microactuators. A muscle cell was attached to the micropillar and it was illustrated that the extension and contraction of this cell, induced by chemical stimuli, was able to bend the micropillar.[107] These methods are in general limited in throughput and are invasive for the cell as the binding to a bead might limit its further use in a multimodal approach.

Non-contact methods offer interesting potential. Acoustic methods for mechanical phenotyping use standing acoustic waves to generate an acoustic radiation force on the cell that moves it to the pressure nodes.[108] The velocity at which the cell moves is used to extract its compressibility. A novel development in this method utilizes standing acoustic waves together with an acoustic impedance gradient in a microchannel.[109] Due to the acoustic radiation force, cells migrate to the equilibrium point in the microchannel, the point where its acoustic impedance matches the surroundings. This method works similar as density gradient

centrifugation and is size insensitive. Overall, the combination of label free and high throughput methods for mechanical characterizations of the cells have a potential for implementation in a multimodal approach.

5.2 Perspective techniques for MSCA

Another approach to MSCA is to perform single cell analysis on one cell parameter and later integrated other cellular parameters from different experiments. However, the correspondence between individual cells is absent when data from multiple experiments derived from different cell populations are incorporated. The methods presented for these analyses have great potential to be transformed into multimodal analysis. For example, Zhong *et al.* have investigated various cell types, cell linages, molecular features and transcriptional regulation of the developing human hippocampus.[110] To understand the molecular features of developing hippocampal cells, the authors performed scRNA-seq and chromatin analysis with the 10× chromium platform and ATAC-seq, respectively. They identified spatially specific gene expression in both the pre-frontal cortex and the hippocampus, which could be used as a tool for investigating other short-term or long-term memory related diseases. In another study exploring neural cell heterogeneity, Lake *et al.* have analysed single-cell transcriptional and epigenetic states in the human adult brain with droplet microfluidic methods.[111] Through scRNA-seq and epigenetic states on separate samples, the data sets can be computationally integrated.

To reveal additional spatial relationships between cells multimodal measurements have been performed on tissue samples. Using microfluidic methods for adding barcode beads to the sample, simultaneous mapping of mRNAs and proteins has been performed directly on the tissue sample.[112]

5.3 Clinical perspectives: current and future applications

As described above, single cell multimodal analysis allows for biological differences between individual cells to be inferred, and has thus broadened knowledge of cellular heterogeneity and its implications in cell function. Single cell multimodal analysis could substantially advance clinical research and applications, particularly regarding early diagnostics and disease monitoring, by tracking the precise composition and distribution of specific cell populations with the cellular changes. Several projects have integrated MSCA platforms to analyse patient-derived samples, an overview of the recent progress is in oncology, immunology and neurology presented below.

5.3.1 Oncology. Tumors are composed of a large variety of cell types and cell states. Because of both inter- and intratumor heterogeneity, therapy resistance and tumor relapse remain the greatest challenges in cancer treatments.[113] At the single cell level, cells have different drug treatment responses, and even a small number of resistant cells in a tumor can affect treatment outcomes. Because therapy resistant cells may be rare in tumors,[114] highly sensitive methods are urgently needed for detecting these cells. Single cell multimodal analysis has the unique potential to reveal the biological variations within the tumor[115] and to relate specific acquired mutations to molecular outcomes, thereby enabling the detection of therapy resistant cells at an early stage and subsequent rapid diagnosis of medical outcomes.[116]

Multimodal analysis can also be used to create detailed lineage trees of cancer cell evolution.[117] By reconstructing cell lineage trees according to the extent to which cells share somatic variations, the understanding of how tumors evolve over time and the prediction of treatment outcomes can be improved. As a result, more specific and efficient treatments will be possible for patients. Projects such as The Human Tumor Atlas Network[118] and CancerSEA[119] aim at identifying cancer cell heterogeneity to create single-cell longitudinal atlases. The Human Tumor Atlas Network will use omic analyses and spatial multiplex *in situ* methods on patient derived tumors to create accessible three-dimensional atlases of multiple different sets of cancers. By studying genetic differences and integrating them with clinical outcomes, these projects aim to identify new biomarkers or therapeutically relevant cell types. The CancerSEA database focuses on decoding functional states of cancer cells at the single-cell level by using single cell transcriptomic data. These methods may serve as key stepping-stones for the ambitious goal of mapping multimodal data in cancer research.

5.3.2 Immunology. The immune system is highly complex and consists of many types of cells, which have previously been defined primarily through cell surface markers and scRNA-seq.[120] Although cell surface markers provide a good indication of the protein expression of a cell, a complete picture with multiple cellular parameters is desirable to understand the immune system in depth.[121] For example, lymphoid cells communicate with their environment in a variety of ways, including cell–cell interactions and recruitment of new cells through chemokine secretion. A variety of cell types are known by their specific functions in this ecosystem, but only bulk data on the secretome are available, whereas cell–cell variations and their effects are underexplored to date. By culturing cells in individual compartments in multimodal analysis platforms, not only RNA and intracellular proteins but also individual secretomes, then transcriptomes or genomes can be analysed.

Unterman *et al.* have analysed the peripheral lymphocyte population in patients with COVID-19. Using CITE-seq surface proteins on lymphocytes, B cell and T cells receptors have been analysed together with scRNA-seq. The authors concluded that both B cells and T cells have an altered distribution in the primary response to COVID-19.[122]

5.3.3 Neurology. MSCA have the potential to unravel complex nervous system interactions and discover new cell-signaling mechanisms controlling functions within the

central nervous system. Furthermore, studying cellular development and differentiation will also be possible by tracking different cell trajectories, to predict cell lineages and visualize how these diverse cells are organized within neural tissues.[123] Another possible parameter that may be integrated in neurology is the analysis of cell electrophysiological properties to identify new subclasses of cells and establish cellular heterogeneity.[124] As described above, Mayer *et al.* have analysed cell diversity in the developing human neocortex and have found new sub-populations of cells.[88] These types of approaches are key stepping-stones in assessing the full complexity of the nervous system.

5.4 Challenges for transitioning MSCA to clinical research

Several challenges must be addressed before single cell multimodal analyses can be used in clinical applications. First, an emerging need exists to develop guidelines and workflows specifically for clinical settings, and to minimize variations in sample quality due to sample collection and preservation procedures, for which standardized protocols and specific sample clean-up steps are required. Other key aspects in translating single cell multimodal analysis to clinical research include achieving high analysis sensitivity and high throughput while minimizing costs. Crucially, multimodal data must be properly analysed, and computational methods specifically tailored for analysing multiplexed data must be developed.[125]

6. Conclusion

Single cell analysis have recently benefited from the technologies developed to simultaneously determine multiple parameters of individual cells. These developments are leading to unprecedented insight into cell fate decisions, genotype–phenotype relationships and cell heterogeneity. However, simultaneously evaluating multiple aspects of single cells remains difficult with several limitations still to be overcome: low genomic coverage, limited sample volume and low sensitivity of analytical methods. Microfluidic technologies combine advantages such as precise manipulation of fluids, automated liquid handling, high throughput and the potential for coupling to different analytical measuring systems. The development of microfluidic devices and their applications currently provides and will continue to provide new research methodologies with unprecedented accuracy for single cell analysis. These technologies are therefore likely to shape the future direction of multimodal analysis with a potential for translation into clinical research in years to come.

Conflicts of interest

V. Taly and J.-C. Baret are co-founders and scientific advisors of emulseo.

Acknowledgements

This work is part of a project that has received funding from the European Union's Horizon 2020 research and innovation programme under the Marie Skłodowska-Curie grant agreement No 813786. W. Xiao received funding from the SIRIC CARPEM (CAncer Research and Personalized Medicine) and the ITMO CANCER through the program single cell COCAHEMISCLE. The work was conducted with the support of the Ligue Nationale Contre le Cancer (LNCC, Program "Equipe labelisée LIGUE"; no. EL2016. LNCC). This work was also supported by the Ministère de l'Enseignement Supérieur et de la Recherche, the Université Paris-Descartes, the Centre National de la Recherche Scientifique (CNRS), the Institut National de la Santé et de la Recherche Médicale (INSERM) and Canceropole Ile-de-France.

References

1 E. Z. Macosko, Highly Parallel Genome-wide Expression Profiling of Individual Cells Using Nanoliter Droplets, *Cell*, 2015, **161**(5), 1202–1214.
2 C. Gawad, W. Koh and S. R. Quake, Dissecting the clonal origins of childhood acute lymphoblastic leukemia by single-cell genomics, *Proc. Natl. Acad. Sci. U. S. A.*, 2014, **111**(50), 17947–17952.
3 N. Navin, J. Kendall, J. Troge, P. Andrews, L. Rodgers and J. McIndoo, *et al.*, Tumour evolution inferred by single-cell sequencing, *Nature*, 2011, **472**(7341), 90–94.
4 T. Nagano, *et al.*, Cell-cycle dynamics of chromosomal organization at single-cell resolution, *Nature*, 2017, **547**(7661), 61–67.
5 A. M. Klein, L. Mazutis, I. Akartuna, N. Tallapragada, A. Veres and V. Li, *et al.*, Droplet Barcoding for Single-Cell Transcriptomics Applied to Embryonic Stem Cells, *Cell*, 2015, **161**(5), 1187–1201.
6 S. Guo, C. Zhang and A. Le, *Curr. Opin. Biotechnol.*, 2021, **71**, 115–122.
7 A. J. Hughes, D. P. Spelke, Z. Xu, C. C. Kang, D. V. Schaffer and A. E. Herr, Single-cell western blotting, *Nat. Methods*, 2014, **11**(7), 749–755.
8 L. Qiu, F. Wimmers, J. Weiden, H. A. Heus, J. Tel and C. G. Figdor, A membrane-anchored aptamer sensor for probing IFNc secretion by single cells, *Chem. Commun.*, 2017, **53**(57), 8066–8069.
9 G. Chen, B. Ning and T. Shi, Single-Cell RNA-Seq Technologies and Related Computational Data Analysis, *Front. Genet.*, 2019, **10**, 317.
10 J. Lee, D. Y. Hyeon and D. Hwang, Single-cell multiomics: technologies and data analysis methods, *Exp. Mol. Med.*, 2020, **52**(9), 1428–1442.
11 S. W. Lin, C. H. Chang and C. H. Lin, High-throughput Fluorescence Detections in Microfluidic Systems, *Genomic Med., Biomarkers, Health Sci.*, 2011, **3**(1), 27–38.
12 M. Sesen and G. Whyte, Image-Based Single Cell Sorting Automation in Droplet Microfluidics, *Sci. Rep.*, 2020, **10**(1), 8736.

13 Q. Xiong, C. Y. Lim, J. Ren, J. Zhou, K. Pu and M. B. Chan-Park, *et al.*, Magnetic nanochain integrated microfluidic biochips, *Nat. Commun.*, 2018, **9**(1), 1743.
14 R. R. Svejdal, D. Sticker, C. Sønderby, J. P. Kutter and K. D. Rand, Thiol-ene microfluidic chip for fast on-chip sample clean-up, separation and ESI mass spectrometry of peptides and proteins, *Anal. Chim. Acta*, 2020, **1140**, 168–177.
15 J. Sandberg, B. Werne, M. Dessing and J. Lundeberg, Rapid flow-sorting to simultaneously resolve multiplex massively parallel sequencing products, *Sci. Rep.*, 2011, **1**, 108.
16 E. Denisenko, B. B. Guo, M. Jones, R. Hou, L. de Kock and T. Lassmann, *et al.*, Systematic assessment of tissue dissociation and storage biases in single-cell and single-nucleus RNA-seq workflows, *Genome Biol.*, 2020, **21**(1), 130.
17 R. Hanamsagar, T. Reizis, M. Chamberlain, R. Marcus, F. O. Nestle and E. de Rinaldis, *et al.*, An optimized workflow for single-cell transcriptomics and repertoire profiling of purified lymphocytes from clinical samples, *Sci. Rep.*, 2020, **10**(1), 2219.
18 M. D. Young and S. Behjati, SoupX removes ambient RNA contamination from droplet-based single-cell RNA sequencing data, *Gigascience*, 2020, **9**(12), giaa151.
19 H. Tavakoli, W. Zhou, L. Ma, S. Perez, A. Ibarra and F. Xu, *et al.*, Recent advances in microfluidic platforms for single-cell analysis in cancer biology, diagnosis and therapy, *TrAC, Trends Anal. Chem.*, 2019, **117**, 13–26.
20 P. Shinde, L. Mohan, A. Kumar, K. Dey, A. Maddi and A. Patananan, *et al.*, Current Trends of Microfluidic Single-Cell Technologies, *Int. J. Mol. Sci.*, 2018, **19**(10), 3143.
21 J. Wang, H. C. Fan, B. Behr and S. R. Quake, Genome-wide Single-Cell Analysis of Recombination Activity and De Novo Mutation Rates in Human Sperm, *Cell*, 2012, **150**(2), 402–412.
22 M. A. Unger, Monolithic Microfabricated Valves and Pumps by Multilayer Soft Lithography, *Science*, 2000, **288**(5463), 113–116.
23 J. Yuan and P. A. Sims, An Automated Microwell Platform for Large-Scale Single Cell RNA-Seq, *Sci. Rep.*, 2016, **6**(1), 33883.
24 T. M. Gierahn, M. H. Wadsworth, T. K. Hughes, B. D. Bryson, A. Butler and R. Satija, *et al.*, Seq-Well: portable, low-cost RNA sequencing of single cells at high throughput, *Nat. Methods*, 2017, **14**(4), 395–398.
25 R. Zilionis, J. Nainys, A. Veres, V. Savova, D. Zemmour and A. M. Klein, *et al.*, Single-cell barcoding and sequencing using droplet microfluidics, *Nat. Protoc.*, 2017, **12**(1), 44–73.
26 D. J. Collins, A. Neild, A. deMello, A. Q. Liu and Y. Ai, The Poisson distribution and beyond: methods for microfluidic droplet production and single cell encapsulation, *Lab Chip*, 2015, **15**(17), 3439–3459.
27 Y. Bai, X. He, D. Liu, S. N. Patil, D. Bratton and A. Huebner, *et al.*, A double droplet trap system for studying mass transport across a droplet-droplet interface, *Lab Chip*, 2010, **10**(10), 1281.
28 J. G. Riess and M. P. Krafft, Fluorinated materials for in vivo oxygen transport (blood substitutes), diagnosis and drug delivery, *Biomaterials*, 1998, **19**(16), 1529–1539.
29 P. Gruner, B. Riechers, L. A. Chacòn Orellana, Q. Brosseau, F. Maes and T. Beneyton, *et al.*, Stabilisers for water-in-fluorinated-oil dispersions: Key properties for microfluidic applications, *Curr. Opin. Colloid Interface Sci.*, 2015, **20**(3), 183–191.
30 A. R. Abate, T. Hung, P. Mary, J. J. Agresti and D. A. Weitz, High-throughput injection with microfluidics using picoinjectors, *Proc. Natl. Acad. Sci. U. S. A.*, 2010, **107**(45), 19163–19166.
31 C. Priest, S. Herminghaus and R. Seemann, Controlled electrocoalescence in microfluidics: Targeting a single lamella, *Appl. Phys. Lett.*, 2006, **89**(13), 134101.
32 D. R. Link, S. L. Anna, D. A. Weitz and H. A. Stone, Geometrically Mediated Breakup of Drops in Microfluidic Devices, *Phys. Rev. Lett.*, 2004, **92**(5), 054503.
33 L. Mazutis, J. Gilbert, W. L. Ung, D. A. Weitz, A. D. Griffiths and J. A. Heyman, Single-cell analysis and sorting using droplet-based microfluidics, *Nat. Protoc.*, 2013, **8**(5), 870–891.
34 D. Di Carlo, N. Aghdam and L. P. Lee, Single-Cell Enzyme Concentrations, Kinetics, and Inhibition Analysis Using High-Density Hydrodynamic Cell Isolation Arrays, *Anal. Chem.*, 2006, **78**(14), 4925–4930.
35 S. Bhattacharya, T. C. Chao, N. Ariyasinghe, Y. Ruiz, D. Lake and R. Ros, *et al.*, Selective trapping of single mammalian breast cancer cells by insulator-based dielectrophoresis, *Anal. Bioanal. Chem.*, 2014, **406**(7), 1855–1865.
36 C. Liberale, G. Cojoc, F. Bragheri, P. Minzioni, G. Perozziello and R. La Rocca, *et al.*, Integrated microfluidic device for single-cell trapping and spectroscopy, *Sci. Rep.*, 2013, **3**(1), 1258.
37 D. J. Collins, B. Morahan, J. Garcia-Bustos, C. Doerig, M. Plebanski and A. Neild, Two-dimensional single-cell patterning with one cell per well driven by surface acoustic waves, *Nat. Commun.*, 2015, **6**(1), 8686.
38 J. Clausell-Tormos, D. Lieber, J. C. Baret, A. El-Harrak, O. J. Miller and L. Frenz, *et al.*, Droplet-Based Microfluidic Platforms for the Encapsulation and Screening of Mammalian Cells and Multicellular Organisms, *Chem. Biol.*, 2008, **15**(5), 427–437.
39 P. K. Periyannan Rajeswari, H. N. Joensson and H. Andersson-Svahn, Droplet size influences division of mammalian cell factories in droplet microfluidic cultivation: Microfluidics and Miniaturization, *Electrophoresis*, 2017, **38**(2), 305–310.
40 T. Zhang, H. Zhang, W. Zhou, K. Jiang, C. Liu and R. Wang, *et al.*, One-Step Generation and Purification of Cell-Encapsulated Hydrogel Microsphere With an Easily Assembled Microfluidic Device, *Front. Bioeng. Biotechnol.*, 2022, **9**, 816089.
41 L. Mahler, M. Tovar, T. Weber, S. Brandes, M. M. Rudolph and J. Ehgartner, *et al.*, Enhanced and homogeneous oxygen availability during incubation of microfluidic droplets, *RSC Adv.*, 2015, **5**(123), 101871–101878.
42 N. de Lange, T. M. Tran and A. R. Abate, Electrical lysis of cells for detergent-free droplet assays, *Biomicrofluidics*, 2016, **10**(2), 024114.

43 H. Shintaku, H. Nishikii, L. A. Marshall, H. Kotera and J. G. Santiago, On-Chip Separation and Analysis of RNA and DNA from Single Cells, *Anal. Chem.*, 2014, **86**(4), 1953–1957.
44 J. Lamanna, E. Y. Scott, H. S. Edwards, M. D. Chamberlain, M. D. M. Dryden and J. Peng, *et al.*, Digital microfluidic isolation of single cells for -Omics, *Nat. Commun.*, 2020, **11**(1), 5632.
45 R. Marie, M. Pødenphant, K. Koprowska, R. C. M. Vulders, J. Wilding and N. Ashley, *et al.*, Sequencing of human genomes extracted from single cancer cells isolated in a valveless microfluidic device, *Lab Chip*, 2018, **12**, 1891–1902.
46 J. Q. Zhang, C. A. Siltanen, L. Liu, K. C. Chang, Z. J. Gartner and A. R. Abate, Linked optical and gene expression profiling of single cells at high-throughput, *Genome Biol.*, 2020, **21**(1), 49.
47 T. N. Chen, A. Gupta, M. D. Zalavadia and A. Streets, μCB-seq: microfluidic cell barcoding and sequencing for high-resolution imaging and sequencing of single cells, *Lab Chip*, 2020, **20**(21), 3899–3913.
48 K. Lane, D. Van Valen, M. M. DeFelice, D. N. Macklin, T. Kudo and A. Jaimovich, *et al.*, Measuring Signaling and RNA-Seq in the Same Cell Links Gene Expression to Dynamic Patterns of NF-κB Activation, *Cell Syst.*, 2017, **4**(4), 458–469.e5.
49 J. Yuan, J. Sheng and P. A. Sims, SCOPE-Seq: a scalable technology for linking live cell imaging and single-cell RNA sequencing, *Genome Biol.*, 2018, **19**(1), 227.
50 K. Taniguchi, T. Kajiyama and H. Kambara, Quantitative analysis of gene expression in a single cell by qPCR, *Nat. Methods*, 2009, **6**(7), 503–506.
51 Y. Hou, H. Guo, C. Cao, X. Li, B. Hu and P. Zhu, *et al.*, Single-cell triple omics sequencing reveals genetic, epigenetic, and transcriptomic heterogeneity in hepatocellular carcinomas, *Cell Res.*, 2016, **26**(3), 304–319.
52 Q. R. Xing, N. O. Cipta, K. Hamashima, Y. C. Liou, C. G. Koh and Y. H. Loh, Unraveling Heterogeneity in Transcriptome and Its Regulation Through Single-Cell Multi-Omics Technologies, *Front. Genet.*, 2020, **11**, 662.
53 L. Han, X. Zi, L. X. Garmire, Y. Wu, S. M. Weissman and X. Pan, *et al.*, Co-detection and sequencing of genes and transcripts from the same single cells facilitated by a microfluidics platform, *Sci. Rep.*, 2015, **4**, 6485.
54 S. Sohrabi, N. Kassir and M. K. Moraveji, Droplet microfluidics: fundamentals and its advanced applications, *RSC Adv.*, 2020, **10**(46), 27560–27574.
55 S. M. Prakadan, A. K. Shalek and D. A. Weitz, Scaling by shrinking: empowering single-cell "omics" with microfluidic devices, *Nat. Rev. Genet.*, 2017, **18**(6), 345–361.
56 S. Chen, B. B. Lake and K. Zhang, High-throughput sequencing of the transcriptome and chromatin accessibility in the same cell, *Nat. Biotechnol.*, 2019, **37**(12), 1452–1457.
57 A. R. Abate, C. H. Chen, J. J. Agresti and D. A. Weitz, Beating Poisson encapsulation statistics using close-packed ordering, *Lab Chip*, 2009, **9**(18), 2628.
58 Q. R. Xing, C. A. E. Farran, Y. Y. Zeng, Y. Yi, T. Warrier and P. Gautam, *et al.*, Parallel bimodal single-cell sequencing of transcriptome and chromatin accessibility, *Genome Res.*, 2020, **30**(7), 1027–1039.
59 L. F. Cheow, E. T. Courtois, Y. Tan, R. Viswanathan, Q. Xing and R. Z. Tan, *et al.*, Single-cell multimodal profiling reveals cellular epigenetic heterogeneity, *Nat. Methods*, 2016, **13**(10), 833–836.
60 I. Hajji, M. Serra, L. Geremie, I. Ferrante, R. Renault and J. L. Viovy, *et al.*, Droplet microfluidic platform for fast and continuous-flow RT-qPCR analysis devoted to cancer diagnosis application, *Sens. Actuators, B*, 2020, **303**, 127171.
61 D. W. Ruff, D. M. Dhingra, K. Thompson, J. A. Marin and A. T. Ooi, High-Throughput Multimodal Single-Cell Targeted DNA and Surface Using the Mission Bio Tapestri Platform, in: Single-Cell Protein Analysis, *Methods Mol. Biol.*, 2022, **2386**, 171–188.
62 F. Tang, C. Barbacioru, Y. Wang, E. Nordman, C. Lee and N. Xu, *et al.*, mRNA-Seq whole-transcriptome analysis of a single cell, *Nat. Methods*, 2009, **6**(5), 377–382.
63 J. Cao, The single cell transcriptional landscape of mammalian organogenesis, *Nature*, 2019, **566**(7745), 496–502.
64 D. Hebenstreit, Methods, Challenges and Potentials of Single Cell RNA-seq, *Biology.*, 2012, **1**(3), 658–667.
65 V. Svensson, R. Vento-Tormo and S. A. Teichmann, Exponential scaling of single-cell RNA-seq in the past decade, *Nat. Protoc.*, 2018, **13**(4), 599–604.
66 J. D. Buenrostro, B. Wu, H. Y. Chang and W. J. Greenleaf, ATAC-seq: A Method for Assaying Chromatin Accessibility Genome-Wide, *Curr. Protoc. Mol. Biol.*, 2015, **109**, 21.29.1.
67 J. Cao, D. A. Cusanovich, V. Ramani, D. Aghamirzaie, H. A. Pliner and A. J. Hill, *et al.*, Joint profiling of chromatin accessibility and gene expression in thousands of single cells, *Science*, 2018, **361**(6409), 1380–1385.
68 A. J. Rubin, K. R. Parker, A. T. Satpathy, Y. Qi, B. Wu and A. J. Ong, *et al.*, Coupled Single-Cell CRISPR Screening and Epigenomic Profiling Reveals Causal Gene Regulatory Networks, *Cell*, 2019, **176**(1–2), 361–376.e17.
69 K. Kuriyama, H. Shintaku and J. G. Santiago, Isotachophoresis for fractionation and recovery of cytoplasmic RNA and nucleus from single cells, *Electrophoresis*, 2015, **36**(14), 1658–1662.
70 M. N. Abdelmoez, K. Iida, Y. Oguchi, H. Nishikii, R. Yokokawa and H. Kotera, *et al.*, SINC-seq: correlation of transient gene expressions between nucleus and cytoplasm reflects single-cell physiology, *Genome Biol.*, 2018, **19**(1), 66.
71 A. L. Richer, K. A. Riemondy, L. Hardie and J. R. Hesselberth, Simultaneous measurement of biochemical phenotypes and gene expression in single cells, *Nucleic Acids Res.*, 2020, **48**(10), e59.
72 S. L. Kong, H. Li, J. A. Tai, E. T. Courtois, H. M. Poh and D. P. Lau, *et al.*, Concurrent Single-Cell RNA and Targeted DNA Sequencing on an Automated Platform for Comeasurement of Genomic and Transcriptomic Signatures, *Clin. Chem.*, 2019, **65**(2), 272–281.

73 V. M. Peterson, K. X. Zhang, N. Kumar, J. Wong, L. Li and D. C. Wilson, *et al.*, Multiplexed quantification of proteins and transcripts in single cells, *Nat. Biotechnol.*, 2017, **35**(10), 936–939.
74 M. Stoeckius, C. Hafemeister, W. Stephenson, B. Houck-Loomis, P. K. Chattopadhyay and H. Swerdlow, *et al.*, Simultaneous epitope and transcriptome measurement in single cells, *Nat. Methods*, 2017, **14**(9), 865–868.
75 Y. Hao, S. Hao, E. Andersen-Nissen, W. M. Mauck, S. Zheng and A. Butler, *et al.*, Integrated analysis of multimodal single-cell data, *Cell*, 2021, **184**(13), 3573–3587.e29.
76 E. P. Mimitou, A. Cheng, A. Montalbano, S. Hao, M. Stoeckius and M. Legut, *et al.*, Multiplexed detection of proteins, transcriptomes, clonotypes and CRISPR perturbations in single cells, *Nat. Methods*, 2019, **16**(5), 409–412.
77 F. Mair, J. R. Erickson, V. Voillet, Y. Simoni, T. Bi and A. J. Tyznik, *et al.*, A Targeted Multi-omic Analysis Approach Measures Protein Expression and Low-Abundance Transcripts on the Single-Cell Level, *Cell Rep.*, 2020, **31**(1), 107499.
78 J. M. Granja, S. Klemm, L. M. McGinnis, A. S. Kathiria, A. Mezger and M. R. Corces, *et al.*, Single-cell multiomic analysis identifies regulatory programs in mixed-phenotype acute leukemia, *Nat. Biotechnol.*, 2019, **37**(12), 1458–1465.
79 B. Budnik, E. Levy, G. Harmange and N. Slavov, SCoPE-MS: mass spectrometry of single mammalian cells quantifies proteome heterogeneity during cell differentiation, *Genome Biol.*, 2018, **19**(1), 161.
80 A. M. Xu, Q. Liu, K. L. Takata, S. Jeoung, Y. Su and I. Antoshechkin, *et al.*, Integrated measurement of intracellular proteins and transcripts in single cells, *Lab Chip*, 2018, **18**(21), 3251–3262.
81 J. George and J. Wang, Assay of Genome-Wide Transcriptome and Secreted Proteins on the Same Single Immune Cells by Microfluidics and RNA Sequencing, *Anal. Chem.*, 2016, **88**(20), 10309–10315.
82 A. T. Satpathy, N. Saligrama, J. D. Buenrostro, Y. Wei, B. Wu and A. J. Rubin, *et al.*, Transcript-indexed ATAC-seq for precision immune profiling, *Nat. Med.*, 2018, **24**(5), 580–590.
83 S. Darmanis, C. J. Gallant, V. D. Marinescu, M. Niklasson, A. Segerman and G. Flamourakis, *et al.*, Simultaneous Multiplexed Measurement of RNA and Proteins in Single Cells, *Cell Rep.*, 2016, **14**(2), 380–389.
84 A. S. Genshaft, S. Li, C. J. Gallant, S. Darmanis, S. M. Prakadan and C. G. K. Ziegler, *et al.*, Multiplexed, targeted profiling of single-cell proteomes and transcriptomes in a single reaction, *Genome Biol.*, 2016, **17**(1), 188.
85 H. Gong, X. Wang, B. Liu, S. Boutet, I. Holcomb and G. Dakshinamoorthy, *et al.*, Single-cell protein-mRNA correlation analysis enabled by multiplexed dual-analyte co-detection, *Sci. Rep.*, 2017, **7**(1), 2776.
86 N. Altemose, A. Maslan, C. Rios-Martinez, A. Lai, J. A. White and A. Streets, μDamID: A Microfluidic Approach for Joint Imaging and Sequencing of Protein-DNA Interactions in Single Cells, *Cell Syst.*, 2020, **11**(4), 354–366.e9.
87 S. T. Gebreyesus, A. A. Siyal, R. B. Kitata, E. S. W. Chen, B. Enkhbayar and T. Angata, *et al.*, Streamlined single-cell proteomics by an integrated microfluidic chip and data-independent acquisition mass spectrometry, *Nat. Commun.*, 2022, **13**(1), 37.
88 S. Mayer, J. Chen, D. Velmeshev, A. Mayer, U. C. Eze and A. Bhaduri, *et al.*, Multimodal Single-Cell Analysis Reveals Physiological Maturation in the Developing Human Neocortex, *Neuron*, 2019, **102**(1), 143–158.e7.
89 R. J. Kimmerling, S. M. Prakadan, A. J. Gupta, N. L. Calistri, M. M. Stevens and S. Olcum, *et al.*, Linking single-cell measurements of mass, growth rate, and gene expression, *Genome Biol.*, 2018, **19**(1), 207.
90 E. Samiei, M. Tabrizian and M. Hoorfar, A review of digital microfluidics as portable platforms for lab-on a-chip applications, *Lab Chip*, 2016, **16**(13), 2376–2396.
91 A. Gérard, A. Woolfe, G. Mottet, M. Reichen, C. Castrillon and V. Menrath, *et al.*, High-throughput single-cell activity-based screening and sequencing of antibodies using droplet microfluidics, *Nat. Biotechnol.*, 2020, **8**(6), 715–721.
92 Q. Rezard, G. Perret, J. C. Gerbedoen, D. Pekin, F. Cleri and D. Collard, *et al.*, Developing A Mems Device for High-Throughput Multi-Parameter Single Cell Biophysical Analysis, in 2021 IEEE 34th International Conference on Micro Electro Mechanical Systems (MEMS). Gainesville, FL, USA, *IEEE*, 2021, 494–497.
93 B. Gong, Y. Zhou and E. Purdom, Cobolt: integrative analysis of multimodal single-cell sequencing data, *Genome Biol.*, 2021, **22**(1), 351.
94 R. Argelaguet, D. Arnol, D. Bredikhin, Y. Deloro, B. Velten and J. C. Marioni, *et al.*, MOFA+: a statistical framework for comprehensive integration of multi-modal single-cell data, *Genome Biol.*, 2020, **21**(1), 111.
95 Y. Hao, T. Stuart, M. Kowalski, S. Choudhary, P. Hoffman, A. Hartman, A. Srivastava, G. Molla, S. Madad, C. Fernandez-Granda and R. Satija, Dictionary learning for integrative, multimodal, and scalable single-cell analysis, bioRxiv, 2022.
96 A. Ravetto, P. D. A. Anderson, C. V. C. Bouten and J. M. J. den Toonder, Microfluidics for Single Cell Mechanical Characterization: A Review, *SM Journal of Biomedical Engineering*, 2017, 3(2), 1016.
97 A. C. Rowat, J. Lammerding and J. H. Ipsen, Mechanical Properties of the Cell Nucleus and the Effect of Emerin Deficiency, *Biophys. J.*, 2006, **91**(12), 4649–4664.
98 K. D. Nyberg, M. B. Scott, S. L. Bruce, A. B. Gopinath, D. Bikos and T. G. Mason, *et al.*, The physical origins of transit time measurements for rapid, single cell mechanotyping, *Lab Chip*, 2016, **16**(17), 3330–3339.
99 L. A. Lautscham, Migration in Confined 3D Environments Is Determined by a Combination of Adhesiveness, Nuclear Volume, Contractility, and Cell Stiffness, *Biophys. J.*, 2015, **109**(5), 900–913.
100 K. Alessandri, B. R. Sarangi, V. V. Gurchenkov, B. Sinha, T. R. Kießling and L. Fetler, *et al.*, Cellular capsules as a

tool for multicellular spheroid production and for investigating the mechanics of tumor progression in vitro, *Proc. Natl. Acad. Sci.*, 2014, **110**(37), 14843–14848.

101 L. J. Holt, O. Hallatschek and M. Delarue, *Methods Cell Biol.*, 2018, **147**, 215–231.

102 I. De Vlaminck and C. Dekker, Recent Advances in Magnetic Tweezers, *Annu. Rev. Biophys.*, 2012, **41**(1), 453–472.

103 S. Khakshour, T. V. Beischlag, C. Sparrey and E. J. Park, Probing Mechanical Properties of Jurkat Cells under the Effect of ART Using Oscillating Optical Tweezers, *PLoS One*, 2015, **10**(4), e0126548.

104 F. Ziemann, J. Rädler and E. Sackmann, Local measurements of viscoelastic moduli of entangled actin networks using an oscillating magnetic bead microrheometer, *Biophys. J.*, 1994, **66**(6), 2210–2216.

105 S. Khakshour, M. P. Labrecque, H. Esmaeilsabzali, F. J. S. Lee, M. E. Cox and E. J. Park, *et al.*, Retinoblastoma protein (Rb) links hypoxia to altered mechanical properties in cancer cells as measured by an optical tweezer, *Sci. Rep.*, 2017, **7**(1), 7833.

106 L. Chen, V. Maybeck, A. Offenhäusser and H. J. Krause, Implementation and application of a novel 2D magnetic twisting cytometry based on multi-pole electromagnet, *Rev. Sci. Instrum.*, 2016, **87**(6), 064301.

107 Y. Tanaka, K. Sato, T. Shimizu, M. Yamato, T. Okano and I. Manabe, *et al.*, Demonstration of a bio-microactuator powered by vascular smooth muscle cells coupled to polymer micropillars, *Lab Chip*, 2008, **8**(1), 58–61.

108 D. Hartono, Y. Liu, P. L. Tan, X. Y. S. Then, L. Y. L. Yung and K. M. Lim, On-chip measurements of cell compressibility via acoustic radiation, *Lab Chip*, 2011, **11**(23), 4072.

109 P. Augustsson, J. T. Karlsen, H. W. Su, H. Bruus and J. Voldman, Iso-acoustic focusing of cells for size-insensitive acousto-mechanical phenotyping, *Nat. Commun.*, 2016, **7**(1), 11556.

110 S. Zhong, W. Ding, L. Sun, Y. Lu, H. Dong and X. Fan, *et al.*, Decoding the development of the human hippocampus, *Nature*, 2020, **577**(7791), 531–536.

111 B. B. Lake, S. Chen, B. C. Sos, J. Fan, G. E. Kaeser and Y. C. Yung, *et al.*, Integrative single-cell analysis of transcriptional and epigenetic states in the human adult brain, *Nat. Biotechnol.*, 2018, **36**(1), 70–80.

112 Y. Liu, High-Spatial-Resolution Multi-Omics Sequencing via Deterministic Barcoding in Tissue, *Cell*, 2020, **183**(6), 1665.

113 D. P. Tabassum and K. Polyak, Tumorigenesis: it takes a village, *Nat. Rev. Cancer*, 2015, **15**(8), 473–483.

114 S. V. Sharma, D. Y. Lee, B. Li, M. P. Quinlan, F. Takahashi and S. Maheswaran, *et al.*, A Chromatin-Mediated Reversible Drug-Tolerant State in Cancer Cell Subpopulations, *Cell*, 2010, **141**(1), 69–80.

115 D. Ramazzotti, A. Lal, B. Wang, S. Batzoglou and A. Sidow, Multi-omic tumor data reveal diversity of molecular mechanisms that correlate with survival, *Nat. Commun.*, 2018, **9**(1), 4453.

116 M. A. Ortega, O. Poirion, X. Zhu, S. Huang, T. K. Wolfgruber and R. Sebra, *et al.*, Using single-cell multiple omics approaches to resolve tumor heterogeneity, *Clin. Transl. Med.*, 2017, **6**(1), 46.

117 I. C. Macaulay, C. P. Ponting and T. Voet, Single-Cell Multiomics: Multiple Measurements from Single Cells, *Trends Genet.*, 2017, **33**(2), 155–168.

118 O. Rozenblatt-Rosen, A. Regev, P. Oberdoerffer, T. Nawy, A. Hupalowska and J. E. Rood, *et al.*, The Human Tumor Atlas Network: Charting Tumor Transitions across Space and Time at Single-Cell Resolution, *Cell*, 2020, **181**(2), 236–249.

119 H. Yuan, M. Yan, G. Zhang, W. Liu, C. Deng and G. Liao, *et al.*, CancerSEA: a cancer single-cell state atlas, *Nucleic Acids Res.*, 2019, **8**(47), D900–D908.

120 M. J. T. Stubbington, O. Rozenblatt-Rosen, A. Regev and S. A. Teichmann, Single-cell transcriptomics to explore the immune system in health and disease, *Science*, 2017, **358**(6359), 58–63.

121 E. Papalexi and R. Satija, Single-cell RNA sequencing to explore immune cell heterogeneity, *Nat. Rev. Immunol.*, 2018, **18**(1), 35–45.

122 A. Unterman, T. S. Sumida, N. Nouri, X. Yan, A. Y. Zhao and V. Gasque, *et al.*, Single-Cell Omics Reveals Dyssynchrony of the Innate and Adaptive Immune System in Progressive COVID-19, *Nat. Commun.*, 2022, **13**(1), 440.

123 J. Fuzik, A. Zeisel, Z. Máté, D. Calvigioni, Y. Yanagawa and G. Szabó, *et al.*, Integration of electrophysiological recordings with single-cell RNA-seq data identifies neuronal subtypes, *Nat. Biotechnol.*, 2016, **34**(2), 175–183.

124 M. van den Hurk and C. Bardy, Single-cell multimodal transcriptomics to study neuronal diversity in human stem cell-derived brain tissue and organoid models, *J. Neurosci. Methods*, 2019, **325**, 108350.

125 K. Leonavicius, J. Nainys, D. Kuciauskas and L. Mazutis, Multi-omics at single-cell resolution: comparison of experimental and data fusion approaches, *Curr. Opin. Biotechnol.*, 2019, **55**, 159–166.

Clinical Infectious Diseases

MAJOR ARTICLE

Circulating Ubiquitous RNA, A Highly Predictive and Prognostic Biomarker in Hospitalized Coronavirus Disease 2019 (COVID-19) Patients

Thomas Bruneau,[1,a] Maxime Wack,[2,3,a] Geoffroy Poulet,[4,a] Nicolas Robillard,[1,a] Aurélien Philippe,[5,6] Pierre-Laurent Puig,[4] Laurent Bélec,[1,7] Jérôme Hadjadj,[8,9] Wenjin Xiao,[4] Julia-Linnea Kallberg,[4] Solen Kernéis,[10,11] Jean-Luc Diehl,[5,12] Benjamin Terrier,[7,8] David M. Smadja,[5,6] Valerie Taly,[4,b] David Veyer,[1,13,b] and Hélène Péré[13,b]

[1]Department of Microbiology, Assistance Publique Hôpitaux de Paris, Centre-Université de Paris (APHP.CUP) Hôpital Européen Georges Pompidou, Paris, France; [2]Department of Medical Informatics, Assistance Publique Hôpitaux de Paris, Centre-Université de Paris (APHP.CUP) Hôpital Européen Georges Pompidou, Paris, France; [3]Centre de Recherche des Cordeliers, INSERM, Université Sorbonne Paris Cité, Université de Paris, Information Sciences to Support Medicine, Paris, France; [4]Centre de Recherche des Cordeliers, INSERM, CNRS, Université Sorbonne Paris Cité, Université de Paris, Equipe labellisée Ligue Nationale contre le cancer, CNRS SNC 5096, Paris, France; [5]Hematology department, Assistance Publique Hôpitaux de Paris-Centre (AP-HP.CUP), Paris, France; [6]Université de Paris, Innovative Therapies in Hemostasis, INSERM, Paris, France, and Biosurgical Research Lab (Carpentier Foundation) European Georges Pompidou Hospital, Paris, France; [7]Université de Paris, INSERM U970, PARCC, Paris, France; [8]Department of Internal Medicine, National Referral Center for Rare Systemic Autoimmune Diseases, AP-HP CUP, Paris, France; [9]Université de Paris, Institut Imagine, INSERM, Laboratory of Immunogenetics of Pediatric Autoimmunity, Paris, France; [10]Equipe de Prévention du Risque Infectieux (EPRI), Assistance Publique Hôpitaux de Paris, Hôpital Bichat, Paris, France; [11]Université de Paris, INSERM, IAME, Paris, France; [12]Intensive Care Unit, Assistance Publique, Hôpitaux de Paris-Centre (APHP-CUP), Georges Pompidou European Hospital, Paris, France; and [13]Centre de Recherche des Cordeliers, INSERM, Université Sorbonne Paris Cité, Université de Paris, Equipe FunGest, Paris, France

Background. Approximately 15–30% of hospitalized coronavirus disease 2019 (COVID-19) patients develop acute respiratory distress syndrome, systemic tissue injury, and/or multi-organ failure leading to death in around 45% of cases. There is a clear need for biomarkers that quantify tissue injury, predict clinical outcomes, and guide the clinical management of hospitalized COVID-19 patients.

Methods. We herein report the quantification by droplet-based digital polymerase chain reaction (ddPCR) of the severe acute respiratory syndrome coronavirus 2 (SARS-CoV-2) RNAemia and the plasmatic release of a ubiquitous human intracellular marker, the ribonuclease P (RNase P) in order to evaluate tissue injury and cell lysis in the plasma of 139 COVID-19 hospitalized patients at admission.

Results. We confirmed that SARS-CoV-2 RNAemia was associated with clinical severity of COVID-19 patients. In addition, we showed that plasmatic RNase P RNAemia at admission was also highly correlated with disease severity ($P < .001$) and invasive mechanical ventilation status ($P < .001$) but not with pulmonary severity. Altogether, these results indicate a consequent cell lysis process in severe and critical patients but not systematically due to lung cell death. Finally, the plasmatic RNase P RNA value was also significantly associated with overall survival.

Conclusions. Viral and ubiquitous blood biomarkers monitored by ddPCR could be useful for the clinical monitoring and the management of hospitalized COVID-19 patients. Moreover, these results could pave the way for new and more personalized circulating biomarkers in COVID-19, and more generally in infectious diseases, specific from each patient organ injury profile.

Keywords. ddPCR; hospitalized COVID-19 patient; predictive and prognostic biomarkers; SARS-CoV-2 and RNAseP RNAemia; tissue/cell lysis biomarker.

Coronavirus disease 2019 (COVID-19) is a global public health problem that has already caused more than 3 million deaths worldwide. A wide spectrum of disease severity was rapidly described ranging from asymptomatic or mild diseases to respiratory failure and multiple organ dysfunction syndromes, or failure requiring intensive care management of patients and leading to a high mortality rate. In severe cases, clinical observations rapidly described a 2-step disease progression, starting with a mild-to-moderate presentation followed by a secondary respiratory worsening 9–12 days after the onset of first symptoms [1–3]. Clinical deterioration is typically dominated by worsening of respiratory symptoms, which are potentially concomitant with severe systemic organ failure, including cardiovascular, renal, and/or liver injuries [4–8]. Evidence tended to demonstrate that the second phase of COVID-19 was associated with a cytokine storm contributing to the development of acute respiratory distress syndrome (ARDS), systemic tissue injury, and multi-organ failure observed in severe cases of COVID-19 [9]. Approximately 5% of patients infected with severe acute respiratory syndrome coronavirus 2 (SARS-CoV-2)

Received 26 August 2021; editorial decision 29 November 2021; published online 11 December 2021.

[a]T. B., M. W., G. P., and N. R. contributed equally to this work.

[b]V. T., D. V., and H. P. contributed equally to this work.

Correspondence: H. Péré, Unité de Virologie, Service de Microbiologie, Hôpital Européen George Pompodou, 20-40 rue Leblanc 75015 Paris, France (helene.pere@aphp.fr).

Clinical Infectious Diseases® 2022;75(1):e410–7

https://doi.org/10.1093/cid/ciab997

require intensive care and admission for severe lung damage [7, 10] and 15–30% of patients hospitalized with COVID-19 develop ARDS [11, 12] leading to death in around 45% of cases [13]. Therefore, biomarkers that can quantify tissue injury, analyze disease pathogenesis, predict clinical outcomes, and guide the clinical management of hospitalized COVID-19 patients are clearly needed.

In recent years, the democratization of ultrasensitive technologies, such as droplet-based digital polymerase chain reaction (ddPCR), has fostered the development of circulating markers, making them suitable for several clinical applications. Recently, we and others provided evidence that highly sensitive quantification of SARS-CoV-2 RNAemia by ddPCR in peripheral blood could be a reliable marker of disease severity and that it could be used as a potential predictive biomarker of clinical worsening in COVID-19 patient follow-up in the second phase of COVID-19 pathology [14, 15]. Besides SARS-CoV-2 RNAemia, plasmatic release of ubiquitous human intracellular markers could be an accurate biomarker to evaluate tissue injury and cell lysis induced by COVID-19. In addition, we monitored the plasmatic release of the intracytoplasmic ribonuclease P (RNase P), targeting its H1 RNA catalytic part [16] to evaluate tissue injury and cell lysis induced by COVID-19 in this global study bringing together 2 cohorts of comparable COVID-19 patients hospitalized for respiratory deterioration during the first wave in Paris, France.

We herein report the quantification of SARS-CoV-2 RNAemia and circulating RNase P in the plasma of 139 COVID-19 hospitalized patients at admission. We evaluated the interest of both markers in specifying the degree of clinical severity of COVID-19 at admission and correlated them with clinical outcome of hospitalized COVID-19 patients during their medical follow-up.

METHODS

Study Design and Patients

A first cohort of 60 COVID-19 patients admitted to the Cochin-Port Royal Hospital, Paris, France, was primarily included; to complete and extend our previous observations, we further retrospectively included another series of 79 patients admitted to the European George Pompidou Hospital (HEGP), Paris, France, between 19 March 2020 and 26 June 2020 for COVID-19 during the first wave of the epidemic in France, for the quantification of SARS-CoV-2 plasma RNAemia and RNase P RNAemia by ddPCR. Inclusion criteria for COVID-19 inpatients were age between 18 and 80 years, diagnosis of COVID-19 according to World Health Organization (WHO) interim guidance (https://www.who.int/emergencies/diseases/novel-coronavirus-2019/technical-guidance/infection-prevention-and-control), and positive SARS-CoV-2 real-time PCR (RT-PCR) testing on a respiratory sample (nasopharyngeal swab or invasive respiratory sample). The clinical severity of COVID-19 was described according to the adaptation of the Sixth Revised Trial Version of the Novel Coronavirus Pneumonia Diagnosis and Treatment Guidance published on 19 February 2020 (http://www.kankyokansen.org/uploads/uploads/files/jsipc/protocol_V6.pdf). Mild cases were defined as patients with mild clinical symptoms (fever, myalgia, fatigue, and diarrhea) and no sign of pneumonia on thoracic computed tomography (CT) scan. Moderate cases were defined as patients with clinical symptoms associated with dyspnea and radiological findings of pneumonia on thoracic CT scan and requiring a maximum of 3 L/minute of oxygen. Severe cases were defined as respiratory distressed patients requiring over 3 L/minute of oxygen with no other organ failure. Critical cases were defined as patients requiring mechanical ventilation, into shock, and/or with other organ failures that required management in an intensive care unit (ICU). Biological collection and informed consent were approved by the Direction de la Recherche Clinique et Innovation (DRCI) and the French Ministry of Research (no. 2019-3677). The 2 cohorts conformed to the principles outlined in the Declaration of Helsinki, and received approval by the appropriate Institutional Review Board (Cochin-Port Royal Hospital, Paris, France; number AAA-2020-08018; European Georges Pompidou Hospital, Paris, France, SARCODO study: CPP 2020-04-048/ 2020-A01048-31/ 20.04.21.49318-ClinicalTrials.gov Identifier: NCT04624997).

RNA Extraction

Total plasma RNA (140 µL) was extracted using QIAamp® Viral RNA Mini Kit (QIAGEN®, Hilden, Germany), according to the manufacturer's instructions. The elution volume was 35 µL, and 10.5 µL of the elution were added to the RT-PCR mix for amplification [15].

Quantification of Plasmatic SARS-CoV2 RNA

Plasmatic SARS-CoV-2 RNAemia in each COVID-19 patient from HEGP cohort was quantified at admission by droplet-based Crystal Digital PCR™ (Stilla Technologies, Villejuif, France) on a Naica™ System (Stilla Technologies, Villejuif, France) using the following commercial RT-PCR amplification kit (Novel Coronavirus [2019-nCoV] Digital PCR Detection Kit, Apexbio™, Beijing, China), according to the manufacturer's instructions. The kit includes primers and FAM- and HEX-labeled probes specific to 2 distinct regions [ORF1ab and Nucleocapside (N) genes] of the SARS-CoV-2 positive strand RNA genome [15].

Quantification of Plasmatic RNase P

Ubiquitous plasmatic RNase P RNAemia from all COVID-19 patients of both cohorts was quantified using 10.5 µL of eluted RNA at each time point by droplet-based Crystal Digital PCR™ (Stilla Technologies, Villejuif, France) on the Naica™ System

(Stilla Technologies, Villejuif, France) using the following commercial RT-PCR amplification kit (Novel Coronavirus [2019-nCoV] Digital PCR Detection Kit, Apexbio™, Beijing, China), according to the manufacturer's instructions. The kit includes primers and a Cy5-labeled probe for the detection of RNase P detected on the third channel of the Naica™ system. RNase P positivity was necessary to validate the RT-PCR assay prior to any further analysis. The results were automatically analyzed using the "Crystal reader" and "Crystal Miner" software (Stilla Technologies). RNase P concentrations were finally calculated considering the extracted volume of plasma and expressed in copies per milliliter of plasma (cp/mL).

Statistical Analysis

Descriptive statistics were computed for the population at hospital admission. Quantitative variables were described as mean ± standard deviation (SD), if normally distributed, or median and interquartile range (IQR), otherwise. Categorical variables were described as group sizes and percentages.

Bivariate comparisons between clinical classes were computed using the Fisher exact test for categorical variables, 1-way analysis of variance (ANOVA) for continuous variables when all groups were normally distributed, and the Kruskal-Wallis ANOVA otherwise. When comparing control and COVID-19 patients, the Student *t* test was used for quantitative variables when both groups were normally distributed, and the Mann-Whitney rank-sum test was used otherwise.

The Cox proportional hazards model was used to evaluate the risk of death at inclusion between patients with low and high plasmatic RNase P concentration. Patients' clinical outcomes are presented using Kaplan-Meier curves.

Computations were performed using the R software, and the survival package for the Cox proportional hazards model. *P* values < .05 were considered statistically significant.

RESULTS

Patient Characteristics

Global and per-cohort demographic and clinical characteristics of the patients are shown in Table 1. Mean age was 58 years (SD = 14), and 78% were male. Patients in both cohorts were comparable, except for patients from Cochin-Port Royal Hospital cohort who were slightly younger (mean age 54 ± 13 vs. 62 ± 14 years) and presented less comorbidities (hypertension 30% vs 53%, chronic renal failure 3% vs 15%) at inclusion. The degree of severity of COVID-19 was categorized as mild-to-moderate in 37 (27%) patients, severe in 35 (25%) and critical in 67 (48%).

Correlation Between SARS-CoV-2 RNAemia, Clinical Severity, Invasive Mechanical Ventilation (IMV) and Pulmonary Severity at Admission

SARS-CoV-2 RNAemia by ddPCR was significantly correlated with clinical severity (respectively at a median of 25 (101) copy/mL; 36 (330) copy/mL in severe patients and 113 (528) copy/mL in critical patients) in hospitalized patients at admission (Figure 1A; $P = .021$). Plasma SARS-CoV-2 RNAemia was also correlated with mechanical ventilation status, with a higher concentration in IMV (median of 113 (528) copy/mL) than in nonventilated COVID-19 patients (median of 36 (199) copy/mL) (Figure 1B; $P = .012$). No correlation was found between SARS-CoV-2 RNAemia and pulmonary severity objected by CT scan at admission (Figure 1C; Kruskal-Wallis test, $P = .47$).

Correlation Between Plasmatic RNase P Concentration and Clinical Severity, Invasive Mechanical Ventilation, and Pulmonary Severity at Admission

Plasmatic RNase P concentration was highly correlated with clinical severity classes (Figure 2A; $P < .001$ on log values) and the invasive mechanical ventilation status (Figure 2B; $P < .001$), with median plasma RNase P concentration of 14345 copy/mL (IQR = 27 500 copy/mL) in non-IMV patients and 103 482 (192 500) copy/mL in IMV patients. Median plasma RNase P concentration in the control group of no disease patients (n = 18) was 3053 (1051) copy/mL. No correlation was found between RNase P RNAemia and pulmonary severity objected by CT scan at admission (Figure 2C; $P = .53$).

Clinical Outcome and Correlation With Baseline SARS-CoV-2 RNAemia and Plasmatic RNase P RNA Concentration

During hospitalization and clinical monitoring of COVID-19 patients, 27 of the 139 patients died. Plasma RNase P RNA concentration at hospital admission predicted overall survival of the hospitalized COVID-19 patients. Plasma RNase P RNA concentration >4.63 log copy/mL at admission (median value of the log plasma RNase P RNA concentration in the dataset) was significantly associated with death during follow-up (Hazard Ratio (4.6 95% confidence interval [CI]: 2.18, 9.80), $P = .0039$) (Figure 3), whereas SARS-CoV-2 RNAemia value did not predict mortality in our study (data not shown). Interestingly, the median of delay between elevated plasma RNase P RNA concentration (>4.63log copy/mL) and death was of 4 days. Intubated patients without deadly outcome despite a concentration of RNAse P superior to 4.63log cp/mL (n = 31) were finally extubated. Among the 16 moderate and severe patients with a concentration of RNAse P superior to 4.63log cp/mL, 50% of them presented a clinical deterioration, such as intensive care unit transfer during their hospitalization but with a final favorable clinical outcome.

DISCUSSION

We measured SARS-CoV-2 RNAemia and plasma RNase P RNA concentrations at admission in a cohort of 139 COVID-19 patients referred at the time of disease worsening. SARS-CoV-2 RNAemia was detectable in most hospitalized patients. These results confirmed previous data on the correlation between

Table 1. Demographic and Clinical Findings of 139 Patients Suffering From Coronavirus Disease 2019 (COVID-19) Hospitalized in Paris During the First Wave of the Epidemic

	N	%	Med	IQR
Age	139		58.61	17.30
Sex	139			
Women	31	22		
Men	108	78		
Classes	139			
Moderate	37	27		
Severe	35	25		
Critical	67	48		
DSO	139		11	5
Tobacco status	138			
Active smoking	4	2.9		
Never smoker	109	79		
Weaned smoker	25	18		
Cardiovascular history	135			
No	114	84		
Yes	21	16		
Hypertension	139			
No	79	57		
Yes	60	43		
Diabetes	139			
No	110	79		
Yes	29	21		
Cancer history	139			
No	126	91		
Yes	13	9.4		
Chronic renal failure	139			
No	125	90		
Yes	14	10		
Mechanical ventilation	67	48		
Pulmonary severity (% of lung involvement)	115			
<10%	12	10		
10–25%	22	19		
25–50%	46	40		
50–75%	29	25		
75–100%	6	5.2		
Death	139			
No	112	81		
Yes	27	19		

Abbreviations: DSO, delay from symptoms onset; IQR, interquartile range; Med, median.

viral RNAemia and clinical severity, showing higher viral loads in severe and even more in critical patients compared to the mild-to-moderate patients [14, 15, 17, 18].

We also observed that RNase P RNA concentration, a ubiquitous and aspecific human intracellular RNA marker, was also highly correlated with disease severity and invasive mechanical ventilation status in hospitalized COVID-19 patients, indicating a consequent cell lysis process in severe and critical patients.

Moreover, correlation between plasma RNase P RNA concentration > 4.63 log cp/mL at admission and overall survival pointed out the use of this quantitative biomarker as an accurate prognosis tool in hospitalized COVID-19 patients, in addition to routine collected clinical parameters. These observations reflect the powerful clinical value of plasma RNase P RNA as a surrogate biomarker of COVID-19-induced global cell/tissue damage and likely to underline the severity of COVID-19 pathology. The question of the influence of comorbidities on RNase P concentrations is important to ask. In our study, the proportion of patients with co-morbidities is equivalent the different clinical classes from moderate to critical classes (Supplementary Table 1A; test χ^2 p = NS). Moreover, the percentage of patients with comorbidities in the group with elevated RNaseP concentration (>median of 4.63 log copy/mL) is not statistically different from the percentage of patients with comorbidities in the group with RNaseP concentration below 4.63 log copy/mL (61% vs 48%,

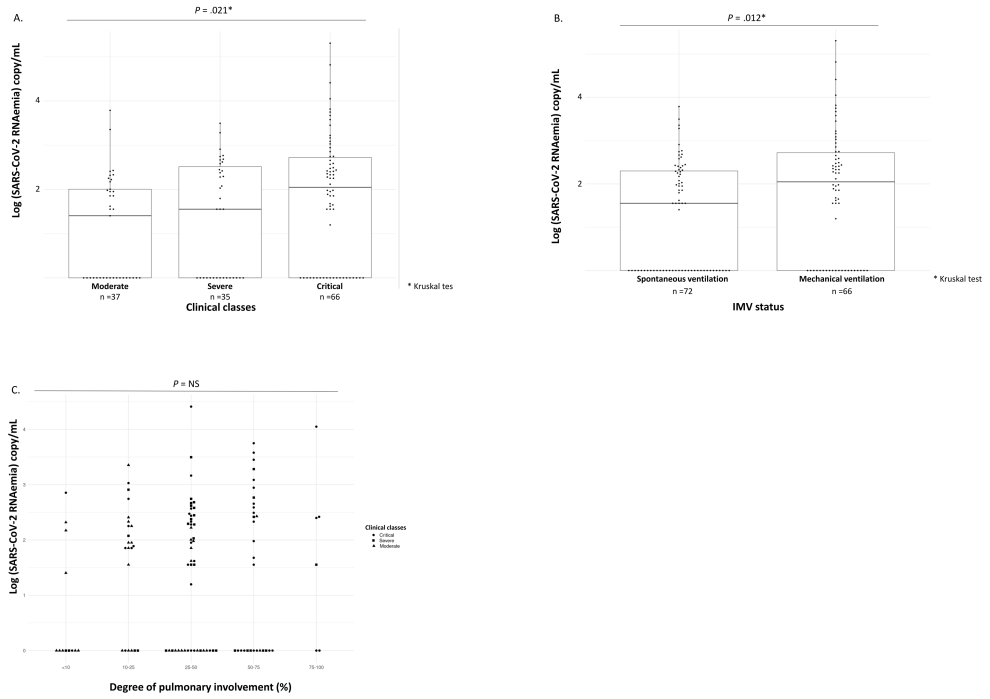

Figure 1. *A*, SARS-CoV-2 RNAemia concentrations in 139 patients suffering from COVID-19 according to clinical severity. *B*, SARS-CoV-2 RNAemia concentrations in 139 patients suffering from COVID-19 according to IMV status. *C*, Correlation between SARS-CoV-2 RNAemia concentrations (log copy/mL) and pulmonary severity. Abbreviations: COVID-19, coronavirus disease 2019; IMV, invasively mechanically ventilated; SARS-CoV-2, severe acute respiratory syndrome coronavirus 2.

respectively; Fisher test $P = .12$; Supplementary Table 1B). Therefore, RNase P RNA alone appears to be an interesting biomarker to determine COVID19 severity. Finally, even if additional experiments are needed to confirm our data, circulating RNase P appears as a highly predictive and prognostic marker in COVID19.

Our data strongly support the use of this cell-free RNA (cfRNA) quantification by ddPCR as a prognostic tool for early detection and monitoring of cell and tissue injury associated with COVID-19. Ordinarily, circulating endogenous RNA is considered to be extremely fragile and not sufficiently stable to represent a marker for monitoring, as compared to circulating DNA. However, in our study, the massive release of this endogenous marker seems to counteract the intrinsic weakness of RNA properties making it a marker of choice to quantify and monitor the degree of cell lysis in parallel of systemic viral invasion regarding the viral RNAemia. Another hypothesis would be that this particular RNA, as a subunit of a protein complex, may be more protected from degradation and therefore more easily detected and quantitated than classical RNA.

Solely based on CT-scan imaging, a lytic and an inflammatory process cannot be distinguished. However, a high plasma level of RNase P RNA may more likely indicate a lytic process rather than an inflammatory one. In the case of a more frequent lytic pulmonary process in COVID-19, our data can also explain and predict the longer mean stay in ICU observed in critical COVID-19 patients (15 days) compared to critical seasonal influenza infected patients (8 days) [19] that could correlate with the highest degree of pulmonary cell lysis in COVID-19 patients and thus a longer time to recover functional lung cells. Distinction between pulmonary lytic and inflammatory lesions could be of great interest for the clinical management of COVID-19 patients, especially in a therapeutic perspective, considering that anti-inflammatory treatments would be more efficient in the context of inflammatory process and maybe not in the context of lytic process. Finally, the delay between elevated RNase P (>4.63 log copy/mL) and death of patients of 4 days (from 0 to 28 days) also asks the question of refining timing therapeutics early to patients with elevated RNase P at admission. Obviously, such

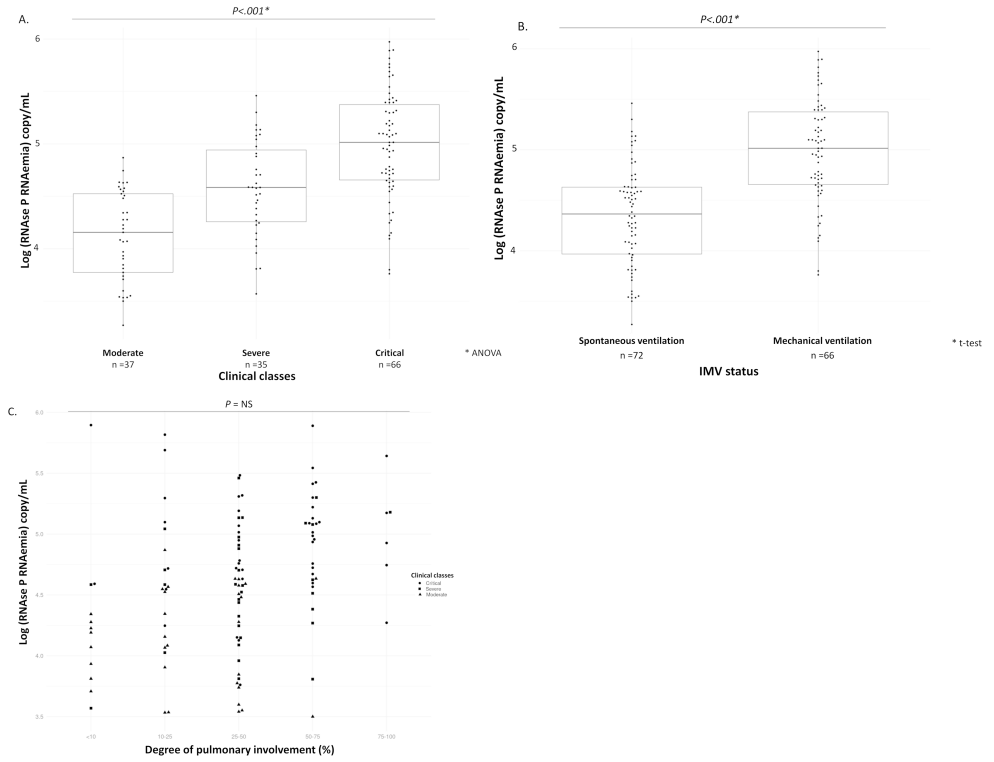

Figure 2. *A*, Plasmatic RNase P concentrations in 139 patients suffering from COVID-19 according to clinical severity. *B*, Plasmatic RNase P concentrations in 139 patients suffering from COVID-19 according to the IMV status. *C*, Correlation between RNase P RNAemia concentrations (log copy/mL) and pulmonary severity. Abbreviations: COVID-19, coronavirus disease 2019; IMV, invasively mechanically ventilated; SARS-CoV-2, severe acute respiratory syndrome coronavirus 2.

considerations could be applied to other pulmonary infectious pathologies.

The lack of correlation between RNase P RNA concentration and pulmonary severity estimated by the percentage of lung damage on CT-scan illustrates that radiologic lesions may not systematically reflect lytic process but both lytic and inflammatory lesions. This lack of correlation could also be explained by the fact that RNase P RNA level is not lung-specific and could therefore reflect extra-pulmonary tissue lysis. Therefore, we investigated the 9 patients (6 critical, 2 severe, and 1 moderate; Figure 2C) with plasmatic RNase P concentration above 4.63 log copy/mL in the two less severe pulmonary groups (<10% and 10–25%). Very interestingly, in 6 of these 9 specific patients for whom other biological information were available, we found signal for other organ injury such as kidney, liver, or heart with, respectively, elevated blood creatinine, ASAT/ALAT, or troponin levels. Finally, a possible hypothesis is that endogenous RNA release in plasma comes directly from infected cells lysis where SARS-CoV-2 replication occurs. However, we found 12 critical patients, with plasmatic RNase P levels above 4.63 log copy/mL but without any plasmatic SARS-CoV-2 RNA detection concurrently. In such patients, cfRNA plasmatic release could reflect the destruction of noninfected cells probably due to immunopathological mechanisms. As COVID-19 has been described as a systemic disease with multi-organ involvement, with regard to our preliminary results, we need further tissue-specific molecular markers to understand and specify the origin of observed cell lysis. In this way, Cheng et al. recently reported a blood test to quantify cell-, tissue-, and organ-specific injury due to COVID-19 [20]. The authors assessed the utility of this test to identify subjects with severe disease and report an evidence of injury to the lung and liver and the involvement of red blood cell progenitors associated with severe COVID-19. In their study, the concentration of cfDNA correlated with the

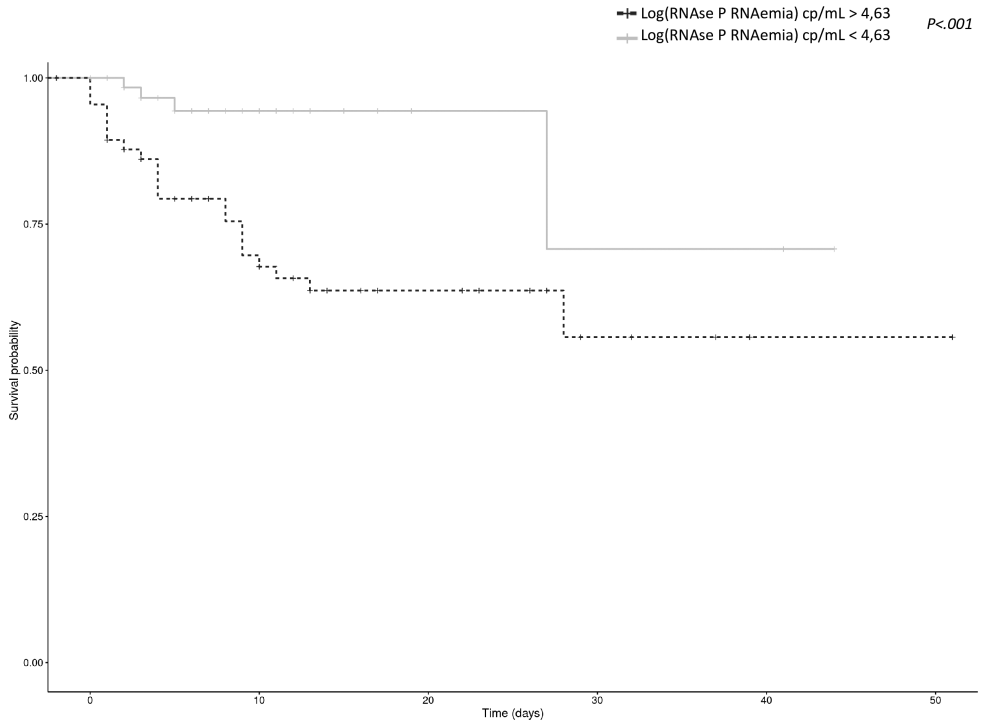

Figure 3. Overall survival regarding RNase P RNAemia (log copy/mL).

WHO ordinal scale for disease progression and was significantly increased in patients requiring intubation.

Such a reproducible molecular blood test allowing a more accurate assessment of clinical severity and prognosis in COVID-19 patients at hospital admission can also be used in clinical trials of candidate COVID-19 treatments to monitor their efficacy and select eligible patients.

Overall, monitoring of blood biomarkers could guide the management of hospitalized COVID-19 patients. Our results could pave the way for new and more personalized therapeutic options in infectious diseases, based on each patient-specific organ injury profile.

Supplementary Data

Supplementary materials are available at *Clinical Infectious Diseases* online. Consisting of data provided by the authors to benefit the reader, the posted materials are not copyedited and are the sole responsibility of the authors, so questions or comments should be addressed to the corresponding author.

Notes

Acknowledgments. The authors thank the patients who participated in the study, the clinical staff involved in their management.

Author contributions.

Experimental strategy design, experiments: T. B., G. P., M. W., N. R., V. T., D. V., and H. P.

Vital materials: A. P., J. H., S. K., P. L. P., J. L.D., B. T., and D. S.

Manuscript writing: M. W., L. B., V. T., D. V., and H. P.

Manuscript editing: T. B., M. W., G. P., N. R., A. P., L. B., W. X., J. L. K., J. L. D., B. T., V. T. , D. V., and H. P.

Financial support. This work was supported by IdeX AAP EMERGENCE-Université de Paris., Mécénat COVID-GHU APHP.CUP. V. T. acknowledges funding from Ligue Nationale Contre le Cancer (LNCC, Program "Equipe Labelisée LIGUE"; grant number EL2016.LNCC). This project has received funding from the European Union's Horizon 2020 research and innovation programme under the Marie Skłodowska-Curie grant agreement No 813786 (JK salary).

Potential conflicts of interest. G. P., P. L. P., V. T., D. V., and H. P. have a pending patent application related to this work (patent numbers PCT/EP2021/065863 and PCT/ EP20305571.0). V. T. reports Evodrops Innovative Training Network (ITN) (JK) and Erganeo (patent); reports serving on Scientific Board and as founder for Emulseo (no direct link to present work); reports serving on Scientific board and as founder for Methys Dx (no direct link to present work). S. K. reports research grants to their institution and consulting fees (2018–2019) from bioMérieux; reports payment/honoraria for education activities form bioMérieux (2019) and Accelerate Diagnostics (2018); reports travel support from bioMérieux (2019) and MSD (2019). All other authors report no potential conflicts.

All authors have submitted the ICMJE Form for Disclosure of Potential Conflicts of Interest. Conflicts that the editors consider relevant to the content of the manuscript have been disclosed.

References

1. Huang AT, Garcia-Carreras B, Hitchings MDT, et al. A systematic review of antibody mediated immunity to coronaviruses: kinetics, correlates of protection, and association with severity. Nat Commun **2020**; 11:4704.
2. Grasselli G, Zangrillo A, Zanella A, et al. Baseline characteristics and outcomes of 1591 patients infected with SARS-CoV-2 admitted to ICUs of the Lombardy Region, Italy. JAMA - J Am Med Assoc **2020**; 323:1574–81.
3. Li Q, Guan X, Wu P, et al. Early transmission dynamics in Wuhan, China, of Novel Coronavirus–infected pneumonia. N Engl J Med **2020**; 382:1199–207.
4. Huang C, Wang Y, Li X, et al. Clinical features of patients infected with 2019 novel coronavirus in Wuhan, China. Lancet **2020**; 395:497–506.
5. Yang F, Shi S, Zhu J, Shi J, Dai K, Chen X. Analysis of 92 deceased patients with COVID-19. J Med Virol **2020**; 92:2511–5.
6. Ronco C, Reis T, Husain-Syed F. Management of acute kidney injury in patients with COVID-19. Lancet Respir. Med **2020**; 8:738–42.
7. Wu Z, McGoogan JM. Characteristics of and important lessons from the Coronavirus Disease 2019 (COVID-19) outbreak in China: summary of a report of 72314 cases from the Chinese center for disease control and prevention. JAMA **2020**; 323:1239–42.
8. Chen N, Zhou M, Dong X, et al. Epidemiological and clinical characteristics of 99 cases of 2019 novel coronavirus pneumonia in Wuhan, China: a descriptive study. Lancet **2020**; 395:507–13.
9. Leisman DE, Ronner L, Pinotti R, et al. Cytokine elevation in severe and critical COVID-19: a rapid systematic review, meta-analysis, and comparison with other inflammatory syndromes. Lancet Respir. Med **2020**; 8: 1233–44.
10. Chen T, Wu D, Chen H, et al. Clinical characteristics of 113 deceased patients with coronavirus disease 2019: retrospective study. BMJ **2020**; 368: m1091.
11. Wiersinga WJ, Rhodes A, Cheng AC, Peacock SJ, Prescott HC. Pathophysiology, transmission, diagnosis, and treatment of coronavirus disease 2019 (COVID-19): a review. JAMA **2020**; 324:782–93.
12. Attaway AH, Scheraga RG, Bhimraj A, Biehl M, Hatipoğ Lu U. Severe covid-19 pneumonia: Pathogenesis and clinical management. BMJ **2021**; 372:n436.
13. Tzotzos SJ, Fischer B, Fischer H, Zeitlinger M. Incidence of ARDS and outcomes in hospitalized patients with COVID-19: a global literature survey. Crit Care **2020**; 24: 516.
14. Hadjadj J, Yatim N, Barnabei L, et al. Impaired type I interferon activity and inflammatory responses in severe COVID-19 patients. Science **2020**:eabc6027. Doi:10.1126/science.abc6027. Accessed 20 July 2020.
15. Veyer D, Kernéis S, Poulet G, et al. Highly sensitive quantification of plasma SARS-CoV-2 RNA sheds light on its potential clinical value. Clin Infect Dis **2020**; 73:e2890–7.
16. Jarrous N, Reiner R. Human RNase P: A tRNA-processing enzyme and transcription factor. Nucleic Acids Res **2007**; 35:3519–24.
17. Bermejo-Martin JF, González-Rivera M, Almansa R, et al. Viral RNA load in plasma is associated with critical illness and a dysregulated host response in COVID-19. Crit Care **2020**; 24:691.
18. Ram-Mohan N, Kim D, Zudock EJ, et al. SARS-CoV-2 RNAemia predicts clinical deterioration and extrapulmonary complications from COVID-19. Clin Infect Dis **2021**:ciab394.
19. Piroth L, Cottenet J, Mariet AS, et al. Comparison of the characteristics, morbidity, and mortality of COVID-19 and seasonal influenza: a nationwide, population-based retrospective cohort study. Lancet Respir Med **2021**; 9:251–9.
20. Cheng AP, Cheng MP, Gu W, et al. Cell-free DNA tissues of origin by methylation profiling reveals significant cell, tissue, and organ-specific injury related to COVID-19 severity. Med **2021**; 2:411–22.e5.